Magmatic and volcanic processes at near-ridge seamounts.

Jason P. Coumans

Department of Earth and Planetary Sciences

McGill University

Montréal, Québec, Canada

August 2015

A thesis submitted to McGill University in partial fulfillment of the requirements of the degree of Doctor of Philosophy

© Jason P. Coumans

ABSTRACT

Short chains of seamounts are common on the flanks of fast- to intermediate-spreading mid-ocean ridges in the Pacific Ocean. They have been studied extensively in order to understand the nature of off-axis magma production from melting anomalies in an upwelling mantle. One of the most important characteristics of near-ridge seamounts is their larger trace element and isotopic variation when compared to an adjacent spreading center. This larger variation implies that near-ridge seamount magma bypasses mixing and homogenization processes at the axial reservoir, thus making them excellent geologic targets for investigating heterogeneity in the depleted upper mantle. However, a number of important questions remain regarding the spatial and temporal scale of mantle heterogeneities, melting processes in the mantle, modification during transport to a shallow crustal reservoir, and magmatic processes occurring in a sub-caldera reservoir.

Taney Seamount-A, the largest and oldest seamount in the Taney near-ridge chain, exhibits complex shallow and surface processes such as repeated caldera collapses and explosive volcanism. Taney Seamount-A has four well-defined calderas with clear cross-cutting relationships, providing a relative chronology of volcanism. Therefore, Taney Seamount-A represents an ideal target site to investigate the unresolved questions outlined above. To address these questions, I have undertaken a multi-tiered approach incorporating submersible sampling and observation, geochemical analysis and modelling, and scaled analogue experiments.

Geochemical analyses and modelling of lavas, crystals, and melt inclusions show that the magmatic history beneath Taney Seamount-A is complex. Lavas vary from typical peridotite-derived mid-ocean ridge basalt compositions (N-MORB) to those with an apparent residual

garnet signature. Geochemical modelling suggests that the observed garnet signature can be reproduced by decompression melting of a MORB mantle peridotite which has been re-fertilized by garnet pyroxenite partial melts. Large anorthite-rich plagioclase crystals entrained in lavas have textural evidence of melt-rock interaction. Furthermore, melt inclusions within plagioclase exhibit a non mantle-derived geochemical signal indicating partial melting of a plagioclase-rich cumulate. Volatile saturation pressures from H₂O-CO₂ relationships in the melt inclusions imply that the large plagioclase crystals formed at the Moho. During transport from the mantle to a shallow magma reservoir, melts ponded at the Moho and underwent melt-rock interaction characterized by episodic partial melting, magma mixing, and recrystallization of plagioclase cumulates. Temporal changes of major elements of the lavas are consistent with an open-system sub-caldera reservoir that undergoes periodic caldera collapse, replenishment, shallow crystallization and eruption. In summary, the magmatic history at Taney Seamount-A comprises magma generation by melting of a two-component mantle, melt-rock interaction at the Moho, open system evolution in a sub-caldera magma reservoir, and caldera collapse.

Caldera collapse processes at Taney Seamount-A and other near-ridge seamounts are complex and dependent upon the orientation of the edifice above the magma reservoir. Scaled analogue experiments of caldera collapse at near-ridge seamounts suggests that an offset position of the volcanic edifice induces a trapdoor style of caldera collapse. This style of collapse is characterized by initial subsidence on a reverse fault resulting in the buildup of antithetic flexural tension in a hinge area and formation of a graben structure. The tilting of offset near-ridge seamount calderas towards the ridge axis, as well as structures observed on trapdoor basaltic volcanoes, suggest that complicated asymmetric caldera collapse processes illustrated in analogue experiments also occur in nature.

RÉSUMÉ

Dans l'Océan Pacifique, des chaînes courtes de monts sous-marins apparaissent fréquemment sur les flancs des dorsales océaniques à expansion rapide et intermédiaire. Ils ont été largement étudiés afin de comprendre la nature de la production de magma hors axe, caractéristique des anomalies de fonte ascendante du manteau Une des caractéristiques les plus importantes de monts sous-marins quasi-crête est la variation plus importante de leurs éléments de trace et de leurs isotopes par rapport aux centres d'expansion adjacents. Cette variation plus grande implique que le magma provenant de ces monts sous-marin évite de se mélanger et de s'homogénéiser dans le réservoir axiale, les rendant ainsi d'excellentes cibles géologiques pour étudier l'hétérogénéité dans le manteau supérieur appauvri. Cependant, un certain nombre de questions importantes demeurent quant à l'échelle spatiale et temporelle des hétérogénéités du manteau, les processus de fonte dans le manteau, la modification durant le transport à un réservoir de la croûte peu profonde, et les processus magmatiques se produisant dans un réservoir sous-caldeira.

Taney Seamount-A, le mont sous-marin le plus grand et le plus ancien dans la chaîne quasi-crête de Taney, présente des processus complexes sous la surface et à la surface, tels que l'effondrement répété de caldeira et un volcanisme explosif. Taney Seamount-A dispose de quatre caldeiras bien définis avec des relations transversales claires, fournissant une chronologie relative du volcanisme. Par conséquent, Taney Seamount-A représente un site idéal pour enquêter sur les questions en suspens mentionnées ci-dessus. Pour répondre à ces questions, je me suis engagé dans une démarche multi-niveaux intégrant un échantillonnage du sol sous-marin et l'observation, l'analyse et la modélisation géochimique et des expérimentations analogiques à l'échelle.

Les analyses géochimiques et la modélisation de laves, des cristaux, et des inclusions de fonte montrent que l'histoire magmatique sous Taney Seamount-A est complexe. La composition des laves varie entre la composition typique de dorsales basaltiques dérivés des péridotites (N-MORB) à une signature de grenat résiduel. La modélisation géochimique permet de croire que la signature de grenat observé peut être reproduite par fusion décompressive d'un manteau péridotite MORB qui a été réensemencé par fusion partielle de grenat pyroxénite. De gros cristaux de plagioclase riche en anorthite entraînés dans les laves créent une texture qui suggère une interaction entre le magma et les roches. En outre, des inclusions de fontes dans la plagioclase présentent un signal géochimique non dérivé du manteau, indiquant la fusion partielle d'un produit riche en plagioclase. La pression des saturations volatiles issues de relations H2O-CO2 dans les inclusions vitreuses implique que les grands cristaux de plagioclase se sont formés dans le Moho. Pendant le transport du manteau à un réservoir magmatique peu profond, des masses fondues se sont accumulées dans le Moho et ont subies une interaction fonte-roche caractérisée par une fusion partielle épisodique, un mélange de magmas, et la recristallisation de cumulats de plagioclase. Les changements temporels des éléments majeurs des laves sont compatibles avec un réservoir sous-caldeira à système ouvert qui subit un effondrement périodique de la caldeira, le réapprovisionnement, la cristallisation superficielle et des éruptions. En résumé, l'histoire magmatique au Taney Seamount-A comprend la production de magma en fusion d'un manteau à deux composants, l'interaction fonte-roche au Moho, l'évolution de système ouvert dans un réservoir de magma sous-caldeira, et des effondrements de la caldeira.

Des processus d'effondrement caldeira à Taney Seamount-A et d'autres monts sousmarins quasi-crête sont complexes et dépendent de l'orientation de la structure au-dessus du réservoir de magma. Des expérimentations analogiques à l'échelle de l'effondrement de caldeira de monts sous-marins quasi-crête suggère qu'une position décalée de l'édifice volcanique induit un style d'effondrement de la caldeira trapdoor. Ce style d'effondrement est caractérisé par la subsidence initiale d'une faille inversée provoquant l'accumulation de la tension de flexion antithétique dans une zone charnière et la formation d'une structure de graben. Le basculement de caldeiras décalées provenant de monts sous-marins quasi-crête vers l'axe de la crête, ainsi que les structures observées sur les volcans basaltiques trapdoor, suggèrent que les processus d'effondrement asymétriques complexe de la caldeira illustrés dans les expérimentations analogues sont représentatifs des évènements observés dans la nature.

CONTRIBUTIONS OF AUTHORS

The thesis is manuscript-based, each of the main chapters is a manuscript that has been either published or will be submitted to scientific journals. I am the main author on each of these chapters. John Stix, my primary research supervisor, is a co-author on all three chapters. William Minarik, my co-supervisor, is a co-author on the first two chapters. David Clague, a co-author on the first two chapters, provided the samples and was the chief scientist on the Taney Seamounts expedition. Graham Layne provided assistance with the SIMS trace element measurements at Memorial University Newfoundland. Nobu Shimizu provided assistance with SIMS volatile element analyses. John Stix, William Minarik, David Clague and Graham Layne provided advice on development of ideas and assisted with editing. I developed the approaches used in the discussions and models proposed in each paper. I performed all chemical analysis and designed / performed all experiments used in these papers. As the main investigator for each of these papers, I performed all sample observations, data acquisition, writing, table and figure design.

Acknowledgements:

First and foremost I would like to thank my primary supervisor, John Stix, for his constant and continued support for my project. He was always available to assist me at all junctions of this project, and for that I am very grateful. I would also like to think his family, Dora, Adam, Ben, Skitty and Mika for hosting the "volcano" group and our occasional raucous behaviour.

I would like to extend a special thank you to David Clague, for without him this project would not exist. Furthermore, he is the most knowledge oceanic volcanologist I know, and I am grateful for his assistance. I would also like to thank the scientific crew of the Taney Expedition (Jenny Paduan, Lonny Lundsten, Issy Yeo, Ryan Portner, Lucas Koth, Craig McClain, Justine Jackson-Ricketts, and Sarah Hardy) for their hard work and interesting conversations.

I would like to thank William Minarik, who was very supportive and always available to have impromptu conversations about geochemical data whenever I knocked on his door, even if he was busy with his own work. Without his technical expertise, it would have been quite difficult to obtain the LA-ICPMS data from GEOTOP. I would like to thank Lang Shi, Brian Monteleone, Glenn Piercey, Graham Layne, Nobu Shimizu and André Poirier for their technical skills during geochemical analysis. I would like to thank Anne-Sophie Berg, Philip Lypaczewski, Sarah Bodeving and Rowan Wollenberg for assistance with experiments.

I would like to thank everybody in the volcano group (Gregor Lucic, Brandon Bray, Charlie beard an Kalina Malowany) for their close support over the years. I would also like to thank the entire department of Earth and Planetary Sciences for making EPS such a wonderful place to study. I would like to give a big shout-out to the STONERS and TUFF SCHIST hockey

teams, and all of their players. I have had a wonderful 5 years playing for the stoners and coaching the tuff schist.

I would like to thank my family (Peter, Louise, Steven, Mark) who have supported me since the very beginning. This thesis is dedicated to my late mother (Laurie Ellen Chess-Coumans) and my late grandfather (Dr. Gordon Frederick Chess).

Table of contents:

Abstractii
Résuméiv
Contributions of authorsvii
Acknowledgements viii
Table of contentsx
List of tablesxvii
List of figures
List of supplementary information
General introduction1
INTRODUCTION
Near-ridge seamounts
Mantle heterogeneity and melting processes at seamounts
Melt modification during transport to the seafloor
Sub-caldera magmatic processes and caldera collapse
THE TANEY SEAMOUNTS AND THESIS RATIONALE
THESIS ORGANIZATION7
REFERENCES9
Link to Chapter 1

Chapter 1	13
ABSTRACT	14
INTRODUCTION	15
FIELD AREA, SAMPLING AND STRATIGRAPHY	18
Taney Seamounts	18
Relative Stratigraphy of Taney Seamount-A	20
METHODOLOGY	22
Sampling by remotely operated vehicle (ROV)	22
Sample preparation	23
Electron microprobe analysis	24
Whole-rock inductively coupled plasma mass-spectrometry and X-ray fluorescence	· 25
Laser-ablation inductively coupled plasma mass-spectrometry	25
Secondary ion mass spectrometry (SIMS)	26
RESULTS	27
Petrography	27
Major and trace element compositions	28

Chemostratigraphy	31
DISCUSSION	32
Crystallization	33
Lower oceanic crustal assimilation	35
Assimilation of a plagioclase cumulate	37
Diffusive exchange during percolation of melt through a plagioclase cumulate matrix	38
Mantle source and partial melting	42
Model 1: Deeper melt segregation	44
Model 2: Role of garnet pyroxenite and a mixed mantle lithology	46
A MODEL FOR MAGMA EVOLUTION BENEATH TANEY SEAMOUNT-A	51
CONCLUSIONS	52
ACKNOWLEDGEMENTS	54
REFERENCES	54

Link to Chapter 2	123
Chapter 2	124
ABSTRACT	125
INTRODUCTION	126
STUDY AREA	128
MATERIALS AND METHODS	
Sampling and Preparation	130
Electron microprobe analysis	130
Secondary ion mass spectrometry	131
Melt inclusion post-entrapment correction	135
RESULTS	136
Petrography	136
Major element compositions	137
Trace element compositions	138
Volatile element compositions	139
Chlorine and fluorine	139

CO_2 and H_2O	140
Sulfur	140
DISCUSSION	141
High-Mg melts in calcium-rich plagioclase	141
Crystallization depths	143
Melt-rock interaction at the Moho	143
Modelling the melt-cumulate interaction	145
A PETROGENETIC MODEL	148
Stage 1: Melt ponding and crystallization at the Moho	149
Stage 2: Melt replenishment and injection into the cumulate pile	150
Stage 3: Melt mixing and crystallization	151
Stage 4: Entrainment of plagioclase crystals during porous flow	151
Application to nature	152
CONCLUSIONS	153
ACKNOWLEDGEMENTS	155
REFERENCES	156

Link to Chapter 3	210
Chapter 3	211
ABSTRACT	212
INTRODUCTION	213
METHODOLOGY	215
Scaling	215
Experimental Setup	218
Laser scanning	219
Digital particle image velocimetry	220
RESULTS	221
Caldera development	221
Completely offset volcanic edifice	221
Centered volcanic edifice	222
Offset volcanic edifice (10 cm and 20 cm offsets)	
Vertical cross sections and fault maps	224

Digital particle image velocimetry	
DISCUSSION	226
Centrally-located and fully offset calderas on volcanic edifices	
Partial offset calderas	229
Fault mechanics	230
Application to near-ridge seamounts	232
CONCLUSIONS	235
ACKNOWLEDGEMENTS	236
REFERENCES	
General conclusions	255
The main findings of this thesis	
Contributions to knowledge	256
Tonics for future research	257

List of tables:

Chapter 1:

Table 1: Major and trace element data for volcanic glasses from Taney Seamount-A 63-66
Table S1.1: List of standards used in electron microprobe analysis
Table S1.2: Reproducibility and accuracy of the electron microprobe for VG-2
Table S1.3: Reproducibility and accuracy for trace elements using the ICP-MS linked scan
method for P1326-2
Table S1.4: Reproducibility and accuracy for trace elements using the ICP-MS deflector method
for P1326-2
Table S1.5: Calibration standards for SIMS analysis
Table S1.6: Reproducibility and accuracy for CO ₂ and H ₂ O using SIMS for P1326-2 91
Table S2.1: Major element data for volcanic glasses from Taney Seamounts-B and C 92-93
Table S2.2: Major and trace element data for whole rocks from Taney Seamount-A 94-97
Table S2.3: Major and trace element data for whole rocks from
Taney Seamounts-B and C
Table S3.1: Corrected volatile concentrations for plagioclase melt inclusions and host volcanic
glass

Table S4.1: Mathematical model notation	.06
Table S4.2: Model chemical parameters	.11
Table S4.3: Model physical parameters	.11
Table S4.4: Sensitivity analysis	.12
Table S5.1: Model compositions for DMM and re-fertilized peridotite	.15
Table S5.2: Partition coefficients from experiments at 3 GPa between G2 eclogite and basaltic	
melt from Perterman et al., (2004)	16
Table S6.1: Parameters for fractional crystallization model	.18
Chapter 2:	
Table 1: Corrected major, trace, and volatile element data for melt inclusions and matrix glasse	es
from Taney Seamount-A	68
Table 2: Plagioclase major element data from Taney Seamount-A	.71
Table S1.1: List of standards	.86
Table S1.2: Reproducibility and accuracy of the electron microprobe for VG-2	.87
Table S1.3a: Reproducibility and accuracy of trace elements by SIMS for P1326-2	.88
Table S1.3b: Reproducibility and accuracy of trace elements by SIMS for standard 73 1	.89
Table S1.4: reproducibility and accuracy of volatile elements by SIMS for P1326-2 1	.90
Table S1.5: Compositions of standards used for volatile element calibration	91

Table S2.1: Major, trace and volatile element data for melt inclusions and matrix glasses f	rom
Taney Seamount-A	.95-198
Table S3.1: partition coefficients used for post entrapment crystallization correction	200
Table S4.1: partition coefficients used for alphaMELTS equilibrium melting models	204
Table S4.2: Average mineral compositions from lower crustal rocks at Hess Deep	204
Table S4.3: Comparison between bulk and alphaMELTS solidus equilibrated mineral mod	les and
compositions	205-206

List of figures:

Chapter 1:

Figure 1: Geologic location	. 67
Figure 2: Taney-A sample map	. 68
Figure 3 Images of field area	. 69
Figure 4: Stratigraphic column70)-71
Figure 5: False colour calibrated backscattered electron images of large plagioclase crystals	. 72
Figure 6: Plagioclase composition histogram	. 73
Figure 7: Major element compositional variations of Taney Seamount-A74	1 -75
Figure 8: Laser ICP-MS trace element plots of the Taney Seamount-A volcanic glasse76	5-77
Figure 9: Trace element and rare earth element plots normalized to	
average Pacific MORB78	3-79
Figure 10: Chemostratigraphy80)-81
Figure 11: Results from numerical diffusion models	. 82
Figure 12: One-component melting model	. 83
Figure 13: Pyroxenite partial melt mixing model	. 84
Figure 14: Two-component melting model	85

Figure 15: Magmatic architecture of Taney Seamount-A	86
Figure S2.1: Comparison between glass and whole-rock trace element analyses	100
Figure S3.1: Drift in water concentrations of P1326-2	103
Figure S3.2: Post entrapment crystallization correction	104
Figure S3.3: Dissolved CO ₂ and H ₂ O contents in melt inclusions and host glasses	105
Figure S4.1: Sensitivity analysis for diffusion model parameters	113
Figure S5.1: Sensitivity analysis of alphaMELTS modelling	-117
Figure S6.1: Best fit fractional crystallization model using CaO and Al ₂ O ₃	119
Figure S6.2: Fractional crystallization models using the geochemical modelling program	
Petrolog3	120
Chapter 2:	
Figure 1: Geologic location	172
Figure 2: Electron backscattered images of large plagioclase crystals in glassy	
pillow margins	173
Figure 3: Transmitted light photomicrographs of melt inclusions in plagioclase crystals	174
Figure 4: Major element variations of Taney Seamount-A plagioclase melt inclusions 175-	-176
Figure 5: SIMS trace element plots of the Taney Seamount-A melt inclusions and lavas	177
Figure 6: Trace element spidergrams normalized to PUM	178

Figure 7: Volatile element variations for melt inclusions	180
Figure 8: Major element variations for lavas and melt inclusions from various systems	181
Figure 9: Melt inclusion saturation depths.	182
Figure 10: Modelling results of a cumulate equilibrium partial melting array	183
Figure 11: Trace element results of the best fit melting model using two sets of partition	
coefficients	184
Figure 12: Schematic diagram of magmatic processes at Moho depths	185
Figure S1.1: Known standard compositions versus measured isotope ratios	192
Figure S1.2: Drift in water concentrations of P1326-2	193
Figure S1.3: Full SIMS volatile analysis block	194
Figure S3.1: Post entrapment crystallization correction	201
Figure S3.2: Histogram of calculate post entrapment crystallization percentages	202
Figure S4.1: The differences between the alphaMELTS equilibration calculation and the mine	ral
mixing model	207
Chapter 3:	
Figure 1: DEM image of the Taney Seamounts	240
Figure 2: Experimental setup	241

Figure 3	3: Digital	elevation m	naps (DEM)) of select	experiments at
5		010 / 0001 011 11		, 01 501000	p

2.5 minute increments	242
Figure 4: The subsidence evolution of select experiments during each	
2.5 minute increment	244
Figure 5: The fault progression for select experiments for each	
2.5 minute increment	245
Figure 6: Final fault maps of select experiments	246
Figure 7: Cross sections and plan view images of select experiments	247
Figure 8: DPIV results	248
Figure 9: Close up images of the graben structures	249
Figure 10: Schematic diagrams for fault mechanics observed in selected experiments	250
Figure 11: Digital elevation maps from a ridge perspective of near-ridge seamount chains in th	ıe
northeast Pacific Ocean	251
Figure 12: Geological map from Reynolds <i>et al.</i> , (1995) of the western part of Sierra Negra's	
summit	252

List of supplementary information:

Chapter 1:

S1: Standard and error analysis for volcanic glass, plagioclase and melt inclusion analyses	87
S2: Additional glass and whole rock chemical analyses	92
S3: Volatile data from SIMS microprobe	. 101
S4: Numerical model for diffusive exchange during percolation of melt through a plagio	clase
cumulate matrix.	. 106
S5: alphaMELTS mantle source modelling parameters	. 114
S6: Fractional crystallization models	. 118
Chapter 2:	
S1: Standards, error analysis, and volatile calibration	. 186
S2: Melt inclusion and matrix glass data not corrected for post entrapment crystallization	. 195
S3: Post entrapment crystallization correction	. 199
S4: Parameters for alphaMELTS modelling.	. 200
Chapter 3:	
S1: Reproducibility of experiments	. 253

INTRODUCTION

Mid-ocean ridges are the largest continuous volcanic features on Earth and represent approximately 70% of Earth's volcanic activity (Crisp, 1984). A large fraction of the documented volcanic output at mid-ocean ridges occurs at the ridge axis, which has led to an axial-centric focus on studies of magmatic activity. However, recent observations of off-axis volcanism at fast-spreading ridges, such as the East Pacific Rise (Waters *et al.*, 2013), and ultraslow-spreading ridges, such as the Southwest Indian Ridge (Standish & Sims, 2010) demonstrate that off-axis magmatic activity is an important and under-appreciated component of mid-ocean ridge systems. At fast- to intermediate-spreading ridges, which are more magmatically robust than slower spreading ridges, off-axis volcanism is prevalent and manifested as pillow mounds, ridges, extensive lava fields, seamounts and seamount chains. The seismic imaging of a network of melt bodies at a distance of 4-8 km from the East Pacific Rise axis further supports the importance of off-axis volcanism as a component of the mid-ocean ridge system (Canales *et al.*, 2012).

Near-ridge seamounts

Seamounts and seamount chains which formed adjacent to fast- to intermediate-spreading ridges are the most abundant types of seamounts on earth, numbering several orders of magnitude higher than hotspot-related volcanoes (Scheirer & Macdonald, 1995). They are formed by decompression melting of the mantle near fast- to intermediate-spreading mid-ocean ridges, but their relationship with the spreading center is not entirely clear. The observation that young Pacific seamount chains are commonly asymmetric about the ridge axis, aligned with subaxial asthenophere flow vectors and constructed in a region 5-30 km from the axis has led

researchers to the suggestion that they are created by a melting anomaly embedded in the upwelling mantle around a mid-ocean ridge (Clague *et al.*, 2000). This region of near-ridge seamount formation has a relatively thin lithosphere and extensive ridge parallel faulting, which probably provide pathways for magma generated at the melting anomaly to migrate to the surface.

Advances in bathymetric mapping and sampling by dredge and remotely operated vehicle (ROV) have enabled more detailed studies, allowing investigators to better understand the nature of off-axis volcanism. The key observation from these studies is that near-ridge seamount basalts are more geochemically variable in terms of isotopes and trace elements than mid-ocean ridge basalts (MORB) erupted at adjacent spreading axes. For example, a study of a single near-ridge seamount basalt in the Pacific Ocean has documented a trace element and isotopic variability that exceeds the nearby spreading ridge, and is comparable to the range of all near-ridge seamounts investigated to date (Brandl et al., 2012). Researchers have suggested that the this variability of near-ridge seamounts is due to a separate plumbing system that bypasses the mixing and homogenization processes suggested to occur at the ridge axis. Therefore, studies of near-ridge seamounts are important because they provide a mechanism to investigate mantle heterogeneity far from hot spots. However, questions still remain regarding the spatial and temporal scale of mantle heterogeneity and melting processes beneath seamounts, modification of melts during transport to the seafloor, and sub-caldera magmatic processes. Hence the focus of this thesis is to investigate these questions at the Taney Seamounts, a near-ridge chain in the northeast Pacific ocean.

Mantle heterogeneity and melting processes at seamounts

Zindler et al. (1984) was the first study to utilize the trace element and isotopic variability of near-ridge seamounts adjacent to the East Pacific Rise to identify chemical heterogeneity in the upper mantle. The aforementioned study also proposed that the ridge axis acts as a filter which homogenizes the chemical variability of the mantle, and hypothesized that near-ridge seamounts have a plumbing system which bypasses the ridge axis. Subsequent studies utilized the geochemical variability of near-ridge seamounts in order to investigate the origin of chemical heterogeneity and melting processes beneath seamounts (Batiza et al., 1990, Brandl et al., 2012, Fornari et al., 1988a, Niu & Batiza, 1997, Niu et al., 2002). The prevailing view is that chemical heterogeneity in the mantle is created by the recycling of subducted material resulting in the formation of a trace element enriched component within a trace element depleted upper mantle matrix. The formation mechanism of the enriched component is contentious. The heterogeneities in the mantle are argued to be created by either low degree slab melts which metasomatise the depleted mantle (Donnelly et al., 2004), or mafic veins formed by stretching and thinning of subducted oceanic crust (Sobolev et al., 2007). Regardless of the exact mechanism or mechanisms, the resulting model is a two-component mantle with enriched mafic heterogeneities (pyroxenite) within a depleted peridotite matrix. Therefore, current studies of near-ridge seamounts focus on the origin of the enriched component and the implications of melting a twocomponent mantle (e.g., Brandl et al. (2012)).

Melt modification during transport to the seafloor

The nature of oceanic crust accretion has been an important aspect of mid-ocean ridge research. It was originally hypothesized that all phenocrysts that make up the oceanic crust crystallize in a shallow melt lens and then subside downward and/or outward to create the lower oceanic crust, referred to as the 'gabbro glacier'. This model has been challenged by a more distributed accretion model where crystallization occurs over a range of depths (Kelemen *et al.*, 1997). Recent studies utilizing volatile analyses of melt inclusions and seismic studies at fast- to intermediate-spreading ridges have identified melt reservoirs as deep as the crust-mantle boundary (Canales *et al.*, 2009, Wanless & Shaw, 2012). Therefore, the top-down 'gabbro glacier' model has fallen out of favour for a model where oceanic crust is formed by continuous crystallization through the crust and/or injection of mantle-derived magma into a series of sills that crystallize to various degrees. The significance is that crustal accretion by distributed melt injections imparts an increased likelihood for melt-rock interactions.

Many studies of oceanic basalts from mid-ocean ridges and their adjacent seamounts commonly make the assumption that melts erupted at the seafloor have been primarily modified by fractional crystallization. Therefore, measured compositions are frequently back-calculated in order to reconstruct mantle melt compositions (Klein & Langmuir, 1987). However, some studies of oceanic plutonic rocks suggest that interactions occur between melts generated in the mantle and the oceanic crust which can be significant (Bedard *et al.*, 2000). Various melt-rock interaction processes have been proposed utilizing plutonic rocks, phenocryst melt inclusions, and xenoliths. Although each proposed model is unique, they can generally be grouped into assimilation processes (Danyushevsky *et al.*, 2004), and porous flow interaction (Saal *et al.*, 2007). Assimilation processes in oceanic environments include partial melting / dissolution of

oceanic crustal material followed by mixing. Porous flow processes involve chemical diffusion associated with melt-crystal disequilibrium. Thus, studies of oceanic systems should account for the potential of melt-rock interaction before making statements about mantle processes.

Sub-caldera magmatic processes and caldera collapse

An important paradox in the study of near-ridge seamounts is the nature of the magmatic system which influences the construction and destruction of the volcanic edifice. Early geochemical studies observed that near-ridge seamount lavas have generally undergone less crystallization when compared to the adjacent spreading ridges. These early observations led some researchers to suggest that processes involving a shallow crustal reservoir are not important (Fornari *et al.*, 1988b). Yet, morphological studies clearly indicating the presence of substantial caldera structures in addition to explosive volcanic deposits on many near-ridge seamounts suggest that shallow magma reservoirs are indeed present and important. In order to relate primitive melt compositions to physical evidence for shallow magmatic activity, Clague *et al.* (2000) suggested that melts simply pass through shallow crustal reservoirs quickly. Therefore, substantial volumes of melt are delivered to the volcano episodically, creating a shallow reservoir from which magma either erupts to the surface, solidifies within the crust, or intrudes laterally inducing a caldera collapse.

Caldera collapse has been widely observed at basaltic volcanoes and is frequently attributed to lateral magma drainage. Examples include the caldera collapse at Miyakejima in 2000 which was attributed to a northwestward dyke injection (Ueda *et al.*, 2005), and the 1968 caldera collapse at Fernandina volcano in the Galápagos islands, where no explosive deposits

were observed (Stix & Kobayashi, 2008). Basaltic volcanoes can have variable styles of caldera collapse. For example, piston style collapse occurred at Miyakejima when the roof of the magma reservoir subsided as a coherent symmetrical block. By contrast, trapdoor collapse observed at Sierra Negra caldera represents asymmetric subsidence of the coherent caldera block (Jónsson *et al.*, 2005). Chaotic or piecemeal caldera collapse occurs when a block does not remain intact during subsidence.

Little is known about the style of caldera collapse that occurs at near-ridge seamounts, because access is limited and their calderas are largely infilled by later lavas. Physical observations indicate that caldera collapse at the seamounts occurs when the volcanic edifice is centered over the magma reservoir, and when the edifice is offset relative to the magma reservoir due to plate motion (Hammond, 1997). Furthermore, analogue studies of caldera collapse suggest that topography plays a role in caldera collapse dynamics (Lavallée *et al.*, 2004). Therefore, how the offset of a near-ridge volcanic edifice affects caldera collapse dynamics is an important question which needs to be addressed.

THE TANEY SEAMOUNTS AND THESIS RATIONALE

The Taney Seamounts are a linear chain of near-ridge seamounts off the coast of California which were associated with the now subducted Farallon spreading centre. The chain consists of five volcanoes, Taney-A through Taney-E, labeled from oldest to youngest under the assumption that the seamounts migrate away from the ridge. The morphology of the seamount edifices resemble truncated cones with volumes ranging from 11 km³ (Taney-E) to 187 km³ (Taney-A). The largest and oldest seamount in the chain (Taney-A) is unique because of

modification by a series of at least four caldera collapses. Each successive caldera collapse truncates the previously formed caldera and exposes infilled lavas on near vertical walls, resulting in a step-like appearance breached towards the ridge axis.

The presence of at least four calderas with clear cross-cutting relationships at Taney Seamount-A is unique among documented near-ridge seamounts and provides an ideal target to investigate complex magmatic processes at the spatial scale of a single seamount. This thesis utilizes a multi-tiered approach incorporating submersible observation and stratigraphic sampling by ROV, geochemical analysis of lavas and crystals, and scaled analogue experiments of caldera collapse in order to address three unresolved questions at near-ridge seamounts:

- 1. What is the nature of the magmatic source and what are the processes responsible for magma genesis?
- 2. What is the nature and extent of melt-rock interaction during melt transport to the shallow magma reservoir?
- 3. How does the presence and orientation of a volcanic edifice affect caldera collapse dynamics at near-ridge seamounts?

THESIS ORGANIZATION

This thesis is divided into a general introduction which includes a literature review, three main chapters, and a concluding chapter. Each of the three main chapters is a manuscript which has either been published, submitted, or is intended to be submitted to scientific journals. The

final concluding chapter summarizes the main discoveries and contributions to the scientific community and provides recommendations for future work.

Chapter 1 is a characterization of the magmatic architecture beneath Taney Seamount-A. I use bulk rock and volcanic glass major, trace and rare earth elements in order to investigate the geochemical signals imparted by crystallization in a shallow magma reservoir, melt-rock interaction in the lower-oceanic crust, and mantle processes during magma genesis. With these observations in combination with geochemical modelling, the nature of the magmatic plumbing system beneath Taney Seamount-A, and potentially other near-ridge seamounts as well, is discussed.

Chapter 2 is a more detailed investigation of melt-rock interaction at Taney Seamount-A. I use major, volatile, trace and rare earth elements in melt inclusion contained within plagioclase separated from pillow margin glass in order to study melt ponding in the lower oceanic crust and assimilation processes. This chapter utilizes geochemical modelling in order to identify the nature and extent of assimilation processes occurring at the crust-mantle boundary.

Chapter 3 investigates caldera collapse dynamics occurring at near-ridge seamounts. I use scaled analogue experiments utilizing 3D-laser scanning and digital particle image velocimetry (DPIV) in order to investigate caldera collapse dynamics. The principle objective of this chapter is to identify the differences in caldera collapse dynamics when a volcanic edifice is centered over a magma reservoir and offset from the reservoir.

REFERENCES

- Batiza, R., Niu, Y. & Zayac, W. C. (1990). Chemistry of seamounts near the East Pacific Rise: Implications for the geometry of subaxial mantle flow. *Geology* **18**, 1122-1125.
- Bedard, J. H., Hebert, R., Berclaz, A. & Varfalvy, V. (2000). Syntexis and the genesis of lower oceanic crust. *Ophiolites and Oceanic Crust: New Insights from Field Studies and Ocean Drilling Program*, 105-119.
- Brandl, P. A., Beier, C., Regelous, M., Abouchami, W., Haase, K. M., Garbe-Schoenberg, D. & Galer, S. J. G. (2012). Volcanism on the flanks of the East Pacific Rise: Quantitative constraints on mantle heterogeneity and melting processes. *Chemical Geology* **298**, 41-56.
- Canales, J. P., Carton, H., Carbotte, S. M., Mutter, J. C., Nedimovic, M. R., Xu, M., Aghaei, O., Marjanovic, M. & Newman, K. (2012). Network of off-axis melt bodies at the East Pacific Rise. *Nature Geoscience* 5, 279-283.
- Canales, J. P., Nedimovic, M. R., Kent, G. M., Carbotte, S. M. & Detrick, R. S. (2009). Seismic reflection images of a near-axis melt sill within the lower crust at the Juan de Fuca ridge. *Nature* **460**, 89-93.
- Clague, D. A., Reynolds, J. R. & Davis, A. S. (2000). Near-ridge seamount chains in the northeastern Pacific Ocean. *Journal of Geophysical Research* **105**, 16541-16561.
- Crisp, J. A. (1984). Rates of magma emplacement and volcanic output. *Journal of Volcanology* and Geothermal Research **20**, 177-211.
- Danyushevsky, L. V., Leslie, R. A. J., Crawford, A. J. & Durance, P. (2004). Melt inclusions in primitive olivine phenocrysts: The role of localized reaction processes in the origin of anomalous compositions. *Journal of Petrology* **45**, 2531-2553.
- Donnelly, K. E., Goldstein, S. L., Langmuir, C. H. & Spiegelman, M. (2004). Origin of enriched ocean ridge basalts and implications for mantle dynamics. *Earth and Planetary Science Letters* **226**, 347-366.
- Fornari, D. J., Perfit, M. R., Allan, J. F. & Batiza, R. (1988a). Small-scale heterogeneities in depleted mantle sources: near-ridge seamount lava geochemistry and implications for mid-ocean-ridge magmatic processes. *Nature* **331**, 511-513.
- Fornari, D. J., Perfit, M. R., Allan, J. F., Batiza, R., Haymon, R., Barone, A., Ryan, W. B. F., Smith, T., Simkin, T. & Luckman, M. A. (1988b). Geochemical and structural studies of the Lamont seamounts: seamounts as indicators of mantle processes. *Earth and Planetary Science Letters* **89**, 63-83.
- Hammond, S. R. (1997). Offset caldera and crater collapse on Juan de Fuca Ridge-flank volcanoes. *Bulletin of Volcanology* **58**, 617-627.

- Jónsson, S., Zebker, H. & Amelung, F. (2005). On trapdoor faulting at Sierra Negra volcano, Galápagos. *Journal of Volcanology and Geothermal Research* **144**, 59-71.
- Kelemen, P. B., Koga, K. & Shimizu, N. (1997). Geochemistry of gabbro sills in the crust-mantle transition zone of the Oman ophiolite: Implications for the origin of the oceanic lower crust. *Earth and Planetary Science Letters* **146**.
- Klein, E. M. & Langmuir, C. H. (1987). Global correlations of ocean ridge basalt chemistry with axial depth and crustal thickness. *Journal of Geophysical Research-Solid Earth and Planets* **92**, 8089-8115.
- Lavallée, Y., Stix, J., Kennedy, B., Richer, M. & Longpre, M. A. (2004). Caldera subsidence in areas of variable topographic relief: results from analogue modeling. *Journal of Volcanology and Geothermal Research* **129**.
- Niu, Y. & Batiza, R. (1997). Trace element evidence from seamounts for recycled oceanic crust in the Eastern Pacific mantle. *Earth and Planetary Science Letters* **148**, 471-483.
- Niu, Y., Regelous, M., Wendt, I. J., Batiza, R. & O'Hara, M. J. (2002). Geochemistry of near-EPR seamounts: importance of source vs. process and the origin of enriched mantle component. *Earth and Planetary Science Letters* **199**, 327-345.
- Saal, A. E., Kurz, M. D., Hart, S. R., Blusztajn, J. S., Blichert-Toft, J., Liang, Y. & Geist, D. J. (2007). The role of lithospheric gabbros on the composition of Galapagos lavas. *Earth and Planetary Science Letters* **257**, 391-406.
- Scheirer, D. S. & Macdonald, K. C. (1995). Near-axis seamounts on the flanks of the East Pacific Rise, 8°N to 17°N. *Journal of Geophysical Research* **100**, 2239–2259.
- Sobolev, A. V., Hofmann, A. W., Kuzmin, D. V., Yaxley, G. M., Arndt, N. T., Chung, S.-L., Danyushevsky, L. V., Elliott, T., Frey, F. A., Garcia, M. O., Gurenko, A. A., Kamenetsky, V. S., Kerr, A. C., Krivolutskaya, N. A., Matvienkov, V. V., Nikogosian, I. K., Rocholl, A., Sigurdsson, I. A., Sushchevskaya, N. M. & Teklay, M. (2007). The amount of recycled crust in sources of mantle-derived melts. *Science* **316**, 412-417.
- Standish, J. J. & Sims, K. W. W. (2010). Young off-axis volcanism along the ultraslow-spreading Southwest Indian Ridge. *Nature Geosci* **3**, 286-292.
- Stix, J. & Kobayashi, T. (2008). Magma dynamics and collapse mechanisms during four historic caldera-forming events. *Journal of Geophysical Research-Solid Earth* **113**.
- Ueda, H., Fujita, E., Ukawa, M., Yamamoto, E., Irwan, M. & Kimata, F. (2005). Magma intrusion and discharge process at the initial stage of the 2000 activity of Miyakejima, Central Japan, inferred from tilt and GPS data. *Geophysical Journal International* **161**, 891-906.
- Wanless, V. D. & Shaw, A. M. (2012). Lower crustal crystallization and melt evolution at midocean ridges. *Nature Geoscience* **5**.

- Waters, C. L., Sims, K. W. W., Klein, E. M., White, S. M., Reagan, M. K. & Girard, G. (2013). Sill to surface: Linking young off-axis volcanism with subsurface melt at the overlapping spreading center at 9 degrees 03 'N East Pacific Rise. *Earth and Planetary Science Letters* **369**, 59-70.
- Zindler, A., Staudigel, H. & Batiza, R. (1984). Isotope and trace element geochemistry of young Pacific seamounts: implications for the scale of upper mantle heterogeneity. *Earth and Planetary Science Letters* **70**, 175-195.

Link to Chapter 1

Chemical heterogeneity has been observed in lavas erupted at mid-ocean ridges and small volcanoes that form adjacent to the axial spreading centers. A greater degree of chemical and isotopic heterogeneity at near-ridge seamounts has led to the suggestion that they have a separate plumbing system, thus avoiding the mixing and homogenization effects of the mid-ocean ridge axial reservoir. This discovery has made near-ridge seamounts ideal field areas for investigating heterogeneity in the upper mantle. Although a number of different models for heterogeneity in the upper mantle have been proposed, as reviewed in the introduction, the prevailing view is a two-component mantle with pyroxenite heterogeneities in a depleted peridotite matrix. However, the temporal and spatial scales of heterogeneities in the depleted upper mantle, magmatic processes involved with melting a two-component mantle, and modification during transport to the seafloor remain unclear.

Taney Seamount-A in the northeast Pacific Ocean exhibits a complex caldera collapse structure that enables the creation of a relative chronology and investigation of geochemical evolution of the seamount. In the following chapter I use lava, crystal, and melt inclusion geochemistry in conjunction with the relative chronology in order to investigate magmatic processes from generation in the mantle to eruption on the seafloor. Based on geochemical modelling of melting, diffusive melt-crystal interaction, and fractional crystallization, I develop a petrogenetic model characterized by the melting of a two-component mantle, melt-rock interaction at the Moho, and open-system evolution in a sub-caldera magma reservoir.

Chapter 1

The magmatic architecture of Taney Seamount-A, NE Pacific Ocean

Jason P. Coumans, John Stix, David A. Clague and William G. Minarik

Manuscript published in Journal of Petrology

ABSTRACT

Seamounts formed adjacent to mid-ocean ridges are the most abundant on earth, numbering several orders of magnitude higher than hotspot related seamounts. The Taney Seamounts are a linear NW-SE trending, near mid-ocean ridge chain consisting of five volcanoes located on the Pacific plate 300 km west of San Francisco, California. Taney Seamount-A, the largest and oldest in the chain, has four well-defined calderas. These calderas have clear crosscutting relationships, creating a relative chronology. The caldera walls and intracaldera pillow mounds were sampled systematically by a remotely operated vehicle (ROV) to obtain stratigraphically-controlled samples, a unique aspect of this study. Changes in lava geochemistry are consistent with an open-system sub-caldera reservoir that undergoes periodic collapse, replenishment, shallow crystallization, and eruption. Replenishing magmas contain large, anorthite-rich plagioclase crystals that exhibit sieve textures and zoning indicating interaction with percolating melt. The enrichment of elements in the lavas that are incorporated in plagioclase (e.g., aluminum, strontium) provides chemical evidence for the interaction between mantle-derived melts and plagioclase cumulates in the lower oceanic crust or upper mantle (8-12 km), prior to magmas entering the sub-caldera plumbing system. Based on trace element variations, the erupted lavas vary from typical peridotite-derived N-MORB compositions to those with an apparent residual garnet signature. Geochemical and thermodynamic modeling shows that decompression melting of a MORB mantle peridotite re-fertilized by garnet pyroxenite partial melts can reproduce the garnet signature observed in the Taney-A edifice lavas. Hence the magmatic architecture of Taney Seamount-A is characterized by the melting of a mixed lithology mantle, melt-rock interaction in the upper mantle to lower oceanic crust, and open system evolution in a sub-caldera magma reservoir.

INTRODUCTION

The majority of volcanism on Earth is associated with the creation of young seafloor at mid-ocean ridges. If volcanism were restricted to the rift axis, the resulting ocean crust would be uniform and featureless aside from axial hills, valleys, and ridge offsets. In reality, however, the oceanic crust is littered with volcanic islands, seamounts, ridges and platforms. The volcanic features range from small lava piles only meters high to large volcanic outpourings and seamount chains, such as the Ontong Java Plateau, Emperor Seamount Chain, and a newly discovered massive volcano that forms the Shatsky Rise (Sager et al., 2013). Near-ridge seamounts are the most abundant seamounts on earth, numbering orders of magnitude greater than hotspot volcanoes (Scheirer & Macdonald, 1995). They are produced by mantle upwelling at mid-ocean ridges, although the process is not completely clear. The distribution of young near-ridge seamounts in the Pacific Ocean suggests that they form in a narrow "window" 5-30 km from the ridge axis and are commonly asymmetric about the axis (Scheirer & Macdonald, 1995). The paucity of seamounts at distances < 5 km from the ridge axis has been attributed to melt focusing towards the ridge (Katz et al., 2006), whereas the lack of seamounts at distances > 30 km is caused by insufficient melt supply. This near-ridge seamount window is located in a region of relatively thin lithosphere, with extensive ridge-parallel faulting which probably provides pathways for melt transport to sub-caldera magma reservoirs (Clague et al., 2000). Near-ridge seamounts are most common on flanks of inflated ridges with large cross-sectional area and abundant melt supply, features characteristic of medium to fast spreading segments. Near-ridge seamount chains in the northeast Pacific Ocean are not aligned with the orientation of relative or absolute plate motion vectors, but appear to parallel Pacific subaxial asthenosphere flow vectors (e.g., Clague et al., 2000). This has led to the suggestion that near-ridge seamounts form due to

oceanic plate motion above a melting anomaly embedded in the upwelling mantle around the mid-ocean ridge (Clague *et al.*, 2000).

Morphologically, near-ridge seamounts are similar to many subaerial shield volcanoes, such as the Galapagos Islands (Batiza, 1982, Batiza et al., 1989, Lonsdale, 1983, Rappaport et al., 1997, Smith, 1988). They are characterized by truncated cones with steep flanks (~25°), flat to slightly domed summit plateaus, and modification by complex caldera collapse structures, which are commonly offset towards the ridge (Batiza & Vanko, 1984, Hammond, 1997, Smith, 1988). The flat topped nature of many near-ridge seamounts has been attributed to infilling and overflowing of older calderas by younger lavas (Clague et al., 2000). The observation that nearly all offset caldera collapse features are located on the ridge axis side of the volcano, and furthermore that they are breached towards the ridge, indicates that the volcanoes migrate away from the magma source (Hammond, 1997). The distance between the center of each volcano and the offset caldera, in conjunction with the volcanic propagation rates calculated from relative plate motions, suggest lifespans on the order of 70 - 100 Kyr (Clague et al., 2000). The eruption rate over the lifespan of a volcano increases to a peak, followed by a decrease as the volcano migrates away from the magma source. The rate of increase or decrease is estimated by volcanic features such as empty versus filled calderas, the presence or absence of late cones, and caldera sizes. Bedded volcaniclastites, an indicator of explosive volcanism, have been observed as thin deposits blanketing caldera flanks and floors, and also frequently capping seamounts. These volcaniclastic deposits are commonly associated with calderas and craters (Batiza & Vanko, 1984, Clague et al., 2009, Clague et al., 2000, Helo et al., 2011, Portner et al. 2014)

Near-ridge seamounts in the Pacific Ocean have been studied extensively in order to understand the nature of off-axis magma production near the East Pacific Rise (Allan *et al.*,

1989, Allan et al., 1994, Batiza et al., 1990, Batiza & Vanko, 1984, Brandl et al., 2012, Fornari et al., 1988a, Fornari et al., 1988b, Graham et al., 1988, Niu et al., 2002, Shen et al., 1995) and the Gorda and Juan de Fuca ridges (Clague et al., 2000, Cousens et al., 1999, Cousens et al., 1995, Cousens et al., 1985, Davis & Clague, 2000). A key observation from these studies is that near-ridge seamount basalts have more variable trace element compositions than do mid-ocean ridge basalts erupted at adjacent spreading axes. Therefore, near-ridge seamounts have been hypothesized to develop from a magmatic plumbing system independent from the mid-ocean ridge, offering a geochemical window into the mantle. Due to the predominantly primitive (high MgO) nature of near-ridge seamount lavas compared to mid-ocean ridge basalts, it has been suggested that the plumbing system is one of primarily magma transport by dikes from the upper mantle to the seafloor (e.g., Fornari et al., 1988b). However, structural evidence in the form of calderas suggests that near-ridge seamounts also have relatively shallow magma chambers (Clague et al., 2000), where the roof subsides into the chamber during periods of significant magma withdrawal (Geyer et al., 2006, Kennedy et al., 2004, Martí et al., 1994, Roche et al., 2000).

The Taney Seamounts are a linear chain of near-ridge seamounts off the coast of California consisting of five volcanic edifices with an Ar-Ar age of $\sim 26 \pm 1.5$ Ma which formed adjacent to the now subducted Farallon spreading center (Fig. 1). Uncertainties in the Ar-Ar dating method and the geomagnetic timescale during this time period make it difficult to constrain the differences in age between the seamounts and the underlying seafloor (Clague *et al.*, 2000). It is unknown whether there was a symmetrical chain on the other side of the ridge. Taney Seamount-A is unique due to its prominent edifice modification by a series of caldera collapses (Fig. 2). Successive calderas truncate older calderas and expose infilled lavas on their

near-vertical walls, resulting in a step-like appearance of the volcanic edifice enabling stratigraphic access to the seamount. This ability to investigate spatial and temporal geochemical changes at Taney Seamount-A allows us to make inferences about the magmatic architecture of near-ridge seamounts by (1) investigating the signal imparted by shallow magmatic processes such as crystallization in an open magma reservoir, (2) examining the geochemical effect of melt-rock interaction in the lower oceanic crust or upper mantle, and (3) understanding and distinguishing the overprint signals of melt-rock interaction and shallow crystallization, hence enabling new insight into the nature and scale of mantle source compositions and heterogeneities.

FIELD AREA, SAMPLING AND STRATIGRAPHY

Taney Seamounts

The Taney Seamounts are located at 36° 45' N and 125° 25' W, approximately 300 km west-southwest of San Francisco, California, on the Pacific Plate (Fig. 1). The seamounts are a short linear chain that formed adjacent to the western spreading section of the now subducted Farallon Plate. The seamount chain consists of five co-linear volcanoes designated Taney-A through Taney-E from northwest to southeast, or oldest to youngest based on age of the underlying plate under the assumption that near-ridge seamounts migrate away from their magma source (Hammond, 1997) (Fig. 1b). The measured azimuth of the Taney seamount chain is 294° – 298°, which is slightly oblique to Farallon Plate motion perpendicular to the ridge axis (~270°). The chain covers seafloor formed over 0.9 Myr (Clague *et al.*, 2000). The volumes of

the Taney Seamounts are 11 km³ (Taney-E), 25 km³ (Taney-D), 116 km³ (Taney-C), 91 km³ (Taney-B), and 187 km³ (Taney-A).

Taney Seamount-A is the largest and oldest seamount in the chain, and is the primary field target of this study (Fig. 2). The seamount is 15 km in diameter at its base with a minimum pre-collapse height of 1400 m. The edifice has been strongly modified by the sequential formation of four calderas. The first caldera (C1), the most northwesterly, has a diameter of 4.5 km and a minimum subsidence of 400 m. The second caldera (C2) is 3.5 km in diameter with at least 150 m of subsidence. Caldera C2 is located further to the southeast; it may truncate the southern rim of caldera C1 or may be completely nested within (the uncertainty is due to truncation by a later caldera). The third caldera (C3) is relatively small and completely nested within caldera C2; it has a diameter of 2.5 km and minimum subsidence of 50 m. The fourth, youngest, and most southeasterly caldera (C4) has the largest diameter at 5 km with a minimum subsidence of 400 m. Caldera C4 is offset from earlier collapses and has consumed most of the volcano's eastern flank, resulting in truncation of the southeastern portions of the first three calderas. In turn, the southeastern portion of the youngest caldera (C4) has been infilled by lavas and by many small 0.5 - 1.0 km diameter cones. Abundant evidence of caldera infilling, such as the cones, indicates that the amounts of caldera subsidence are minimum values. Furthermore, the younger calderas truncate lava flows that partially filled older calderas. Therefore, each caldera exposes the previous episode of lava infilling. There are also volcaniclastic deposits found on the southwestern flank of the seamount and the western rim of caldera C1. These deposits may be indications of explosive activity, as illustrated by the presence of glassy bubble wall fragments (Clague et al., 2009, Helo et al., 2011, Portner et al., 2014).

Relative stratigraphy of Taney Seamount-A

The oldest samples were collected in a 1980 dredge on the southwestern flank of the volcano at a stratigraphic level below the base of the C1 caldera. Due to the imprecise nature of dredge sampling, however, mass wasting of younger parts of the edifice cannot be ruled out. The dredge samples consist of pillow fragments and volcaniclastic material with fresh glass. The oldest caldera (C1) exposes lavas from the upper 400 m of the volcanic edifice. The C1 caldera floor is flat-lying, heavily sedimented with pelagic material and coated with Mn-oxide-encrusted sponge skeletons and slabs which vary from gravel to cobble sized. Some of these slabs reach up to several meters long. Silicified deposits are occasionally observed near caldera walls and indicate hydrothermal activity. There is occasional blocky talus covered with Mn-oxide crusts up to several centimeters thick. The base of the C1 caldera wall is a shallow talus slope with angular blocks. Towards the top of the talus slope where it intersects the subvertical caldera wall, the talus blocks are more angular, larger, and less coated with manganese, representing proximal mass wasting deposits. On the subvertical caldera wall, outcrops are 10 cm to 1 m diameter truncated pillows (Fig. 3a). In some cases, massive and pillowed flows are separated by thin brecciated zones. The summit of the C1 caldera consists of layered volcaniclastic deposits, up to 50 cm thick, which commonly have a potholed appearance (Fig. 3b).

The C2 caldera exposes the upper 150 m of the lavas that partially infilled the C1 caldera. The base of the caldera is covered by thick sediment and coated with Mn-nodules and Mn-oxide-encrusted sponge skeletons, as seen at the C1 caldera. The base of the C2 caldera wall is defined by a talus slope that grades to larger, more angular blocks with thinner Mn-oxide crusts towards the top. The sub-vertical caldera wall exposes truncated pillow lavas, especially at the summit.

The upper edge of the caldera-bounding fault is heavily sedimented and represents the floor of the C1 caldera.

Caldera C3 is the smallest caldera on the volcano, exposing the upper 50 m of the lavas which infill the C2 caldera. The base of the caldera has a sediment thickness of at least 1 m, as estimated by the penetration depth of a push core. Near the base of the caldera wall, the sediment-covered floor has ripples that are oriented perpendicular to the wall and have Mn-oxide nodules concentrated on their crests (Fig. 3c). Similar to the bases of other caldera walls, the C3 caldera has a talus slope, while the caldera top comprises a ridge of small 20-50 cm diameter truncated pillows.

Caldera C4 is the largest structure on the seamount and truncates calderas C1, C2, and C3, making it the most recent caldera to form on Taney Seamount-A. A talus slope is present at the base of the caldera wall, consistent with observations at the other three calderas. Just beyond the top of the caldera wall, towards the west, is a constructional cone. At the top of the cone beyond the debris apron are in situ lava flows with lobate to pillow morphology. Therefore, this constructional feature was not disrupted by collapse of the C4 caldera and may be a younger post-collapse constructional mound.

The youngest lavas at Taney-A are constructional cones that infill caldera C4. The cones range in size from 0.5-1 km in diameter and are aligned north-south parallel to the Farallon spreading center (Clague *et al.*, 2000), suggesting that their location and alignment may be controlled by ridge-parallel regional faults (Fig. 2). The cones consist of steep slopes of intact pillows from 0.5-2 m in cross-section. Some of the pillows are fractured along radial joints producing angular wedges ideal for sampling. The base of the pillow mounds are not as talus-

laden as at the base of the caldera walls, due to more stable slopes. The space between pillow mounds contains Pleistocene sediment older than 55000 years up to 70 cm thick, as is the case for the caldera floors.

Thus, the physical history of Taney Seamount-A was defined by episodic construction through lava eruption on the seafloor and destruction by caldera collapse with several phases of each before the volcano was no longer active. Prior to caldera C1, constructional phases were more prominent than destructive phases, resulting in the volumetric growth of the edifice. After caldera 1 the subsequent growth phases between each caldera collapse were much smaller, resulting in a decrease in edifice volume. We define five chronological units that can be arranged stratigraphically: (1) constructional edifice, (2) post-caldera C1 infill, (3) post-caldera C2 infill, (4) post caldera-C3 infill, and (5) pillow cones (Fig. 4).

METHODOLOGY

Sampling by remotely operated vehicle (ROV)

Sampling of the Taney Seamounts was performed during a 5-15 August 2010 Monterey Bay Aquarium Research Institute (MBARI) research cruise using the remotely operated vehicle (ROV) *Doc Ricketts* and research vessel R / V *Western Flyer*. Taney Seamount-A was sampled during dives D174-177, Taney Seamount-B was sampled during dive D173, and Taney Seamount-C was sampled during dive D178. The primary target was Taney Seamount-A due to its complex caldera collapse structures with prominent cross-cutting relationships which exhibit a well-defined relative chronology, and also because 1.5 m multibeam bathymetry (collected previously by the MBARI autonomous underwater vehicle (AUV) *D. Allan B.*) was available to

guide sampling. Sampling took place on the northwestern caldera C1, caldera C2, calderas C3, C4 and the construction feature on the caldera C4 margin, and young constructional cones at the base of caldera C4 (Fig. 2). These sampling sites were chosen to obtain material from the different stratigraphic units on Taney Seamount-A. Samples were collected with the manipulator arm on the ROV, imaged, positioned using ship GPS and ultra-short baseline (ROV) navigation, and stored in baskets on the ROV before transport to the surface. Error on the ultra-short baseline navigation is ~ 35m with error on the underlying Simrad EM300 ~50m. Once the samples were at the surface, they were cleaned and catalogued. Sampling was difficult because the outcrops are commonly coated with 1-2 cm thick Mn-oxide crusts, which also obscured visual identification of in-situ samples. In order to have confidence in the stratigraphic location, samples that appeared to be in place or proximal (<1 m) to truncated pillows were chosen for analysis. Pillow fragments or pillow wedges were the best material for precise stratigraphic sampling, and also generally had volcanic glass rims and showed the least alteration.

Sample preparation

Glass samples were chipped off pillow wedges and dredged material, crushed and sieved at 1 mm, 500 µm, 250 µm, and 125 µm. A volcanic glass shard size fraction of 250-500 µm was used to create grain mounts. Each of the glass grain mounts consisted of two shards of each sample as well as one shard of internal standard P1326-2, a Juan de Fuca ridge basalt (Stix *et al.*, 1995). Polished thin sections of glassy pillow margins were also made for glass analysis and to maintain plagioclase crystals intact for later electron microprobe analysis. Plagioclase fragments

were also picked from the 250-500 µm size fraction in order to make three separate grain mounts which consisted of approximately 5-10 crystals per sample.

Electron microprobe analysis

Major element compositions of volcanic glass and plagioclase crystals were measured with a JEOL 8900 instrument at McGill University, Montréal, Canada. The following routine was used for volcanic glass samples: an accelerating voltage of 15 kV, a sample current of 20 nA for Si, Ti, Al, Fe, Mn, Mg, Ca, and Na (20 s); K and P (40 s); Cl (120 s); and S (60 s count time) using a defocused 5 μm beam. Si, Al, Fe, Mg, Ca, and Na were calibrated against Smithsonian mid-ocean ridge glass VG-2 standard (with MgO content adjusted to 7.07%, see supplementary information S1) and K against Yellowstone rhyolite glass VG-568 standard, with other elements against synthetic and natural minerals or oxides (the list of standards can be found in supplementary information S1). Analytical uncertainties were obtained by repeat measurements of VG-2 and our in-house standard P1326-2. The 2σ analytical errors are reported in supplementary information Table S1.1. The detection limits for Cl and S were 45 and 265 ppm, respectively. We observed no sodium loss in the volcanic glasses analyzed.

The following routine was used for the plagioclase analyses: an accelerating voltage of 15 kV and a sample current of 20 nA for Si, Ti, Al, Fe, Mg, Ca, Na, and K (20 s count time) using a defocused 5 µm beam. Synthetic and natural minerals or oxides were used for calibration (see supplementary information S1). Analytical uncertainties were obtained by repeat measurements of the Astimex sanidine standard. Using the above analytical routine we observed no sodium loss over the measurement time of approximately 3.5 minutes.

Whole-rock inductively coupled plasma mass-spectrometry and X-ray fluorescence

Collected rocks were cut for thin sections and the least altered material was selected for major and trace element analyses by XRF and rare-earth (REE) and additional trace-elements by ICP-MS. Centimeter-sized fragments were leached in reverse osmosis water and the whole-rocks were analyzed in the GeoAnalytical Laboratory of Washington State University. Information on methods, precision, and accuracy has been given by Johnson *et al.* (1999) and Knaack *et al.* (1994), for XRF and ICP-MS, respectively. Glass analyses indicate that the erupted magmas have P₂O₅ concentrations from 0.090 - 0.248 wt. % (Table 1). Many whole-rock analyses have P₂O₅ concentrations above 0.25 wt. %, with concentrations as high as 2.1 wt. %. This suggests that even the freshest whole-rock samples have undergone some degree of phosphate addition. REE and high field-strength elements (HFSE) tend to be resistant to secondary alteration (Davis *et al.*, 2010). Comparison of trace element analyses in whole-rock and volcanic glasses from identical samples (supplementary information figure S2.1), however, indicates that only Ce, Th, Nb, Zr are unaffected by the addition of phosphate and hence petrologically useful.

Laser-ablation inductively coupled plasma mass-spectrometry

Trace element compositions of the volcanic glasses were measured with a laser-ablation inductively coupled plasma mass-spectrometer (LA ICP-MS) using a Nu AttoM ICP-MS coupled with a 193 nm excimer laser (Photon Machines) at the Université du Québec à Montréal, Canada. A 6 mJ beam pulsed at 5 Hz on a 85 μm spot, ablated material which was carried to the ICP-MS via helium gas. The ablation time ranged from 20 – 30 seconds with a 20 second gas background. A total of 6 analysis points were made per sample to assess reproducibility. The

following primary standards were used for calibration: BHVO-2g, BIR-1g, BCR-2g, and NIST612. Our P1326-2 secondary internal standard was analyzed as an unknown and used as an independent check for accuracy and drift. Since the AttoM is a magnetic sector instrument, two separate analysis techniques were used to obtain the highest precision data. A linked-scan mode was used to obtain the entire desired mass range. A deflector-scan mode with a fixed magnet current was used to obtain better precision on the high mass elements Ta, U, Th, Lu; these data were calibrated to the linked-scan mode using Yb concentrations. The concentration of calcium, previously determined by EMPA with a relative error of 1.9% (2σ), was used as a normalizing element during the analysis of the volcanic glasses. The 2σ analytical errors are reported in supplementary information Tables S1.3 and S1.4.

Secondary ion mass spectrometry (SIMS)

Volatile concentrations (H₂O, CO₂, F, Cl, and S) were measured on melt inclusions in plagioclase crystals using a Cameca IMS 1280 ion microprobe at Woods Hole Oceanographic Institution. In this paper we report H₂O and CO₂ data (see supplementary information S3). Melt inclusion selection was performed using transmitted light microscopy. We only selected melt inclusions that were far from cracks and had no shrinkage bubbles. Selected plagioclase crystals with exposed melt inclusions were mounted into indium metal to reduce carbon background. The mounts were dried in a vacuum oven at 110°C and 10⁻³ torr for ~12 hours. Storage prior to analysis was under 10⁻⁷ torr vacuum for ~24 hours. The samples were held under higher vacuum (10⁻⁹ torr) in the machine airlock prior to analysis. The principle analytical procedure is described in Hauri *et al.* (2002). A ¹³³Cs⁺ beam with a 1.2-1.5 nA current and a 15 μm diameter

beam was used to measure 12 C, 16 O 1 H, 19 F, 30 Si, 32 S and 35 Cl. The magnet position for the beam was calibrated for each spot and an electron beam was fired at the surface in order to eliminate positive charging. The primary beam was rastered over a 30 x 30 μ m area. A 15 x 15 μ m mechanical aperture was placed in the secondary ion image plane after pre-sputtering for three minutes resulting in a 15 x 15 μ m analysis window. The element concentrations were calculated from a reference calibration curve using standard glasses (supplementary information Table 1.5). Reproducibility using our in-run standard glass P1326-2 is shown in supplementary information Table S1.6. Plagioclase grains were analyzed to determine background levels of CO₂ and H₂O which are 30 - 170 ppm and 0.02 - 0.07 wt. %, respectively.

RESULTS

Petrography

The Taney Seamount-A lavas are tholeiitic basalts with 0-20 vol% phenocrysts. The primary phenocryst assemblage is plagioclase with minor amounts of olivine and very rarely clinopyroxene. The most plagioclase-phyric and most primitive samples (highest MgO wt. % in glass) are from the pillow cones, which represent the last magmatic activity at Taney-A. Plagioclase crystals occur as large single megacrysts or glomerocrysts up to 1.5 cm in length. The crystals vary widely in morphology with tabular, acicular, resorbed, euhedral and glomerocrystic forms containing olivine all present. Olivine is less common, smaller, up to 400 µm in diameter, and subhedral, anhedral and skeletal (hopper shape).

The plagioclase crystals from the young cones have complex normal, reversed, to oscillatory zoning patterns (Fig. 5). In some cases, the crystals exhibit synneusis growth textures,

suggesting mechanical attachment during melt percolation through a crystal cumulate (Schwindinger, 1999). They commonly have subrounded cores with anorthite contents typically ranging from An_{80} to An_{90} (Fig. 5). Rare plagioclase crystals recovered from the constructional edifice and caldera infill lavas have anorthite contents that range from An_{62} to An_{70} and are not strongly zoned compared to the young cone crystals.

The young cone plagioclase crystals commonly have more sodic rims that represent later stage growth in more differentiated melts (Fig. 6). The small 10-150 µm microlites and glomerocrysts in pillow rinds have anorthite compositions which are slightly lower than the rims of the larger crystals, likely representing the last stages of crystallization (Fig. 6). These features suggest that the large plagioclase crystals experienced a complex and protracted crystallization history.

Major and trace element compositions

Major and trace element compositions from Taney Seamount-A were determined by analyzing both the whole rock and their glassy margins. Volcanic glass is fresh and probably represents the pristine composition of the rapidly quenched lava. Most whole rocks have undergone some crystallization and sometimes show evidence of seawater alteration as illustrated by the behaviour of seawater-mobile elements such as Ba²⁺ and the elevated P₂O₅ as discussed earlier. Because of the potential complications with alteration in the whole rock samples, we use only Th, Nb and Zr from whole-rock data, which are immobile and correlate with associated volcanic glass (supplementary information, Figure 2.1). Volcanic glass data for Taney Seamounts-A, B, C are presented in Table 1 and supplementary information Table 2.1.

Whole-rock data for Taney Seamounts-A, B, C are in supplementary information Tables 2.2 and 2.3.

Volcanic glasses from Taney Seamount-A are subalkaline basalts varying between 8.7 and 6.2 wt. % MgO, similar in major element composition to MORB suites. TiO₂, Na₂O, and K₂O increase with decreasing MgO (Fig. 7b, f, h) whereas Al₂O₃ decreases (Fig. 7c). CaO/Al₂O₃ and SiO₂ show an inflection at 7.5 wt. % MgO indicating the onset of clinopyroxene crystallization. Compared to other near-ridge seamount suites from the northern Pacific Ocean (e.g., Vance, President Jackson Seamounts), Taney-A lavas have a broader range of major element compositions including more differentiated lavas. The Taney-A lavas also exhibit a distinct liquid line of descent on a plot of SiO₂-Al₂O₃ defined by elevated Al₂O₃ and lower SiO₂ when compared to MORB (supplementary information S6).

Representative incompatible and compatible trace-element diagrams are shown in Figure 8. As samples from Taney Seamount-A decrease in MgO, concentrations of elements incompatible during crystallization (e.g., REE, Y, Zr, Th, Ta, Nb, Hf, Ba, Rb) increase whereas Ni decreases with decreasing MgO (Fig. 8b-f). Cr behaves differently from Ni; between 8.7 and 7.5 wt. % MgO, Cr shows incompatible behaviour (negative slope), whereas between 7.5 and 6.2 wt. % MgO, it is compatible (positive slope). Ranges in incompatible element concentrations vary depending on their relative incompatibility with respect to melting of the MORB mantle. Highly incompatible elements, such as Th and La, range from 0.152-0.651 and 2.70-8.42 ppm, respectively, indicating enrichment by a factor of 3-4. Less incompatible elements, such as Y and Lu, range from 28.6-38.3 and 0.33-0.54 ppm, respectively, indicating enrichment factors of only 1.3-1.6.

Ratios of highly to moderately incompatible (e.g., La/Sm, Fig. 8g) and moderately to slightly incompatible elements with respect to melting of the MORB mantle (e.g., Zr/Y, Fig. 8h) decrease with increasing MgO. The ratio of La/Sm ranges from 1.0 to 1.6, whereas Zr/Y ranges from 2.6 to 4.2. The northern cone from the lineament on caldera C4 floor has the lowest Th, Ba and La/Sm. The pillow cone on the C3 caldera wall can be distinguished from the other cone lavas based on its distinct Th and Ba (0.25 and 22 ppm, respectively). Fractional crystallization of olivine, plagioclase, and clinopyroxene does not significantly separate the trace element ratios (Fig. 8g, h). Strontium is fractionated relative to neighbouring incompatible trace elements when normalized to primitive upper mantle (McDonough & Sun, 1995) according to Sr/Sr*, where Sr* $= \sqrt{Pr_N Nd_N}$ This is due to the compatible behaviour of strontium in plagioclase relative to the incompatible behaviour of neighbouring REE (Pr, Nd). The variation in trace element ratios must be due to other processes such as variable partial melting or mantle source composition.

Representative trace element and REE patterns normalized to average Pacific MORB (Arevalo & McDonough, 2010) for the entire suite are shown in Figure 9a, b. Compared to average Pacific MORB, the constructional edifice and caldera infill lavas exhibit an enrichment from highly to slightly incompatible elements (Fig. 9a, b). The most trace element depleted cones exhibit profiles similar to average Pacific MORB. Overall Taney Seamount-A lavas are more enriched than other northern Pacific seamount chains (Vance, and to a lesser extent President Jackson) and are intermediate between the most enriched and depleted samples from northeastern East Pacific Rise near-ridge seamounts (NEPR), including the Lamont Seamounts (Fig.9c, http://earthchem.org/petdb).

Chemostratigraphy

We have grouped the samples in their stratigraphic order based on their sampling location, as already discussed in the relative stratigraphy section. Elements that behave compatibly during crystallization, such as MgO and Ni, indicate that erupted lava compositions are systematically less differentiated after a caldera collapse and overall became less differentiated during the volcano's lifespan (Fig. 10a, b). This pattern is mirrored for incompatible elements such as Zr, where the constructional edifice was formed from the most differentiated lavas with 122 to 160 ppm Zr, whereas the pillow cone on the caldera C3 wall and the northernmost pillow cone in the north-south lineament in the caldera C4 floor have the least differentiated compositions with 60-90 ppm Zr (Fig. 10d). The systematic evolution from more differentiated compositions at an early stage in the volcano's history to less differentiated compositions at the end of the volcano's lifetime is opposite to the trend expected for progressive fractional crystallization and eruption.

In detail, the chemostratigraphic record exhibits additional complexity in the stratigraphically-unconstrained samples from caldera floors. In the case of the two samples collected on the floor of caldera C1 (Fig. 10d, light blue circles), their Zr concentrations are similar to lava exposed on the C2 caldera wall (light blue diamonds), suggesting that they may be related. However, in the case of the four stratigraphically-unconstrained samples collected on the floors of calderas C2 and C3 (Fig. 10d, dark and light green circles), the lavas have a range in chemistry, making it difficult to infer their initial location. For example, the high-Zr sample from the post-caldera C3 lavas (light green circle) may have been sourced from the constructional edifice.

Ratios of trace elements incompatible during melting of the MORB mantle in volcanic glass are affected by the crystallization of olivine, plagioclase, and clinopyroxene, but the effect is small and cannot explain the full range in variability (Fig. 8g, h). Therefore, trace element ratios are useful for investigating changes in source-related geochemistry as a function of time. The Taney Seamount-A constructional edifice and post-caldera infilling lavas (C1-C3) exhibit fairly constant ratios of incompatible elements normalized to average Pacific MORB, such as (Th/Zr)_N, which vary from ~2.0 to 2.5 (Fig. 10e). Eruption of the young eastern cones marks a distinct change in the geochemical signature of the recharged melts as manifested by a decrease in (Th/Zr)_N to 1.4 (Fig. 10e). This decrease in highly incompatible elements relative to moderately incompatible elements (e.g., K₂O/TiO₂) is also revealed at the younger Taney Seamount-B edifice lavas, which overlap with the Taney-A cones (Fig. 10f). Furthermore, Taney Seamount-C edifice lavas are more depleted in highly incompatible elements than Taney-B edifice, Taney-A cone, and Taney-A edifice lavas over the full range of MgO (Fig. 10f, g). The progressive decrease in trace element ratios independent of MgO indicates that magmatic source geochemistry became more depleted on timescales of individual seamounts and the seamount chain as a whole. In contrast, some near-ridge seamounts and seamounts formed at fossil spreading ridges erupt more trace element enriched compositions at the end of their lifetime (Brandl et al., 2012, Haase et al., 2011).

DISCUSSION

Previous studies of near-ridge seamounts have focused primarily on probing the chemistry of the underlying mantle using a plumbing system that bypasses the mid-ocean ridge

axial magma reservoir. However, it is well known that the chemical signal from the mantle can be modified by a number of crustal processes such as assimilation, mixing and crystallization (e.g., Rubin *et al.*, 2009). Therefore, it is important to understand what role these processes may play at near-ridge seamounts before we make inferences about the nature of the mantle beneath them. Our study is exceptional as we have established a detailed stratigraphy of Taney Seamount-A that allows us to investigate the geochemical signals imparted by crystallization, assimilation and melting processes as a function of time. This top-down approach provides insight into the magmatic architecture beneath Taney Seamount-A.

Crystallization

Previous studies have shown that, in general terms, near-ridge seamounts erupt more primitive lava compositions compared to the nearby axial ridge (e.g., Niu *et al.* (2002); Batiza *et al.* (1990); Allan *et al.* (1989); Batiza & Vanko (1984)) with more than 50% plotting in a restricted range between 8.5 and 7.5 wt. % MgO. However, lavas erupted at Taney Seamount-A vary from 8.7 – 6.2 wt. % MgO, demonstrating that many of the lavas are considerably more differentiated and that they have a greater range than those erupted at several entire near-ridge seamount chains (e.g., Vance, President Jackson, Fig. 7a-h). The change in geochemistry with time does not follow a progressive fractionation trend, as shown by the distinct geochemical jumps after a caldera collapse event. Caldera infilling lavas typically have less differentiated compositions with a systematic progression to primitive compositions over the lifespan of the volcano. Furthermore, the incompatible trace element ratios are quite variable indicating that the

lavas are not from a single fractionating body (Fig. 8g, h). These observations suggest that the sub-caldera magmatic system is open and undergoes periodic recharge and eruption.

The young cones are aligned north-south, parallel to the Farallon spreading center, suggesting that their emplacement may have been tectonically controlled. Ridge parallel faults and lack of a shallow crustal reservoir due to a previous caldera forming eruption could provide a mechanism for rapid magma transport from deep levels to the seafloor, resulting in shorter crustal residence time and less differentiated compositions. We propose that a primitive melt replenishment mechanism could explain the distinct geochemical jumps to less differentiated compositions after a caldera forming event.

Although the trace element data suggest that the lavas do not belong to a single liquid line of descent, they do not rule out similar crystallization histories for the different melts. A downturn in CaO at ~7.5 wt. % MgO for Taney Seamount-A samples is indicative of clinopyroxene crystallization (Fig. 7e). Similarily, Cr shows a downturn at this MgO level, consistent with clinopyroxene fractionation (Fig. 8a). These changes at relatively low MgO contents are indicative of shallow crystallization pressures (Herzberg, 2004, Langmuir *et al.*, 1992).

The Taney Seamount-A lavas have erupted a crystal cargo that includes plagioclase crystals up to 1.5 cm long. The lavas from the pillow cones have the most abundant and largest plagioclase crystals; these lavas are the most primitive and represent the last stage of magmatism at the seamount. The plagioclase crystals exhibit disequilibrium textures such as highly variable zoning patterns, embayed edges in core and mantle zones, and sieve textures, suggesting interaction with various melts (Fig. 5). The cores are more calcic than the rims and microlites,

implying early crystallization from a primitive melt with later crystallization in a more differentiated melt (Fig. 6). The plagioclase cores are riddled with melt inclusions up to 100 μm; a typical size is 20 μm. CO₂-H₂O analyses of the plagioclase hosted melt inclusions indicate that the cores primarily crystallized at pressures between 250-400 MPa, or at lower crustal to upper mantle depths (supplementary information Figure 3.1). Therefore, the crustal architecture beneath Taney Seamount-A consists of a lower crustal to upper mantle mush zone with plagioclase-rich cumulates and a shallow sub-caldera magma reservoir with more differentiated melt compositions. The sieve textures of the crystals and the more sodic rims suggest the crystals were remobilized and transported from this deep zone and subsequently introduced into the sub-caldera magma reservoir containing more evolved melt.

Lower oceanic crustal assimilation

Basaltic lava with low SiO₂ and high Al₂O₃ at a given MgO (e.g., Al₂O₃ > 16.5 wt. %, SiO₂ < 48.5 wt. % at MgO > 8.0 wt. %) has been observed on the Lamont and Vance near-ridge seamounts, the Galapagos Seamounts, and on axial ridge segments. Explanations for these characteristics include (1) high water contents resulting in suppression of plagioclase crystallization (Danyushevsky, 2001); (2) high-pressure clinopyroxene fractionation (Allan *et al.*, 1989, Eason & Sinton, 2006, Zhang *et al.*, 2009); and (3) interaction of melt with oceanic crust (Danyushevsky *et al.*, 2004, Danyushevsky *et al.*, 2003, Kamenetsky *et al.*, 1998, Kamenetsky & Gurenko, 2007, Kvassnes & Grove, 2008, Laubier *et al.*, 2012, Lissenberg & Dick, 2008, Lissenberg *et al.*, 2013, Wanless *et al.*, 2010). At Taney Seamount-A, lavas with high Al₂O₃ and low SiO₂ also have elevated Sr concentrations relative to elements with similar incompatibilities

(Fig. 9a). Elevated Sr concentrations were also observed in high-Al, low-Si samples from Vance Seamount lavas (Hann, 2012), Galapagos lavas (Saal *et al.*, 2007) and in high-Al melt inclusions from the FAMOUS area (Laubier *et al.*, 2012).

Water concentrations in melt inclusions from Taney Seamount-A lavas are ~0.2 - 0.4 wt. %, similar to values in MORB on the East Pacific Rise (le Roux *et al.*, 2006), suggesting that water concentrations are insufficient to suppress plagioclase crystallization. Deep crystallization of clinopyroxene does not sufficiently fractionate Sr from Nd in order to produce the observed Sr anomaly, using the partition coefficients of Hauri *et al.* (1994). Furthermore, the modeled pressure of crystallization required to decrease SiO₂ sufficiently from the MORB liquid line of descent is approximately 600-800 MPa (supplementary information S6). Yet the majority of plagioclase melt inclusions have CO₂-H₂O vapour saturation pressures of ~250-400 MPa, which is too shallow for this scenario. Therefore, the high-Al, low-Si, and Sr enrichment signal observed in Taney Seamount-A lavas cannot be explained by high water concentrations or high-pressure clinopyroxene crystallization. We will now explore if melt-cumulate interaction is the principal process involved.

Taney Seamount-A lavas with positive Sr anomalies are those which contain large plagioclase crystals. These crystals have undergone variable amounts of crystal-melt interaction, as shown by the complex zonation and sieve textures. Other studies of chemical zonation in large plagioclase crystals also demonstrate that crystal-melt interactions are an important process in oceanic magma systems (Costa *et al.*, 2010, Lange *et al.*, 2013). Therefore, we propose that seamount lavas with high-Al, low-Si, and elevated Sr concentrations acquired their geochemical signature from melt-plagioclase cumulate interaction in the lower crust and/or upper mantle beneath Taney Seamount-A.

Assimilation of a plagioclase cumulate

Assimilation of a plagioclase cumulate and mixing into the host magma is primarily limited by thermal constraints. Assimilation-fractional crystallization models (Kvassnes & Grove, 2008) suggest that a primitive magma at 1270° C can melt at least 50 wt. % ($M_a/M_c = 0.5$) of a plagioclase and olivine cumulate (troctolite) at 800° C. If plagioclase cumulates are assimilated, the modified magmas will be higher in Al_2O_3 and saturated with clinopyroxene at a lower temperature as a result of lower SiO_2 . The perturbation of the liquid line of descent caused by assimilation of plagioclase cumulate into primitive magma (Kvassnes & Grove, 2008, Laubier *et al.*, 2012) is consistent with the elevated Al_2O_3 and reduced SiO_2 concentrations in the Taney Seamount-A lavas.

Calculations using the geochemical modeling program Petrolog (Danyushevsky & Plechov, 2011) indicate that ~18-20 % crystallization of Siqueiros-type melt is required to reach ~9 wt. % MgO, representative of primitive MORB. A M_a/M_c (mass assimilated/mass crystallized) value of 0.5 indicates that the system assimilated 6-7 % plagioclase from a cumulate containing plagioclase and olivine in a 3:1 ratio. We use mass balance to investigate the concentration of Sr in plagioclase required to increase the strontium anomaly (Sr/Sr*) of a primitive melt from 1 to 1.35, when normalized to primitive upper mantle (McDonough & Sun, 1995). If we assume that a primitive melt with a strontium anomaly (Sr/Sr*) of 1 (i.e., no anomaly) and an initial Sr concentration of 50-100 ppm assimilates 7 % cumulate plagioclase, then the concentration of Sr in plagioclase required to increase the melt Sr/Sr* to 1.35 is calculated

$$C_{Sr}^{Plag} = \frac{\left(Sr/Sr^*\right)C_{Sr}^{Melt} - \left(X_{Melt}C_{Sr}^{Melt}\right)}{X_{Plag}} \tag{1}$$

 C_{Sr}^{Plag} and C_{Sr}^{Melt} represent the concentrations of Sr in plagioclase and initial melt. X_{Melt} and X_{Plag} represent the mass fraction of melt (93%) and plagioclase (7%), respectively. This simple calculation estimates that assimilated plagioclase would require 300-600 ppm Sr (C^{plag}), assuming an initial melt concentration of 50-100 ppm Sr (C^{melt}), to create a positive Sr anomaly of 1.35 (representative of Taney-A). These Sr concentrations in plagioclase are typically unrealistic in lower oceanic crust plagioclase (Drouin *et al.*, 2009). Assimilation of a plagioclase cumulate can explain the high-Al, low-Si geochemical character of the Taney-A lavas, therefore, a separate process must be invoked to explain the enrichment in Sr.

Diffusive exchange during percolation of melt through a plagioclase cumulate matrix

Cations with different chemical properties (e.g., charge and ionic radii) diffuse at different rates in plagioclase resulting in fractionation of trace elements. Because the diffusivity of Sr^{2+} is 1-2 orders of magnitude higher than REE³⁺ (Cherniak, 2010), percolating melt will acquire a strontium anomaly (Sr/Sr^*) when normalized to primitive upper mantle. In the model considered here, plagioclase saturated basaltic melt percolates through a porous plagioclase and olivine cumulate matrix and undergoes diffusive exchange with the solid, as long as the melt and the solid are not in trace element equilibrium. This is a simplified case as open magmatic systems will cause fluctuations in plagioclase saturation, resulting in resorption and precipitation, which is observed in the erupted crystals. Our model assumes that plagioclase is the only phase undergoing diffusive exchange, as olivine does not significantly contribute to the trace element budget. For one-dimensional melt percolation through a porous medium with a spherical matrix geometry, mass conservation of an element within the solid matrix ($0 \le r \le R$) may be written (Iwamori, 1992, Korenaga & Kelemen, 1998, Navon & Stolper, 1987):

$$\frac{\partial C_r}{\partial t} = D_s \left(\frac{\partial^2 C_r}{\partial r^2} + \frac{2}{r} \frac{\partial C_r}{\partial r} \right) \tag{2}$$

where D_s is the diffusion rate in the solid and C_r is the concentration of an element in the solid phase (grain). The mass conservation of an element in the melt may be expressed as:

$$\frac{\partial C_m}{\partial t} + V_m \frac{\partial C_m}{\partial z} = -\frac{(1 - \phi)}{\phi} K_d \frac{\rho_r}{\rho_m} \frac{\partial C_s}{\partial t} \text{ where, } \frac{\partial C_s}{\partial t} = \frac{3}{R^3} \frac{\partial}{\partial t} \left[\int_0^R C_r r^2 \partial r \right]$$
(3)

Here, $C_{\rm m}$ is the concentration of an element in the melt, V_m velocity of the melt $({\rm m\,s^{-1}})$, φ porosity of the column, $\rho_{\rm r}$ density of the solid phase $({\rm kg\,m^{-3}})$, $\rho_{\rm m}$ density of the melt phase $({\rm kg\,m^{-3}})$ $K_{\rm d}$ is the solid-melt partition coefficient, and R is the grain radius. In this model we ignore diffusion in the z direction because it is negligible for the timescales of interest. The grain boundary remains in chemical equilibrium with the melt such that:

$$C_r(z,R,t) = K_d C_m(z,t) \tag{4}$$

The above equations are solved numerically using a two-step Crank-Nicolson algorithm (Ames, 1977). The full derivation of the mathematical model of 1-d flow through a porous media including boundary conditions, numerical parameters, model parameters, and program formulation, is presented in supplementary information S4. For an initial melt composition, we use the least differentiated Taney Seamount-A lava (D176-R25) with the most positive Sr anomaly. It is important to note that even the least differentiated samples have fractionated some plagioclase; hence the magnitude of the positive Sr anomaly is a minimum. Because the diffusivities of REE³⁺ and HFSE^{4+, 5+} are slow and their concentrations low in plagioclase (Drouin *et al.*, 2009, Lissenberg *et al.*, 2013), we recalculate Sr²⁺ and Ba²⁺ concentrations relative to the neighbouring incompatible trace element according to Sr* = $\sqrt{Pr_N Nd_N}$ and Ba* =

 $\sqrt{\text{Rb}_{N}\text{Th}_{N}}$. For the initial plagioclase composition, we use lower oceanic crust cumulate plagioclase from a troctolite sampled at Atlantis Massif, Mid-Atlantic Ridge (Drouin *et al.*, 2009) with 177 ppm Sr and an anorthite content of An₈₂. Seismic studies of melt distribution at the Moho beneath the East Pacific Rise at 9° - 10°N suggest that melt porosities range from 2.5 - 17 % (Crawford & Webb, 2002, Dunn *et al.*, 2000); therefore, we perform model runs at 0.025 ϕ , 0.05 ϕ and 0.1 ϕ . Studies of the crust-mantle transition zone in ophiolites constrain the grain size of plagioclase phases at 0.5 - 2 mm (Garrido *et al.*, 2001). The velocity of the melt determines the minimum column height for the interaction time. For our model we selected a melt velocity at the Moho of 10^{-8} m/s, which is representative of melt migration at a mid-ocean ridge with a half spreading rate of 50 mm/yr (Korenaga & Kelemen, 1998), although we note that the velocity is likely slower off-axis.

Modelling results from the 1-d porous flow diffusion model are illustrated in Figure 11a-c. The diagram shows that the Sr enrichment observed in the Taney Seamount-A lavas can be created by diffusive exchange with a plagioclase cumulate. During melt percolation, Ba/Th and Sr/Nd ratios will diverge from those produced during mantle melting as long as the melt and solid are not in chemical equilibrium ($C_m \neq C_{p'}K_d$). The melts which form the constructional edifice and caldera infill lavas are trace element enriched compared to the pillow cone lavas with positive Sr anomalies (Fig. 8a, b). Therefore, cumulate products from earlier trace element enriched melts will be in disequilibrium with the trace element depleted pillow cones. The larger diffusion coefficients of Sr^{2+} and Ba^{2+} compared to REE^{3+} and $HFSE^{4+,5+}$ create the "plagioclase signature" that has been observed in many lavas (Danyushevsky *et al.*, 2004, Gurenko & Sobolev, 2006, Laubier *et al.*, 2012, Sobolev *et al.*, 2000). A further benefit of this model is that for a melt with ~110 ppm Sr (Sr^* D176-R25), the plagioclase only requires ~ 1.5 times the Sr

concentration of the melt, in contrast to at least 3.7 times estimated using the assimilation model described earlier.

Estimates of interaction timescales between cumulate and melt require precise knowledge of the percolating melt and cumulate compositions, partition and diffusion coefficients, porosity, and grain size. Although we cannot precisely define these parameters, our best estimates suggest timescales on the order of 10^{0} - 10^{2} years. A sensitivity analysis and description of the effects of varying parameters are discussed in supplementary information S4. The presence of isotopic disequilibria in anorthite-rich plagioclase at mid-ocean ridges indicates that the crystals cannot be held at elevated temperatures for timescales which erase the disequilibria (Lange *et al.*, 2013). The calculated time to erase disequilibria at a length scale of 0.250 mm within a crystal at 1200° C is $> 4.5 \times 10^{2}$ years. Therefore, it is evident that from our results that a simple 1-d porous flow diffusion model requires very short but plausible timescales.

In summary, assimilation of a plagioclase cumulate can explain the high-Al and low-Si character of the Taney-A lavas but is inadequate to explain the magnitude of Sr enrichment. Nevertheless, a portion of the Sr anomaly may be derived by assimilation of a plagioclase cumulate. Conversely, diffusive exchange can explain the magnitude of Sr enrichment, assuming cumulate formation from a trace element enriched melt such as the constructional edifice lavas. Due to the ultraslow diffusion rate of the NaSi-CaAl couple, however, this model cannot explain the high-Al and low-Si signature. Furthermore, assimilation of plagioclase cumulate provides a mechanism to saturate a primitive melt in plagioclase, a requirement for the diffusive exchange model. Dynamic recrystallization of the plagioclase crystal may provide another mechanism to enrich the melt in Sr, although this process also cannot itself explain the high-Al and low-Si signature (Ashley *et al.*, 2014). We propose that the high-Al, low-Si, and positive Sr anomaly

signature of the Taney Seamount-A lavas is a combination of the processes presented above.

Studies of lower oceanic crustal cumulates show a wide range in trace elements in addition to Sr (Coogan *et al.*, 2000, Lissenberg *et al.*, 2013). An important question has been whether these variations are linked to mantle source or crustal processes. It has been suggested that reactive porous flow through a lower oceanic crust cumulate pile can enrich the melt in highly incompatible elements more rapidly than can fractional crystallization (Lissenberg *et al.*, 2013). One key aspect of this model is that reactive porous flow is accompanied by decreasing melt mass so that more incompatible element enriched compositions are also more differentiated (lower MgO). This model is attractive because it combines the degree of differentiation and highly incompatible trace element enrichment into a single process.

At Taney Seamount-A the more differentiated edifice lavas are the most highly incompatible element enriched, while the less differentiated cone lavas are the most depleted (Fig. 9g, h), consistent with the melt-cumulate interaction models. However, edifice lavas erupted at the younger Taney Seamounts B and C are as depleted or even more depleted in highly incompatible trace elements than the Taney-A cones, but have similar MgO as the Taney-A edifice lavas (Fig. 10f, g). These observations suggest that the degree of highly incompatible element enrichment is decoupled from the degree of differentiation.

Mantle source and partial melting

The oldest Taney Seamount-A lavas, represented by the edifice-building and caldera infill stages, differ from characteristic EPR MORB. Due to the proximity of near-ridge seamounts to the spreading center (<30 km) a key question is where the melts are generated. If

the melts were generated from the wings of the MORB melting region, than the melting column would be shorter with a deeper extraction (Wanless *et al.*, 2014). Alternatively, the generation of Taney Seamount lavas could be derived from a separate source. When compared to average Pacific MORB, the edifice and caldera infill lavas are enriched in MREE (Dy) relative to HREE (Yb), and LREE (La) relative to MREE (Sm) (Fig. 12). By contrast, the young Taney-A cones in the east have trace element ratios resembling average Pacific MORB. The edifice and caldera infill lavas are interesting due to their depletion of HREE, resulting in an elevated (Dy/Yb)_N ratio at a given (La/Sm)_N ratio when compared to the spectrum of EPR MORB compositions (Fig. 12).

Heavy rare earth elements, such as Lu and Yb, are compatible in garnet but incompatible in other mantle minerals (olivine, pyroxene, spinel). Therefore, the depletion of HREE relative to MREE is consistent with melt segregated from a source with residual garnet. We present two models for a garnet-bearing source and evaluate them: (1) aggregate melt from a depleted MORB mantle peridotite lithology which segregated at depth (shorter melting column) resulting in a larger proportion of deep garnet peridotite equilibrated melts compared to typical MORB, and (2) interaction of deep garnet pyroxenite-derived melts with typical depleted MORB mantle, followed by partial melting of the re-fertilized mantle peridotite. The first scenario models chemical heterogeneity of a homogenous lithology (peridotite), whereas the second models chemical and lithological heterogeneity (peridotite + pyroxenite).

Model 1: Deeper melt segregation

The first model requires that the near-ridge seamount volcanic system is fed by incremental or continuous melting of an adiabatic upwelling mantle as inferred for the mid-ocean ridge system. For this model, the trace elements are heterogeneous within a peridotite lithology. The trace element composition for the depleted mantle endmember is the depleted MORB mantle or "DMM" (McKenzie & O'Nions, 1991). The major element composition used for the melting models is a depleted MORB mantle (DMM) spinel peridotite calculated from the mineral compositions and modal abundances from McKenzie and O'Nions (1991). We assume an isentropic mantle adiabatic temperature of 1400°C at 3 GPa which produces a crustal thickness (Zc) of approximately 6.0 km, corresponding to the minimum oceanic crustal thickness. A sensitivity analysis addressing the effects of variable mantle major and trace element geochemistry in addition to adiabatic temperature is provided in supplementary information S5. The sensitivity analysis illustrates that other trace element compositions of the DMM (Salters & Stracke, 2004, Workman & Hart, 2005) do not intersect the dominant MORB field, justifying our choice of DMM from McKenzie & O'Nions (1991). Furthermore, varying the mantle potential temperature controls the pressure at which the mantle adiabat crosses the solidus, thus affecting the HREE-MREE fractionation. It is well known that the pMELTS algorithm used in alphaMELTS underestimates the degree of partial melting when compared to experiments for a given temperature (Ghiorso et al., 2002). To compensate for this underestimation, alphaMELTS model runs were performed at the mantle potential temperature plus 50° C (e.g., $1400 + 50 = 1450^{\circ}$ C). The modeling parameters are shown in supplementary information Table S5.1.

Our results show that the depletion of HREE relative to LREE is affected by different degrees of partial melting (Fig. 12). Because the continuous melting algorithm integrates over the entire melting column, aggregate melts extracted from the mantle at greater depth (P_f) have a larger proportion of lower degree partial melts. Typical N-MORB is modeled by a comparatively high degree of partial melting (15 %) of a DMM source with an initial pressure of melting (P_0) of 2.2 GPa, consistent with melting in the stability field of spinel. The melting model suggests that Taney Seamount-A compositions can be generated by lower degrees (5-11 %) of melting of a depleted source with P₀ of 2.2 GPa. The main edifice and caldera infilling lavas have the highest $(Dy/Yb)_N$, thus represent the lowest degree of partial melting. These smaller degree melts (F = ~5%) have a P_f of 1.3 GPa (40-50 km below the seafloor), deeper than the thickness of the offaxis lithosphere (15-30 km) assuming a formation window 5-30 km distant from the ridge. Lavas from the young constructional cones have the lowest (Dy/Yb)_N and therefore represent the highest degree of partial melting (F = \sim 11%), resulting in a P_f of 0.85 GPa (25-35 km below seafloor). Hence in this model, the early erupted lavas represent melt segregated at greater depth, while the later erupted magmas represent melt released at shallower depths.

Although this model can explain our geochemical observations, the relative volumes of melt generated are paradoxical. The largest volumes of lava erupted at Taney Seamount-A are represented by the edifice building and older caldera infilling lavas. If the first model is valid, the more voluminous older lavas are generated from a mantle which has undergone the lowest degrees of partial melting ($F = \sim 5\%$), while the less voluminous and younger pillow cones are generated from a mantle which has undergone the highest degrees of partial melting ($F = \sim 11\%$). Logically, higher degrees of partial melting would result in a greater magma supply and viceversa, assuming the volume of mantle undergoing melting remains approximately constant. This

reasoning is supported by geochemical differences between fast and slow spreading mid-ocean ridges, where spreading rate is an analogue to melt supply (Niu & Hékinian, 1997). Therefore, the paradox between the apparent degree of partial melting and volume of erupted lava suggests that the answer lies elsewhere.

Model 2: Role of garnet pyroxenite and a mixed mantle lithology

Trace element and isotopically enriched mid-ocean ridge basalts are found at locations far from the influence of hotspots and are commonly coeval with more voluminous N-MORB material (Allan *et al.*, 1989, Donnelly *et al.*, 2004, Fornari *et al.*, 1988a, Niu & Batiza, 1997, Niu *et al.*, 1999, Zindler *et al.*, 1984). The similarity of E-MORB and N-MORB in terms of their major element geochemistry suggests that they share a similar melting history. Therefore, the trace element and isotopic enrichment in E-MORB is derived from source heterogeneity (Lundstrom *et al.*, 2000). The positive correlations of Rb-Sr, Sm-Nd, and ²³⁸U-²⁰⁶Pb isochron plots for basalts from all ocean basins indicate an apparent source age of ~300 Ma (Donnelly *et al.*, 2004). This age defines the continuous creation and destruction of the enriched source, which has been interpreted as recycled oceanic crust resulting in the formation of mafic veins (pyroxenites) within a depleted peridotite matrix (Allegre & Turcotte, 1986, Mallik & Dasgupta, 2012, Niu & Batiza, 1997, Niu *et al.*, 1999, Sobolev *et al.*, 2007).

There have been numerous recent studies inferring the role of pyroxenite heterogeneities in the generation of mid-ocean ridge basalts (Hirschmann & Stolper, 1996, Lambart *et al.*, 2012, Lambart *et al.*, 2009, Lambart *et al.*, 2013, Pertermann & Hirschmann, 2003b, Sobolev *et al.*, 2007, Stracke & Bourdon, 2009, Waters *et al.*, 2011, Yaxley & Green, 1998, Zhang *et al.*, 2012),

although the origin of the lithological variation remains controversial. Pyroxenite heterogeneities are argued to be derived from low degree slab melts which metasomatise the peridotite mantle (Donnelly *et al.*, 2004, Niu *et al.*, 2002), or from garnet pyroxenite veins formed by stretching and thinning of subducted oceanic crust (Hirschmann & Stolper, 1996, Sobolev *et al.*, 2007). Although the calculated fraction of pyroxenite in the upper mantle is only 2-5%, it may contribute a larger proportion of melt due to its lower solidus temperature and higher melt productivity. Garnet remains stable at lower pressures (1.3-1.7 GPa) in pyroxenite than in peridotite (2.5 GPa), indicating that melts from a mixed lithology containing garnet can be produced at lower pressures (Hirschmann & Stolper, 1996, Pertermann & Hirschmann, 2003b). We now examine if the garnet signature (elevated MREE/HREE) and trace element enrichment found in the Taney Seamount-A samples involve, in part, partial melting of a garnet pyroxenite lithology.

We model the trace element composition of pyroxenite partial melting by utilizing the results from melting experiments on volatile-free basaltic pyroxenite G2 at 3 GPa, performed at conditions under which the peridotite matrix is subsolidus (Pertermann & Hirschmann, 2003a). The pertinent experiments are from 1375°C-1425°C, consistent with the temperature regime utilized for the periodotite melting models as explained earlier. The initial pyroxenite trace element compositions chosen were an average N-MORB (Arevalo & McDonough, 2010) for the depleted end member and a representative E-MORB sample from the East Pacific Rise (http://earthchem.org/petdb) for the enriched end member. The composition of fluid-mobile elements in subducted oceanic crust is likely to change due to dehydration reactions. However, the REE and HFSE concentrations should not change significantly as these elements are generally immobile in fluids. The partition coefficients used in this model are from garnet/melt

and clinopyroxene/melt experiments on G2 basaltic pyroxenite at 3 GPa (Pertermann *et al.*, 2004) and are presented in supplementary information Table S5.2. We calculate the trace element compositions of each experimental melt using the standard batch melting equation:

$$C_{l} = \frac{C_{0}}{D_{0}(1-F)+F} \tag{5}$$

where for a given element C_l is the concentration in the liquid at a given degree of partial melting F, D_0 is the bulk partition coefficient, and C_0 is the concentration in the initial source. The degree of partial melting is determined by the amount of quenched glass in the experiments. We use batch melting as it accurately approximates aggregate fractional melts, but note that batch melting does not accurately approximate the residue.

The trace element modeling results for partial melting of G2 basaltic pyroxenite at 3 GPa and 1375°C-1425°C are illustrated in Figure 13a. Due to the high modal abundance of garnet (14-16 %) in the G2 pyroxenite, partial melts (F = 18-36 %) have elevated MREE/HREE. A simple explanation for the Taney-A trend involves binary mixing between garnet pyroxenite derived melt and peridotite derived melt represented by the EPR N-MORB compositions. This model requires that the older edifice building and caldera infill lavas have a 30:70 mix of pyroxenite and peridotite derived melts. Because a garnet pyroxenite has a lower solidus temperature than peridotite at 3 GPa, the pyroxenite can be up to 32% melt while the peridotite matrix remains unmelted. In this model, deep garnet pyroxenite derived melts travel to shallow levels assuming minimal interaction with the surrounding peridotite matrix. There are significant limitations to this model. Recent studies indicate that reactions between basaltic pyroxenite melts with a subsolidous matrix periodotite consume large amounts of melt, indicating that melt transport to the surface without interaction is difficult (Lambart *et al.*, 2012, Mallik & Dasgupta,

2012, Sobolev *et al.*, 2007, Yaxley & Green, 1998). The major element composition of basaltic pyroxenite partial melts can be highly variable depending on the degree of silica saturation. Low to moderate degrees of partial melting of typical, silica-saturated MORB, represented by the G2 basaltic pyroxenite, produces andesitic compositions (Fig. 13b, c). Therefore, it is difficult to reconcile mixing relationships between the trace and major elements due to the andesitic nature of the partial melts.

These limitations can be addressed by a two-stage melting model where deep garnet pyroxenite derived melts react with the subsolidus depleted MORB mantle peridotite to produce a re-fertilized peridotite with an inherited garnet signature. We model this scenario by adding aliquots of experimentally determined partial melt (F=24% at 1400°C and 3 GPa) of G2 basaltic pyroxenite to the DMM peridotite (McKenzie & O'Nions, 1991). We assume that the trace element composition of the basaltic pyroxenite melt was derived from N-MORB, which is volumetrically the largest component subducted into the mantle. The mineralogy and compositions of the different lithologies are shown in supplementary information Table S5.1. We model the incremental or continuous melting of an adiabatic upwelling re-fertilized peridotite using the same alphaMELTS parameters as the earlier peridotite model for continuity.

Reaction between basaltic pyroxenite-derived melt and DMM in different proportions can produce a variety of lithologies with varying trace element enrichments (Kogiso & Hirschmann, 2006, Mallik & Dasgupta, 2012). The main mineralogical outcome of adding basaltic pyroxenite-derived melt to DMM is to increase modal clinopyroxene and garnet at the expense of olivine (Sobolev *et al.*, 2007). Trace element results from our two-stage model indicate that a re-fertilized source produced by mixing 2.5% of a basaltic melt formed by melting of garnet-bearing pyroxenite with 97.5% DMM reproduces the garnet signature observed in the more

voluminous edifice lavas at a similar degree of partial melting (~15%) invoked for N-MORB formation (Fig. 14a, b). This model has the added benefit of reproducing the apparent garnet signature without invoking deep segregation of peridotite derived melts (model 1) or isolated transport of garnet pyroxenite partial melts to shallower depths, although both processes may still contribute. Depleted MORB mantle re-fertilization has an additional effect of lowering the solidus temperature of the peridotite. A lower solidus would enable melting to occur at distances further from the ridge axis where the mantle temperature may be cooler, explaining melt production off-axis. Transition to lavas with N-MORB affinity, which require a higher mantle temperature at an equivalent degree of partial melting, result from migration of the ridge axis towards the seamount melting anomaly (Hann, 2012).

Near-ridge seamounts in the Pacific Ocean erupt lavas that are typically more depleted than the adjacent ridge (Niu *et al.*, 2002), suggesting generation from a residual refractory periodotite that has undergone previous melting beneath the ridge (Geshi *et al.*, 2007). The observation of the trace element enriched re-fertilization signal in Taney Seamount-A edifice and caldera infill lavas suggests that pyroxenite heterogeneities are pristine, or have not been completely exhausted beneath the spreading center. A similar pyroxenite (garnet) signal has been observed at the Vance Seamounts, indicating that the process modelled here is not unique to Taney. The progressive depletion of trace elements over the lifespan of a single seamount and the entire chain suggests that heterogeneities can be present at both short length and time scales. The preservation of geochemical signals related to these heterogeneities demonstrates the importance of a magmatic plumbing system independent of the nearby spreading center in order to avoid homogenization (Rubin *et al.*, 2009).

A MODEL FOR MAGMA EVOLUTION BENEATH TANEY SEAMOUNT-A

The progressive change in Taney Seamount-A lava geochemistry with time suggests the following scenario for magma evolution from mantle melting to eruption on the seafloor. Early Taney-A edifice lavas acquired a garnet signature by two-stage melting of a two-component mantle. The first stage involved melting of fusible pyroxenite in the garnet stability field and reaction of these andesitic melts with subsolidus peridotite. The second stage involved melting of the re-fertilized peridotite with an inherited garnet signature from the first-stage pyroxenite melts (Fig. 14). The progressive trace element depletion of lavas over the lifespan of Taney Seamount-A (edifice to cones), as well as the seamount chain (Taney Seamounts-A to C, Fig. 10), suggests that the enriched source component was becoming progressively exhausted with time. Primitive melts extracted from the mantle assimilated lower crustal plagioclase cumulates and acquired a high-Al, low-Si, and minor Sr-enriched geochemical signal when compared to MORB. The Sr enrichment was enhanced by diffusive exchange during porous flow under plagioclase-saturated conditions (Fig. 11). The modified melts migrated to a shallow magmatic reservoir where they underwent varying degrees of differentiation which were correlated to their residence time in the upper crust (Fig. 8).

Trace element enrichments at other near-ridge seamounts and seamounts formed at fossil spreading ridges also have been attributed to melting of a two-component mantle (Brandl *et al.*, 2012, Haase *et al.*, 2011). The increase in trace element enrichment at the end of a seamount's lifetime has been explained by a greater contribution from more fusible trace element-enriched lithologies (e.g., pyroxenite) with lower degrees of partial melting expected during the waning stages (Haase *et al.*, 2011). But the late stage Taney Seamount-A cones, which were erupted

during a decrease in melt supply, have more depleted compositions. The low melt supply (low volume) depleted cones are as depleted as the high melt supply edifice lavas of Taney Seamount-B (Fig. 10g). Therefore, we propose that the low melt supply and depleted character of the Taney-A cones can be explained by leakage of melt from an active Taney-B system into a nearly extinct Taney-A system which had moved away from the melt supply. The parallel alignment of the cones with the Farallon spreading center suggests that the leakage was likely tectonically controlled. This does not rule out the possibility of erupting trace element enriched lavas at the end of a seamount's lifetime, but it provides an explanation for the contrasting observations at Taney Seamount-A.

CONCLUSIONS

Near-ridge seamounts are an important component of the mid-ocean ridge system and have been crucial for improving our understanding of Earth's upper mantle. Taney Seamount-A is an exceptional site due to multiple caldera collapse features with clear cross-cutting relationships. We have utilized systematic sampling of these features in order to investigate changes in geochemistry over the lifespan of this seamount. Based on our findings, we propose that the magmatic architecture beneath Taney Seamount-A is characterized by open system evolution in a sub-caldera magma reservoir, melt-rock interaction in the upper mantle and lower oceanic crust, and melting of a mixed lithology mantle (Fig. 15). This study demonstrates that complex magmatic architectures beneath submarine volcanoes modify primary melts from the mantle, revealing that an array of magmatic processes play significant roles at different structural levels beneath a seamount volcano.

Our principal conclusions are the following:

- (1) Taney Seamount-A has a shallow open magmatic system that undergoes repeated cycles of caldera collapse, magmatic rejuvenation, differentiation and eruption.
- (2) Erupted lavas contain large crystals of calcic plagioclase (An_{80} 90) riddled with melt inclusions. The CO_2 H_2O vapour saturation pressures (~ 250 400 MPa) of these melt inclusions indicate that the crystals originate in the lower crust to upper mantle and were transported into the sub-caldera reservoir prior to eruption. Compositional zoning and dissolution textures in the plagioclase crystals demonstrate that melt-rock interaction was an important process.
- (3) Erupted basalts with high Al₂O₃, low SiO₂, and positive Sr anomalies indicate the importance of melt-cumulate interaction. Assimilation of plagioclase-rich material will perturb the liquid line of descent to higher Al₂O₃ and lower SiO₂ concentrations, but Sr concentrations in the cumulate are too low to generate the observed Sr anomaly. Diffusive exchange during percolation of melt through a MORB-type plagioclase cumulate matrix results in kinetic fractionations of Sr which generate the observed positive Sr anomaly.
- (4) The oldest and most voluminous edifice-building lavas are defined by enrichments of MREE relative to HREE on a spidergram normalized to average Pacifc MORB, suggesting melt segregation from a lithology with residual garnet. High pressure experimental data indicate that mafic lithologies (G2-basaltic pyroxenite) are capable of producing a high proportion of melt within the garnet stability field compared to peridotite lithologies. Reaction of these melts with the depleted MORB mantle produces a re-fertilized peridotite with an inherited garnet signature. Decompression melting of the re-fertilized peridotite reproduces the garnet signature observed in

Taney Seamount-A lavas without invoking the need for deep melt segregation or isolated transport of melts.

ACKNOWLEDGEMENTS

We would like to thank the Monterey Bay Aquarium Research Institute (MBARI) for providing an opportunity for J.C. and J.S. to participate in the 2010 Taney Seamounts cruise. We thank the crew of the R.V. Western Flyer for insuring a safe and successful cruise and the operators of the ROV Doc Ricketts for collecting precious samples. We also thank the Science Party (Jenny Paduan, Lonny Lundsten, Issy Yeo, Ryan Portner, Lucas Koth, Craig McClain, Justine Jackson-Ricketts, and Sarah Hardy) for their hard work executing the scientific program. Lang Shi and André Poirier provided essential support and advice for electron microprobe and ICP-MS analyses, respectively. We thank the Woods Hole Oceanographic Institution, Nobu Shimizu, and Brian Monteleone for their support during SIMS volatile analysis. Discussions with Don Baker, Don Francis, Marc-Antoine Longpré, and Roger Nielsen helped improve this manuscript measurably, as did formal reviews by Marcel Regelous, Johan Lissenberg, and Patricia Gregg. Finally, we would like to thank Colin Devey for editorial handling. This work was funded by scholarships to J.C. from GEOTOP and McGill University, support to D.C. from MBARI through a grant from the David and Lucile Packard Foundation, and grants to J.S. from the Natural Sciences and Engineering Research Council of Canada.

REFERENCES

- Allan, J. F., Batiza, R., Perfit, M. R., Fornari, D. J. & Sack, R. O. (1989). Petrology of lavas from the Lamont Seamount chain and adjacent East Pacific Rise, 10°N. *Journal of Petrology* **30**, 1245-1298.
- Allan, J. F., Batiza, R. & Sack, R. O. (1994). Geochemical characteristics of Cocos Plate seamount lavas. *Contributions to Mineralogy and Petrology* **116**, 47-61.

- Allegre, C. J. & Turcotte, D. L. (1986). Implications of a two-component marble-cake mantle. *Nature* **323**, 123-127.
- Ames, W. F. (1977). *Numerical methods for partial differential equations*. 111 Fifth Avenue, New York, New York 10003: Academic Press Inc.
- Arevalo, R. & McDonough, W. F. (2010). Chemical variations and regional diversity observed in MORB. *Chemical Geology* **271**, 70-85.
- Ashley, K. T., Carlson, W. D., Law, R. D. & Tracy, R. J. (2014). Ti resetting in quartz during dynamic recrystallization: Mechanisms and significance. *American Mineralogist* **99**, 2025-2030.
- Batiza, R. (1982). Abundances, distribution and sizes of volcanoes in the Pacific Ocean and implications for the origin of non-hotspot volcanoes. *Earth and Planetary Science Letters* **60**, 195-206.
- Batiza, R., Niu, Y. & Zayac, W. C. (1990). Chemistry of seamounts near the East Pacific Rise: Implications for the geometry of subaxial mantle flow. *Geology* **18**, 1122-1125.
- Batiza, R., Smith, T. L. & Niu, Y. (1989). Geological and petrologic evolution of seamounts near the EPR based on submersible and camera study. *Marine Geophysical Researches* **11**, 169-236.
- Batiza, R. & Vanko, D. (1984). Petrology of young Pacific seamounts. *Journal of Geophysical Research* **89**, 11235-11260.
- Brandl, P. A., Beier, C., Regelous, M., Abouchami, W., Haase, K. M., Garbe-Schoenberg, D. & Galer, S. J. G. (2012). Volcanism on the flanks of the East Pacific Rise: Quantitative constraints on mantle heterogeneity and melting processes. *Chemical Geology* **298**, 41-56.
- Cherniak, D. J. (2010). Cation Diffusion in Feldspars. *Reviews in Mineralogy & Geochemistry* **72**, 691-733.
- Clague, D. A., Paduan, J. B. & Davis, A. S. (2009). Widespread strombolian eruptions of midocean ridge basalt. *Journal of Volcanology and Geothermal Research* **180**, 171-188.
- Clague, D. A., Reynolds, J. R. & Davis, A. S. (2000). Near-ridge seamount chains in the northeastern Pacific Ocean. *Journal of Geophysical Research* **105**, 16541-16561.
- Coogan, L. A., Saunders, A. D., Kempton, P. D. & Norry, M. J. (2000). Evidence from oceanic gabbros for porous melt migration within a crystal mush beneath the Mid-Atlantic Ridge. *Geochemistry Geophysics Geosystems* 1, 10.1029/2000GC000072.
- Costa, F., Coogan, L. A. & Chakraborty, S. (2010). The time scales of magma mixing and mingling involving primitive melts and melt-mush interaction at mid-ocean ridges. *Contributions to Mineralogy and Petrology* **159**, 371-387.

- Cousens, B., Dostal, J. & Hamilton, T. S. (1999). A near-ridge origin for seamounts at the southern terminus of the Pratt-Welker Seamount Chain, northeast Pacific Ocean. *Canadian Journal of Earth Sciences* **36**, 1021-1031.
- Cousens, B. L., Allan, J. F., Leybourne, M. I., Chase, R. L. & Vanwagoner, N. (1995). Mixing of magmas from enriched and depleted mantle sources in the northeast Pacific: West Valley segment, Juan de Fuca Ridge. *Contributions to Mineralogy and Petrology* **120**, 337-357.
- Cousens, B. L., Chase, R. L. & Schilling, J. G. (1985). Geochemistry and origin of volcanic rocks from Tuzo Wilson and Bowie seamounts, northeast Pacific Ocean. *Canadian Journal of Earth Sciences* **22**, 1609-1617.
- Crawford, W. C. & Webb, S. C. (2002). Variations in the distribution of magma in the lower crust and at the Moho beneath the East Pacific Rise at 9°-10°N. *Earth and Planetary Science Letters* **203**, 117-130.
- Danyushevsky, L. V. (2001). The effect of small amounts of H₂O on crystallisation of mid-ocean ridge and backarc basin magmas. *Journal of Volcanology and Geothermal Research* **110**, 265-280.
- Danyushevsky, L. V., Leslie, R. A. J., Crawford, A. J. & Durance, P. (2004). Melt inclusions in primitive olivine phenocrysts: The role of localized reaction processes in the origin of anomalous compositions. *Journal of Petrology* **45**, 2531-2553.
- Danyushevsky, L. V., Perfit, M. R., Eggins, S. M. & Falloon, T. J. (2003). Crustal origin for coupled 'ultra-depleted' and 'plagioclase' signatures in MORB olivine-hosted melt inclusions: evidence from the Siqueiros Transform Fault, East Pacific Rise. *Contributions to Mineralogy and Petrology* **144**, 619-637.
- Danyushevsky, L. V. & Plechov, P. (2011). Petrolog3: Integrated software for modeling crystallization processes. *Geochemistry Geophysics Geosystems* **12**, 10.1029/2011GC003516.
- Davis, A. S. & Clague, D. A. (2000). President Jackson Seamounts, northern Gorda Ridge: Tectonomagmatic relationship between on- and off-axis volcanism. *Journal of Geophysical Research* **105**, 27939-27956.
- Davis, A. S., Clague, D. A., Paduan, J. B., Cousens, B. L. & Huard, J. (2010). Origin of volcanic seamounts at the continental margin of California related to changes in plate margins. *Geochemistry Geophysics Geosystems* **11**, 10.1029/2010gc003064.
- Donnelly, K. E., Goldstein, S. L., Langmuir, C. H. & Spiegelman, M. (2004). Origin of enriched ocean ridge basalts and implications for mantle dynamics. *Earth and Planetary Science Letters* **226**, 347-366.
- Drouin, M., Godard, M., Ildefonse, B., Bruguier, O. & Garrido, C. J. (2009). Geochemical and petrographic evidence for magmatic impregnation in the oceanic lithosphere at Atlantis Massif, Mid-Atlantic Ridge (IODP Hole U1309D, 30° N). *Chemical Geology* **264**, 71-88.

- Dunn, R. A., Toomey, D. R. & Solomon, S. C. (2000). Three-dimensional seismic structure and physical properties of the crust and shallow mantle beneath the East Pacific Rise at 9°30'N. *Journal of Geophysical Research* **105**, 23537-23555.
- Eason, D. & Sinton, J. (2006). Origin of high-Al N-MORB by fractional crystallization in the upper mantle beneath the Galapagos Spreading Center. *Earth and Planetary Science Letters* **252**, 423-436.
- Fornari, D. J., Perfit, M. R., Allan, J. F. & Batiza, R. (1988a). Small-scale heterogeneities in depleted mantle sources: near-ridge seamount lava geochemistry and implications for mid-ocean-ridge magmatic processes. *Nature* **331**, 511-513.
- Fornari, D. J., Perfit, M. R., Allan, J. F., Batiza, R., Haymon, R., Barone, A., Ryan, W. B. F., Smith, T., Simkin, T. & Luckman, M. A. (1988b). Geochemical and structural studies of the Lamont seamounts: seamounts as indicators of mantle processes. *Earth and Planetary Science Letters* **89**, 63-83.
- Garrido, C. J., Kelemen, P. B. & Hirth, G. (2001). Variation of cooling rate with depth in lower crust formed at an oceanic spreading ridge: Plagioclase crystal size distributions in gabbros from the Oman ophiolite. *Geochemistry Geophysics Geosystems* **2**, 10.1029/2000gc000136.
- Geshi, N., Umino, S., Kumagai, H., Sinton, J. M., White, S. M., Kisimoto, K. & Hilde, T. W. (2007). Discrete plumbing systems and heterogeneous magma sources of a 24 km³ off-axis lava field on the western flank of East Pacific Rise, 14°S. *Earth and Planetary Science Letters* **258**, 61-72.
- Geyer, A., Folch, A. & Martí, J. (2006). Relationship between caldera collapse and magma chamber withdrawal: An experimental approach. *Journal of Volcanology and Geothermal Research* **157**, 375-386.
- Ghiorso, M. S., Hirschmann, M. M., Reiners, P. W. & Kress, V. C. (2002). The pMELTS: A revision of MELTS for improved calculation of phase relations and major element partitioning related to partial melting of the mantle to 3 GPa. *Geochemistry Geophysics Geosystems* 3, 10.1029/2001gc000217.
- Graham, D. W., Zindler, A., Kurz, M. D., Jenkins, W. J., Batiza, R. & Staudigel, H. (1988). He, Pb, Sr and Nd isotope constraints on magma genesis and mantle heterogeneity beneath young Pacific seamounts. *Contributions to Mineralogy and Petrology* **99**, 446-463.
- Gurenko, A. A. & Sobolev, A. V. (2006). Crust–primitive magma interaction beneath neovolcanic rift zone of Iceland recorded in gabbro xenoliths from Midfell, SW Iceland. *Contributions to Mineralogy and Petrology* **151**, 495-520.
- Haase, K. M., Regelous, M., Duncan, R. A., Brandl, P. A., Stroncik, N. & Grevemeyer, I. (2011). Insights into mantle composition and mantle melting beneath mid-ocean ridges from postspreading volcanism on the fossil Galapagos Rise. *Geochemistry Geophysics Geosystems* **12**, 10.1029/2010gc003482.

- Hammond, S. R. (1997). Offset caldera and crater collapse on Juan de Fuca Ridge-flank volcanoes. *Bulletin of Volcanology* **58**, 617-627.
- Hann, N. L. (2012). Geochemical diversity of near-ridge seamounts: Insights into oceanic magmatic processes and sources through trace element and isotopic chemistry. *Ph. D.* University of Florida, Gainesville, FL 32611, United States.
- Hauri, E. H., Wagner, T. P., Grove, T. L. (1994). Experimental and natural partitioning of Th, U, Pb and other trace-elements between garnet, clinopyroxene and basaltic melts. Chemical Geology 117, 149-166.
- Hauri, E., Wang, J. H., Dixon, J. E., King, P. L., Mandeville, C. & Newman, S. (2002). SIMS analysis of volatiles in silicate glasses 1. Calibration, matrix effects and comparisons with FTIR. *Chemical Geology* **183**, 99-114.
- Helo, C., Longpre, M.-A., Shimizu, N., Clague, D. A. & Stix, J. (2011). Explosive eruptions at mid-ocean ridges driven by CO₂-rich magmas. *Nature Geoscience* **4**, 260-263.
- Herzberg, C. (2004). Partial crystallization of mid-ocean ridge basalts in the crust and mantle. *Journal of Petrology* **45**, 2389-2405.
- Hirschmann, M. M. & Stolper, E. M. (1996). A possible role for garnet pyroxenite in the origin of the "garnet signature" in MORB. *Contributions to Mineralogy and Petrology* **124**, 185-208.
- Iwamori, H. (1992). Melt-solid flow with diffusion-controlled chemical reaction. *Geophysical Research Letters* **19**, 309-312.
- Johnson, D. M., Hooper, P. R. & Conrey, R. M. (1999). XRF analysis of rocks and minerals for major and trace elements on a single low dilution Li-tetraborate fused bead. *Advances in X-ray Analysis* **41**, 843-867.
- Kamenetsky, V. S., Eggins, S. M., Crawford, A. J., Green, D. H., Gasparon, M. & Falloon, T. J. (1998). Calcic melt inclusions in primitive olivine at 43°N MAR: evidence for melt–rock reaction/melting involving clinopyroxene-rich lithologies during MORB generation. *Earth and Planetary Science Letters* **160**, 115-132.
- Kamenetsky, V. S. & Gurenko, A. A. (2007). Cryptic crustal contamination of MORB primitive melts recorded in olivine-hosted glass and mineral inclusions. *Contributions to Mineralogy and Petrology* **153**, 465-481.
- Katz, R. F., Spiegelman, M. & Holtzman, B. (2006). The dynamics of melt and shear localization in partially molten aggregates. *Nature* **442**, 676-679.
- Kennedy, B., Stix, J., Vallance, J. W., Lavallee, Y. & Longpre, M. A. (2004). Controls on caldera structure: Results from analogue sandbox modeling. *Geological Society of America Bulletin* **116**, 515-524.

- Knaack, C., Cornelius, S. & Hooper, P. R. (1994). Trace element analysis of rocks and minerals by ICP-MS. *Open File Report*, Department of Geology, Washington State University, Pullman, WA.
- Kogiso, T. & Hirschmann, M. M. (2006). Partial melting experiments of bimineralic eclogite and the role of recycled mafic oceanic crust in the genesis of ocean island basalts. *Earth and Planetary Science Letters* **249**, 188-199.
- Korenaga, J. & Kelemen, P. B. (1998). Melt migration through the oceanic lower crust: a constraint from melt percolation modeling with finite solid diffusion. *Earth and Planetary Science Letters* **156**, 1-11.
- Kvassnes, A. J. S. & Grove, T. L. (2008). How partial melts of mafic lower crust affect ascending magmas at oceanic ridges. *Contributions to Mineralogy and Petrology* **156**, 49-71.
- Lambart, S., Laporte, D., Provost, A. & Schiano, P. (2012). Fate of pyroxenite-derived melts in the peridotitic mantle: Thermodynamic and experimental constraints. *Journal of Petrology* **53**, 451-476.
- Lambart, S., Laporte, D. & Schiano, P. (2009). An experimental study of pyroxenite partial melts at 1 and 1.5 GPa: Implications for the major-element composition of Mid-Ocean Ridge Basalts. *Earth and Planetary Science Letters* **288**, 335-347.
- Lambart, S., Laporte, D. & Schiano, P. (2013). Markers of the pyroxenite contribution in the major-element compositions of oceanic basalts: Review of the experimental constraints. *Lithos* **160-161**, 14-36.
- Lange, A. E., Nielsen, R. L., Tepley, F. J., III & Kent, A. J. R. (2013). Diverse Sr isotope signatures preserved in mid-oceanic-ridge basalt plagioclase. *Geology* **41**, 279-282.
- Langmuir, C. H., Klein, E. M. & Plank, T. (1992). Petrological systematics of mid-ocean ridge basalts: Constraints on melt generation beneath ocean ridges. In: Phipps Morgan, J., Blackman, D. K. & Sinton, J. M. (eds.) *Mantle Flow and Melt Generation at Mid-Ocean Ridges. American Geophysical Union Monograph* **71**, 183-280.
- Laubier, M., Gale, A. & Langmuir, C. H. (2012). Melting and crustal processes at the FAMOUS segment (Mid-Atlantic Ridge): New insights from olivine-hosted melt inclusions from multiple samples. *Journal of Petrology* **53**, 665-698.
- le Roux, P. J., Shirey, S. B., Hauri, E. H., Perfit, M. R. & Bender, J. F. (2006). The effects of variable sources, processes and contaminants on the composition of northern EPR MORB (8-10°N and 12-14°N): Evidence from volatiles (H₂O, CO₂, S) and halogens (F, Cl). *Earth and Planetary Science Letters* **251**, 209-231.
- Lissenberg, C. J. & Dick, H. J. B. (2008). Melt–rock reaction in the lower oceanic crust and its implications for the genesis of mid-ocean ridge basalt. *Earth and Planetary Science Letters* **271**, 311-325.

- Lissenberg, C. J., MacLeod, C. J., Howard, K. A. & Godard, M. (2013). Pervasive reactive melt migration through fast-spreading lower oceanic crust (Hess Deep, equatorial Pacific Ocean). *Earth and Planetary Science Letters* **361**, 436-447.
- Lonsdale, P. (1983). Laccoliths(?) and small volcanoes on the flank of the East Pacific Rise. *Geology* **11**, 706-709.
- Lundstrom, C. C., Gill, J. & Williams, Q. (2000). A geochemically consistent hypothesis for MORB generation. *Chemical Geology* **162**, 105-126.
- Mallik, A. & Dasgupta, R. (2012). Reaction between MORB-eclogite derived melts and fertile peridotite and generation of ocean island basalts. *Earth and Planetary Science Letters* **329-330**, 97-108.
- Martí, J., Ablay, G. J., Redshaw, L. T. & Sparks, R. S. J. (1994). Experimental studies of collapse calderas. *Journal of the Geological Society* **151**, 919-929.
- McDonough, W. F. & Sun, S. S. (1995). The composition of the Earth. *Chemical Geology* **120**, 223-253.
- McKenzie, D. & O'Nions, R. K. (1991). Partial melt distributions from inversion of rare earth element concentrations. *Journal of Petrology* **32**, 1021-1091.
- Navon, O. & Stolper, E. (1987). Geochemical consequences of melt percolation: The upper mantle as a chromatographic column. *Journal of Geology* **95**, 285-307.
- Niu, Y. & Batiza, R. (1997). Trace element evidence from seamounts for recycled oceanic crust in the Eastern Pacific mantle. *Earth and Planetary Science Letters* **148**, 471-483.
- Niu, Y., Collerson, K. D., Batiza, R., Wendt, J. I. & Regelous, M. (1999). Origin of enriched-type mid-ocean ridge basalt at ridges far from mantle plumes: The East Pacific Rise at 11°20′N. *Journal of Geophysical Research* **104**, 7067-7087.
- Niu, Y. & Hékinian, R. (1997). Spreading-rate dependence of the extent of mantle melting beneath ocean ridges. *Nature* **385**, 326-329.
- Niu, Y., Regelous, M., Wendt, I. J., Batiza, R. & O'Hara, M. J. (2002). Geochemistry of near-EPR seamounts: importance of source vs. process and the origin of enriched mantle component. *Earth and Planetary Science Letters* **199**, 327-345.
- Pertermann, M. & Hirschmann, M. M. (2003a). Anhydrous partial melting experiments on morb-like eclogite: Phase relations, phase compositions and mineral—melt partitioning of major elements at 2–3 GPa. *Journal of Petrology* **44**, 2173-2201.
- Pertermann, M. & Hirschmann, M. M. (2003b). Partial melting experiments on a MORB-like pyroxenite between 2 and 3 GPa: Constraints on the presence of pyroxenite in basalt source regions from solidus location and melting rate. *Journal of Geophysical Research* **108** (B2), doi: 10.1029/2000jb000118.

- Pertermann, M., Hirschmann, M. M., Hametner, K., Günther, D. & Schmidt, M. W. (2004). Experimental determination of trace element partitioning between garnet and silica-rich liquid during anhydrous partial melting of MORB-like eclogite. *Geochemistry Geophysics Geosystems* 5, 10.1029/2003gc000638.
- Portner, R. A., Clague, D. A. & Paduan, J. B. (2014). Caldera formation and varied eruption styles on North Pacific seamounts: the clastic lithofacies record. *Bulletin of Volcanology* **76**(845), 1-28.
- Rappaport, Y., Naar, D. F., Barton, C. C., Liu, Z. J. & Hey, R. N. (1997). Morphology and distribution of seamounts surrounding Easter Island. *Journal of Geophysical Research* **102**, 24713–24728.
- Roche, O., Druitt, T. H. & Merle, O. (2000). Experimental study of caldera formation. *Journal of Geophysical Research* **105**, 395–416.
- Rubin, K. H., Sinton, J. M., Maclennan, J. & Hellebrand, E. (2009). Magmatic filtering of mantle compositions at mid-ocean-ridge volcanoes. *Nature Geoscience* **2**, 321-328.
- Saal, A. E., Kurz, M. D., Hart, S. R., Blusztajn, J. S., Blichert-Toft, J., Liang, Y. & Geist, D. J. (2007). The role of lithospheric gabbros on the composition of Galapagos lavas. *Earth and Planetary Science Letters* 257, 391-406.
- Sager, W. W., Zhang, J., Korenaga, J., Sano, T., Koppers, A. A. P., Widdowson, M. & Mahoney, J. J. (2013). An immense shield volcano within the Shatsky Rise oceanic plateau, northwest Pacific Ocean. *Nature Geoscience* **6**, 976-981.
- Salters, V. J. M. & Stracke, A. (2004). Composition of the depleted mantle. *Geochemistry Geophysics Geosystems* 5, 10.1029/2003gc000597.
- Scheirer, D. S. & Macdonald, K. C. (1995). Near-axis seamounts on the flanks of the East Pacific Rise, 8°N to 17°N. *Journal of Geophysical Research* **100**, 2239–2259.
- Schwindinger, K. R. (1999). Particle dynamics and aggregation of crystals in a magma chamber with application to Kilauea Iki olivines. *Journal of Volcanology and Geothermal Research* **88**, 209-238.
- Shen, Y., Scheirer, D. S., Forsyth, D. W. & Macdonald, K. C. (1995). Trade-off in production between adjacent seamount chains near the East Pacific Rise. *Nature* **373**, 140-143.
- Smith, D. K. (1988). Shape analysis of Pacific seamounts. *Earth and Planetary Science Letters* **90**, 457-466.
- Sobolev, A. V., Hofmann, A. W., Kuzmin, D. V., Yaxley, G. M., Arndt, N. T., Chung, S.-L., Danyushevsky, L. V., Elliott, T., Frey, F. A., Garcia, M. O., Gurenko, A. A., Kamenetsky, V. S., Kerr, A. C., Krivolutskaya, N. A., Matvienkov, V. V., Nikogosian, I. K., Rocholl, A., Sigurdsson, I. A., Sushchevskaya, N. M. & Teklay, M. (2007). The amount of recycled crust in sources of mantle-derived melts. *Science* **316**, 412-417.

- Sobolev, A. V., Hofmann, A. W. & Nikogosian, I. K. (2000). Recycled oceanic crust observed in 'ghost plagioclase' within the source of Mauna Loa lavas. *Nature* **404**, 986-990.
- Stix, J., Gauthier, G. & Ludden, J. N. (1995). A critical-look at quantitative laser-ablation ICP-MS analysis of natural and synthetic glasses. *Canadian Mineralogist* **33**, 435-444.
- Stracke, A. & Bourdon, B. (2009). The importance of melt extraction for tracing mantle heterogeneity. *Geochimica Et Cosmochimica Acta* **73**, 218-238.
- Wanless, V. D., Behn, M. D., Shaw, A. M. & Plank, T. (2014). Variations in melting dynamics and mantle compositions along the Eastern Volcanic Zone of the Gakkel Ridge: insights from olivine-hosted melt inclusions. *Contributions to Mineralogy and Petrology* **167**, doi: 10.1007/s00410-014-1005-7.
- Wanless, V. D., Perfit, M. R., Ridley, W. I. & Klein, E. (2010). Dacite petrogenesis on midocean ridges: Evidence for oceanic crustal melting and assimilation. *Journal of Petrology* **51**, 2377-2410.
- Waters, C. L., Sims, K. W. W., Perfit, M. R., Blichert-Toft, J. & Blusztajn, J. (2011). Perspective on the genesis of E-MORB from chemical and isotopic heterogeneity at 9-10°N East Pacific Rise. *Journal of Petrology* **52**, 565-602.
- Workman, R. K. & Hart, S. R. (2005). Major and trace element composition of the depleted MORB mantle (DMM). *Earth and Planetary Science Letters* **231**, 53-72.
- Yaxley, G. M. & Green, D. H. (1998). Reactions between eclogite and peridotite: Mantle refertilisation by subduction of oceanic crust. *Schweizerische Mineralogische Und Petrographische Mitteilungen* **78**, 243-255.
- Zhang, G. L., Zeng, Z. G., Yin, X. B., Wang, X. Y. & Chen, D. G. (2009). Deep fractionation of clinopyroxene in the East Pacific Rise 13°N: Evidence from high MgO MORB and melt inclusions. *Acta Geologica Sinica-English Edition* **83**, 266-277.
- Zhang, G. L., Zong, C. L., Yin, X. B. & Li, H. (2012). Geochemical constraints on a mixed pyroxenite-peridotite source for East Pacific Rise basalts. *Chemical Geology* **330**, 176-187.
- Zindler, A., Staudigel, H. & Batiza, R. (1984). Isotope and trace element geochemistry of young Pacific seamounts: implications for the scale of upper mantle heterogeneity. *Earth and Planetary Science Letters* **70**, 175-195.

Table 1: Major and trace element data for volcanic glasses from Taney Seamount-A

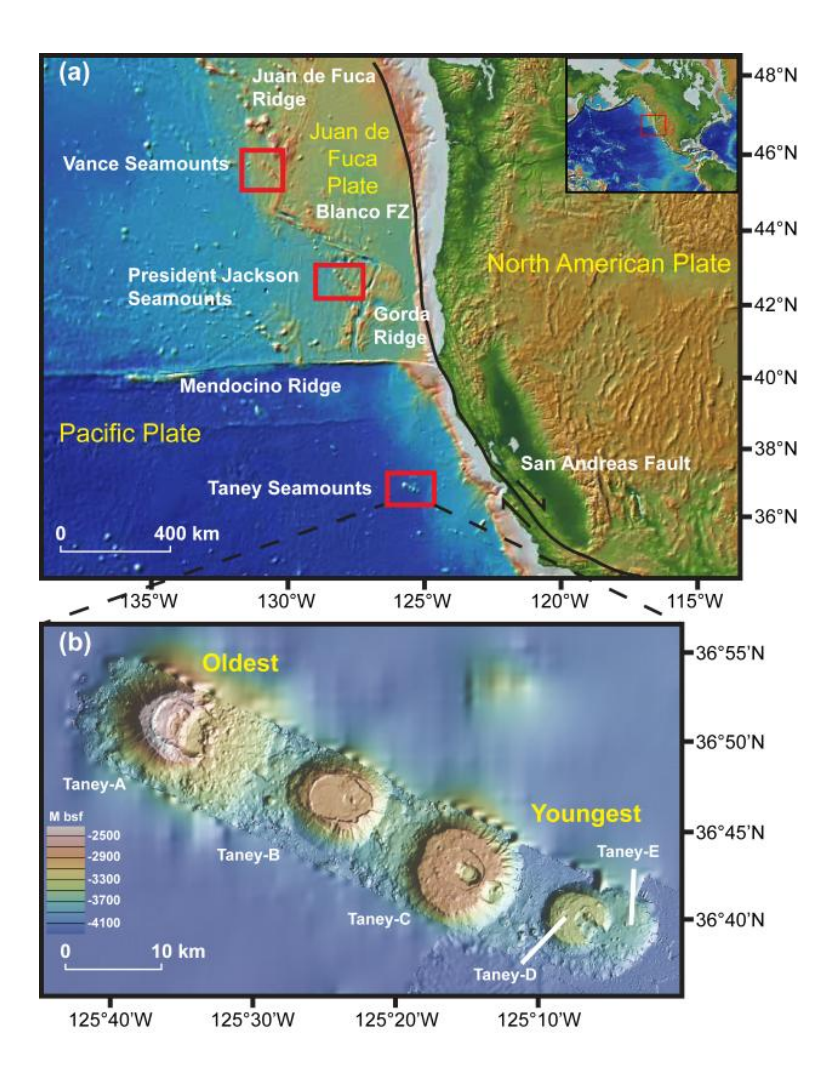
Relative Ortonology Constructions Co		D4_1	D4_2	D4_3	D4_7	D4_14	D4_20	D4_21	D4_22	D4_23	D4_24
March Dredge Dr	Relative Chronology	Constructional edifice (flank)	Constructional edifice (flank)	Constructional edifice (flank)							
	Sample Type	Dredge	Dredge								
Applied Appl	Lat (°N)		1	•	•			i	•	•	•
depth (m) 48.8 49.5 49.9 49.7 50.0 49.6 22.2 2.28 2.18 2.10 2.18 1.98 2.06 2.20 2.29 2.29 2.29 2.18 2.10 2.18 1.98 2.06 2.20 2.29 2.29 2.20 2.29 2.20 2.29 2.20 2.20	Long (°W)		•					1	•		•
49.8 49.9 49.7 6.0 2.22 2.29 2.23 2.18 49.9 49.9 49.7 6.0 2.22 2.29 1.40 14.1 14.2 13.9 14.4 14.1 14.1 14.1 14.1 14.1 14.1 14.1 14.1 14.1 14.1 14.1 14.1 14.1 14.1 14.1 14.1 14.1 14.1 14.1 14.1 14.1 14.1 14.1 14.1 14.1 14.1 14.1 14.1 14.1 14.1 14.1 14.1 14.1 14.1 14.1 14.1 14.1 14.1 14.1 14.1 14.1 14.1 14.1 14.1 14.1 14.1 14.1 14.1 14.1 14.1 14.1 14.1 14.1 14.1 14.1 14.1 14.1 14.1 14.1 14.1 14.1 14.1 14.1 14.1 14.1 14.1 14.1 14.1 14.1 14.1 14.1 14.1 <td>Water depth (m)</td> <td></td> <td></td> <td></td> <td></td> <td></td> <td></td> <td></td> <td>•</td> <td></td> <td></td>	Water depth (m)								•		
2.23 2.18 1.98 2.06 2.22 2.29 14.0 14.1 14.2 14.4 14.1 14.1 14.1 12.1 14.2 14.4 14.3 14.1 14.1 14.1 12.1 14.2 11.2 14.1 14.1 14.1 14.1 12.2 6.20 0.20 0.20 0.21 0.193 0.21 0.193 6.23 6.22 6.22 6.74 6.55 6.28 6.28 6.28 6.28 6.28 6.28 6.28 6.28 6.28 6.28 6.28 6.28 6.28 6.28 6.28 6.28 6.28 6.28 6.28 6.28 6.28 6.28 6.28 6.28 6.28 6.28 6.28 6.28 6.28 6.28 6.28 6.28 6.28 6.28 6.28 6.28 6.28 6.28 6.28 6.28 6.28 6.28 6.28 6.28 6.28 6.28 6.28 6.28	SiO ₂	49.8	49.8	49.5	49.9	49.9	49.7	20.0	49.6	20.0	49.7
14,0 14,1 14,2 14,3 14,1 14,1 14,1 12,1 11,9 12,9 11,4 14,3 14,1 14,1 12,1 11,9 0.20 0.20 0.20 0.21 0.190 6,23 6,27 6,42 6,27 6,28 6,23 6,23 10,7 11,1 10,7 11,1 10,6 10,6 3,39 3,41 3,29 3,36 3,35 3,35 0,246 0,245 0,245 0,222 0,226 0,229 0,229 0,246 0,245 0,245 0,222 0,222 0,224 0,245 0,246 0,245 0,245 0,222 0,237 0,245 0,245 0,246 0,027 0,029 0,323 0,327 0,357 0,245 0,256 0,026 0,029 0,249 0,245 0,245 0,026 0,029 0,323 0,327 0,357 0,245 0,026 0,029 0,323 0,327 0,357 0,348 1,186 0,026 0,323 0,323 0,324 0,338 1,186 0,323 0,323 0,324 0,324		2.23	2.18	2.10	2.18	1.98	2.06	2.22	2.29	2.14	2.13
12.1 11.9 11.8 12.2 11.1 11.6 12.0 0.189 0.189 0.189 0.180 0.22 0.11 0.193 6.23 6.20 6.22 6.74 6.56 6.28 6.21 0.193 6.23 6.24 6.22 6.74 6.56 6.28 6.29 6.28 6.29 6.29 6.29 6.29 6.29 6.29 6.29 6.29 6.29 6.29 6.29 6.29 6.29 6.29 6.29 6.29 6.29 6.29 6.29 6.29 6.29 6.29 6.29 6.29 6.29 6.29 6.29 6.29 6.29 6.29 6.29 6.29 6.29 6.29 6.29 6.29 6.29 6.29 6.29 6.29 6.29 6.29 6.29 6.29 6.29 6.29 6.29 6.29 6.29 6.29 6.29 6.29 6.29 6.29 6.29 6.29 6.29 6.29 6.29 6.	Al ₂ O ₃	14.0	14.1	14.2	13.9	14.4	14.3	14.1	14.1	14.3	14.2
6.23 6.195 0.200 0.201 0.211 0.193 6.23 6.195 6.22 6.74 6.55 6.28 6.23 10.7 10.7 11.1 10.7 11.5 10.6 10.6 3.39 3.41 3.29 3.34 3.35 3.33 3.35 0.300 0.301 0.289 0.302 0.289 0.290 0.299 0.352 0.028 0.029 0.245 0.245 0.245 0.247 0.025 0.352 0.028 0.029 0.322 0.237 0.357 0.025 0.026 0.028 0.027 0.022 0.039 0.026 0.024 0.024 0.025 0.026 0.028 0.027 0.022 0.039 0.026 0.025 0.026 0.026 0.025 0.026 0.027 0.025 0.026 0.026 0.026 0.026 0.026 0.026 0.026 0.026 0.026 0.026 0.026 0.026<	FeO _T	12.1	11.9	11.8	12.2	11.1	11.6	12.0	12.0	12.0	11.9
6.23 6.24 6.25 6.74 6.55 6.28 6.23 6.29 6.29 6.29 6.29 6.29 6.29 6.29 6.29 6.29 6.29 6.29 6.29 0.298 0.298 0.298 0.298 0.298 0.298 0.298 0.299 0.298 0.299 0.298 0.298 0.299 0.298 0.298 0.299 0.298 0.298 0.299 0.298 0.299 0.298 0.299 0.299 0.298 0.299 0.299 0.298 0.299 0.299 0.298 0.299 0.299 0.299 0.299 0.299 0.299 0.299 0.299 0.299 0.299 0.299 0.299 0.299 0.299 0.299 0.299 0.299 0.299 0.299 0.299 0.299 0.299 0.299 0.299 0.299 0.299 0.299 0.299 0.299 0.299 0.299 0.299 0.299 0.249 0.249 0.249 0.249 0.249 0.249	MnO	0.189	0.195	0.200	0.205	0.180	0.202	0.211	0.193	0.204	0.201
107 107 111 116 116 116 116 116 116 116 116 116 116 116 116 116 116 116 116 116 116 116 116 116 116 116 116 116 116 116 116 116 116 116 116 116 116 116 116 116 116 116 116 116 116 116 116 116 116 116 116 116 116 116 116 116 116 116 116 116 116 116 116 116 116 116 116 116 116 116 116 116 116 116 116 116 116 116 116 116 116 116 116 116 116 116 116 116 116 116 116 116 116 116 116 116 116 <td>MgO</td> <td>6.23</td> <td>6.20</td> <td>6.42</td> <td>6.22</td> <td>6.74</td> <td>6.55</td> <td>6.28</td> <td>6.23</td> <td>6.34</td> <td>6.41</td>	MgO	6.23	6.20	6.42	6.22	6.74	6.55	6.28	6.23	6.34	6.41
3.39 3.41 3.29 3.42 3.26 3.15 3.33 3.35 0.300 0.301 0.269 0.303 0.222 0.247 0.249 0.299 0.298 0.298 0.246 0.247 0.246 0.222 0.237 0.347 0.245 0.247 0.246 0.026 0.027 0.027 0.027 0.026 0.027 0.026 0.027 9.6 99.6 99.6 99.6 99.6 99.7 99.3 7.88 7.88 99.6 99.6 99.7 99.3 8.54 1.856 1.89 1.49 1.74 8.6 1.6 1.6 1.74 1.38 9.6 1.40 1.89 1.89 6.33 1.40 1.36 1.74 1.40 1.40 1.36 1.37 1.40 1.40 1.36 1.37 1.41 1.40 1.43 3.49 1.42 1.43 3.49 1.44 1.44 1.43 4.43 1.45 1.43 4.43 4.43 1.44 1.43 1.43 4.43 1.44 1.44 1.44 1.44 <tr< td=""><td>cão</td><td>10.7</td><td>10.7</td><td>11.1</td><td>10.7</td><td>11.2</td><td>11.1</td><td>10.6</td><td>10.6</td><td>10.6</td><td>11.0</td></tr<>	cão	10.7	10.7	11.1	10.7	11.2	11.1	10.6	10.6	10.6	11.0
0.300 0.301 0.269 0.305 0.299 0.298 0.346 0.245 0.217 0.245 0.247 0.245 0.247 0.245 0.326 0.326 0.327 0.327 0.357 0.357 0.357 0.026 0.028 0.027 0.022 0.357 0.027 0.027 9.0 0.028 0.027 0.029 0.026 0.027 0.027 9.0 0.028 0.027 0.027 0.026 0.027 0.027 9.0 0.028 0.029 0.026 0.029 0.027 0.027 21.59 0.028 0.027 0.027 0.027 0.027 0.027 1.0 0.0 0.0 0.0 0.0 0.0 0.0 0.0 0.0 0.0 0.0 0.0 0.0 0.0 0.0 0.0 0.0 0.0 0.0 0.0 0.0 0.0 0.0 0.0 0.0 0.0 0.0 0.0 0	Na ₂ O	3.39	3.41	3.29	3.42	3.26	3.15	3.33	3.35	3.36	3.21
0.248 0.245 0.217 0.246 0.227 0.247 0.245 0.352 0.356 0.330 0.327 0.357 0.357 0.357 0.026 0.027 0.027 0.023 0.037 0.035 0.027 0.026 0.027 0.027 0.029 0.027 0.025 0.027 0.025 2.159 0.027 0.029 0.029 0.029 0.027 0.025 2.159 0.027 0.029 0.029 0.027 0.027 0.025 1.856 0.029 0.029 0.029 0.027 0.025 0.027 0.025 1.40 0.027 0.029 0.56 0.56 0.56 0.56 0.56 0.56 0.56 0.56 0.56 0.56 0.56 0.56 0.56 0.56 0.56 0.56 0.56 0.56 0.56 0.56 0.56 0.56 0.56 0.56 0.56 0.56 0.56 0.56 0.56 0.56	, , ,	0.300	0.301	0.269	0.303	0.289	0.305	0.299	0.298	0.299	0.315
0.352 0.356 0.330 0.349 0.327 0.357 0.355 0.026 0.028 0.027 0.022 0.039 0.026 0.027 9.05 9.95 9.96 9.96 9.96 9.97 9.93 7.88 7.89 7.91 8.23 21.43 8.23 2.159 21.59 21.44 21.44 3.38 5.64 5.64 1.95 5.49 5.41 5.64 5.64 1.95 5.49 5.41 5.07 6.33 6.49 5.49 5.41 5.49 6.85 6.85 6.88 6.88 5.96 1.776 6.85 6.85 6.88 6.82 6.97 1.37 1.03 1.04 1.06 1.06 1.07 0.56 9.56 9.56 9.59 9.59 0.57 9.24 4.49 9.25 0.65 9.24 9.25 9.24 0.65 <td< td=""><td>P₂O₅</td><td>0.248</td><td>0.245</td><td>0.217</td><td>0.245</td><td>0.222</td><td>0.232</td><td>0.247</td><td>0.245</td><td>0.240</td><td>0.241</td></td<>	P ₂ O ₅	0.248	0.245	0.217	0.245	0.222	0.232	0.247	0.245	0.240	0.241
0.026 0.028 0.027 0.022 0.039 0.026 0.027 99.6 99.6 99.6 99.6 99.6 99.6 99.7 21.59 3.54 7.91 8.23 21.59 3.54 13.4 3.34 18.56 5.64 5.49 5.41 5.64 5.64 5.49 5.41 6.33 6.38 6.38 5.96 1.03 6.85 6.97 1.09 6.85 6.82 6.97 1.37 1.40 1.36 1.36 5.96 1.40 1.36 1.36 6.97 1.40 1.36 1.36 6.97 1.40 1.36 1.37 3.49 0.56 0.56 0.56 0.56 4.4 0.50 0.50 0.50 4.4 0.50 0.50 0.50 4.4 0.50 0.50 0.50 2.7 2.7 2.7	S _O	0.352	0.356	0.330	0.349	0.323	0.327	0.357	0.355	0.345	0.333
99.6 99.6 99.6 99.6 99.7 99.3 7.88 21.59 27.20 27.49 27.44 3.38 18.56 5.64 18.06 17.76 17.76 17.76 17.76 17.76 17.76 17.76 17.76 17.76 17.76 17.76 17.76 17.76 17.76 17.76 17.76 17.76 17.76 17.76 17.76 17.76 17.76 17.76 17.76 17.76 17.76 17.76 17.76 17.76 17.76 17.76 17.76 17.77 17.89 17.77 17.89 17.77 17.89 17.77 17.89 17.77 17.89 17.77 17.89 17.77 17.89 17.77 17.89 17.77 17.89 17.77 17.89 17.77 17.89 17.79 17.99 17.99 17.99 17.99 17.99 17.99 17.99 17.99 17.99 17.99 17.99 17.79 17.99 17.79 17.79 17.79 17.79	ĵo	0.026	0.028	0.027	0.027	0.022	0.039	0.026	0.027	0.027	0.039
7.88 7.91 8.23 21.59 21.20 21.49 3.54 3.44 18.05 21.49 5.64 1.89 17.76 5.49 5.64 1.95 1.74 1.77 6.33 6.85 6.87 1.09 6.85 6.85 6.87 1.09 6.85 6.85 6.87 1.09 6.85 6.85 6.87 1.09 6.85 6.82 6.87 1.37 1.40 1.06 6.87 1.37 3.89 0.56 0.56 0.58 3.73 0.57 0.58 3.49 6.53 4.4 4.95 3.49 6.52 0.52 0.58 3.49 6.53 4.4 4.49 4.49 50.72 3.98 4.43 3.79 237 2.24 2.23 4.17 3.96 0.607 6.65 0.667 0.607 6.65 0.607 3.50 6.67 0.607 3.69 7.41 3.50 3.69 7.41 3.50 3.69 7.41 3.50 3.69 7.41 3.50 <td>Total</td> <td>9.66</td> <td>9.66</td> <td>99.5</td> <td>9.66</td> <td>9.66</td> <td>9.66</td> <td>2.66</td> <td>99.3</td> <td>99.7</td> <td>9.66</td>	Total	9.66	9.66	99.5	9.66	9.66	9.66	2.66	99.3	99.7	9.66
21.50 21.50 21.50 3.54 18.56 18.56 5.64 5.64 5.64 5.63 6.38 6.38 6.38 6.38 6.38 6.38 6.38 6	-		7 00				7 04		0 00	7 66	
2.1.39 3.1.40 3.1.49 3.64 3.1.49 3.1.49 5.64 6.85 6.38 6.37 6.85 6.85 6.87 6.97 1.03 6.85 6.97 1.09 6.85 6.82 6.97 1.09 6.85 6.82 6.97 1.09 6.85 6.82 6.97 1.09 6.85 6.82 6.97 1.09 7.73 3.89 3.56 3.49 8 4.4 4.0 3.49 9.74 4.95 4.2 44 4.9 4.9 4.9 4.17 3.96 3.96 3.92 9.24 9.24 9.25 0.667 0.607 0.607 14.19 1.79 1.79 14.10 1.39 1.79 14.11 3.96 3.96 14.11 3.96 3.96 14.11 3.96 3.96 14.11 3.96 3.96 14.11 3.96 3.96 14.11 3.96 3.96 14.11 3.96 3.96 14.11 3.96 3.96 14.11 3.96 </td <td>ָר בּ</td> <td></td> <td>0.5</td> <td></td> <td></td> <td></td> <td>9.7</td> <td></td> <td>0.23</td> <td>0.73</td> <td></td>	ָר בּ		0.5				9.7		0.23	0.73	
3.54 3.44 3.38 1.55 5.49 1.776 5.64 5.49 1.89 6.33 6.38 5.41 1.03 6.85 6.87 1.40 1.36 1.09 6.85 6.82 6.97 1.40 1.36 1.09 6.86 6.82 6.97 1.40 1.36 1.37 3.73 3.56 3.49 0.56 0.50 0.50 69 0.52 0.50 69 1.43 4.4 50.72 4.9 4.4 4 4.9 4.9 237 2.37 2.34 237 2.34 3.79 24 4.17 3.96 9.02 0.662 0.607 0.651 0.607 0.607 14.10 1.30 1.50 14.10 1.30 1.50 14.10 1.30 1.50 14.10 1.30 1.50 14.10 1.30 1.50 14.10 1.30 1.50 14.10 1.30 1.50 14.10 1.30 1.50 14.10 1.30	့ ငိ		21.59				21.20		21.49	20.12	
18.56 1.856 1.776 2.02 6.38 6.38 5.41 2.02 6.38 1.89 5.96 1.03 1.06 1.09 1.89 6.85 6.38 6.38 5.96 1.03 6.82 6.97 1.09 1.40 1.36 6.97 1.37 3.89 0.56 0.56 0.58 3.73 0.56 0.56 0.50 69 44 49 42 44 49.34 44.35 3.79 2.37 2.34 2.23 2.23 4.17 3.96 3.96 3.96 9.02 0.667 0.607 0.651 0.667 0.607 14.4 3.36 3.69 34.5 3.36 3.69 34.5 3.36 3.69 34.5 3.36 3.69 34.5 3.36 3.69 34.5 3.36 3.69 34.5 3.36 3.36 34.6 3.36 <	<u></u>		3.54				3.44		3.38	3.08	
2.02 2.02 6.33 6.33 6.38 6.38 6.38 6.38 6.38 6.38	20		18.56				18.05		17.76	16.43	
6.32 6.33 6.33 6.34 6.85 6.85 6.85 6.85 6.85 6.87 1.40 7.36 7.36 6.87 1.36 7.36 6.97 6.92 6.97 6.92 6.92 6.92 6.92 6.92 6.92 6.92 6.92	E i		0.0 40.0				5.49		5.41	4.96	
6.35 6.35 6.36 6.85 6.85 6.85 6.85 6.85 6.82 6.87 6.89 6.89 6.89 6.89 6.80 6.80 6.81 6.87 6.80 6.87 6.80 6.87 6.80 6.87 6.80 6.80 6.80 6.80 6.80 6.80 6.80 6.80			2.02				CS: 0		. r	70.	
6.85 6.85 7.00 7.00 7.00 7.00 7.00 7.00 7.00 7.0	5 £		6.33 50				6.38		5.90	5.21	
0.05 0.05 3.89 0.56 0.53 3.73 0.53 0.534 0.534 0.520 0.501 0.520 0.501 0.520 0.501 0.520 0.501 0.520 0.501 0.520 0.501 0.520 0.521 0.522 0.523 0.544 0.549 44,95 44,95 44,95 44,95 44,95 44,95 44,95 44,95 44,95 44,95 44,95 44,95 44,95 44,95 44,95 44,95 44,95 44,95 44,95 44,95 44,95 44,95 44,95 44,95 44,95 44,95 44,95 44,95 44,95 44,95 44,95 44,95 44,95	<u> </u>						0.0		0.03	0.90	
1.30 3.89 3.89 3.73 3.73 3.73 3.73 3.74 0.534 0.534 0.501 0.534 4.13 3.98 2.37 2.37 4.17 0.662 0.667 0.607 34.5 36.9	25		0.63				0.82		0.97	0.00	
2.59 0.56 3.73 0.53 0.53 0.53 0.54 0.52 0.50 0.50 0.50 1.43 68 8.9 4.13 2.37 2.37 2.37 2.37 2.37 2.37 2.37 2.37 2.37 2.37 2.37 2.37 2.37 2.37 2.37 2.37 2.37 2.37 2.37 2.37 2.37 2.37 2.37 2.37 2.37 2.37 2.37 2.37 2.37 2.37 2.37 2.37 2.37 2.37 2.37 2.37 2.37 2.37 2.37 2.37 2.37 2.37 2.37 2.37 2.37 2.37 2.37 2.37 2.37 2.37 2.37 2.37 2.37 2.37 2.37 2.37 2.37 2.37 2.37 2.37 2.37 2.37 2.37 2.37 2.37 2.37 2.37 2.37 2.37 2.37 2.37 2.37 2.37 2.37 2.37 2.37 2.37 2.37 2.37 2.37 2.37 2.37 2.37 2.37 2.37 2.37 2.37 2.37 2.37 2.37 2.37 2.37 2.37 2.37 2.37 2.37 2.37 2.37 2.37 2.37 2.37 2.37 2.37 2.37 2.37 2.37 2.37 2.37 2.37 2.37 2.37 2.37 2.37 2.37 2.37 2.37 2.37 2.37 2.37 2.37 2.37 2.37 2.37 2.37 2.37 2.37 2.37 2.37 2.37 2.37 2.37 2.37 2.47 2.47 2.47 2.47 2.47 2.47 2.47 2.47 2.47 2.47 2.47 2.47 2.47 2.47 2.47 2.47 2.47 2.47 2.47 2.47 2.47 2.47 2.47 2.47 2.47 2.47 2.47 2.47 2.47 2.47 2.47 2.47 2.47 2.47 2.47 2.47 2.47 2.47 2.47 2.47 2.47 2.47 2.47 2.47 2.47 2.47 2.47 2.47 2.47 2.47 2.47 2.47 2.47 2.47 2.47 2.47 2.47 2.47 2.47 2.47 2.47 2.47 2.47 2.47 2.47 2.47 2.47 2.47 2.47 2.47 2.47 2.47 2.47 2.47 2.47 2.47 2.47 2.47 2.47 2.47 2.47 2.47 2.47 2.47 2.47 2.47 2.47 2.47 2.47 2.47 2.47 2.47 2.47 2.47 2.47 2.47 2.47 2.47 2.47 2.47 2.47 2.47 2.47 2.47 2.47 2.47 2.47 2.47 2.47 2.47 2.47 2.47 2.47 2.47 2.47 2.47 2.47 2.47 2.47 2.47 2.47 2.47 2.47 2.47 2.47 2.47 2.47 2.47 2.47 2.47 2.47 2.47 2.47 2.47 2.47 2.47 2.47 2.47 2.47 2.47 2.47 2.47 2.47 2.47 2.47 2.47 2.47 2.47 2.47 2.47 2.47 2.47 2.47 2.47 2.47 2.47 2.47 2.47 2.47 2.47 2.47 2.47 2.47 2.47 2.47 2.47 2.47 2.47 2.47 2.47 2.47 2.47 2.47 2.47 2.47 2.47 2.47 2.47 2.47 2.47 2.47 2.47 2.47 2.47 2.47 2.47 2.47 2.47 2.47 2.47 2.47 2.47 2.47 2.47 2.4	2 .		- c				5.5			2 42	
0.534 0.520 0.534 0.534 0.520 0.501 69 44 49 67.72 49.34 42 44.95 43.34 44.95 237 234 223 4.17 3.96 9.25 9.02 0.662 0.611 0.651 0.657 0.607 141 9 36.9 141 9 36.9	□ [}]		0.0				20.4		9.0	0.4.0 0.4.0	
5.75 5.30 6.34 6.9 4.4 4.1 5.0.72 5.0.72 6.8 4.1 4.9 4.1 6.8 4.1 4.1 6.8 4.1 4.1 6.8 4.1 6.8 4.1 6.8 6.8 6.8 6.1 6.0 6.0 6.0 6.0 6.0 6.0 6.0 6.0	\ - -		0.30				0.30		0.00	0.40	
69 44 49 49 49 49 49 49 50.72 9.02 9.02 9.02 9.02 9.02 9.02 9.02 9.0	2 =		0.73				0.30		0.43	50.0	
44 49 50.72 49.34 3.98 41.3 237 234 4.13 3.79 237 223 4.13 3.79 223 223 4.13 3.79 223 223 4.13 3.79 223 3.92 9.24 3.92 9.25 9.25 0.667 0.611 0.657 0.607 141 9 139 8 142 9 152 8	3 2		t 06				143		- 89	02	
50.72 49.34 44.95 3.98 2.37 2.34 3.79 2.37 2.34 2.23 4.17 3.96 3.92 9.02 9.24 9.25 9.02 9.25 0.662 0.668 0.611 0.651 3.69	ō Z		8 8				<u>}</u> 6		3 6	2 7	
3.98 3.98 2.37 4.13 2.37 2.37 4.13 3.79 2.38 2.39 2.39 2.39 2.39 2.39 2.39 2.39 2.39	- M		50 72				40.34		44 05	43.26	
237 234 223 237 234 223 4.17 3.96 9.25 9.02 0.662 0.668 0.661 0.651 0.637 0.607 34.5 36.9	2 4		3 08				5.5		02.5	25.5	
4.17 3.96 3.92 9.02 9.24 9.25 0.662 0.668 0.611 0.651 0.637 0.607 34.5 36.9	2 0		237				234		223	202	
9.25 9.02 9.25 0.662 0.668 0.617 0.637 0.607 34.5 34.5 34.5 14.1 9	iΞ		4 17				3 06		3 00	2	
0.662 0.611 0.651 0.637 0.607 34.5 35.0 36.9	: 2		60.6				9.26		9.25	8 60	
34.5 35.0 36.9 36.9 36.9 36.9 36.9 36.9 36.9 36.9	<u>.</u> ⊏		0.662				0.668		0.611		
36.9 152 8	<u> </u>		0.651				0.637		0.607		
152.8	>		34.5				35.0		36.9	34.3	
0.50	Żr		141.9				139.8		152.8	143.7	

Sample	D4_25	D4_26	D174-R5	D174_R6	D174_R8	D174_R10	D174_R12	D174_R13	D175_R4	D175_R10
Relative Chronology	Constructional edifice (flank)	Constructional edifice (flank)	Post-caldera C3 infill	Post-caldera C3 infill	Pillow cone (wall)	Pillow cone (wall)	Pillow cone (wall)	Pilow cone (wall)	Post-caldera C2 infill	Post-caldera C1 infill
Sample Type	Dredge	Dredge (volcaniclastic)	Pillow fragment	Pillow fragment	Pillow fragment	Pillow fragment	Pillow fragment	Pillow fragment	Talus	Pillow fragment
Lat (°N)	,	•	36.847	36.848	36.849	36.850	36.850	36.850	36.844	36.843
Long (°W)		•	-125.581	-125.581	-125.584	-125.586	-125.588	-125.589	-125.597	-125.598
Water depth (m)			2884	2882	2828	2844	2823	2814	2755	2657
SiO ₂	49.5	49.5	50.2	50.2	49.0	48.9	49.1	49.1	49.6	20.0
TIO ₂	2.13	2.26	1.62	1.65	1.27	1.30	1.37	1.34	1.811	2.08
Al_2O_3	14.3	14.1	15.1	15.1	16.1	16.1	16.0	16.0	15.2	14.6
FeO₁	11.8	12.1	10.0	10.2	6.6	10.1	9.93	10.2	10.4	11.4
MnO	0.206	0.199	0.171	0.149	0.147	0.176	0.173	0.157	0.188	0.189
MgO	6.52	6.26	7.27	7.24	8.32	8.06	8.13	8.04	7.31	6.56
S 2	10.9	10.5	11.9	11.9	11.9	12.1	11.94	12.0	11.8	11.3
Na ₂ O	3.21	3.36	2.39	2.98	2.73	2.77	2.73	7.8.1	Z.33	3.12
O. C ≥ a	0.307	0.230	0.232	0.233	0.140	0.132	0.147	0.130	0.219	0.234
	0.233	0.254	0.100	0.268	0.130	0.55	0.130	0.00	0.00	0.235
် ဝ	0.040	0.027	0.009	0.008	0.006	0.005	0.006	0.005	0.019	0.033
Total	99.5	99.2	6.66	100.0	99.9	99.9	6.66	100.2	100.1	100.1
<u></u>	7 98	8 42	7. 87.	8.05	4 04	4 24	4 11	4.20	5.72	7 94
3 8	20.69	22.50	15.54	15.21	11.55	11.49	11.88	11.40	15.55	20.78
à	3.23	3.46	2.51	2.48	1.83	1.87	1.86	1.89	2.44	3.17
P	16.85	17.69	12.85	12.91	9.50	9.66	9.63	29.6	13.01	16.64
Sm	5.14	5.63	4.15	4.21	3.06	3.32	3.19	3.15	4.19	4.89
⊒	1.76	1.86	1.50	1.51	1.19	1.19	1.22	1.25	1.50	1.75
ලි 1	5.61	5.79	4.82	4.87	3.91	3.95	3.74	3.83	4.50	5.33
₽ 6	1.07	1.10	0.81	0.79	0.66	0.69	0.70	0.68	0.79	0.94
23	0.00 0.00	0.90	5.3/	5.48	4.0	7.4	50.4	74.4	5.32	67.0
2 ů	67. ¢	14.1	 80 80	3 - CO	0.94	0.34	0.93 62	0.92 0.02	20	3.41
ع د	0.54	0.56	0.40	0.6	0.38	0.39	0.39	0.42	0.38	0.46
Yb	3.32	3.55	2.69	2.83	2.36	2.48	2.42	2.50	2.62	3.14
3	0.474	0.500	0.392	0.414	0.354	0.367	0.356	0.370	0.381	0.460
Ö	140	74	293	288	290	316	297	282	314	177
Z	46	48	29	22	100	87	92	82	65	52
Ba	43.82	45.08	39.18	38.17	21.49	21.44	21.77	21.88	33.19	45.45
£ (3.66	3.83	2.89	2.89	1.63	1.55	1.7	1.63	2.69	3.61
<u>ਂ</u>	215	522	217	217	194	196	194	188	216	277
Ī Ž	3.65	3.92	2.82	2.99	2.20	2.22	2.20	2.29	2.79	3.47
9 €	9.09	9.47	0.40	0.39	2.0	0.39	0.30	4.17	0.45	0.00
<u>a</u>	0.010	0.033	0.433	0.432	0.234	0.239	0.233	0.252	0.400	0.330
>	35.4	38.3	27.6	28.8	24.0	25.3	24.3	26.4	28.1	33.6
Zr	145.7	160.3	104.8	108.8	84.3	90.6	86.8	90.5	108.7	142.9
i										

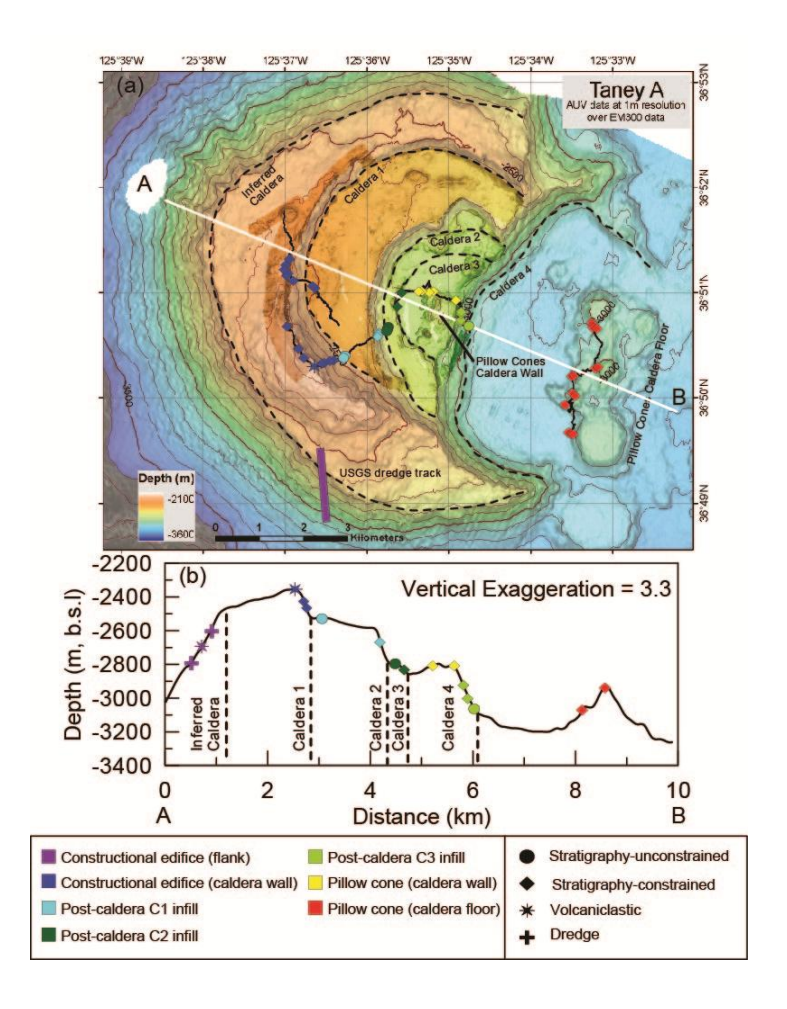
Table 1. Cont'd										
Sample	D175_R36B	D175_R42	D176_R3	D176_R4	D176_R5	D176_R14	D176_R16	D176_R17	D176_R18	D176_R20
Relative Chronology	Constructional edifice (caldera wall)	Constructional edifice (caldera wall)	Pillow cone (floor)							
Sample Type	Volcaniclastic	Pillow fragment	Pillow fragment	Pillow fragment	Pillow fragment	Pillow fragment	Pillow fragment	Pillow fragment	Pillow fragment	Pillow fragment
Lat (°N)	36.838	36.841	36.828	36.829	36.829	36.832	36.834	36.837	36.837	36.838
Long (°W)	-125.611	-125.614	-125.558	-125.558	-125.558	-125.559	-125.558	-125.558	-125.558	-125.554
Water depth (m)	2164	2173	3154	3155	3155	3105	3039	3148	3146	3020
SiO ₂	50.5	49.6	48.9	48.9	49.5	49.0	49.0	48.6	48.6	48.8
0 2 2	2.08	1.90	1.49	1.57	1.64	1.52	1.48	1.43	1.48	1.54
A ² O ³	14.9	14.8	16.0	15.8	16.0	16.1	16.3	16.3	16.2	16.1
₽ <u>₹</u>	4.1.4	5.1.3	70.2	10.1	10.3	10.1	4.0.4	, ic	10.1	10.3
	0.190	0.195	0.192	0.168	0.181	0.164	0.156 9.06	0.178	0.172	0.165
	6.78	0.73	7.83	7.87	08.7	8.U3	8.00	8.0.4 4.0.4	8.02	7.87
Se Cal	7.1.1	2.1.2	2.07	2.1.0	8.1.2	8.1.0	12.1	9.1.6	97.0	9.7.6
Z Z Z	0.252	0.275	0.210	0.216	0.20	0.202	0.189	0.193	0.192	0.197
O d	0.237	0.222	0.156	0.163	0.191	0.155	0.149	0.15	0.149	0.154
ို့တို	0.133	0.220	0.247	0.270	0.107	0.272	0.253	0.240	0.251	0.262
ō	0.031	0.021	0.017	0.019	0.027	0.017	0.018	0.019	0.016	0.019
Total	101.0	93.6	6.66	99.7	100.7	100.2	100.9	2.66	99.8	100.1
Га	7.05	7.48	5.31					4.96	4.97	5.30
පී	18.44	18.72	14.56					13.65	13.47	13.81
<u>å</u> :	2.95	3.29	2.23					2.15	2.15	2.24
2 8	14.95	17.34	11.91					11.38	11.65	12.04
Ēū	4.83 7.3	5.23 1.88	3.78 1.32					3.60	3.00 3.00	3.72 1 38
3 6	68.5	00.9	25 44.4					2.50 4.44	4 23	5.7
3₽	0.97	. t.	0.85					0.83	0.75	0.77
Ճ	6.38	6.94	5.17					2.00	5.15	5.29
오	1.25	1.39	1.09					1.08	1.04	1.10
ů ř	3.81	3.84	3.01					3.04	3.03	3.23
= \$	0.55 3.36	3.67	0.43 2.88					0.42 2.80	0.40 2.78	4 %
2	0.504	0.533	0.416					0.399	0.411	0.410
ŏ	156	147	229					261	274	290
Z	29	54	82					96	06	81
Ba	42.03	46.52	44.41					37.25	33.58	33.01
£ ;	3.45	3.29	2.72					2.38	2.23	2.21
<u>.</u> ק	213	877 0	130					4 5	4 5	200
E Z	3.76 8.28	3.95 3.45	2.73 5.55					2.57 5.07	7.58 7.08	2.63 7.38
<u> </u>	0.553	0.593	0.380					0.346	0.347	0.346
ĭ ←	0.526	0.587	0.409					0.363	0.362	0.368
> 1	34.3	34.9	29.5					28.7	27.6	28.7
72	1.35.7	138.6	101.6					96.7	95.3	100.3

Table 1. Collica								1111	4 1 1 1 1		
Sample	D176_R21	D176_R22	D176_R24	D176_R25	D177_R10	D177_R11	D177_R16	D177_R17	D177_R19	D177_R20	
	Dillow cope (floor)	Pillow cope (floor)	Dillow cope (floor)	Pillow cope (floor)	Constructional	Constructional	Constructional	Constructional	Constructional	Constructional	
Relative Chronology		:			wall)	wall)	wall)	wall)	wall)	wall)	
Sample Type	Pillow fragment	Pillow fragment	Pillow fragment	Pillow fragment	Pillow fragment	Pillow fragment	Pillow fragment	Pillow fragment	Pillow fragment	Pillow fragment	
Lat (°N)	36.838	36.844	36.844	36.845	36.850	36.851	36.854	36.854	36.855	36.855	
Long (°W)	-125.553	-125.553	-125.553	-125.553	-125.610	-125.611	-125.616	-125.616	-125.616	-125.616	
Water depth (m)	3020	3043	3040	3030	2495	2487	2315	2316	2321	2342	
SiO	48.8	48.3	47.6	48.3	49.9	50.0	49.9	49.9	49.8	49.9	
, '0I	1.57	1.19	1.17	1.20	2.04	2.12	2.00	5.06	2.00	2.09	
AŀŌ	15.7	16.8	16.8	16.7	14.5	14.7	14.8	14.7	14.8	14.4	
Fe ^o ,	10.4	10.9	10.6	10.6	11.9	11.5	11.5	11.5	11.5	11.5	
MnO	0.175	0.192	0.187	0.186	0.209	0.204	0.196	0.201	0.192	0.203	
MgO	7.71	8.71	8.61	99.8	6.61	29.9	6.65	69.9	6.61	6.35	
CaO	12.0	12.0	11.8	11.7	11.1	11.1	11.1	11.1	11.1	11.0	
Na_2O	2.82	2.46	2.51	2.48	3.23	3.13	3.16	3.15	3.18	3.28	
κ ₂ 0	0.207	0.111	0.117	0.109	0.274	0.285	0.276	0.273	0.275	0.286	
P ₂ O ₅	0.161	0.092	0.094	0.090	0.226	0.228	0.232	0.222	0.223	0.235	
လိ	0.275	0.258	0.254	0.257	0.307	0.287	0.275	0.281	0.292	0.304	
O F	0.020	0.005	0.004	0.005	0.024	0.023	0.023	0.023	0.025	0.026	
lotal	99.8	1.101	7.66	100.3	100.3	100.3	100.1	100.1	99.9	93.6	
La	5.30	2.85	2.92	2.70	7.17	7.57	7.51	7.70	7.51	69.2	
පී	14.21	8.16	7.70	8.18	18.54	19.72	19.74	20.17	19.78	19.40	
à	2.39	1.38	1.37	1.34	2.91	3.16	3.14	3.16	3.12	2.99	
P	12.84	7.64	8.00	7.34	15.58	16.81	16.42	16.98	16.47	15.76	
Sm	4.12	2.75	2.98	2.57	4.60	5.11	5.22	5.01	2.07	4.79	
Ш	1.54	1.04	1.11	1.02	1.72	1.78	1.81	1.81	1.75	1.76	
P9	5.02	3.62	3.83	3.44	5.82	5.98	5.79	5.74	5.85	5.72	
മ	0.83	0.65	0.72	0.61	0.98	1.05	1.02	0.95	0.98	96.0	
Š	5.59	4.28	4.89	4.00	6.04	6.46	6.33	6.23	6.53	6.18	
운	1.12	0.89	1.02	0.80	1.22	1.30	1.28	1.28	1.31	1.21	
ம்	3.20	2.68	2.99	2.51	3.69	3.78	3.62	3.63	3.80	3.74	
щ	0.43	0.37	0.39	0.34	0.49	0.50	0.47	0.51	0.54	0.50	
Υb	3.01	2.54	2.82	2.27	3.18	3.24	3.16	3.19	3.36	3.24	
T.	0.438	0.368	0.419	0.329	0.459	0.468	0.453	0.458	0.478	0.475	
ర్	273	241	241	241	122	128	136	137	136	103	
Z	75	131	132	131	51	23	22	22	23	44	
Ba	33.65	15.76	14.64	15.49	42.34	43.89	44.35	43.71	42.95	43.63	
82	2.34	1.14	1.07	1.16	3.57	3.43	3.57	3.49	3.48	3.66	
Š	192	155	155	149	211	223	225	233	228	215	
눛	2.79	1.78	1.98	1.57	3.52	3.57	3.48	3.50	3.68	3.68	
Q	5.41	2.54	2.58	2.41	8.57	8.42	8.57	8.31	8.40	8.92	
дa	0.371	0.170	0.188	0.153	0.532	0.543	0.526	0.538	0.550	0.543	
ᆮ	0.389	0.170	0.188	0.152	0.522	0.538	0.529	0.531	0.549	0.521	
- - '	28.4	24.2	27.0	22.6	34.4	35.5	34.8	34.6	36.0	35.8	
7.7	101.1	04.0	70.0	60.9	138.4	143.2	140.4	143.6	147.2	145.8	

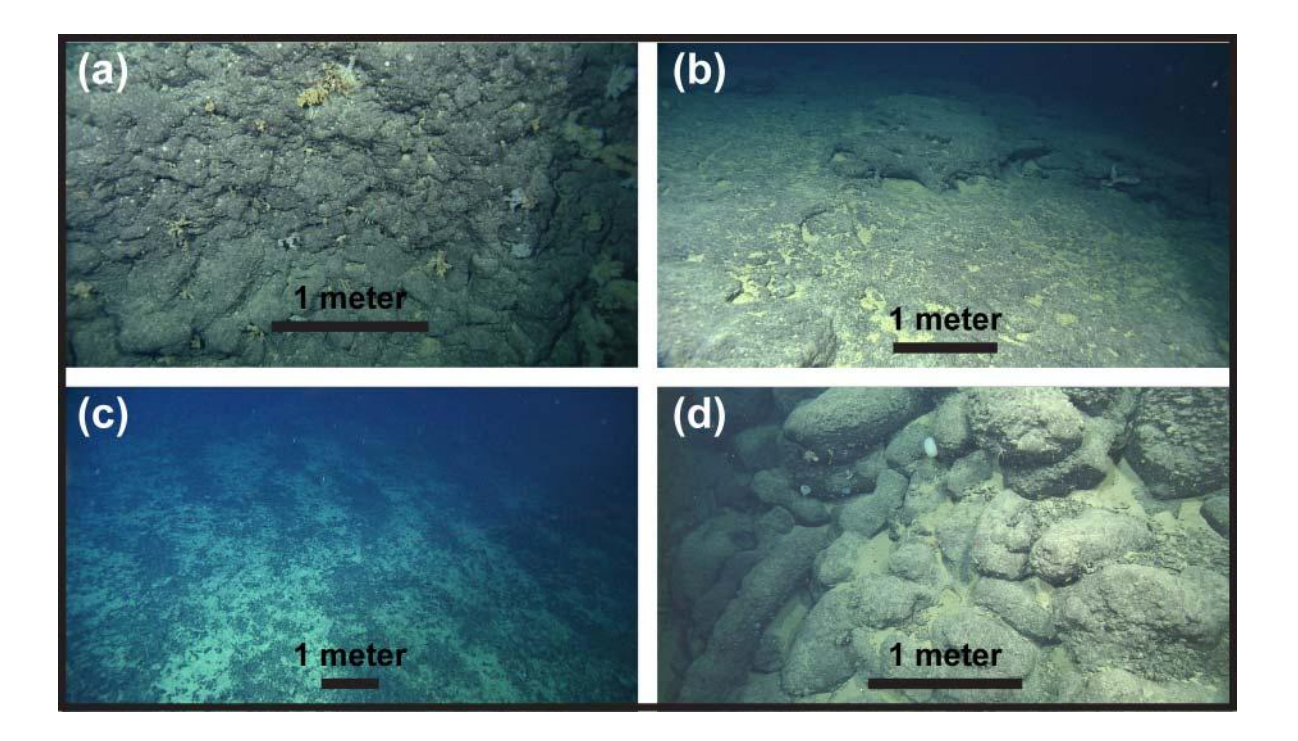
(a) Location of the Taney, Vance and President Jackson seamount chains in relation to other important geologic features. The Taney Seamount chain is located near 36° 45' N and 125° 25' W on the Pacific plate, 300 km west of San Francisco, and formed adjacent to the now subducted Farallon Spreading Center. (b) DEM image of the Taney Seamounts. The volcanoes are labeled from oldest to youngest (Taney A-E) after Clague et al. (2000). Like other near-ridge seamounts, the volcanic edifices are defined by steep sides and truncated tops. Taney Seamount-A is the largest of the five seamounts and exhibits the most complex morphological features including multiple caldera collapses.



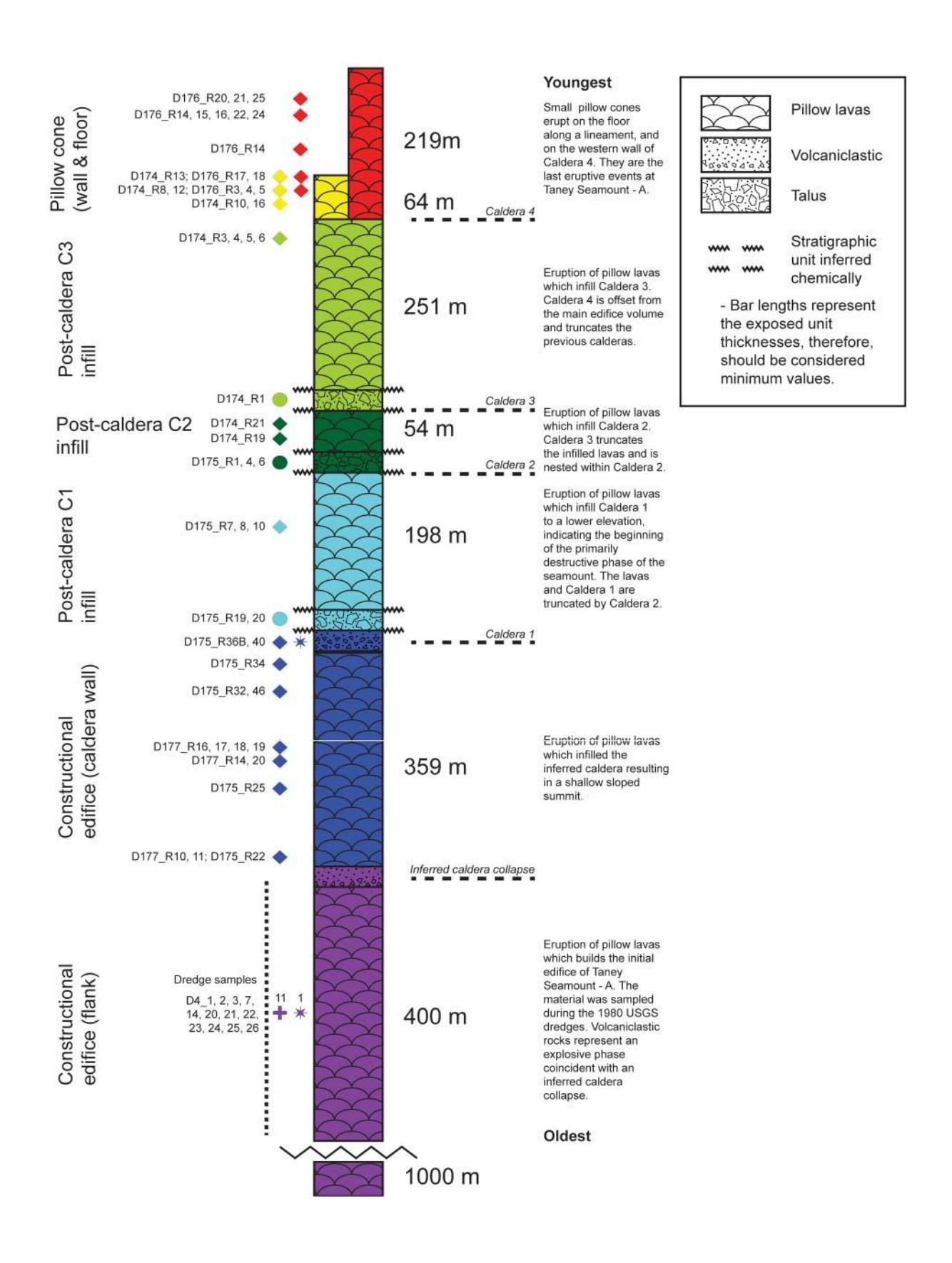
(a) DEM image of the largest and oldest Taney Seamount (A) using 1-meter resolution data collected using an autonomous underwater vehicle superimposed over EM300 data. Remotely operated vehicle (ROV) dive tracks from the 2010 cruise and a USGS dredge track are also shown. Caldera margins are inferred based on the morphology. (b) Cross section of Taney Seamount-A indicating sampling locations and their relationships to the caldera structures. Caldera collapse structures are used to distinguish the eruptive events in a relative chronological order, with samples differentiated by colours defined in the legend.



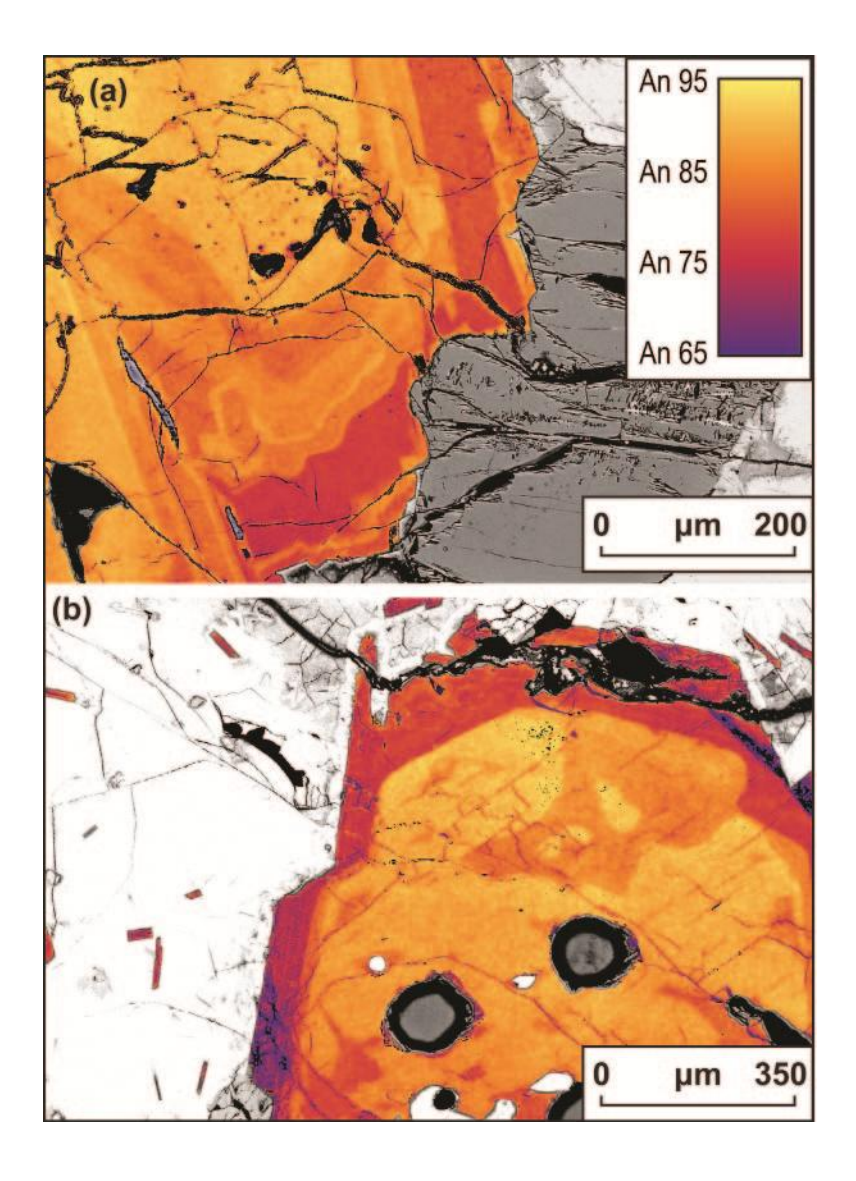
(a) Image of truncated pillows near the summit of Caldera C1. The pillows are coated in a manganese crust that obscures some of the details. (b) Photograph of volcaniclastic deposits at the summit of Caldera C1 exhibiting a "potholed" appearance. (c) Image of manganese nodules concentrated on the crests of parallel sediment ripples. Thick (> 1 m) sediment with manganese nodules and slabs are common on the caldera floors. (d) Photo of elongated pillow lavas on the steep slope of a pillow cone on the floor of caldera C4.



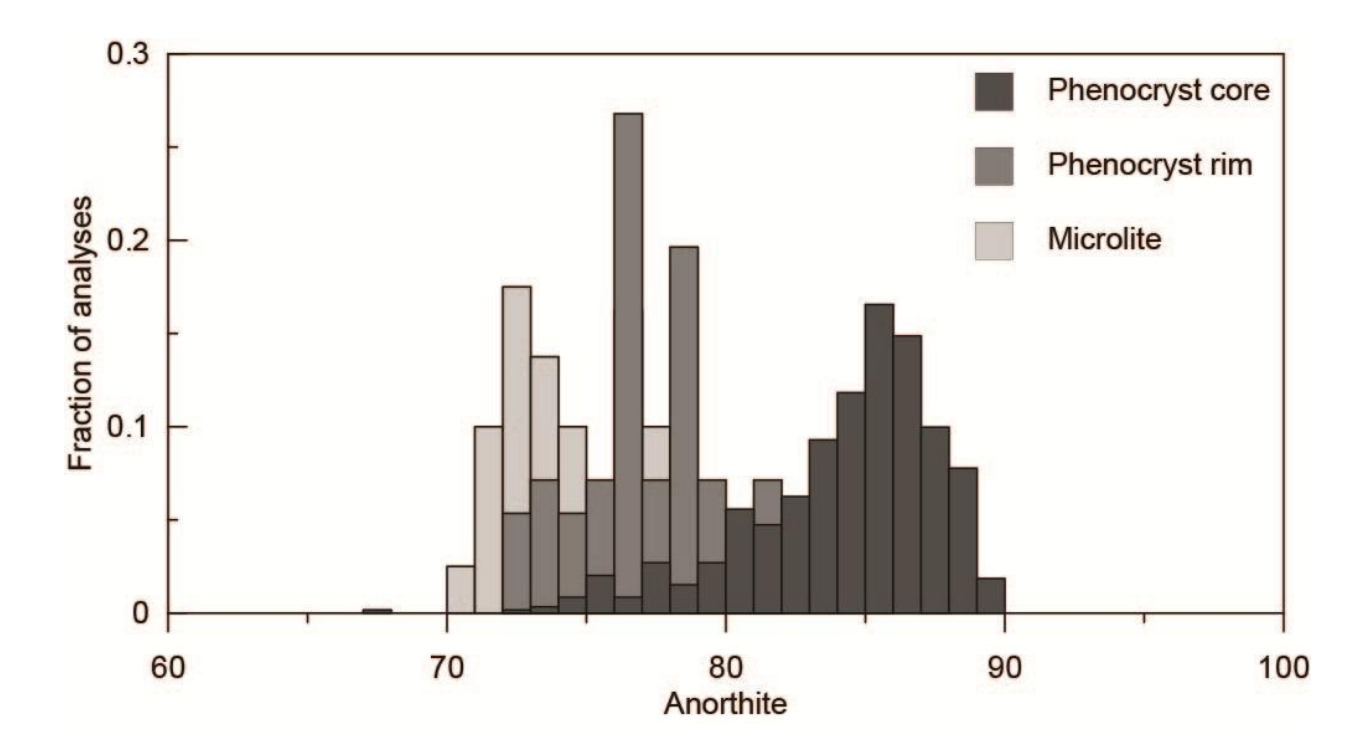
Stratigraphic column schematically illustrating the relative chronology of samples at Taney Seamount-A. Each unit is bounded by caldera collapses representing the draining of the shallow magmatic reservoir followed by replenishment. The scaled thickness of each unit in the diagram represents the exposed thicknesses at the surface. The symbols show the relative sampling locations of each unit with morphology and colours as in Fig. 2b.



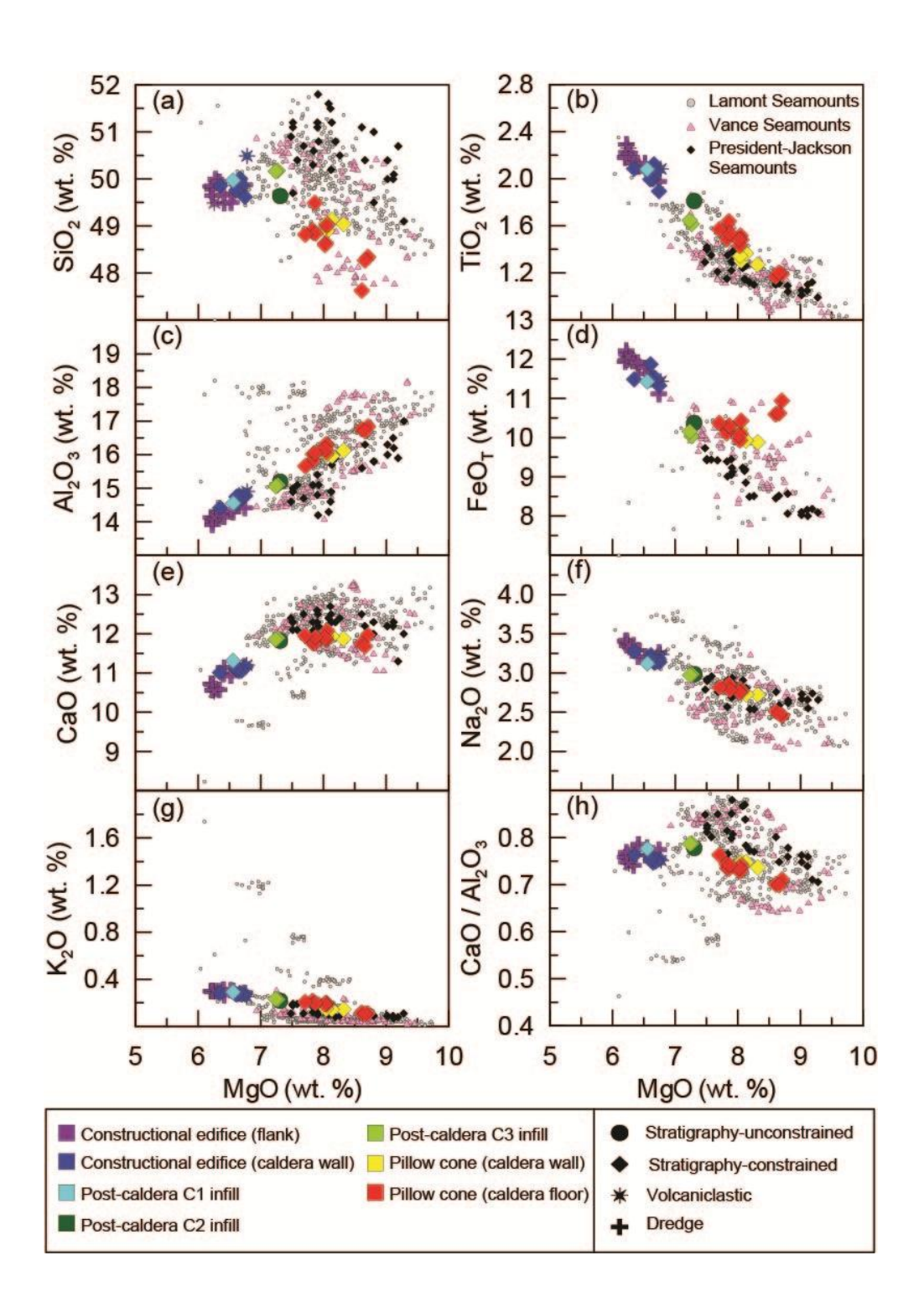
False colour calibrated backscattered electron images of large plagioclase crystals in glassy pillow margins. The crystals exhibit subrounded anorthite-rich cores and mantles with complex zoning. In crystal (a) the mantle has an embayed and patchy texture that is evidence of dissolution. Crystal (b) has a euhedral rim that is more sodic (\sim An₇₅) than the calcium rich core (An₈₅₋₉₀). The crystal to the right of the plagioclase in (a) is an olivine, characteristically glomerocrystic with plagioclase crystal rims and microlites.



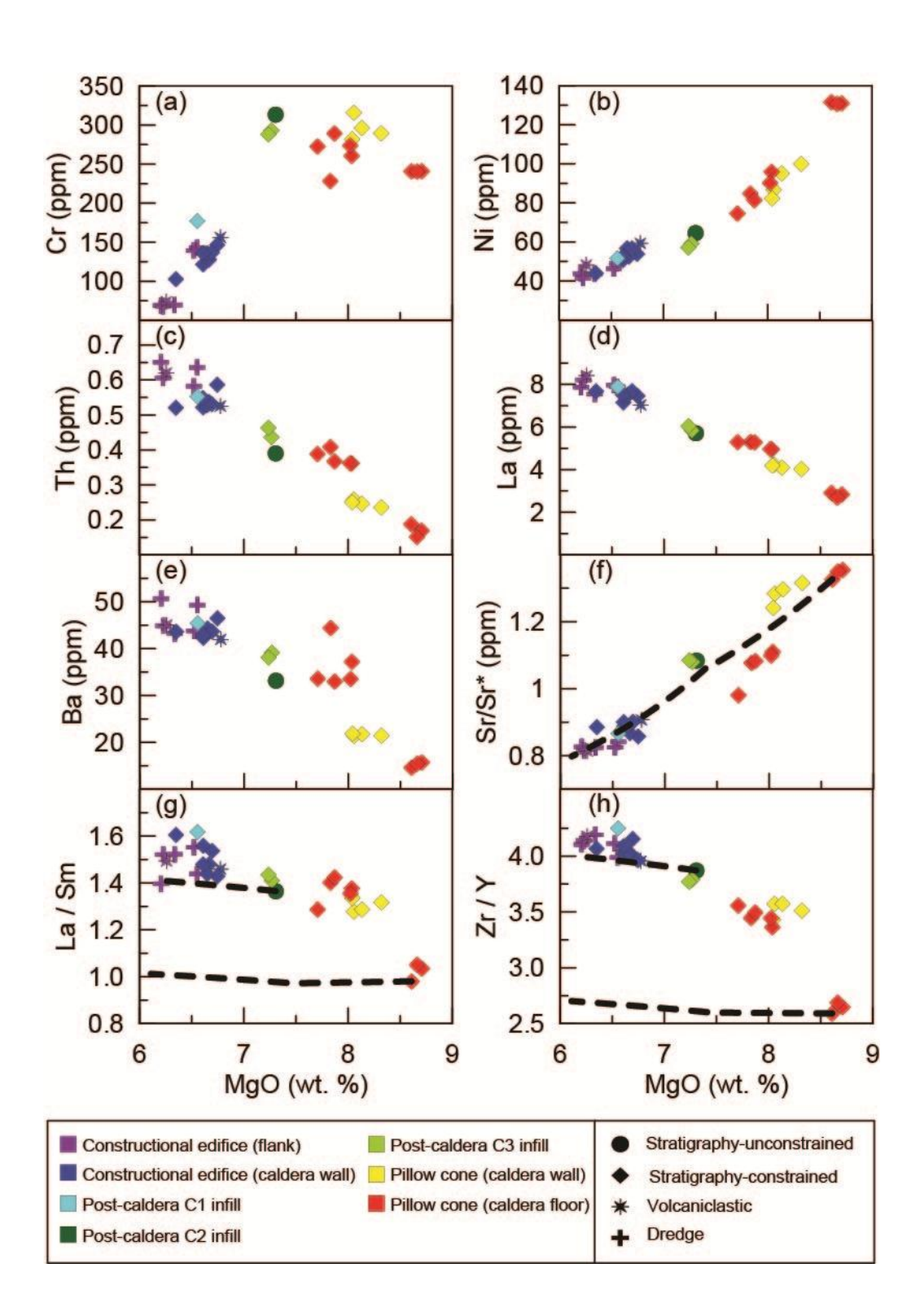
Histogram of 592 core, 56 rim, and 80 microlite plagioclase compositions from Taney Seamount-A young cone samples. The cores have the highest anorthite contents with most analyses at approximately An_{86} with a range from $An_{72} - An_{89}$. The rims of the plagioclase phenocrysts are more sodic, representing crystallization after the introduction of the phenocryst into more differentiated melt. The microlites are the most sodic of all, representing the final stage of crystallization.



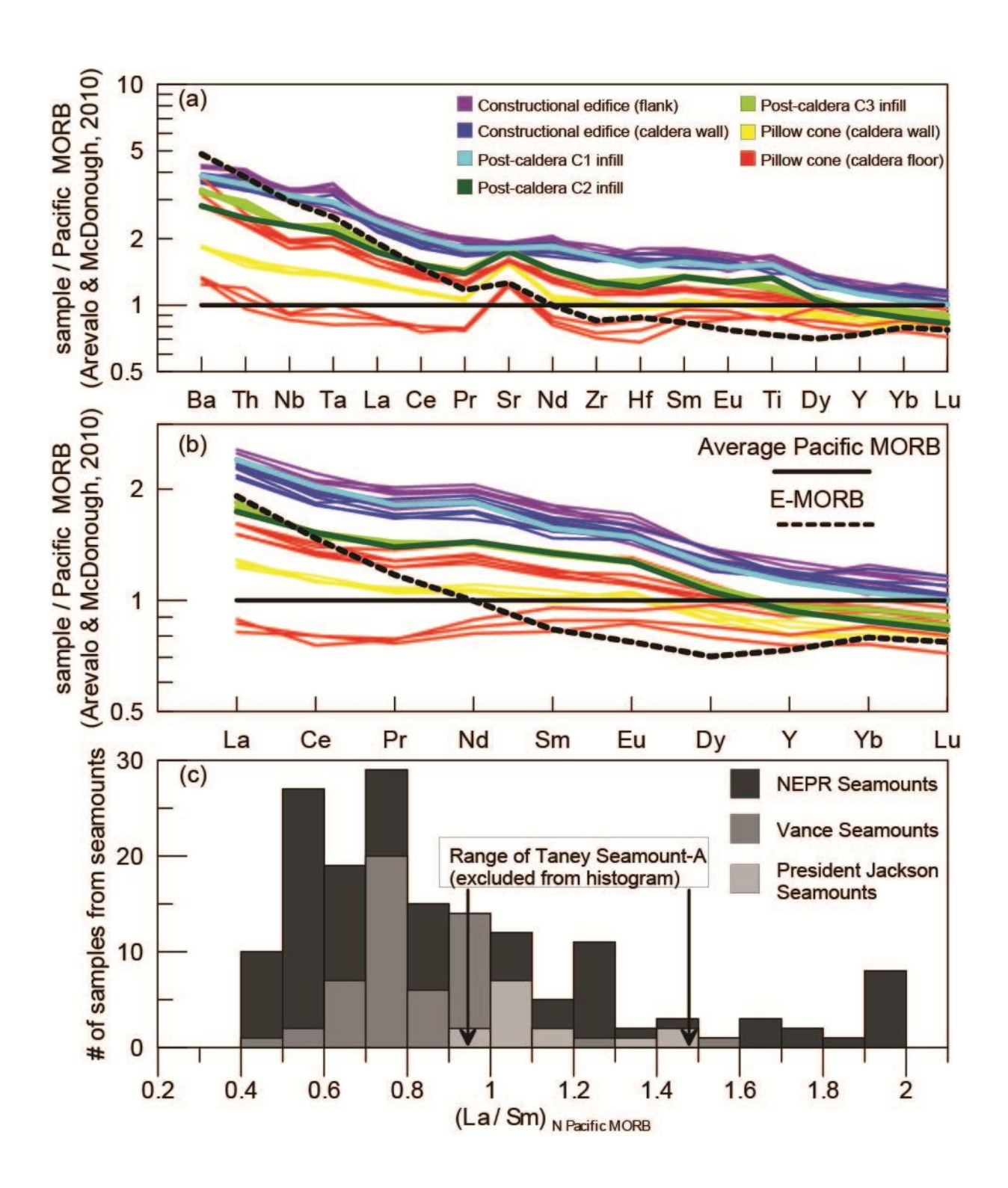
Major element compositional variations of Taney Seamount-A (corrected for VG-2) basalts in comparison to other Pacific near-ridge seamounts. Vance seamount data from Hann (2012), President Jackson seamount data from Davis & Clague (2000), northern EPR seamount data from petDB (http://earthchem.org/petdb). Taney Seamount-A lavas fall on a higher Al_2O_3 – lower SiO_2 liquid line of descent compared to other northeast Pacific near-ridge seamounts. An inflection in CaO at MgO ~7.5 wt. % indicates the onset of clinopyroxene as a crystallizing phase.



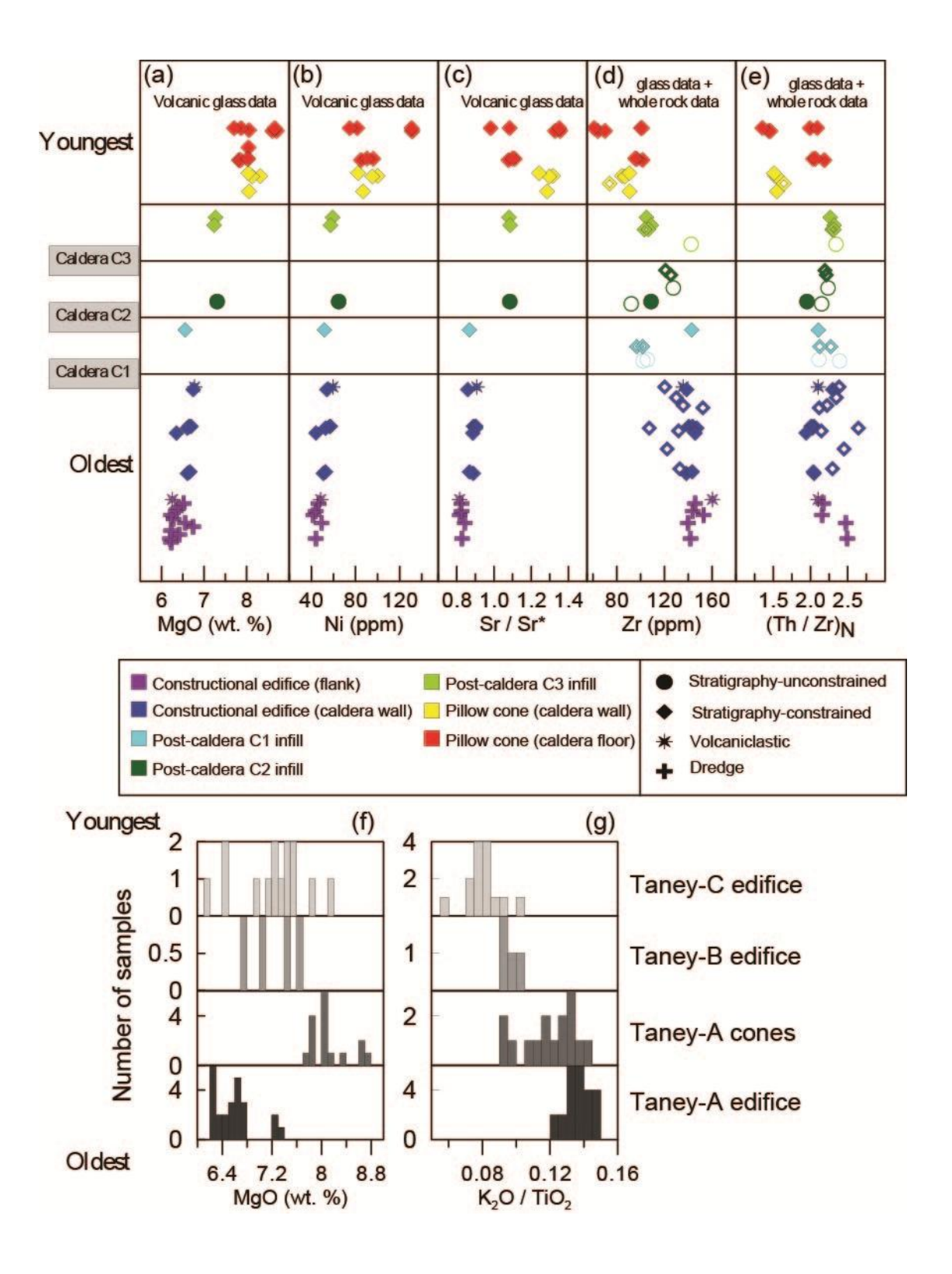
Laser ICP-MS trace element plots of the Taney Seamount-A volcanic glasses. Incompatible trace elements (Th, La, Ba, Zr) increase while compatible trace elements (Cr, Ni) decrease with decreasing MgO. The dashed line represents the crystallization model (supplementary information S6). Crystallization of olivine, plagioclase and clinopyroxene does not significantly affect ratios of incompatible elements with the exception of Sr and Eu which are more compatible in plagioclase. The pronounced changes in trace element ratios (La/Sm, Zr/Y) suggest that mantle processes play an important role in trace element systematics at Taney - A.



(a, b) Trace element and rare earth element plots normalized to average Pacific MORB (Arevalo & McDonough, 2010) of Taney Seamount-A basalts; colours are the same as in Fig. 2b. The samples are characterized by negative slopes from the moderate to moderately incompatible trace elements (Sm-Lu), and positive slopes from the moderate to highly incompatible trace elements (Hf-Rb). Taney-A primitive basalts have a pronounced positive strontium anomaly that becomes a slight negative anomaly with increasing trace element abundances. This change can be attributed to an initial excess plagioclase signature followed by fractional crystallization of plagioclase. (c) In comparison to other northeastern East Pacific Rise near-ridge seamounts (http://earthchem.org/petdb) including the Lamont Seamounts, Taney Seamount-A basalts are generally more enriched in highly incompatible elements.



Chemostratigraphy as defined by the relative chronology from Figure 4. Symbols and colours are as defined in Fig. 2b. Closed symbols represent glass analyses while open symbols represent whole-rock analyses. (a) Glass analyses of MgO, a compatible major element during the crystallization of an olivine and plagioclase (± clinopyroxene) mineral assemblage. (b) Glass analyses of Ni, a trace element which is highly compatible in olivine and moderately compatible in clinopyroxene. (c) Glass analyses of Sr/Sr*, where $Sr^* = \sqrt{Pr_{_{\! N}}Nd_{_{\! N}}}$ represents the magnitude of the strontium anomaly which decreases during crystallization of a plagioclase-rich assemblage. Sr and Sr* are normalized to primitive upper mantle (McDonough & Sun, 1995) in order to avoid the effects of plagioclase crystallization inherent in a MORB normalization. (d) Whole rock and glass analyses of Zr, an incompatible element during the crystallization of an olivine and plagioclase (\pm clinopyroxene) assemblage. (e) (Th/Zr)_N is a ratio of a highly incompatible to moderately incompatible trace element normalized to average Pacific MORB (Arevalo & McDonough, 2010). These plots show that the constructional edifice was formed from the most differentiated lavas with 120 to 160 ppm Zr and (Th/Zr)_N of 2.0 to 2.5, while the young pillow cones were formed from the most primitive lavas with 60 to 100 ppm Zr and (Th/Zr)_N ~1.4. The progression from differentiated to primitive, as well as the changing trace element ratios, indicates that the magmatic system is characterized by open behaviour. (f) Histogram showing differentiation (MgO) for Taney Seamounts A-C; the cones are less differentiated than the edifice samples from Taney Seamounts A-C. (g) The decrease in K₂O/TiO₂, a highly incompatible element over a moderately incompatible element, illustrates that the source is becoming more depleted with time.



Results from numerical models with varying porosities for 1d diffusive exchange during percolation of melt through a plagioclase cumulate matrix. The models assume an initial melt with the trace element composition of sample D176-R25 where Sr and Ba have been recalculated using the following relationships: $Sr^* = \sqrt{Pr_N Nd_N}$ and $Ba^* = \sqrt{Rb_N Th_N}$. The trace elements have been normalized to primitive upper mantle (McDonough & Sun, 1995) in order to avoid the effects of plagioclase crystallization inherent in a MORB normalization. The resident plagioclase has a Sr content of 177 ppm, which would require crystallization from a melt that was more enriched than the percolating melt. The interaction time required to reproduce the observed anomalies varies depending on the porosity of the plagioclase cumulate.

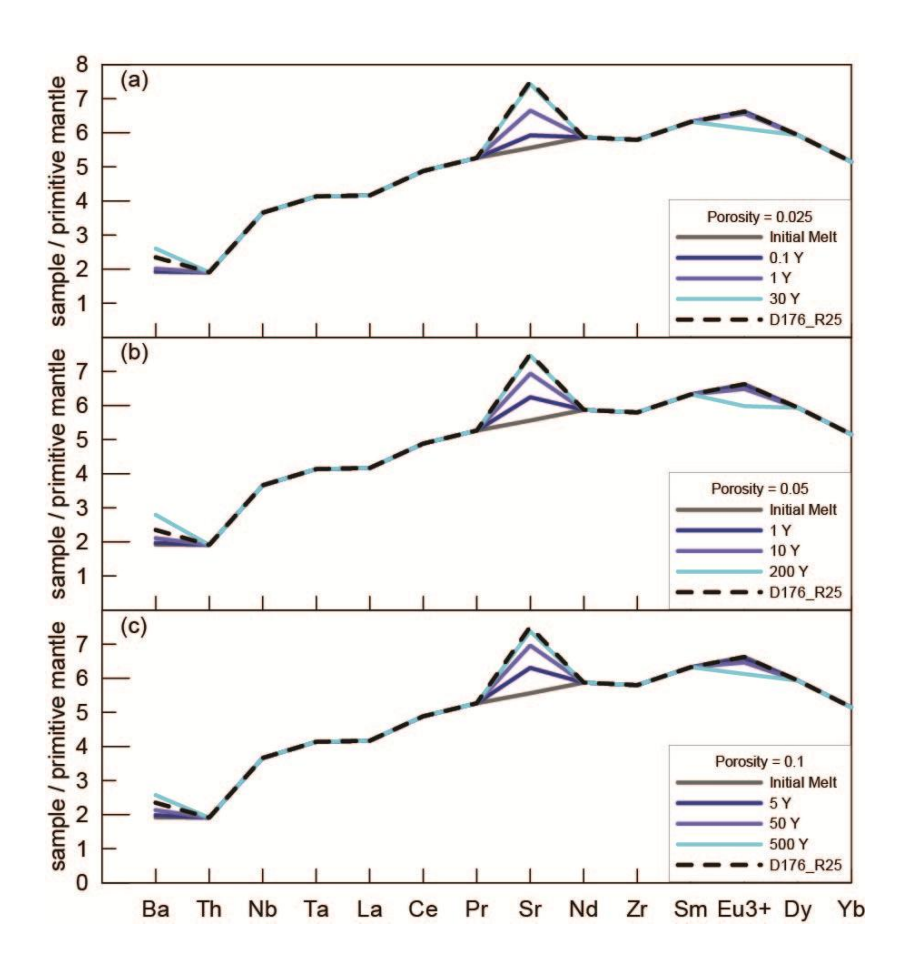
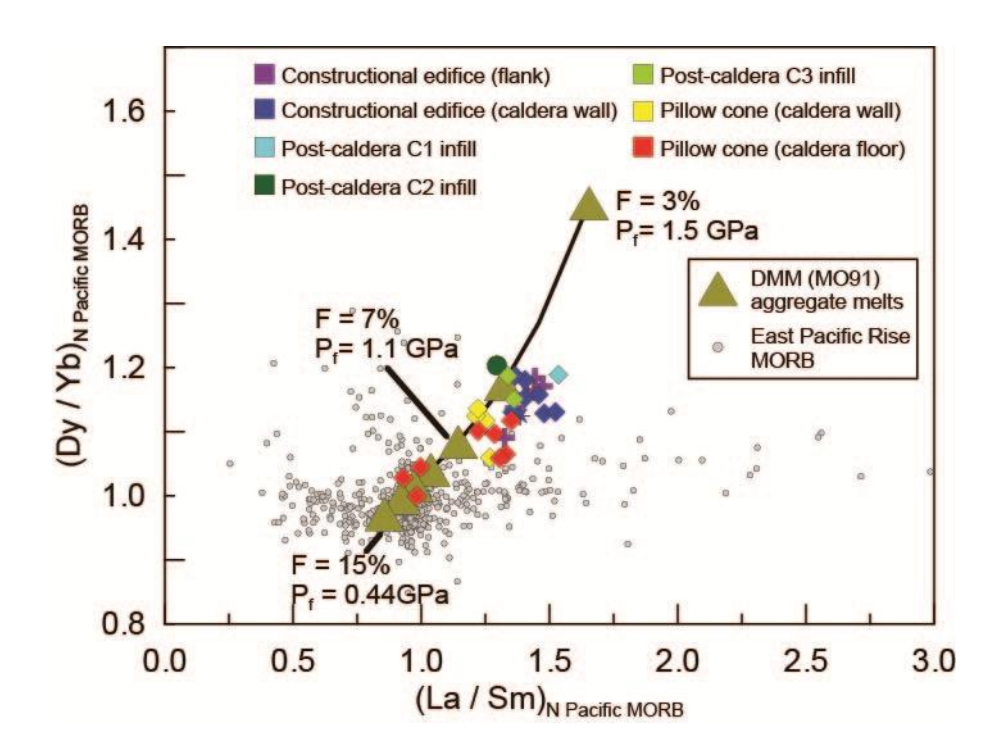


Figure 12

Trace element ratios normalized to average Pacific MORB (Arevalo & McDonough, 2010) for alphaMELTS, EPR MORB (http://earthchem.org/petdb), and Taney Seamount-A data. The range in MREE/HREE can be explained by different degrees of partial melting from a lithologically homogenous source with the composition of depleted MORB mantle (DMM). This model suggests that the most voluminous constructional edifice and caldera infill lavas are derived from the lowest degrees of partial melting, while the least voluminous young pillow cone lavas are derived from the highest degrees of melting.



(a) Trace element ratios normalized to average Pacific MORB (Arevalo & McDonough, 2010) of the pyroxenite batch melting models, Taney Seamount-A data, and the EPR MORB (http://earthchem.org/petdb). The range in MREE/HREE can be explained by different amounts of mixing of deep (3 GPa) garnet pyroxenite derived melts and N-MORB. For this model to be correct, deep garnet pyroxenite melts must segregate and travel to shallower levels with minimal interaction and mix with typical peridotite derived N-MORB at model ratios of 30:70. (b, c) Partial melts of a G2 garnet pyroxenite are andesitic in composition, inconsistent with the binary mixing model, and have been shown experimentally to react with subsolidus peridotite consuming large volumes of melt.

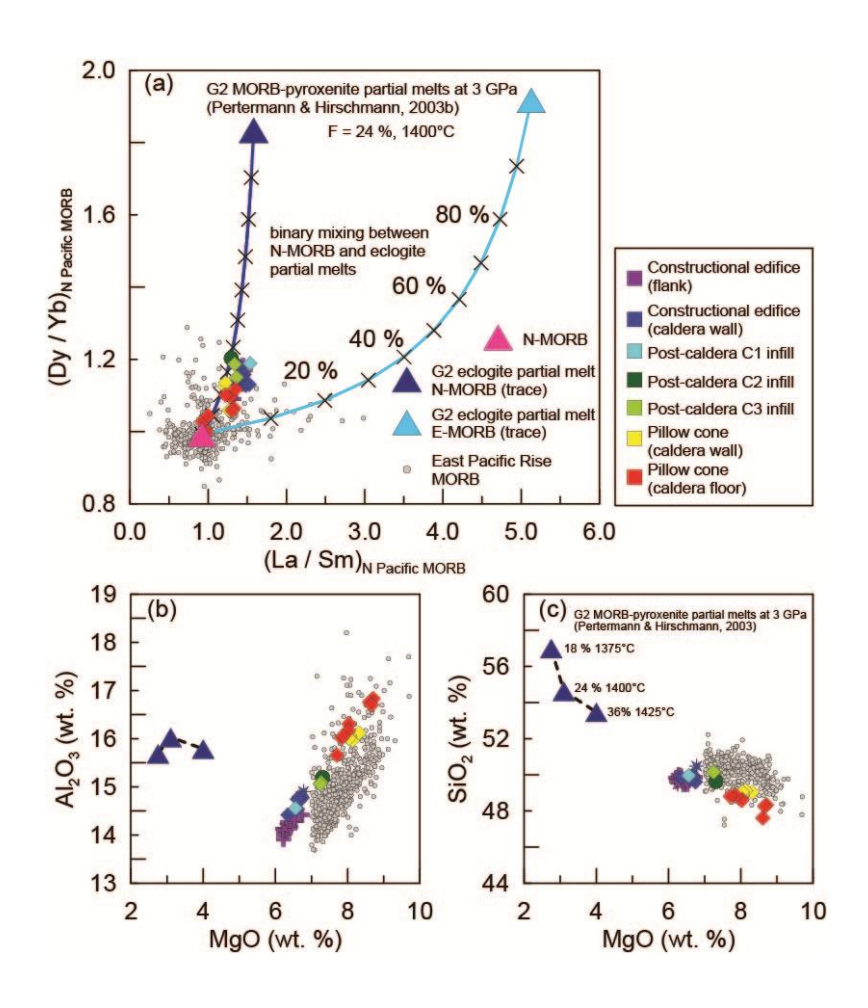


Figure 14

(a, b) Trace element ratios normalized to average Pacific MORB (Arevalo & McDonough, 2010) of the DMM and re-fertilized DMM peridotites. The DMM peridotite was refertilized by 2.5 and 5% addition of a partial melt (F = 24% at 1400°C and 3 GPa) of G2 eclogite with an N-MORB trace element composition. The re-fertilized peridotite has higher modal clinopyroxene and garnet at the expense of olivine, creating a more fusible lithology. This two-stage melting model reproduces the garnet signature observed in the more voluminous edifice lavas at a similar degree of partial melting (~15%) invoked for N-MORB formation. This model also benefits from not requiring deep segregation of partial melts with residual garnet followed by rapid transport to shallow depths. The (Th/Zr)_N model is consistent in terms of direction and magnitude, but is depleted in Th compared to the Taney-A lavas. This suggests that the Taney source is more enriched in Th than the model compositions.

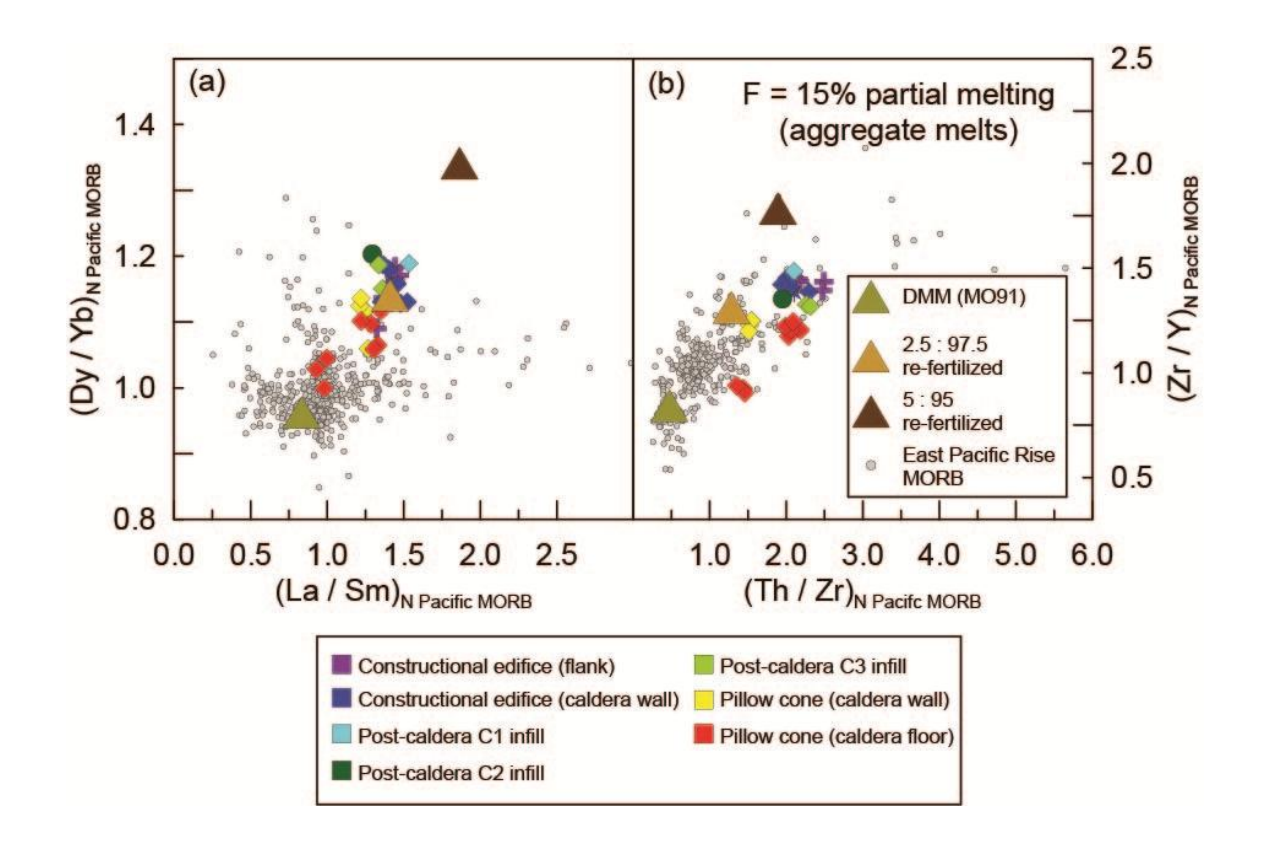
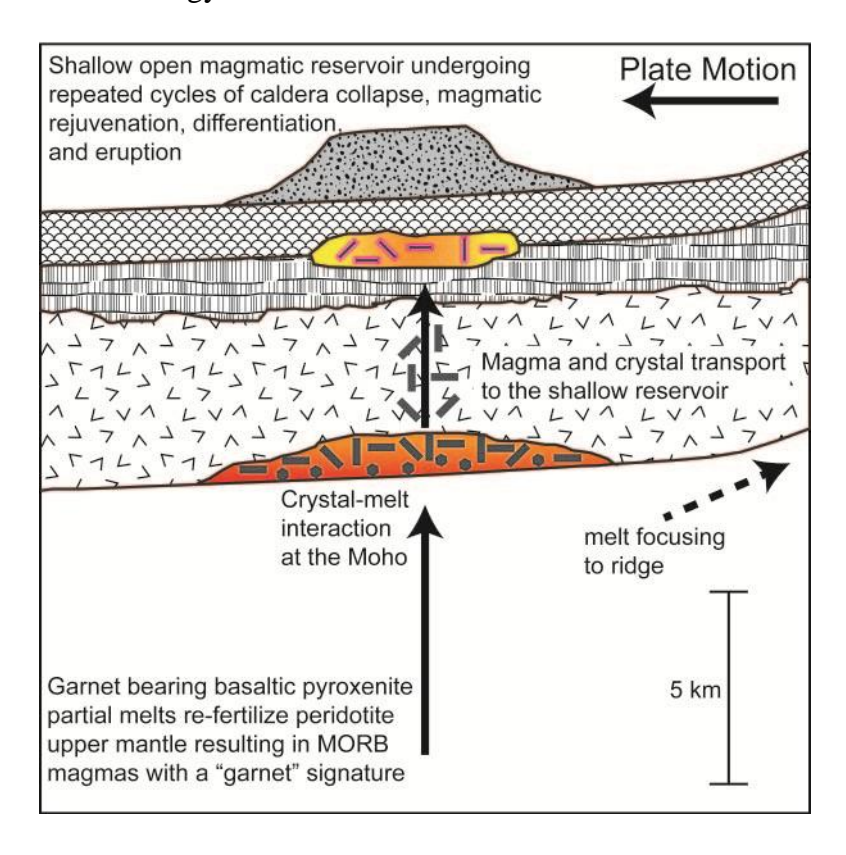


Figure 15

The magmatic architecture of Taney Seamount-A, as characterized by open system evolution in a shallow magma reservoir, melt-cumulate interaction in the upper mantle and lower oceanic crust, and melting of a mixed lithology mantle.



Supplementary Information S1: Standard and error analysis for volcanic glass, plagioclase and melt inclusion analyses.

Table S1.1: List of standards used in electron microprobe analyses.

Standard	Material	Element(s)	Producer	Location	Analyses
VG-2	Basaltic glass	Si, Al, Fe, Mg, Ca, Na	Smithsonian	Juan de Fuca Ridge	Glass
VG-568	Rhyolite Glass	K	Smithsonian	Yellowstone	Glass
SPESS	Spessartine	Mn	C.M.Taylor	-	Glass
FLAP	Apatite	Р	C.M Taylor	Wilberforce	Glass
PYRI	Pyrite	S	C.M Taylor	-	Glass
VANA	Vanadinite	CI	Cameca	-	Glass
TiO ₂	Rutile	Ti	C.M Taylor		Glass,
1102	Rutile	11	C.IVI Taylor	-	Plagioclase
Amelia Albite	Albite	Na	C.M Taylor	-	Plagioclase
Astimex Sanidine	Sanidine	Si, Al, K	Astimex 53	Hoken Falls, Germany	Plagioclase
		•		Germany	9
DIOP	Diopside	Ca, Mg	C.M Taylor	-	Plagioclase
Fe ₂ O ₃	Hematite	Fe	C.M Taylor	-	Plagioclase

Table S1.2: Reproducibility and accuracy of the electron microprobe for VG-2

Oxide	Ana	lysis nun	nber											
(Wt. %)	1	2	3	4	5	6	7	8	9	10	11	12	13	14
SiO ₂	50.7	50.9	50.8	50.7	50.6	50.8	50.7	50.8	50.6	50.8	50.7	50.8	50.6	50.8
TiO ₂	1.81	1.78	1.66	1.57	1.78	1.76	1.80	1.97	1.72	1.89	1.85	1.72	1.79	1.91
Al_2O_3	14.2	14.2	14.1	14.1	14.2	14.1	14.2	14.3	14.1	14.1	14.2	14.1	14.0	14.1
FeO_T	11.7	11.8	12.0	11.6	11.8	11.4	11.8	11.9	11.5	11.9	12.0	11.6	11.7	11.7
MnO	0.212	0.158	0.215	0.215	0.160	0.181	0.193	0.187	0.198	0.205	0.205	0.187	0.194	0.178
MgO	6.61	6.68	6.61	6.70	6.62	6.72	6.70	6.64	6.72	6.75	6.75	6.71	6.73	6.69
CaO	11.1	11.1	11.1	11.0	11.2	11.2	11.1	11.1	10.9	11.2	11.2	11.2	11.1	11.2
Na ₂ O	2.61	2.60	2.65	2.59	2.64	2.59	2.58	2.64	2.68	2.59	2.62	2.59	2.59	2.57
K_2O	0.214	0.204	0.245	0.224	0.216	0.219	0.210	0.219	0.231	0.219	0.228	0.207	0.212	0.227
P_2O_5	0.206	0.204	0.226	0.219	0.220	0.205	0.230	0.207	0.237	0.216	0.213	0.207	0.205	0.217
SO_3	0.337	0.343	0.344	0.330	0.372	0.316	0.316	0.349	0.340	0.301	0.321	0.32	0.362	0.364
CI	0.030	0.027	0.025	0.029	0.028	0.026	0.028	0.029	0.028	0.027	0.029	0.024	0.026	0.026
Total	99.63	99.93	99.99	99.34	99.84	99.54	99.76	100.26	99.28	100.12	100.25	99.53	99.53	99.96

Notes: All oxides and elements in weight per cent. The reference for VG-2 (NMNH 111240-52) is from the Smithsonian microbeam standards (Jarosewich, 2002). † The reported value is 6.71 which was used during analyses, we have corrected our data to 7.07.

Table S1.2 Cont'd

Oxide	Ana	ılysis nun	nber											
(Wt. %)	16	17	18	19	20	21	22	23	24	25	26	27	28	15
SiO ₂	50.7	50.7	50.6	50.5	50.7	50.4	50.7	50.6	50.4	50.4	50.4	50.7	50.7	50.9
TiO ₂	1.99	1.68	1.77	1.85	1.98	1.91	1.49	1.75	1.89	1.61	1.87	1.80	1.75	1.79
Al_2O_3	14.0	14.2	13.9	14.1	13.9	14.1	14.1	14.0	14.1	14.0	14.0	14.1	14.1	14.1
FeO_T	11.8	11.9	11.7	11.8	11.8	11.8	11.8	11.9	11.9	11.8	11.9	11.9	11.9	11.8
MnO	0.233	0.204	0.233	0.181	0.179	0.168	0.212	0.180	0.188	0.204	0.262	0.198	0.158	0.228
MgO	6.66	6.71	6.63	6.76	6.68	6.77	6.69	6.75	6.69	6.79	6.80	6.84	6.63	6.64
CaO	11.2	11.0	11.1	11.1	11.1	11.0	11.1	10.9	11.1	11.0	11.1	11.0	11.1	11.3
Na₂O	2.61	2.63	2.63	2.63	2.64	2.57	2.64	2.68	2.63	2.63	2.65	2.66	2.70	2.66
K_2O	0.224	0.21	0.211	0.212	0.212	0.209	0.21	0.211	0.21	0.221	0.219	0.214	0.198	0.231
P_2O_5	0.236	0.215	0.225	0.202	0.213	0.223	0.21	0.225	0.213	0.204	0.236	0.239	0.209	0.236
SO_3	0.345	0.36	0.325	0.349	0.339	0.346	0.376	0.334	0.364	0.342	0.32	0.336	0.351	0.343
CI	0.027	0.029	0.025	0.024	0.028	0.027	0.027	0.024	0.026	0.027	0.028	0.025	0.022	0.026
Total	99.94	99.84	99.34	99.68	99.81	99.53	99.54	99.58	99.68	99.35	99.84	100.06	99.77	100.09

Table S1.2 Cont'd

Oxide	Λnc	alysis nur	obor											
(Wt. %)	29	30	31	32	33	34	35	36	37	38	39	40	41	42
SiO ₂	50.5	50.2	50.5	50.5	50.1	50.1	49.7	51.4	50.8	51.6	50.4	51.4	49.7	49.7
TiO ₂	1.76	1.69	1.73	1.68	1.82	1.61	1.87	1.75	1.87	1.95	1.84	1.77	1.87	1.83
Al_2O_3	14.1	13.9	14.1	14.1	14.0	13.9	13.8	13.9	13.9	14.0	14.0	13.8	13.7	13.8
FeO _T	11.7	11.4	11.9	11.8	11.7	11.7	12.1	12.0	11.9	12.1	12.1	11.8	12.0	12.2
MnO	0.174	0.204	0.153	0.249	0.226	0.201	0.216	0.212	0.182	0.226	0.164	0.249	0.21	0.21
MgO	6.79	6.65	6.69	6.72	6.67	6.74	6.72	6.78	6.69	6.64	6.67	6.69	6.60	6.68
CaO	11.1	11.1	11.2	11.1	11.0	11.1	11.2	10.9	11.0	10.9	11.0	10.9	11.0	11.0
Na₂O	2.60	2.65	2.57	2.67	2.69	2.65	2.65	2.64	2.66	2.68	2.69	2.71	2.65	2.66
K_2O	0.198	0.203	0.2	0.211	0.214	0.215	0.211	0.206	0.213	0.207	0.212	0.228	0.22	0.223
P_2O_5	0.205	0.191	0.219	0.219	0.223	0.212	0.207	0.226	0.205	0.223	0.226	0.216	0.229	0.219
SO_3	0.332	0.352	0.325	0.355	0.363	0.355	0.371	0.34	0.354	0.345	0.326	0.361	0.355	0.353
CI	0.028	0.024	0.023	0.025	0.025	0.027	0.025	0.028	0.029	0.025	0.028	0.029	0.028	0.029
Total	99.45	98.50	99.55	99.67	98.97	98.87	98.98	100.34	99.80	100.92	99.49	100.19	98.55	98.86

Table S1.2 Cont'd

Oxide (Wt.	Ana	lysis num	ber							Std. Dev. (+ 2σ	Std. Dev.	ref. value
%)	43	44	45	46	47	48	49	50	Average	<u>abs)</u>	<u>(+ 20 %)</u>	(VG-2)
SiO ₂	52.2	50.3	49.6	51.9	51.1	51.4	50.5	49.3	50.6	1.1	2.1	50.8
TiO ₂	1.82	1.71	1.92	1.76	1.82	1.71	1.98	1.86	1.79	0.21	12.0	1.85
Al_2O_3	13.8	14.0	14.1	14.1	14.0	14.0	14.0	14.0	14.0	0.2	1.7	14.1
FeO_T	12.0	11.7	11.7	11.8	11.5	11.9	12.0	11.8	11.8	0.3	2.9	11.8
MnO	0.197	0.249	0.196	0.207	0.236	0.207	0.214	0.212	0.202	0.051	25.1	0.220
MgO	6.60	6.71	6.75	6.75	6.65	6.76	6.79	6.76	6.70	0.12	1.7	† (7.07)
CaO	11.2	11.0	11.1	11.0	10.9	11.0	10.9	10.8	11.1	0.2	1.9	11.1
Na₂O	2.61	2.62	2.58	2.58	2.60	2.61	2.66	2.57	2.63	0.07	2.9	2.62
K_2O	0.217	0.211	0.206	0.222	0.194	0.224	0.208	0.224	0.215	0.019	9.0	0.200
P_2O_5	0.235	0.208	0.197	0.189	0.218	0.231	0.217	0.197	0.216	0.025	11.3	0.220
SO ₃	0.355	0.352	0.353	0.349	0.339	0.356	0.329	0.33	0.34	0.03	9.4	0.350
CI	0.025	0.027	0.024	0.024	0.027	0.026	0.026	0.025	0.026	0.004	14.1	0.030
Total	101.23	99.00	98.66	100.76	99.48	100.49	99.82	98.03	99.65	1.21	1.2	99.86

Table S1.3: Reproducibility and accuracy for trace elements using the ICP-MS linked scan method for P1326-2

Element		Analysis nu	ımber				
(ppm)	1	2	3	4	5	6	7
Cr	294	291	295	293	286	313	287
Ni	49	48	46	49	48	51	47
Rb	2.01	2.06	1.80	2.19	1.98	1.90	1.91
Sr	162	162	152	160	162	167	155
Υ	29.4	32.4	27.8	31.6	31.1	30.0	29.3
Zr	92.4	99.5	84.3	96.9	96.9	94.7	91.1
Nb	4.72	4.90	4.22	4.99	4.67	4.46	4.59
Ва	27.06	29.50	28.30	29.20	29.75	27.21	29.72
La	4.63	5.07	4.52	4.97	4.90	4.81	4.52
Ce	13.61	13.39	12.56	13.27	13.10	13.12	11.96
Pr	1.98	2.27	1.92	2.02	2.09	1.96	2.14
Nd	10.86	10.55	10.47	11.33	11.71	10.74	10.81
Sm	3.62	3.92	3.18	3.17	4.05	3.80	3.77
Eu	1.21	1.32	1.24	1.36	1.37	1.33	1.39
Gd	4.73	4.37	4.33	4.54	4.48	4.10	4.78
Tb	0.81	0.82	0.74	0.82	0.87	0.78	0.84
Dy	5.40	5.43	4.98	5.11	5.69	5.22	5.79
Но	1.22	1.18	0.96	1.21	1.25	1.05	1.13
Er	3.10	3.49	2.95	3.17	3.42	3.14	3.29
Tm	0.48	0.52	0.37	0.44	0.48	0.47	0.47
Yb	2.94	3.27	2.91	3.22	3.29	2.73	3.28

Table S1.3: Cont'd

Element					Std. Dev	Std. Dev	Ref. Value
(ppm)	8	9	10	Average	(+ 2σ abs)	(+ 2 0 %)	(P1326-2)
Cr	338	298	319	303	18.4	6.1	309
Ni	49	48	50	48	3.1	6.4	49
Rb	2.02	1.93	1.78	1.96	0.3	12.9	2.18
Sr	155	164	152	162	10.3	6.3	156
Υ	29.2	31.5	30.8	30.5	3.1	10.3	30.1
Zr	92.6	97.1	96.2	94.6	10.1	10.6	95.8
Nb	4.47	4.53	4.39	4.62	0.5	11.3	4.81
Ва	26.80	27.59	26.71	28.81	2.3	8.1	34.22
La	4.60	4.97	4.58	4.81	0.4	9.2	4.63
Ce	12.61	12.45	12.16	12.97	1.1	8.7	12.66
Pr	2.01	2.19	1.94	2.09	0.2	11.7	2.06
Nd	10.24	11.53	10.74	11.13	0.9	8.0	10.61
Sm	3.02	3.97	3.45	3.63	0.7	19.1	3.42
Eu	1.23	1.38	1.21	1.34	0.1	10.3	1.29
Gd	3.63	4.88	4.24	4.50	0.5	10.5	4.67
Tb	0.70	0.84	0.74	0.80	0.1	10.3	0.75
Dy	4.80	6.08	5.21	5.36	0.6	11.0	5.37
Но	1.02	1.18	1.08	1.15	0.2	17.9	1.14
Er	2.99	3.60	3.29	3.25	0.4	11.6	3.26
Tm	0.43	0.54	0.41	0.47	0.1	20.7	0.49
Yb	2.89	3.48	3.00	3.17	0.5	14.4	3.10

Table S1.4: Reproducibility and accuracy for trace elements using the ICP-MS deflector method for P1326-2

Element									Std. Dev (+ 2σ	Std. Dev (+ 2σ	Ref. Value
(ppm)	1	2	3	4	5	6	7	Average	abs)	%)	(P1326-2)
Lu	0.465	0.460	0.463	0.458	0.454	0.433	0.451	0.455	0.022	4.8	0.444
Hf	2.5	2.5	2.5	2.5	2.4	2.4	2.4	2.5	0.13	5.2	2.6
Ta	0.292	0.294	0.300	0.297	0.286	0.296	0.299	0.295	0.009	3.1	0.277
Th	0.318	0.320	0.323	0.320	0.314	0.319	0.315	0.319	0.006	2.0	0.350

Table S1.5: Calibration standards for SIMS analysis

	Element						
Standard	CO ₂ (ppm)	H ₂ O (Wt. %)					
519-4-1		0.17					
46D	237	0.11					
D52-5	88	1.00					
D51-3	125	0.44					
1649-3	161	0.61					
D20-3		0.05					
JD17H		2.49					
1654-3		1.00					
D20-3		0.05					
NS-1	3150						

Table S1.6: Reproducibility and accuracy for CO_2 and H_2O using SIMS for P1326-2

Repeat analyses of internal standard P1326-2 Element CO₂ (ppm) H₂O (Wt. %) jsv0312-23 508 0.25 jsv0312-37 341 0.25 jsv0312-43 347 0.25 jsv0312-56 344 0.27 jsv0312b-3 361 0.23 jsv0312b-4 515 0.31 jsv0312b-5 365 0.30 jsv0312b-7 403 0.28 jsv0312b-15 395 0.31 jsv0312b-25 378 0.29 jsv0312b-35 378 0.28 jsv0312b-44 443 0.36 jsv0312b-57 374 0.26 jsv0312b-67 357 0.26 jsv0312b-85 359 0.22 jsv0312c-17 357 0.22 jsv0312c-2 346 0.23 jsv0312e-3 394 0.35 jsv0312e-4 347 0.32 jsv0312e-5 437 0.32 jsv0312g-19 373 0.23	00		
standard P1326-2 CO2 (ppm) H2O (Wt. %) jsv0312-23 508 0.25 jsv0312-37 341 0.25 jsv0312-43 347 0.25 jsv0312-56 344 0.27 jsv0312b-3 361 0.23 jsv0312b-4 515 0.31 jsv0312b-5 365 0.30 jsv0312b-7 403 0.28 jsv0312b-15 395 0.31 jsv0312b-25 378 0.29 jsv0312b-35 378 0.28 jsv0312b-44 443 0.36 jsv0312b-57 374 0.26 jsv0312b-67 357 0.26 jsv0312b-85 359 0.22 jsv0312c-17 357 0.22 jsv0312c-2 324 0.30 jsv0312e-3 394 0.35 jsv0312e-4 347 0.32 jsv0312g 334 0.25 jsv0312g 334 0.25 jsv0312g-19	Repeat analyses of internal	Element	
jsv0312-23 508 0.25 jsv0312-32 345 0.26 jsv0312-37 341 0.25 jsv0312-43 347 0.25 jsv0312-56 344 0.27 jsv0312b-3 361 0.23 jsv0312b-4 515 0.31 jsv0312b-5 365 0.30 jsv0312b-7 403 0.28 jsv0312b-15 395 0.31 jsv0312b-25 378 0.29 jsv0312b-35 378 0.28 jsv0312b-44 443 0.36 jsv0312b-57 374 0.26 jsv0312b-67 357 0.26 jsv0312b-85 359 0.22 jsv0312c-17 357 0.22 jsv0312e-2 324 0.30 jsv0312e-3 394 0.35 jsv0312e-3 394 0.35 jsv0312e-4 347 0.32 jsv0312g-3 345 0.30 jsv0312g-19 373 0.23 jsv0312g-24 336 0.26		CO ₂ (ppm)	H ₂ O (Wt. %)
jsv0312-37 341 0.25 jsv0312-43 347 0.25 jsv0312b-3 361 0.23 jsv0312b-4 515 0.31 jsv0312b-5 365 0.30 jsv0312b-7 403 0.28 jsv0312b-15 395 0.31 jsv0312b-25 378 0.29 jsv0312b-35 378 0.28 jsv0312b-44 443 0.36 jsv0312b-57 374 0.26 jsv0312b-67 357 0.26 jsv0312b-85 359 0.22 jsv0312c-17 357 0.22 jsv0312e-2 324 0.30 jsv0312e-3 394 0.35 jsv0312g-3 345 0.30 jsv0312g-3 345 0.30 jsv0312g-3 36	jsv0312-23		0.25
jsv0312-43 347 0.25 jsv0312b-3 361 0.23 jsv0312b-4 515 0.31 jsv0312b-5 365 0.30 jsv0312b-7 403 0.28 jsv0312b-15 395 0.31 jsv0312b-25 378 0.29 jsv0312b-35 378 0.28 jsv0312b-44 443 0.36 jsv0312b-57 374 0.26 jsv0312b-67 357 0.26 jsv0312b-85 359 0.22 jsv0312c-17 357 0.22 jsv0312e-2 324 0.30 jsv0312e-3 394 0.35 jsv0312e-3 394 0.35 jsv0312e-4 347 0.32 jsv0312g-3 334 0.25 jsv0312g-19 373 0.23 jsv0312g-24 336 0.26 jsv0312h-28 364 0.25 jsv0312h-30 376 0.34 jsv0312h-45 35	jsv0312-32	345	0.26
jsv0312-56 344 0.27 jsv0312b-3 361 0.23 jsv0312b-4 515 0.31 jsv0312b-5 365 0.30 jsv0312b-7 403 0.28 jsv0312b-15 395 0.31 jsv0312b-25 378 0.29 jsv0312b-35 378 0.28 jsv0312b-44 443 0.36 jsv0312b-57 374 0.26 jsv0312b-67 357 0.26 jsv0312b-85 359 0.22 jsv0312c-17 357 0.22 jsv0312c-2 324 0.30 jsv0312e-3 394 0.35 jsv0312e-4 347 0.32 jsv0312g-5 437 0.32 jsv0312g 334 0.25 jsv0312g-19 373 0.23 jsv0312g-24 336 0.26 jsv0312h-30 376 0.34 jsv0312h-32 381 0.34 jsv0312h-45 350<	jsv0312-37	341	0.25
jsv0312b-3 361 0.23 jsv0312b-4 515 0.31 jsv0312b-5 365 0.30 jsv0312b-7 403 0.28 jsv0312b-15 395 0.31 jsv0312b-25 378 0.29 jsv0312b-35 378 0.28 jsv0312b-44 443 0.36 jsv0312b-57 374 0.26 jsv0312b-67 357 0.26 jsv0312b-85 359 0.22 jsv0312c-17 357 0.22 jsv0312e-2 324 0.30 jsv0312e-3 394 0.35 jsv0312e-4 347 0.32 jsv0312g 334 0.25 jsv0312g 334 0.25 jsv0312g-19 373 0.23 jsv0312h-28 364 0.25 jsv0312h-30 376 0.34 jsv0312h-45 350 0.29 Average 376 0.28	jsv0312-43	347	0.25
jsv0312b-4 515 0.31 jsv0312b-5 365 0.30 jsv0312b-7 403 0.28 jsv0312b-15 395 0.31 jsv0312b-25 378 0.29 jsv0312b-35 378 0.28 jsv0312b-44 443 0.36 jsv0312b-57 374 0.26 jsv0312b-67 357 0.26 jsv0312b-85 359 0.22 jsv0312c-17 357 0.22 jsv0312e-2 324 0.30 jsv0312e-3 394 0.35 jsv0312e-4 347 0.32 jsv0312g-5 437 0.32 jsv0312g 334 0.25 jsv0312g-19 373 0.23 jsv0312h-28 364 0.25 jsv0312h-30 376 0.34 jsv0312h-45 350 0.29 Average 376 0.28	jsv0312-56	344	0.27
jsv0312b-5 365 0.30 jsv0312b-7 403 0.28 jsv0312b-15 395 0.31 jsv0312b-25 378 0.29 jsv0312b-35 378 0.28 jsv0312b-44 443 0.36 jsv0312b-57 374 0.26 jsv0312b-67 357 0.26 jsv0312b-85 359 0.22 jsv0312c-17 357 0.22 jsv0312e-2 324 0.30 jsv0312e-3 394 0.35 jsv0312e-4 347 0.32 jsv0312g-5 437 0.32 jsv0312g 334 0.25 jsv0312g-19 373 0.23 jsv0312h-28 364 0.25 jsv0312h-30 376 0.34 jsv0312h-45 350 0.29 Average 376 0.28	jsv0312b-3	361	0.23
jsv0312b-7 403 0.28 jsv0312b-15 395 0.31 jsv0312b-25 378 0.29 jsv0312b-35 378 0.28 jsv0312b-44 443 0.36 jsv0312b-57 374 0.26 jsv0312b-67 357 0.26 jsv0312b-85 359 0.22 jsv0312c-17 357 0.22 jsv0312e-2 324 0.30 jsv0312e-3 394 0.35 jsv0312e-4 347 0.32 jsv0312e-5 437 0.32 jsv0312g 334 0.25 jsv0312g-19 373 0.23 jsv0312p-24 336 0.26 jsv0312h-30 376 0.34 jsv0312h-32 381 0.34 jsv0312h-45 350 0.29	jsv0312b-4	515	0.31
jsv0312b-15 395 0.31 jsv0312b-25 378 0.29 jsv0312b-35 378 0.28 jsv0312b-44 443 0.36 jsv0312b-57 374 0.26 jsv0312b-67 357 0.26 jsv0312b-85 359 0.22 jsv0312c-17 357 0.22 jsv0312e-2 324 0.30 jsv0312e-3 394 0.35 jsv0312e-4 347 0.32 jsv0312e-5 437 0.32 jsv0312g 334 0.25 jsv0312g-19 373 0.23 jsv0312p-24 336 0.26 jsv0312h-30 376 0.34 jsv0312h-32 381 0.34 jsv0312h-45 350 0.29 Average 376 0.28	jsv0312b-5	365	0.30
jsv0312b-25 378 0.29 jsv0312b-35 378 0.28 jsv0312b-44 443 0.36 jsv0312b-57 374 0.26 jsv0312b-67 357 0.26 jsv0312b-85 359 0.22 jsv0312c-17 357 0.22 jsv0312e-2 324 0.30 jsv0312e-3 394 0.35 jsv0312e-4 347 0.32 jsv0312e-5 437 0.32 jsv0312f 345 0.30 jsv0312g 334 0.25 jsv0312g-19 373 0.23 jsv0312g-24 336 0.26 jsv0312h-28 364 0.25 jsv0312h-30 376 0.34 jsv0312h-45 350 0.29 Average 376 0.28	jsv0312b-7	403	0.28
jsv0312b-35 378 0.28 jsv0312b-44 443 0.36 jsv0312b-57 374 0.26 jsv0312b-67 357 0.26 jsv0312b-85 359 0.22 jsv0312c-17 357 0.22 jsv0312e-2 324 0.30 jsv0312e-3 394 0.35 jsv0312e-4 347 0.32 jsv0312e-5 437 0.32 jsv0312f 345 0.30 jsv0312g 334 0.25 jsv0312g-19 373 0.23 jsv0312g-24 336 0.26 jsv0312h-28 364 0.25 jsv0312h-30 376 0.34 jsv0312h-45 350 0.29 Average 376 0.28	jsv0312b-15	395	0.31
jsv0312b-44 443 0.36 jsv0312b-57 374 0.26 jsv0312b-67 357 0.26 jsv0312b-85 359 0.22 jsv0312c 346 0.23 jsv0312c-17 357 0.22 jsv0312e-2 324 0.30 jsv0312e-3 394 0.35 jsv0312e-4 347 0.32 jsv0312e-5 437 0.32 jsv0312f 345 0.30 jsv0312g 334 0.25 jsv0312g-19 373 0.23 jsv0312g-24 336 0.26 jsv0312h-28 364 0.25 jsv0312h-30 376 0.34 jsv0312h-45 350 0.29 Average 376 0.28	jsv0312b-25	378	0.29
jsv0312b-57 374 0.26 jsv0312b-67 357 0.26 jsv0312b-85 359 0.22 jsv0312c 346 0.23 jsv0312c-17 357 0.22 jsv0312e-2 324 0.30 jsv0312e-3 394 0.35 jsv0312e-4 347 0.32 jsv0312e-5 437 0.32 jsv0312f 345 0.30 jsv0312g 334 0.25 jsv0312g-19 373 0.23 jsv0312g-24 336 0.26 jsv0312h-28 364 0.25 jsv0312h-30 376 0.34 jsv0312h-45 350 0.29 Average 376 0.28	jsv0312b-35	378	0.28
jsv0312b-67 357 0.26 jsv0312b-85 359 0.22 jsv0312c 346 0.23 jsv0312c-17 357 0.22 jsv0312e-2 324 0.30 jsv0312e-3 394 0.35 jsv0312e-4 347 0.32 jsv0312e-5 437 0.32 jsv0312f 345 0.30 jsv0312g 334 0.25 jsv0312g-19 373 0.23 jsv0312g-24 336 0.26 jsv0312h-28 364 0.25 jsv0312h-30 376 0.34 jsv0312h-32 381 0.34 jsv0312h-45 350 0.29 Average 376 0.28	jsv0312b-44	443	0.36
jsv0312b-85 359 0.22 jsv0312c 346 0.23 jsv0312c-17 357 0.22 jsv0312e-2 324 0.30 jsv0312e-3 394 0.35 jsv0312e-4 347 0.32 jsv0312e-5 437 0.32 jsv0312f 345 0.30 jsv0312g 334 0.25 jsv0312g-19 373 0.23 jsv0312g-24 336 0.26 jsv0312h-28 364 0.25 jsv0312h-30 376 0.34 jsv0312h-45 350 0.29 Average 376 0.28	jsv0312b-57	374	0.26
jsv0312c 346 0.23 jsv0312c-17 357 0.22 jsv0312e-2 324 0.30 jsv0312e-3 394 0.35 jsv0312e-4 347 0.32 jsv0312e-5 437 0.32 jsv0312f 345 0.30 jsv0312g 334 0.25 jsv0312g-19 373 0.23 jsv0312g-24 336 0.26 jsv0312h-28 364 0.25 jsv0312h-30 376 0.34 jsv0312h-32 381 0.34 jsv0312h-45 350 0.29 Average 376 0.28	jsv0312b-67	357	0.26
jsv0312c-17 357 0.22 jsv0312e-2 324 0.30 jsv0312e-3 394 0.35 jsv0312e-4 347 0.32 jsv0312e-5 437 0.32 jsv0312f 345 0.30 jsv0312g 334 0.25 jsv0312g-19 373 0.23 jsv0312g-24 336 0.26 jsv0312h-28 364 0.25 jsv0312h-30 376 0.34 jsv0312h-32 381 0.34 jsv0312h-45 350 0.29 Average 376 0.28	jsv0312b-85	359	0.22
jsv0312e-2 324 0.30 jsv0312e-3 394 0.35 jsv0312e-4 347 0.32 jsv0312e-5 437 0.32 jsv0312f 345 0.30 jsv0312g 334 0.25 jsv0312g-19 373 0.23 jsv0312g-24 336 0.26 jsv0312h-28 364 0.25 jsv0312h-30 376 0.34 jsv0312h-32 381 0.34 jsv0312h-45 350 0.29 Average 376 0.28	jsv0312c	346	0.23
jsv0312e-3 394 0.35 jsv0312e-4 347 0.32 jsv0312e-5 437 0.32 jsv0312f 345 0.30 jsv0312g 334 0.25 jsv0312g-19 373 0.23 jsv0312g-24 336 0.26 jsv0312h-28 364 0.25 jsv0312h-30 376 0.34 jsv0312h-32 381 0.34 jsv0312h-45 350 0.29 Average 376 0.28	jsv0312c-17	357	0.22
jsv0312e-4 347 0.32 jsv0312e-5 437 0.32 jsv0312f 345 0.30 jsv0312g 334 0.25 jsv0312g-19 373 0.23 jsv0312g-24 336 0.26 jsv0312h-28 364 0.25 jsv0312h-30 376 0.34 jsv0312h-32 381 0.34 jsv0312h-45 350 0.29 Average 376 0.28	jsv0312e-2	324	0.30
jsv0312e-5 437 0.32 jsv0312f 345 0.30 jsv0312g 334 0.25 jsv0312g-19 373 0.23 jsv0312g-24 336 0.26 jsv0312h-28 364 0.25 jsv0312h-30 376 0.34 jsv0312h-32 381 0.34 jsv0312h-45 350 0.29 Average 376 0.28	jsv0312e-3	394	0.35
jsv0312f 345 0.30 jsv0312g 334 0.25 jsv0312g-19 373 0.23 jsv0312g-24 336 0.26 jsv0312h-28 364 0.25 jsv0312h-30 376 0.34 jsv0312h-32 381 0.34 jsv0312h-45 350 0.29 Average 376 0.28	jsv0312e-4	347	0.32
jsv0312g 334 0.25 jsv0312g-19 373 0.23 jsv0312g-24 336 0.26 jsv0312h-28 364 0.25 jsv0312h-30 376 0.34 jsv0312h-32 381 0.34 jsv0312h-45 350 0.29 Average 376 0.28	jsv0312e-5	437	0.32
jsv0312g-19 373 0.23 jsv0312g-24 336 0.26 jsv0312h-28 364 0.25 jsv0312h-30 376 0.34 jsv0312h-32 381 0.34 jsv0312h-45 350 0.29 Average 376 0.28	jsv0312f	345	0.30
jsv0312g-24 336 0.26 jsv0312h-28 364 0.25 jsv0312h-30 376 0.34 jsv0312h-32 381 0.34 jsv0312h-45 350 0.29 Average 376 0.28	jsv0312g	334	0.25
jsv0312h-28 364 0.25 jsv0312h-30 376 0.34 jsv0312h-32 381 0.34 jsv0312h-45 350 0.29 Average 376 0.28	jsv0312g-19	373	0.23
jsv0312h-30 376 0.34 jsv0312h-32 381 0.34 jsv0312h-45 350 0.29 Average 376 0.28	jsv0312g-24	336	0.26
jsv0312h-32 381 0.34 jsv0312h-45 350 0.29 Average 376 0.28	jsv0312h-28	364	0.25
jsv0312h-45 350 0.29 Average 376 0.28	jsv0312h-30	376	0.34
Average 376 0.28	jsv0312h-32	381	0.34
	jsv0312h-45	350	0.29
Std Dev 46 0.04	Average	376	0.28
	Std Dev	46	0.04

Supplementary Information S2: Additional glass and whole rock chemical analyses.

Table S2.1: Major element data for volcanic glasses from Taney Seamounts-B and C

Sample	D173_R9	D173_R11	D173_R12	D173_R13	D178_R4	D178_R6	D178_R12
Seamount	Taney-B	Taney-B	Taney-B	Taney-B	Taney-C	Taney-C	Taney-C
SiO ₂	49.8	49.7	49.7	50.1	50.3	49.9	50.2
TiO ₂	1.77	1.53	1.90	1.62	2.06	1.61	1.38
Al_2O_3	14.9	15.2	14.6	15.1	14.1	14.7	15.0
FeO _⊤	11.7	10.8	12.2	10.7	12.7	11.0	10.2
MnO	0.204	0.196	0.206	0.200	0.228	0.194	0.191
MgO	7.05	7.61	6.78	7.40	6.11	7.23	7.88
CaO	11.6	12.0	11.3	12.2	10.9	12.1	12.5
Na ₂ O	3.07	2.92	3.18	2.94	3.27	3.02	2.80
K₂O	0.168	0.153	0.178	0.165	0.192	0.131	0.101
P_2O_5	0.196	0.171	0.214	0.170	0.213	0.181	0.150
SO ₃	0.146	0.122	0.158	0.130	0.152	0.147	0.129
CI	0.034	0.034	0.039	0.020	0.028	0.019	0.027
Total	100.5	100.6	100.4	100.7	100.2	100.3	100.5

Notes: Major elements expressed in oxide weight per cent.

Table S2.1 cont'd

Tubic 02.1 0	Jone						
Sample	D178_R15	D178_R21	D178_R25	D178_R27	D178_R28	D178_R29	D178_R30
Seamount	Taney-C						
SiO ₂	50.0	49.9	50.4	50.0	50.5	50.3	49.9
TiO ₂	1.60	1.65	1.66	1.62	1.92	1.56	1.72
Al_2O_3	15.4	14.6	14.6	14.9	14.1	15.0	14.5
FeO⊤	10.4	11.4	11.2	10.8	12.5	10.8	11.6
MnO	0.186	0.207	0.208	0.185	0.220	0.196	0.208
MgO	7.51	7.30	7.16	7.09	6.10	7.12	6.62
CaO	11.8	12.0	12.1	12.2	11.0	12.2	11.8
Na ₂ O	2.93	2.94	2.97	2.82	3.29	2.84	3.04
K ₂ O	0.167	0.131	0.122	0.137	0.168	0.129	0.133
P_2O_5	0.188	0.168	0.168	0.177	0.193	0.167	0.178
SO₃	0.119	0.147	0.138	0.123	0.158	0.131	0.138
CI	0.051	0.011	0.020	0.021	0.024	0.013	0.015
Total	100.4	100.5	100.7	100.1	100.2	100.5	99.9

Table S2.1 cont'd

Sample D178_R31 D178_R32 D178_R35 D178_R36 Seamount Taney-C Taney-C Taney-C Taney-C SiO2 50.3 49.3 49.9 50.1 TiO2 1.56 1.29 1.72 1.67 Al ₂ O3 15.0 16.0 14.5 14.9 FeO _T 10.8 11.1 11.6 11.0 MnO 0.196 0.186 0.208 0.186 MgO 7.50 8.14 6.97 7.38 CaO 12.2 11.9 11.8 12.1 Na ₂ O 2.84 2.64 3.04 2.95 K ₂ O 0.129 0.076 0.133 0.132 P ₂ O ₅ 0.167 0.116 0.178 0.180 SO ₃ 0.131 0.117 0.138 0.142 Cl 0.013 0.018 0.015 0.022 Total 100.9 101.0 100.3 100.7					
SiO2 50.3 49.3 49.9 50.1 TiO2 1.56 1.29 1.72 1.67 Al2O3 15.0 16.0 14.5 14.9 FeOT 10.8 11.1 11.6 11.0 MnO 0.196 0.186 0.208 0.186 MgO 7.50 8.14 6.97 7.38 CaO 12.2 11.9 11.8 12.1 Na2O 2.84 2.64 3.04 2.95 K2O 0.129 0.076 0.133 0.132 P2O5 0.167 0.116 0.178 0.180 SO3 0.131 0.117 0.138 0.142 CI 0.013 0.018 0.015 0.022	Sample	D178_R31	D178_R32	D178_R35	D178_R36
$\begin{array}{cccccccccccccccccccccccccccccccccccc$	Seamount	Taney-C	Taney-C	Taney-C	Taney-C
$\begin{array}{cccccccccccccccccccccccccccccccccccc$	SiO ₂	50.3	49.3	49.9	50.1
FeO _T 10.8 11.1 11.6 11.0 MnO 0.196 0.186 0.208 0.186 MgO 7.50 8.14 6.97 7.38 CaO 12.2 11.9 11.8 12.1 Na ₂ O 2.84 2.64 3.04 2.95 K ₂ O 0.129 0.076 0.133 0.132 P ₂ O ₅ 0.167 0.116 0.178 0.180 SO ₃ 0.131 0.117 0.138 0.142 CI 0.013 0.018 0.015 0.022	TiO ₂	1.56	1.29	1.72	1.67
MnO 0.196 0.186 0.208 0.186 MgO 7.50 8.14 6.97 7.38 CaO 12.2 11.9 11.8 12.1 Na ₂ O 2.84 2.64 3.04 2.95 K ₂ O 0.129 0.076 0.133 0.132 P ₂ O ₅ 0.167 0.116 0.178 0.180 SO ₃ 0.131 0.117 0.138 0.142 CI 0.013 0.018 0.015 0.022	Al_2O_3	15.0	16.0	14.5	14.9
$\begin{array}{cccccccccccccccccccccccccccccccccccc$	FeO _⊤	10.8	11.1	11.6	11.0
CaO 12.2 11.9 11.8 12.1 Na ₂ O 2.84 2.64 3.04 2.95 K ₂ O 0.129 0.076 0.133 0.132 P ₂ O ₅ 0.167 0.116 0.178 0.180 SO ₃ 0.131 0.117 0.138 0.142 Cl 0.013 0.018 0.015 0.022	MnO	0.196	0.186	0.208	0.186
$\begin{array}{cccccccccccccccccccccccccccccccccccc$	MgO	7.50	8.14	6.97	7.38
$ \begin{array}{cccccccccccccccccccccccccccccccccccc$	CaO	12.2	11.9	11.8	12.1
P2O5 0.167 0.116 0.178 0.180 SO3 0.131 0.117 0.138 0.142 CI 0.013 0.018 0.015 0.022	Na ₂ O	2.84	2.64	3.04	2.95
SO3 0.131 0.117 0.138 0.142 CI 0.013 0.018 0.015 0.022	K_2O	0.129	0.076	0.133	0.132
Cl 0.013 0.018 0.015 0.022	P_2O_5	0.167	0.116	0.178	0.180
	SO ₃	0.131	0.117	0.138	0.142
Total 100.9 101.0 100.3 100.7	CI	0.013	0.018	0.015	0.022
	Total	100.9	101.0	100.3	100.7

Sample	D174_R1	D174_R3	D174_R4	D174_R5	D174_R8	D174_R10	D174_R16	D174_R19
Relative Chronology	Post-caldera C3 infill	Post-caldera C3 infill	Post-caldera C3 infill	Post-caldera C3 infill	Pillow cone (wall)	Pillow cone (wall)	Pillow cone (wall)	Post-caldera C2 infill
Sample Type	Talus	Pillow fragment	Pillow fragment	Pillow fragment	Pillow fragment	Pillow fragment	Pillow fragment	Pillow fragment
Lat (°N)	36.845	36.846	36.846	36.847	36.849	36.850	36.850	36.850
Long (°W)	-125.580	-125.581	-125.581	-125.581	-125.584	-125.586	-125.589	-125.59
Water Depth (m)	2951	2894	2892	2884	1828	2844	2842	2832
SiO ₂	46.48	50.27	49.44	49.86	47.73	47.18	48.16	48.41
TiO ₂	2.500	1.728	1.667	1.698	1.360	1.235	1.215	2.029
Al_2O_3	14.76	16.55	15.79	16.67	19.78	19.54	18.00	15.44
FeO _T	9.89	7.30	8.29	6.93	6.47	5.98	8.78	10.90
MnO	0.289	0.129	0.142	0.130	0.375	0.243	0.161	0.178
MgO	4.51	5.47	5.62	5.35	2.61	3.03	5.24	5.35
CaO	13.81	13.25	13.32	13.74	14.66	15.68	12.46	11.42
Na₂O	3.09	3.07	2.99	3.08	2.78	2.72	2.63	2.90
K₂O	0.36	0.20	0.25	0.22	0.34	0.28	0.25	0.39
P_2O_5	2.100	0.612	0.959	0.849	1.271	1.898	0.157	0.333
Total	97.78	98.58	98.48	98.51	97.38	97.77	97.04	97.35
La	16.86	15.94	11.78	7.46	5.76	18.63	4.56	7.26
Ce	23.63	16.76	18.23	16.25	11.87	11.38	10.35	19.00
Pr	4.21	3.73	3.15	2.63	1.99	2.90	1.74	2.97
Nd	20.63	18.30	15.46	13.23	10.20	14.15	8.87	15.19
Sm	6.23	5.25	4.62	4.22	3.25	3.76	2.92	4.81
Eu	2.29	1.88	1.78	1.64	1.34	1.46	1.22	1.80
Gd	7.67	6.66	5.91	5.22	4.26	5.30	3.75	5.79
Tb	1.33	1.14	1.02	0.92	0.77	0.91	0.67	1.01
Dy	8.44	7.28	6.41	5.83	5.02	6.28	4.33	6.47
Но	1.77	1.55	1.32	1.18	1.05	1.43	0.90	1.31
Er	4.82	4.23	3.53	3.16	2.90	4.06	2.39	3.46
Tm	0.68	0.59	0.49	0.45	0.41	0.58	0.35	0.49
Yb	4.15	3.55	2.93	2.70	2.53	3.59	2.12	2.97
Lu	0.66	0.58	0.45	0.42	0.41	0.59	0.33	0.45
Cr*	68	45	46	50	78	67	63	62
Ni*	109	278	270	278	290	281	272	182
Sc	43.7	45.0	42.3	43.8	40.6	36.5	35.1	37.2
Ва	114	33	400	34	88	69	21	27
Rb	4.7	1.7	3.5	2.2	3.7	3.3	6.1	8.6
Sr	289	243	282	256	266	298	208	213
Hf	4.06	2.91	2.77	2.88	1.96	1.73	1.92	3.35
Nb	9.23	6.16	5.94	6.07	3.07	2.79	3.33	7.68
Та	0.63	0.44	0.41	0.42	0.23	0.20	0.23	0.52
Th	0.61	0.45	0.44	0.44	0.26	0.24	0.22	0.51
Υ	52.83	48.36	37.87	30.78	28.08	52.40	23.08	32.46
Zr	142	106	103	101	76	67	74	125

Notes: Major elements determined by XRF and expressed in oxide weight per cent, trace elements determined by ICP-MS and XRF (Ni*, Cr*) and expressed in ppm.

Table S2.2 cont'd

Sample	D174 R21	D175_R1	D175R6	D175R7	D175R8	D175R19	D175R20	D175R22
Relative								Constructional
Chronology	Post-caldera C2 infill	Post-caldera C2 infill	Post-caldera C2 infill	Post-caldera C1 infill	Post-caldera C1 infill	Post-caldera C1 infill	Post-caldera C1 infill	edifice (caldera wall)
Sample Type	Pillow fragment	Talus	Talus	Pillow fragment	Pillow fragment	Talus	Talus	Pillow fragment
Lat (°N)	36.848	36.844	36.843	36.843	36.843	36.840	36.839	36.840
Long (°W)	-125.594	-125.597	-125.598	-125.598	-125.598	-125.606	-125.606	-125.606
Water Depth (m)	2819	2765	2698	2666	2666	2528	2527	2576
SiO ₂	48.05	49.67	46.68	48.48	49.38	48.21	48.70	48.19
TiO ₂	1.978	1.563	2.026	1.626	1.724	1.626	1.679	2.142
Al_2O_3	16.13	16.03	15.55	15.56	15.74	16.64	16.66	15.15
FeO⊤	9.97	8.31	10.87	9.13	9.12	7.61	7.61	8.44
MnO	0.242	0.217	0.329	0.147	0.130	0.856	0.246	0.161
MgO	4.67	5.60	4.70	5.52	5.65	4.54	4.81	4.84
CaO	12.32	13.15	12.72	13.64	12.70	13.35	13.46	14.14
Na ₂ O	2.92	2.94	3.05	2.81	3.06	2.98	3.03	3.23
K₂O	0.30	0.24	0.34	0.26	0.29	0.26	0.19	0.24
P ₂ O ₅	0.760	0.377	1.279	0.916	0.617	1.012	0.972	1.794
Total	97.33	98.09	97.56	98.09	98.41	97.08	97.36	98.32
La	7.28	6.15	16.05	7.38	10.85	11.23	8.74	9.71
Ce	18.43	14.70	20.09	15.50	15.53	16.77	16.49	21.53
Pr	2.93	2.32	3.98	2.48	2.74	2.93	2.74	3.38
Nd	14.71	11.71	19.35	12.56	13.79	14.39	13.43	16.96
Sm	4.75	3.78	5.50	3.84	4.34	4.26	4.06	5.23
Eu	1.80	1.47	2.03	1.53	1.63	1.61	1.58	1.94
Gd	5.67	4.59	6.99	4.78	5.31	5.20	5.03	6.16
Tb	1.00	0.81	1.21	0.82	0.94	0.90	0.87	1.06
Dy	6.30	5.10	7.59	5.26	5.96	5.71	5.39	6.69
Ho	1.28	1.04	1.61	1.09	1.27	1.19	1.12	1.36
Er	3.46	2.76	4.35	2.99	3.47	3.24	3.04	3.65
Tm	0.49	0.39	0.63	0.41	0.48	0.45	0.43	0.52
Yb	2.92	2.33	3.73	2.50	2.91	2.77	2.62	3.10
Lu	0.45	0.35	0.61	0.40	0.47	0.44	0.42	0.49
Cr*	66	73	94	40	51	122	103	39
Ni*	176	325	191	313	272	259	264	102
Sc	36.0	44.3	41.4	42.5	39.4	36.4	39.7	43.9
Ва	77	38	61	26	28	258	66	60
Rb	5.0	4.5	5.7	5.5	5.5	4.2	2.2	2.7
Sr	238	235	287	249	227	290	297	327
Hf	3.25	2.51	3.37	2.58	2.78	2.67	2.75	3.64
Nb	7.34	5.84	7.66	6.13	5.95	6.16	6.27	8.61
Ta	0.50	0.40	0.54	0.41	0.40	0.43	0.42	0.59
Th	0.49	0.36	0.52	0.40	0.40	0.45	0.41	0.56
Y	32.23	26.16	48.90	29.10	38.11	35.83	31.74	36.08
Zr	121	92	127	97	102	102	106	133
	141	J <u>Z</u>	141		102	102	100	100

Table S2.2 cont'd

Table S2.2 cont'd	D	D	D		D. 1 == D. 10	D.1==D.10	D. (= 0 D. (
Sample Relative	D175R25	D175R32	D175R34	D175R40	D175R42	D175R46	D176R4	D176R14
Chronology	Constructiona I edifice (caldera wall)	Constructional edifice (caldera wall)	Pillow cone (floor)	Pillow cone (floor)				
Sample Type	Pillow fragment	Pillow fragment	Pillow fragment	Pillow fragment	Pillow fragment	Pillow fragment	Pillow fragment	Pillow fragment
Lat (°N)	36.839	36.839	36.839	36.84	36.841	36.845	36.829	36.832
Long (°W)	-125.608	-125.609	-125.610	-125.613	-125.614	-125.616	-125.558	-125.559
Water Depth (m)	2400	2243	2205	2136	2173	2235	3155	3105
SiO ₂	49.93	50.61	49.94	47.12	47.14	49.42	48.04	47.59
TiO ₂	2.214	2.413	2.244	2.126	2.064	2.204	1.252	1.133
Al_2O_3	15.74	16.05	15.95	15.13	14.56	14.77	19.74	20.35
FeO⊤	8.36	7.91	9.39	8.71	9.82	10.62	8.20	7.73
MnO	0.572	0.154	0.192	0.906	0.579	0.182	0.167	0.123
MgO	4.98	4.81	4.86	4.49	5.11	5.47	4.50	4.66
CaO	12.06	12.61	12.24	13.79	13.10	11.50	12.88	12.75
Na₂O	3.25	3.41	3.29	3.12	3.08	3.17	2.61	2.41
K₂O	0.21	0.28	0.25	0.27	0.39	0.42	0.24	0.26
P_2O_5	0.249	0.546	0.376	1.707	1.532	0.352	0.151	0.118
Total	97.56	98.78	98.72	97.37	97.37	98.10	97.77	97.14
La	10.88	9.11	13.26	12.33	14.84	10.37	4.52	4.33
Ce	22.23	23.46	21.45	20.75	19.97	21.02	11.92	10.64
Pr	4.03	3.71	4.38	3.51	4.17	3.75	1.87	1.71
Nd	20.18	18.77	21.71	17.51	21.29	18.83	9.39	8.50
Sm	6.08	5.87	6.50	5.44	6.07	5.73	2.98	2.81
Eu	2.22	2.19	2.31	2.02	2.29	2.14	1.21	1.11
Gd	7.48	7.10	8.10	6.73	8.24	7.00	3.76	3.43
Tb	1.26	1.22	1.37	1.17	1.35	1.20	0.67	0.61
Dy	7.86	7.76	8.58	7.43	8.73	7.41	4.25	3.97
Ho	1.59	1.57	1.78	1.57	1.92	1.51	0.86	0.81
Er	4.19	4.21	4.80	4.36	5.41	3.97	2.32	2.20
Tm	0.56	0.58	0.67	0.62	0.76	0.55	0.33	0.31
Yb	3.41	3.57	3.94	3.92	4.56	3.32	2.03	1.87
Lu	0.53	0.55	0.61	0.63	0.78	0.52	0.32	0.30
Cr*	91	30	45	274	105	52	66	55
Ni*	124	117	151	150	140	111	207	196
Sc	45.8	46.4	45.7	43.7	42.4	43.0	30.3	28.3
Ва	93	41	41	1129	127	38	57	56
Rb	2.9	2.2	3.3	4.3	15.5	10.8	4.6	5.8
Sr	260	269	252	383	291	240	233	229
Hf	3.66	4.01	3.70	3.49	3.44	3.67	2.06	1.87
Nb	7.37	9.31	7.92	7.35	7.63	8.45	4.30	3.80
Та	0.57	0.64	0.57	0.55	0.53	0.58	0.30	0.27
Th	0.55	0.59	0.56	0.53	0.52	0.56	0.33	0.28
Y	40.07	39.11	49.11	49.29	72.09	39.36	21.75	20.36
Zr	122	152	130	120	125	136	77	70

Table S2.2 cont'd

Sample	D176-R15	D176R16	D176R17	D176R21	D176R25	D177R11	D177R14
Relative Chronology	Pillow cone (floor)	Constructional edifice (caldera wall)	Constructional edifice (caldera wall)				
Sample Type	Pillow fragment	Pillow fragment	Pillow fragment	Pillow fragment	Pillow fragment	Pillow fragment	Pillow fragment
Lat (°N)	36.834	36.834	36.837	36.838	36.845	36.851	36.853
Long (°W)	-125.558	-125.558	-125.558	-125.553	-125.553	-125.611	-125.616
Water Depth (m)	3042	3039	3148	3020	3030	2487	2333
SiO ₂	47.73	47.66	48.24	47.94	47.36	48.48	49.47
TiO ₂	1.161	1.104	1.316	1.197	1.189	2.121	2.156
Al_2O_3	19.82	20.27	18.34	19.14	18.74	14.43	14.85
FeO⊤	8.16	7.52	8.33	8.13	10.30	10.23	9.89
MnO	0.118	0.105	0.234	0.190	0.147	0.285	0.251
MgO	5.16	5.14	5.19	5.28	4.16	5.41	5.33
CaO	12.48	12.61	12.37	12.34	12.34	12.15	11.80
Na₂O	2.54	2.42	2.64	2.57	2.65	3.05	3.16
K₂O	0.30	0.26	0.25	0.29	0.24	0.54	0.60
P_2O_5	0.119	0.109	0.152	0.118	0.131	0.972	0.553
Total	97.58	97.21	97.07	97.19	97.27	97.67	98.06
La	4.21	3.92	5.08	4.08	4.51	16.96	21.77
Ce	10.65	10.16	12.15	10.97	8.03	21.53	20.69
Pr	1.72	1.64	1.98	1.74	1.52	4.04	4.92
Nd	8.76	8.25	9.98	8.82	8.03	20.02	24.03
Sm	2.80	2.69	3.21	2.86	2.80	5.61	6.59
Eu	1.13	1.09	1.27	1.16	1.17	2.10	2.35
Gd	3.56	3.31	4.01	3.64	3.90	7.33	8.49
Tb	0.64	0.60	0.72	0.64	0.73	1.22	1.42
Dy	4.04	3.85	4.57	4.06	4.79	7.75	9.17
Ho	0.85	0.78	0.94	0.85	1.00	1.62	1.98
Er	2.24	2.13	2.52	2.30	2.77	4.39	5.42
Tm	0.32	0.29	0.36	0.32	0.40	0.62	0.77
Yb	1.97	1.84	2.23	1.99	2.47	3.73	4.66
Lu	0.30	0.28	0.35	0.31	0.39	0.59	0.76
Cr*	64	71	91	71	85	48	102
Ni*	209	199	227	217	231	122	126
Sc	29.5	28.1	33.7	30.0	36.4	42.5	44.4
Ва	48	117	62	485	24	95	385
Rb	6.5	5.9	4.3	6.1	4.5	17.0	16.0
Sr	210	228	217	249	180	261	273
Hf	1.90	1.79	2.14	1.95	1.74	3.54	3.58
Nb	3.80	3.60	4.24	3.90	2.44	8.07	7.97
Та	0.26	0.24	0.29	0.26	0.17	0.54	0.56
Th	0.26	0.32	0.29	0.28	0.17	0.55	0.52
Υ	21.14	19.71	24.18	21.11	26.95	50.43	64.37
Zr	71	68	80	73	61	133	132

Table S2.3: Major and trace element data for whole rocks from Taney Seamounts-B and C

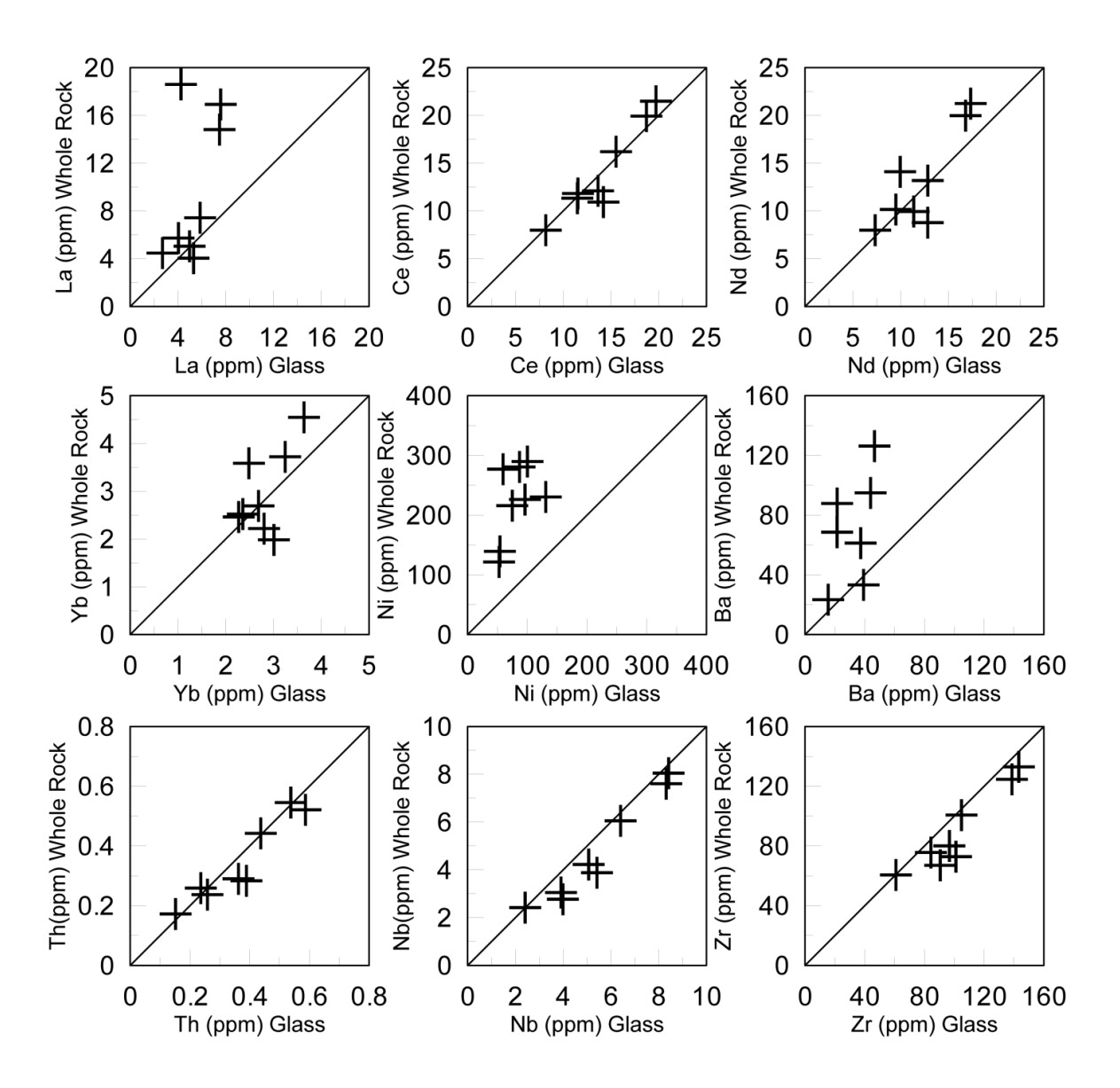
Sample	D173-R9	D173-R14	D178R4	D178R7	D178R8	D178R9	D178R10	D178R13
Seamount	Taney - B	Taney - B	Taney - C					
SiO ₂	47.78	49.23	48.48	48.08	49.96	49.05	48.33	49.07
TiO ₂	1.809	1.723	2.086	2.066	1.626	1.590	1.417	1.443
Al_2O_3	14.90	14.78	14.71	14.04	15.00	14.67	14.86	15.27
FeO⊤	11.17	9.70	10.62	11.02	10.35	10.70	9.80	9.41
MnO	0.164	0.264	0.276	0.235	0.171	0.370	0.856	0.212
MgO	4.40	5.72	5.00	5.52	5.93	5.91	6.65	5.85
CaO	12.39	12.63	12.43	12.17	12.27	12.06	12.36	13.16
Na₂O	2.96	3.07	3.17	3.00	3.03	2.92	2.82	2.67
K ₂ O	0.40	0.26	0.26	0.35	0.25	0.42	0.21	0.29
P_2O_5	0.733	0.710	0.935	1.032	0.200	0.204	0.263	0.272
Total	96.71	98.09	97.96	97.51	98.77	97.90	97.56	97.63
La	5.97	6.66	8.64	6.80	4.91	6.37	4.79	7.60
Ce	15.01	13.78	17.48	17.49	12.75	12.39	10.68	10.62
Pr	2.50	2.37	3.01	2.91	2.18	2.30	1.88	2.18
Nd	12.77	12.30	15.56	15.05	11.50	12.06	10.03	11.26
Sm	4.30	4.11	5.15	5.13	3.90	4.02	3.51	3.75
Eu	1.67	1.62	1.95	1.92	1.55	1.52	1.38	1.40
Gd	5.54	5.41	6.93	6.66	5.32	5.36	4.69	5.15
Tb	1.01	0.99	1.26	1.23	0.96	0.97	0.87	0.92
Dy	6.36	6.32	8.18	7.95	6.33	6.35	5.71	6.10
Но	1.34	1.33	1.76	1.64	1.32	1.33	1.21	1.30
Er	3.65	3.64	4.77	4.52	3.61	3.62	3.28	3.55
Tm	0.53	0.52	0.71	0.66	0.53	0.52	0.47	0.50
Yb	3.17	3.20	4.33	3.99	3.17	3.14	2.91	3.05
Lu	0.49	0.50	0.69	0.64	0.49	0.50	0.45	0.48
Cr*	51	90	49	54	68	68	81	54
Ni*	121	241	105	98	119	117	269	289
Sc	48.3	50.3	46.0	43.5	45.4	44.5	47.6	48.9
Ва	20	52	54	32	18	52	139	19
Rb	8.6	3.9	5.3	12.4	4.3	11.0	5.8	7.4
Sr	194	196	211	208	167	167	163	163
Hf	2.90	2.71	3.52	3.51	2.70	2.58	2.29	2.30
Nb	5.01	4.71	5.01	5.29	3.45	3.39	2.64	2.63
Та	0.35	0.32	0.36	0.37	0.24	0.23	0.18	0.18
Th	0.36	0.32	0.40	0.38	0.24	0.23	0.18	0.18
Υ	34.30	35.14	48.22	42.32	33.39	35.26	31.89	36.57
Zr	107	96	124	131	98	95	85	85

Notes: Major elements determined by XRF and expressed in oxide weight per cent, trace elements determined by ICP-MS and XRF (Ni^* , Cr^*) and expressed in ppm.

Table S2.3 cont'd

Table S2.3			B (=====	D. (=0.0.5.)	D. (=0.0.5.)	B. (=0.0.5 -	D. (=0.D.c.)	
Sample	D178R15	D178R16	D178R19	D178R20	D178R26	D178R30	D178R31	D178R38
Seamount	Taney - C	Taney - C	Taney - C	Taney - C	Taney - C	Taney - C	Taney - C	Taney - C
SiO_2	49.50	49.86	49.51	49.07	49.39	50.11	49.00	49.09
TiO ₂	1.466	1.698	1.678	1.623	2.102	1.972	1.600	1.760
Al_2O_3	15.47	15.50	14.57	14.62	14.24	14.65	14.87	15.32
FeO⊤	7.80	9.62	10.44	10.90	11.07	10.92	10.63	10.68
MnO	0.138	0.342	0.181	0.164	0.167	0.209	0.161	0.171
MgO	6.28	5.47	6.23	6.23	5.63	5.53	6.11	5.59
CaO	13.72	12.96	12.04	11.89	11.35	11.64	12.13	12.54
Na₂O	2.85	3.04	2.98	2.87	3.30	3.26	2.83	3.26
K₂O	0.20	0.20	0.28	0.27	0.29	0.29	0.34	0.25
P_2O_5	0.649	0.332	0.184	0.150	0.517	0.324	0.152	0.630
Total	98.08	99.02	98.10	97.79	98.05	98.91	97.81	99.29
La	9.47	4.62	4.85	5.84	7.13	5.71	4.39	10.81
Ce	11.29	12.98	12.92	12.62	17.76	16.01	12.44	13.98
Pr	2.40	2.21	2.20	2.36	2.93	2.69	2.07	3.01
Nd	12.38	11.56	11.68	12.47	15.31	14.08	10.78	15.20
Sm	3.99	3.94	4.18	4.09	5.11	4.79	3.69	4.80
Eu	1.51	1.56	1.56	1.59	1.92	1.83	1.43	1.82
Gd	5.50	5.32	5.46	5.57	6.77	6.37	4.83	6.52
Tb	1.00	0.98	1.00	1.01	1.23	1.16	0.91	1.17
Dy	6.55	6.45	6.56	6.65	8.00	7.63	5.94	7.90
Но	1.44	1.35	1.38	1.41	1.69	1.62	1.23	1.70
Er	4.00	3.69	3.80	3.84	4.67	4.37	3.38	4.74
Tm	0.57	0.53	0.54	0.55	0.67	0.64	0.49	0.68
Yb	3.51	3.23	3.33	3.27	4.08	3.92	2.89	4.24
Lu	0.56	0.51	0.52	0.51	0.64	0.60	0.44	0.66
Cr*	76	77	57	54	39	58	55	55
Ni*	285	119	137	136	98	34	175	131
Sc	49.7	46.7	48.0	46.3	43.4	47.4	42.6	49.0
Ва	14	100	23	16	30	23	16	46
Rb	7.3	4.2	6.7	7.0	5.5	6.1	7.8	5.0
Sr	181	168	163	156	184	174	156	191
Hf	2.41	2.70	2.77	2.63	3.57	3.31	2.55	2.88
Nb	2.71	3.49	3.55	3.48	5.33	4.46	3.55	3.82
Та	0.19	0.24	0.24	0.24	0.37	0.31	0.25	0.27
Th	0.20	0.25	0.25	0.23	0.39	0.32	0.25	0.27
Υ	43.25	34.16	35.15	35.79	43.44	41.07	30.75	49.60
Zr	87	98	101	97	130	121	96	106

Figure S2.1: Comparison between glass and whole-rock trace element analyses. Some whole-rock samples exhibit phosphate alteration which also affects some of the trace elements. Based on the comparison of whole-rock and glass analyses from the same sample, the elements which are most resistant to secondary processes are the high field strength elements (HFSE) including Th, Nb, Zr.



Supplementary Information S3: Volatile data from SIMS microprobe.

Measured water concentrations were corrected for instrumental drift by repeat analyses of our in-house standard P1326-2 throughout the analytical duration (Fig S3.1). Post-entrapment crystallization of plagioclase affects the chemical composition of melt inclusions and can be observed by their perturbation from the olivine-plagioclase cotectic (Fig S3.2 a, b). Melt inclusion compositions were corrected by adding plagioclase numerically to a linear regressed olivine-plagioclase cotectic. We define the olivine-plagioclase cotectic using East Pacific Rise and Mid-Atlantic Ridge data from the Smithsonian Volcanic Glass File (Melson *et al.*, 2002), and rehomogenized melt inclusions in anorthite crystals (An₈₂₋₉₀) from the Lamont Seamount chain (Nielsen, 2011). The melt inclusions were corrected to the minimum variance from the regressed MgO-Al₂O₃ and MgO-FeO_T olivine-plagioclase cotectics by addition of the plagioclase composition <100 μm from each inclusion (Fig S3.3 c, d). The amount of post-entrapment crystallization was determined by the lever rule.

Volatile elements were corrected by using the standard Rayleigh fractionation equation:

$$C_{liq}^{i} = C_{liq}^{0} F^{(k_d - 1)}$$
 (1)

where for a given element C_{liq}^{i} is the concentration in the liquid at a fraction F of liquid remaining after post-entrapment crystallization determined by lever rule, C_{liq}^{0} is the concentration in the liquid at entrapment, and K_d is the plagiclase-melt partition coefficient. We assume partition coefficients between plagioclase and melt for H_2O and CO_2 are the same as lithophile elements with similar incompatibility (Ce and Nb, respectively). The partition coefficients utilized are from Aigner-Torres *et al.*, (2007) and Tepley *et al.*, (2010). The corrected melt inclusion volatile compositions are shown in Table S3.1.

Table S3.1: Corrected volatile concentrations for plagioclase melt inclusions and host volcanic glass

Sample	Type	Post-entrapment crystallization (%)	CO ₂ (ppm)	H ₂ O (wt. %)
D176 R3 1 2	Melt Inclusion	9	1904	0.32
D176 R3 2 1	Melt Inclusion	0	617	0.38
D176 R3 3 1	Melt Inclusion	10	1278	0.29
D176 R3 3 2	Melt Inclusion	14	3550	0.28
D176 R3 6 1	Melt Inclusion	9	1204	0.33
D176 R3 9 1	Melt Inclusion	6	1298	0.33
D176 R17 1 1	Melt Inclusion	9	3939	0.25
D176 R17 3 1	Melt Inclusion	5	1271	0.30
D176 R17 12 1	Melt Inclusion	8	1144	0.28
D176 R17 13 3	Melt Inclusion	0	1946	0.32
D176 R20 1 1	Melt Inclusion	11	1417	0.31
D176 R20 3 1	Melt Inclusion	5	1257	0.29
D176 R20 11 2	Melt Inclusion	12	1193	0.30
D176 R20 11 4	Melt Inclusion	11	1789	0.33
D176_R20_11_5	Melt Inclusion	11	1262	0.32
D176 R20 14 1	Melt Inclusion	14	1334	0.28
D176 R20 14 2	Melt Inclusion	15	1160	0.29
D176 R20 14 5	Melt Inclusion	15	1104	0.29
D176 R20 20 1	Melt Inclusion	0	1261	0.34
D176 R20 20 1a	Melt Inclusion	0	1623	0.36
D176_R3	Matrix Glass		124	0.40
D176_R17	Matrix Glass		92	0.33
D176_R20	Matrix Glass		89	0.34
D176_R24	Matrix Glass		142	0.23

Figure S3.1: The water concentrations of P1326-2 exhibit a systematic drift, decreasing with elapsed time during analysis. The water concentration of P1326-2 is 0.26 wt. % determined by Fourier transform infrared spectroscopy (FTIR) at McGill University. Water concentrations of melt inclusions were corrected based on deviations of P1326-2 from the accepted value.

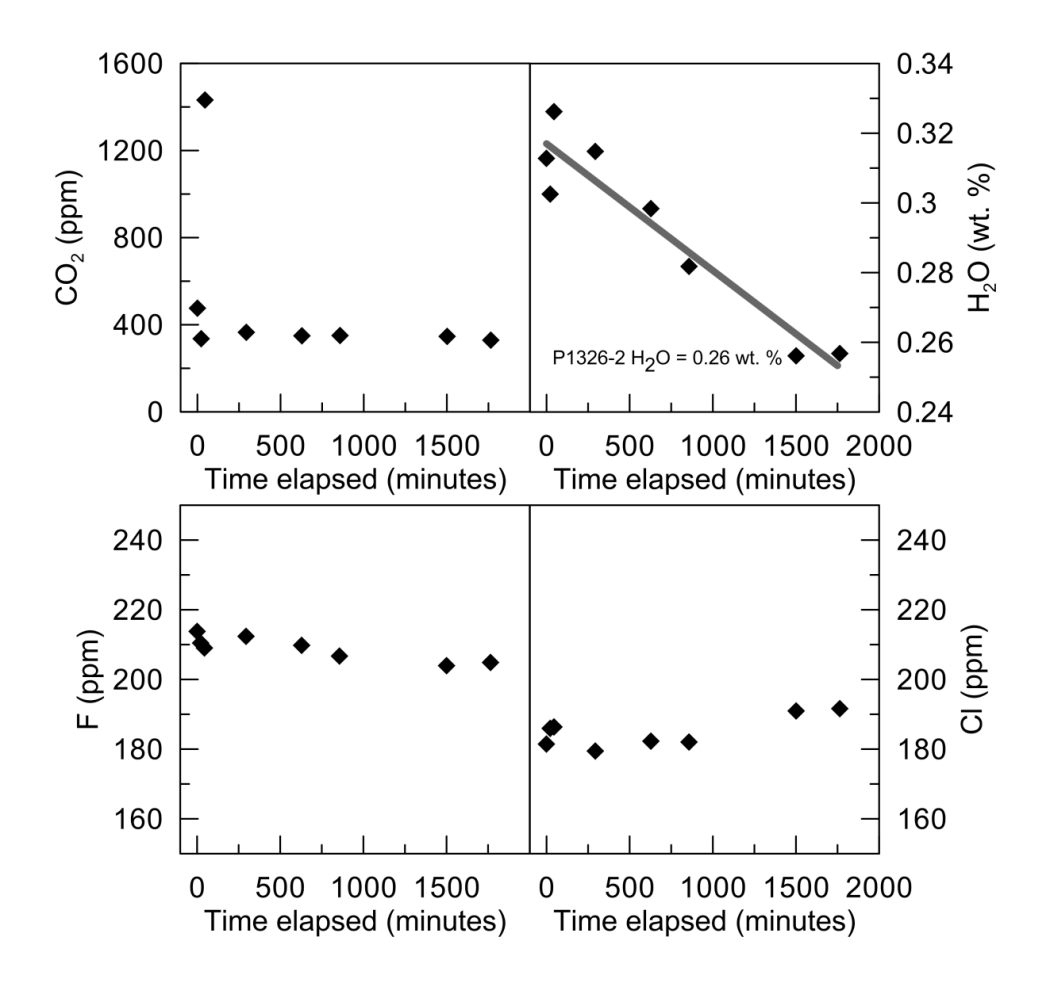


Figure S3.2: Regression of the Al₂O₃ and FeO_T olivine-plagioclase cotectic using lavas erupted at the East Pacific Rise, Mid-Atlantic Ridge, and rehomogenized melt inclusions in high-anorthite plagioclase from the Lamont Seamounts. (a, b) Melt inclusions from Taney Seamount-A deviate from the cotectic by crystallization of the host plagioclase. (c, d) Individual analyses were corrected by numerically adding plagioclase to the minimum variance from the Al₂O₃ and FeO_T cotectic.

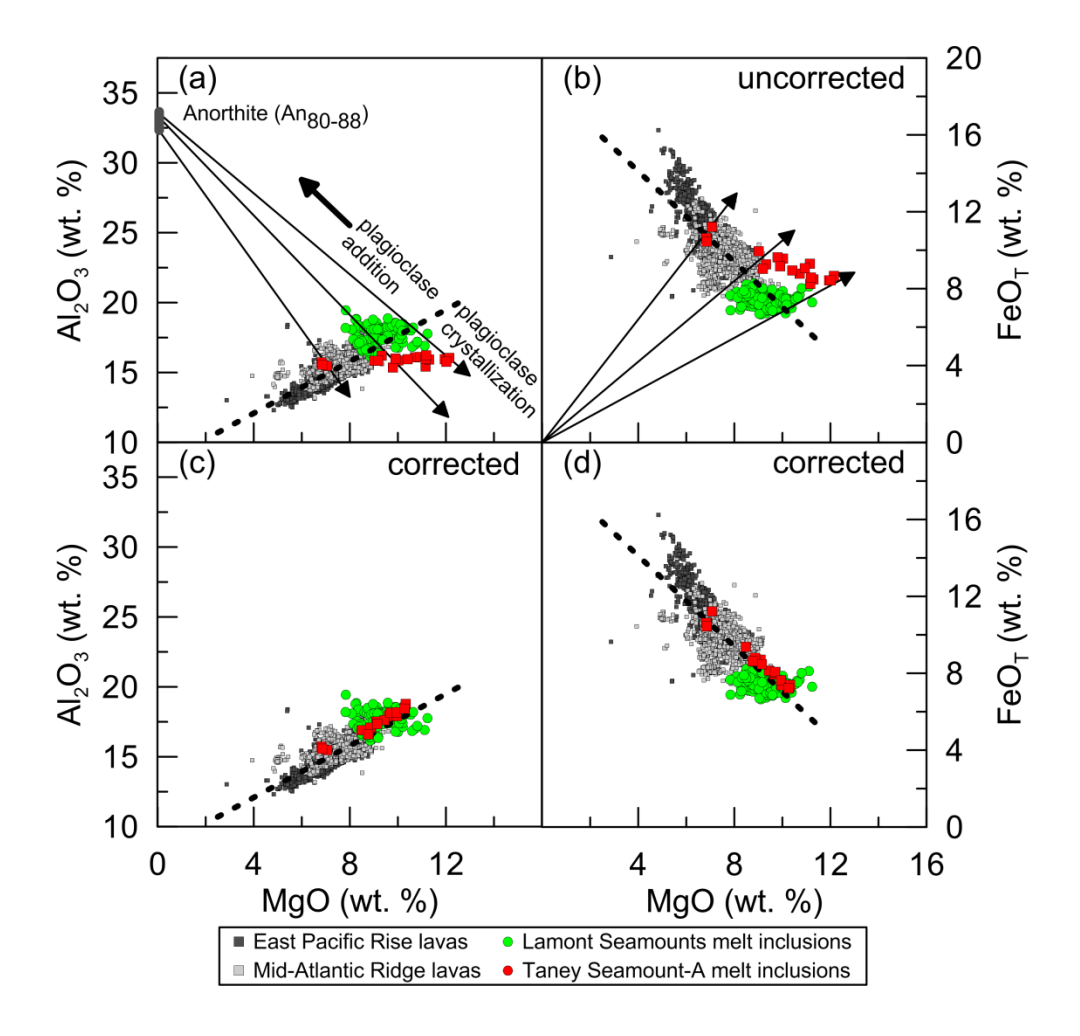
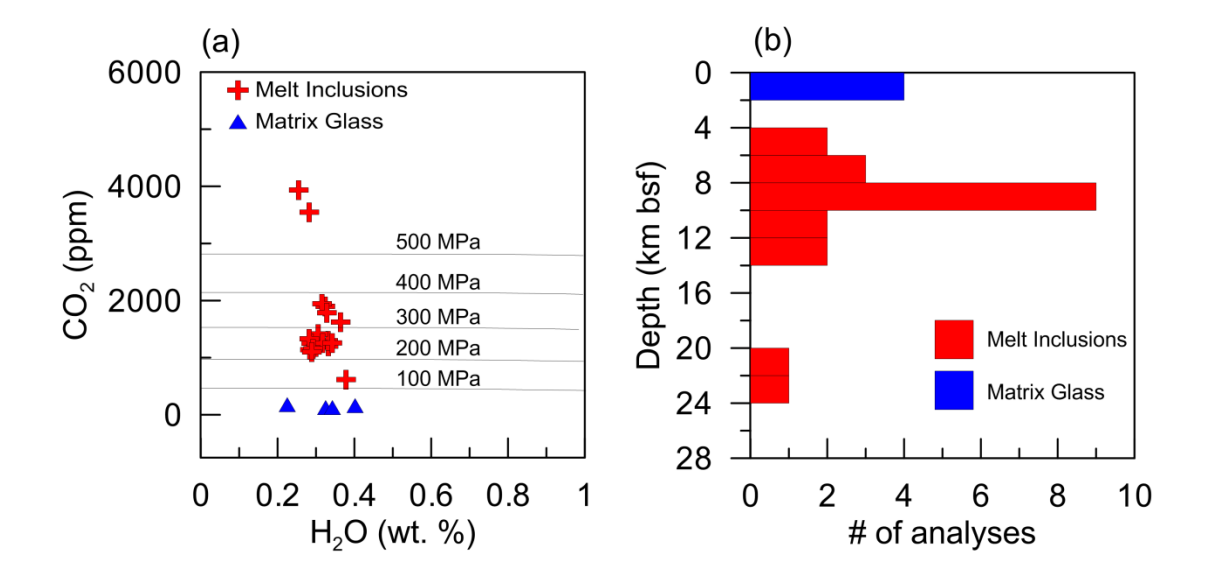


Figure S3.3: Dissolved CO₂ and H₂O contents in melt inclusions and host glasses, measured by secondary-ion mass spectrometry (SIMS). Volatile concentrations have been corrected for postentrapment crystallization (Table S3.1). Melt inclusions have calculated volatile saturation pressures which suggest crystallization depths within the lower oceanic crust or upper mantle. The matrix glasses are degassed in CO₂, due to their eruption on the seafloor.



Supplementary Information S4: Numerical model for diffusive exchange during percolation of melt through a plagioclase cumulate matrix.

Table S4.1: Mathematical model notation

Z	distance traversed along column (m) distance from center of grain
r	(m)
t	time (s)
Δz	change in distance (m)
Δr	change in distance from grain center (m)
Δt	change in time (s)
Н	height of the column (m)
R	grain size (m)
V_m	velocity of the melt (m s ⁻¹)
φ	porosity of the column
$ ho_r$	density of the solid phase (kg m ⁻³)
$ ho_m$	density of the melt phase (kg m ⁻³)
C_r	concentration of an element in the solid phase (ppm)
C_m	concentration of an element in the melt phase (ppm)
C_{r0}	initial concentration of an element in the solid phase (ppm)
C_{m0}	initial concentration of an element in the melt phase (ppm)
D_s	diffusion coefficient (m ² s ⁻¹)
K_d	solid-melt partition coefficient
K_{e}	effective solid-melt partition coefficient
$ au_{ma}$	melt advection timescale
$ au_{sd}$	solid diffusion timescale
D _a	Damkohler number

For one-dimensional melt percolation through a porous medium with a spherical matrix geometry, mass conservation of an element within the solid matrix $(0 \le r \le R)$ may be written as:

(1)
$$\frac{\partial C_r}{\partial t} = D_s \left(\frac{\partial^2 C_r}{\partial r^2} + \frac{2}{r} \frac{\partial C_r}{\partial r} \right)$$

The mass conservation of an element in the melt may be expressed as:

(2)
$$\frac{\partial C_m}{\partial t} + V_m \frac{\partial C_m}{\partial z} = -\frac{(1-\phi)}{\phi} K_d \frac{\rho_r}{\rho_m} \frac{\partial C_s}{\partial t} \text{ where, } \frac{\partial C_s}{\partial t} = \frac{3}{R^3} \frac{\partial}{\partial t} \left[\int_0^R C_r r^2 \partial r \right]$$

We assume that diffusion between solid grains is negligible and that the melt is homogenous at all times, which is justified because diffusion in the melt is six to seven orders of magnitude faster than in the solid (Navon and Stolper, 1987). This simplified model assumes that the diffusion and partition coefficients remain constant for $0 \le z \le H$. This model also assumes that the initial composition is constant for both the solid and melt phase for the entire column distance, z. The above equations are normalized with the following expressions:

(3)
$$t' = \frac{t}{H/V_m}, r' = \frac{r}{R}, C_r' = \frac{C_r}{C_{r0}}, C_m' = \frac{C_m}{C_{r0}}$$

where H is the vertical dimension of the system, V_m is the velocity of the percolating melt, r is the position within the grain $(0 \le r \le R)$, R is the grain size, and C_{r0} is the initial concentration in the solid. For modelling purposes, all concentrations $(C_r$ and $C_m)$ are normalized to the initial solid concentration (C_{r0}) . The non-dimensional equations used in this model are as follows:

(4)
$$\frac{\partial C_{m'}}{\partial t'} = D_{a} \left(\frac{\partial^{2} C_{m'}}{\partial r'^{2}} + \frac{2}{r'} \frac{\partial C_{m'}}{\partial r'} \right)$$

(5)
$$\frac{\partial C_{m'}}{\partial t'} + V_{m} \frac{\partial C_{m'}}{\partial z'} = -\frac{3}{R^{3}} \frac{\left(1 - \phi\right)}{\phi} K_{d} \frac{\rho_{r}}{\rho_{m}} \frac{\partial}{\partial t'} \left[\int_{0}^{1} C_{r'} r'^{2} \partial r' \right], R' = 1$$

where,
$$D_a = \frac{\tau_{ma}}{\tau_{sd}} = \frac{H/V_m}{R^2/D_s}$$

 D_a is the diffusion-controlled Damkohler number which is defined by the relative importance of the melt advection timescale (τ_{ma}) to the solid diffusion timescale (τ_{sd}). We utilize a Crank-Nicolson algorithm (Ames, 1977) in order to numerically solve the above set of equations. We use a $\Delta r' = 0.002$ grid size for the r-direction, and a normalized time step of $\Delta t' = 0.000001$. The numerical model was run with the following boundary and initial conditions:

$$C_{r}'(z',R',t') = K_{d}C_{m}'(z',t')$$

$$C_{r}'(z',0,t') = C_{r0}$$

$$\frac{\partial C_{r}'(z',0',t')}{\partial r'} = 0$$

$$C_{m}'(z',0) = C_{m0}'$$

$$C_{m}'(0,t') = C_{m0}'$$

$$\frac{\partial C_{m}'(0,t')}{\partial z'} = 0$$

The derivation of the discrete form of equation (4) for the Crank-Nicolson algorithm is as follows:

(6)
$$\frac{\partial U}{\partial t} = D_a \left(\frac{\partial^2 U}{\partial r^2} + \frac{2}{r} \frac{\partial U}{\partial r} \right) \text{ where } U = C_m$$

and,

$$\frac{\partial U}{\partial t} = \frac{U_i^{j+1} - U_i^{j-1}}{\Delta t},$$

$$\frac{\partial^2 U}{\partial r^2} = \frac{1}{2} \left\{ \frac{U_{i+1}^{j+1} - 2U_i^{j+1} + U_{i-1}^{j+1}}{\Delta r_2} + \frac{U_{i+1}^{j} - 2U_i^{j} + U_{i-1}^{j}}{\Delta r_2} \right\},$$

$$\frac{\partial U}{\partial r} = \frac{1}{2} \left\{ \frac{U_{i+1}^{j+1} - U_{i-1}^{j+1}}{2\Delta r} + \frac{U_{i+1}^{j} - U_{i-1}^{j}}{2\Delta r} \right\}$$

$$\frac{2}{r} = \frac{2}{\Delta r(i-1)}$$

Substitution of expressions (7) into equation (6) results in the following discretization:

(8)
$$\frac{U_{i}^{j+1} - U_{i}^{j}}{\Delta t} = \frac{1}{2} D_{a} \begin{cases} \frac{1}{\Delta r^{2}} \left(U_{i+1}^{j+1} - 2U_{i}^{j+1} + U_{i-1}^{j+1} + U_{i+1}^{j} - 2U_{i}^{j} + U_{i-1}^{j} \right) \\ + \frac{1}{\Delta r^{2} \left(i - 1 \right)} \left(U_{i+1}^{j+1} - U_{i-1}^{j+1} + U_{i+1}^{j} - U_{i-1}^{j} \right) \end{cases}$$

$$(9) \qquad U_{i}^{j+1} - U_{i}^{j} = Q \begin{cases} \left(U_{i+1}^{j+1} - 2U_{i}^{j+1} + U_{i-1}^{j+1} + U_{i+1}^{j} - 2U_{i}^{j} + U_{i-1}^{j} \right) \\ + \frac{1}{\left(i-1\right)} \left(U_{i+1}^{j+1} - U_{i-1}^{j+1} + U_{i+1}^{j} - U_{i-1}^{j} \right) \end{cases},$$

$$Q = \frac{D_{a} \Delta t}{2\Delta r^{2}}$$

$$(10) \quad 0 = QU_{i+1}^{j+1} + \frac{QU_{i+1}^{j+1}}{(i-1)} - 2QU_{i}^{j+1} - U_{i}^{j+1} + QU_{i-1}^{j+1} - Q\frac{U_{i-1}^{j+1}}{(i-1)} + QU_{i+1}^{j} + \frac{QU_{i+1}^{j}}{(i-1)} - 2QU_{i}^{j} - U_{i}^{j} + QU_{i-1}^{j} - Q\frac{U_{i-1}^{j}}{(i-1)}$$

(11)
$$0 = Q \left(1 + \frac{1}{i-1} \right) U_{i+1}^{j+1} - \left(2Q + 1 \right) U_{i}^{j} + Q \left(1 - \frac{1}{i-1} \right) U_{i-1}^{j+1}$$

$$+ Q \left(1 + \frac{1}{i-1} \right) U_{i+1}^{j} - \left(2Q + 1 \right) U_{i}^{j} + Q \left(1 - \frac{1}{i-1} \right) U_{i-1}^{j}$$

$$-\alpha U_{i-1}^{j+1} + \beta U_{i}^{j+1} - \gamma U_{i+1}^{j+1} = \alpha U_{i-1}^{j} - \beta U_{i}^{j} + \gamma U_{i+1}^{j}$$

$$\alpha = Q \left[1 - \frac{1}{i-1} \right]$$

$$\beta = 2Q + 1$$

$$\gamma = Q \left[1 + \frac{1}{i-1} \right]$$

Equation (12) can be expressed in tridiagonal matrix form with fixed boundary conditions allowing U_i^{j+1} to be solved by the use of the Thomas algorithm.

$$\begin{bmatrix} 1 & 0 & 0 & 0 & 0 \\ -\alpha & \beta & -\gamma & 0 & 0 \\ 0 & -\alpha & \beta & -\gamma & 0 \\ 0 & 0 & -\alpha & \beta & -\gamma \\ 0 & 0 & 0 & 0 & 1 \end{bmatrix} \begin{bmatrix} U_1^{j+1} \\ U_2^{j+1} \\ U_3^{j+1} \\ U_5^{j+1} \end{bmatrix} = \begin{bmatrix} 1 & 0 & 0 & 0 & 0 \\ \alpha & -\beta & \gamma & 0 & 0 \\ 0 & \alpha & -\beta & \gamma & 0 \\ 0 & 0 & \alpha & -\beta & \gamma \\ 0 & 0 & 0 & 0 & 1 \end{bmatrix} \begin{bmatrix} U_1^j \\ U_2^j \\ U_3^j \\ U_4^j \\ U_5^j \end{bmatrix}$$

Recall the relationship between the concentration in the solid and the concentration in the liquid:

(13)
$$\frac{\partial C_{m}'}{\partial t'} + \frac{\partial C_{m}'}{\partial z'} = K_{e} \frac{\partial A}{\partial t'}$$
where,
$$K_{e} = -\frac{3}{R^{3}} \frac{(1-\phi)}{\phi} K_{d} \frac{\rho_{r}}{\rho_{m}}, R' = 1$$

$$A = \int_{0}^{R'} C_{r}' r'^{2} \partial r'$$

"A" represents the area under the solid spherical geometry diffusion curves at a given time step calculated numerically from equation (4). The area can be computed numerically in Matlab using the "trapz" function. The discretization of the relationship is given below:

$$\begin{split} \frac{\partial G'}{\partial t'} &= K_{e} \frac{\partial A}{\partial t'} - \frac{\partial G'}{\partial z'}, G = C_{m}, \\ \frac{G_{i}^{j+1} - G_{i}^{j}}{\Delta t'} &= \frac{K_{e} A_{i}^{j+1} - K_{e} A_{i}^{j}}{\Delta t'} - \frac{1}{4\Delta z'} \left(-G_{i-1}^{j+1} + G_{i+1}^{j+1} - G_{i-1}^{j} + G_{i+1}^{j} \right), \\ (14) \qquad G_{i}^{j+1} - G_{i}^{j} &= K_{e} A_{i}^{j+1} - K_{e} A_{i}^{j} - \lambda \left(-G_{i-1}^{j+1} + G_{i+1}^{j+1} - G_{i-1}^{j} + G_{i+1}^{j} \right), \\ -\lambda G_{i-1}^{j+1} + G_{i}^{j+1} - K_{e} A_{i}^{j+1} + \lambda G_{i+1}^{j+1} &= \lambda G_{i-1}^{j} + G_{i}^{j} - K_{e} A_{i}^{j} - \lambda G_{i+1}^{j}, \\ \lambda &= \frac{\Delta t'}{4\Delta z'} \end{split}$$

Equation (14) can be expressed in tridiagonal matrix form with fixed boundary conditions allowing d_i^{j+1} , where $d_i^{j+1} = G_i^{j+1} - K_e A_i^{j+1}$, to be solved by the use of the Thomas algorithm.

$$\begin{bmatrix} 1 & 0 & 0 & 0 & 0 \\ -\lambda & 1 & \lambda & 0 & 0 \\ 0 & -\lambda & 1 & \lambda & 0 \\ 0 & 0 & -\lambda & 1 & \lambda \\ 0 & 0 & 0 & 0 & 1 \end{bmatrix} \begin{bmatrix} G_1^{j+1} - K_e A_1^{j+1} \\ G_2^{j+1} - K_e A_2^{j+1} \\ G_3^{j+1} - K_e A_3^{j+1} \\ G_4^{j+1} - K_e A_5^{j+1} \end{bmatrix} = \begin{bmatrix} 1 & 0 & 0 & 0 & 0 \\ \lambda & 1 & -\lambda & 0 & 0 \\ 0 & \lambda & 1 & -\lambda & 0 \\ 0 & 0 & \lambda & 1 & -\lambda \\ 0 & 0 & 0 & 0 & 1 \end{bmatrix} \begin{bmatrix} G_1^j - K_e A_1^j \\ G_2^j - K_e A_2^j \\ G_3^j - K_e A_3^j \\ G_4^j - K_e A_4^j \\ G_5^j - K_e A_5^j \end{bmatrix}$$

The solution was programmed in Matlab utilizing a two stage Crank-Nicolson algorithm scheme. The first stage calculates the diffusion profiles and resulting areas at t and $t + \Delta t$ (A_i^j, A_i^{j+l}) . The

second stage utilizes the calculated areas and the concentration in the melt at t (C_m^j) in order to calculate the concentration of the desired element in the melt at $t + \Delta t$ (C_m^{j+1}).

Table S4.2: Model chemical parameters

Element	K _d	$D_{\rm s} ({\rm m}^2 {\rm s}^{-1})$	D175_R25 (melt)	ODP0304-1309D- 062R-001/004- 007 (Plag)	Primitive Mantle (McDonough & Sun, 1995)
Rb			1.93		0.6
Ва	0.1490	8.48E-19 †	1.92 ‡	3.08	6.6
Th	0.0002	3.10E-21	1.91	0.63	0.0795
Nb	0.0011	3.10E-21	3.66	0.06	0.658
Ta	0.0010	3.10E-21	4.13	0.27	0.037
La	0.0347	3.87E-19	4.16	0.22	0.648
Ce	0.0479	3.87E-19	4.88	0.25	1.675
Pr	0.0445	2.92E-19	5.26	0.22	0.254
Sr	1.1097 †	4.43E-18 †	5.56 ‡	8.94	19.9
Nd	0.0229	2.92E-19	5.87	0.19	1.25
Zr	0.0060	3.10E-21	5.80	0.04	10.5
Sm	0.0090	2.92E-19	6.32	0.14	0.406
Eu3+	0.3794	2.92E-19	6.62	0.98	0.154
Eu2+	0.3794	3.37E-17	6.62	0.98	0.154
Dy	0.0250	3.24E-19	5.93	0.05	0.674
Yb	0.0274	5.06E-19	5.15	0.02	0.441

Notes: † The K_d for Sr was calculated from Tepley et al., (2010) and the D_s for Sr was calculated from Zellmer et al., (2012) for An₈₅ at T = 1200° C. The D_s for Bar was calculated from Cherniak, (2002) for labradorite at T = 1200° C. ‡ represents Sr* and Ba*: (Sr* = \sqrt{PrNNdN} and Ba* = \sqrt{RbNThN} . All concentrations have been normalized to primitive mantle.

Table S4.3: Model physical parameters

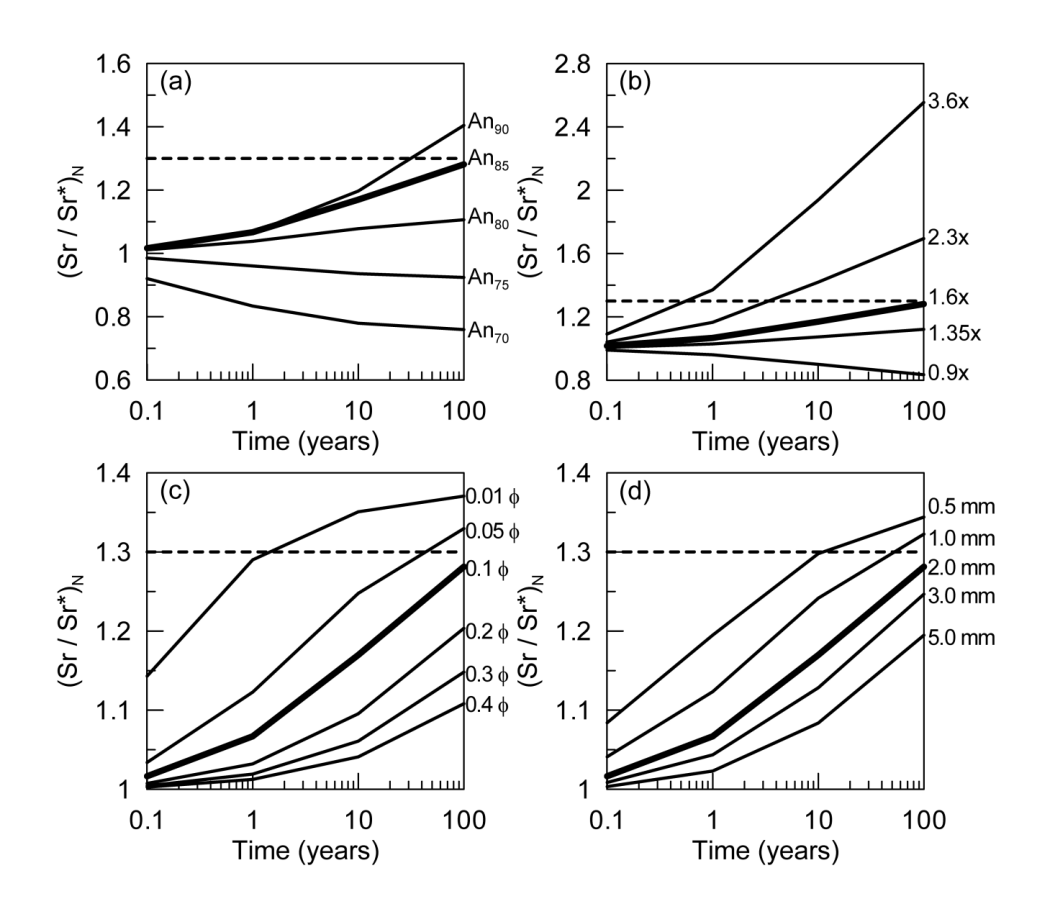
ai parameters		
Model 1	Model 2	Model 3
0.025	0.05	0.1
0.1, 1, 30	1, 10, 200	5, 50, 500
85	85	85
2	2	2
1	1	1
300 m	300	300
1.00E-08	1.00E-08	1.00E-08
5.00E-06	5.00E-06	5.00E-06
2.00E-03	2.00E-03	2.00E-03
1.00E-02	1.00E-02	1.00E-02
	Model 1 0.025 0.1, 1, 30 85 2 1 300 m 1.00E-08 5.00E-06 2.00E-03	Model 1 Model 2 0.025 0.05 0.1, 1, 30 1, 10, 200 85 85 2 2 1 1 300 m 300 1.00E-08 1.00E-08 5.00E-06 5.00E-06 2.00E-03 2.00E-03

Table S4.4: Sensitivity analysis

Deremeter		Cono 2	Cono 2	Cono 1
Parameter	Sens 1	Sens 2	Sens 3	Sens 4
time (years)	0.1, 1, 10, 100	0.1, 1, 10, 100	0.1, 1, 10, 100	0.1, 1, 10, 100
anorthite (mol fraction)	90, 85, 80, 75, 70	85	85	85
Plagioclase Sr (ppm)	177	100, 150, 177, 250, 400	177	177
φ	0.1	0.1	0.01, 0.05, 0.1, 0.2, 0.3, 0.4	0.1
R (mm)	2	2	2	0.1, 1, 1.5, 2, 3, 5
$ ho_r/ ho_m$	1	1	1	1
H(m)	300 m	300	300	300
$V_m (\text{m s}^{-1})$	1.00E-08	1.00E-08	1.00E-08	1.00E-08
$\Delta t'$ (non-dimensional)	5.00E-06	5.00E-06	5.00E-06	5.00E-06
$\Delta r'$ (non-dimensional)	2.00E-03	2.00E-03	2.00E-03	2.00E-03
$\Delta z'$ (non-dimensional)	1.00E-02	1.00E-02	1.00E-02	1.00E-02

The most significant parameters are the anorthite content of the solid, the amount of chemical disequilibrium, the porosity, and the grain size. Higher anorthite content at a constant Sr concentration and temperature decreases the interaction time required. This is primarily due to the solid-melt partition coefficient having a compositional dependence (Tepley et al., 2010) and a diffusion coefficient compositional dependence (Zellmer et al., 2012). The greater the chemical disequilibrium between the percolating melt and the solid, the less interaction time is required. Decreasing the porosity and grain size decreases the interaction time required by increasing the surface area and amount of solid available for interaction. The range of parameters chosen for our models (Table S4.2) is based on robust and realistic estimates of a lower oceanic crust magmatic system.

Figure S4.1: Sensitivity analysis for model parameters defined in Supplementary information table 4. All sensitivity models were performed at constant temperature = 1200° C and velocity = 1×10^{-8} m s⁻¹. (a) The effect of anorthite content on the interaction time. The variation is due to a compositional dependence on K_d (Tepley et al., 2010) and D_s (Zellmer et al., 2012). The greater the anorthite content at a constant solid concentration, the less interaction time required (b) The effect of chemical disequilibrium on the interaction. The greater the chemical disequilibrium between the melt and the plagioclase, the less interaction time is required. (c) the effect of porosity on the interaction time. A lower porosity indicates a higher melt-rock ratio which reduces the interaction time required due to a greater amount of solid available for interaction. (d) the effect of grain size on the interaction time. A smaller grain size increases the amount of surface area available for interaction which decreases the interaction time required.



Supplementary Information S5: alphaMELTS mantle source modelling parameters.

The alphaMELTS sensitivity analysis indicates that melting models with the trace element compositions of Workman & Hart (2005) and Salters & Stracke (2004) do not intersect the dominant EPR MORB field (Fig. S5.1a, b). Therefore, we use the trace element composition of McKenzie & O'Nions (1991). The main effect of mantle potential temperature (T_P) is the pressure at which the mantle adiabat intersects the solidus. At higher T_P, there is a greater proportion of melting in the garnet stability field, resulting in a greater fractionation of HREE+Y relative to moderately incompatible elements (Dy, Zr). Therefore, the melting curves have steeper slopes compared to models with lower T_P (Fig. S5.1c). The 1400°C at 3GPa adiabat best approximates the slope of the Taney Seamount-A data, therefore justifying its use in our models. The mantle major element composition determines the proportions of olivine, clinopyroxene, orthopyroxene, and an aluminous phase (garnet, spinel, plagioclase). The McKenzie & O'Nions (1991) mantle composition has lower clinopyroxene (11%) in comparison to KLB-1 (18%) due to differences in CaO. The main effect of an increase in modal clinopyroxene on the melting models is the increase in the degree of partial melting, but this difference is minor (Fig. S5.1d).

Table S5.1: Model compositions for DMM and refertilized peridotite

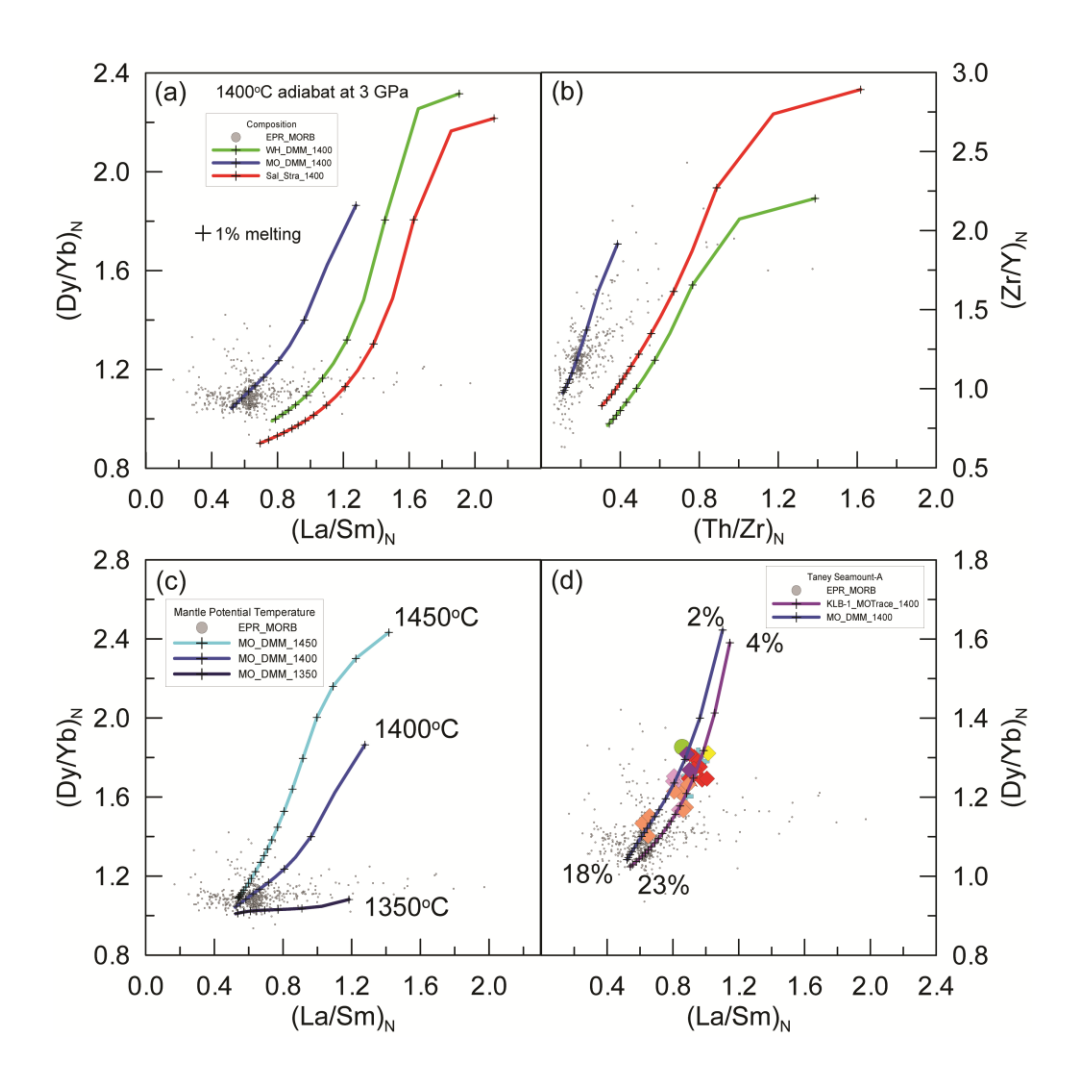
Source	G2 eclogite (NMORB)	23.8% melt_G2 (A195)	MO_DMM	RDMM 2.5 : 97.5	RDMM 5 : 95	KLB-1	WH_DMM
Pressure (GPa)	-	3	3	3	3	3	3
Temperature (°C)	-	1400	1400	1400	1400	1400	1400
† alphaMELTS T (°C)			+ 50	+ 50	+ 50	+ 50	50
Entropy (J mol ⁻¹ K ⁻¹)	-	-	259.60	259.54	259.48	257.19	257.05
Olivine (modal %)	-	-	62.0	59.0	56.0	62.1	59.1
Orthopyroxene (modal %)	-	-	21.5	22.0	22.5	9.6	13.8
Clinopyroxene (modal %)	80	-	11.0	13.0	15.5	18.1	15.2
Garnet (modal %)	20	-	5.5	6.0	6.0	9.5	11.1
alphaMELTS crustal thickness (km)			6.0	6.8	7.6	7.5	7.8
SiO ₂	50.05	54.64	45.57	45.80	46.02	44.92	44.71
TiO ₂	1.97	4.54	0.17	0.28	0.39	0.16	0.13
Al_2O_3	15.76	16.03	2.70	3.03	3.37	3.92	3.98
FeO⊤	9.35	9.44	8.02	8.06	8.09	8.09	8.18
MnO	0.19	0.12	0.11	0.00	0.01	0.12	0.13
MgO	7.9	3.1	40.8	39.9	38.9	38.8	38.7
CaO	11.74	8.22	2.41	2.56	2.70	3.79	3.17
Na ₂ O	3.04	3.79	0.24	0.33	0.42	0.30	0.28
Rb	0.56	2.33	0.03	0.09	0.15	-	0.05
Ва	10.2	42.1	0.7	1.7	2.7	-	0.6
Th	0.137	0.567	0.005	0.019	0.033	-	0.008
Nb	2.27	9.28	0.39	0.61	0.83	-	0.15
Та	0.148	0.580	0.018	0.032	0.046	-	0.010
La	2.94	11.44	0.21	0.49	0.77	-	0.19
Ce	9.49	34.28	0.72	1.56	2.40	-	0.55
Sr	118	419	15	25	35	-	8
Nd	8.67	25.93	0.82	1.44	2.07	-	0.58
Zr	81.6	210.7	7.2	12.3	17.4	-	5.1
Hf	2.20	4.88	0.22	0.34	0.45	-	0.16
Sm	3.03	6.86	0.30	0.46	0.63	-	0.24
Eu	1.15	2.70	0.12	0.18	0.24	-	0.10
Dy	4.97	5.53	0.53	0.65	0.78	-	0.51
Υ	30.0	27.6	3.2	3.8	4.4	-	3.3
Yb	2.97	1.79	0.35	0.38	0.42	-	0.37
Lu	0.450	0.242	0.057	0.062	0.066	-	0.058
Ni	91	24	2000	1951	1901	-	1886

Notes: Major elements expressed in weight per cent, trace elements in ppm. G2 eclogite and the 36.4 partial melt compositions are from Pertermann and Hirschmann (2003). MO_DMM composition is from McKenzie and O'Nions (1991). KLB-1 composition is from Takahashi (1986), WH_DMM is from Workmand and Hart (2005). N-MORB trace element composition used in the G2 eclogite is from Arevalo and McDonough (2010). Mineralogies for the peridotite compositions are calculated using alphaMELTS. † The estimated temperature discrepency between alphaMELTS calculations and partial melting experiments is ~ 50 °C (Ghiorso et al., 2002).

Table S5.2: Partition coefficients from experiments at 3 GPa between G2 eclogite and basaltic melt from Perterman et al. (2004)

		Mineral					
Element	Garnet	Clinopyroxene					
Rb	0.009	0.002					
Ва	0.005	0.006					
Th	0.004	0.005					
Nb	0.013	0.008					
Ta	0.016	0.024					
La	0.004	0.029					
Ce	0.012	0.058					
Sr	0.015	0.065					
Nd	0.081	0.134					
Zr	0.590	0.130					
Hf	0.490	0.244					
Sm	0.363	0.252					
Eu	0.430	0.217					
Dy	2.855	0.535					
Υ	4.113	0.615					
Yb	8.470	0.765					
Lu	9.940	0.825					

Figure S5.1: Sensitivity analysis of alphaMELTS modelling to a change in major and trace element geochemistry, and mantle potential temperature. Continuous melting was performed under isentropic conditions, where the reference entropy was determined at 3 GPa and the temperature of interest (1450, 1400 and 1350° Celsius). (a, b) AlphaMELTS melting curves at a constant temperature adiabat for different MORB mantle compositions: MO_DMM represents the mantle composition of McKenzie & O'Nions (1991), WH_DMM represents the depleted MORB mantle composition of Workman & Hart (2005), KLB-1 represents a spinel lherzolite xenolith from Kilbourne Hill, interpreted to represent the bulk composition of the depleted upper mantle (Takahashi, 1986), and Sal_Stra represents the depleted MORB mantle composition of Salters & Stracke (2004). (c) AlphaMELTS melting curves for MO_DMM at different mantle potential temperatures (T_P) at 3GPa. (d) AlphaMELTS melting curves at 1400°C (+50°C) for MO_DMM and KLB-1 with MO_DMM trace elements.



Supplementary Information S6: Fractional crystallization models.

Table S6.1: Parameters for fractional crystallization model.

Element	Olivine	Plagioclase	Clinopyroxene	R176_R24	D175_R4			
SiO ₂	39.4	48.8	51.3	47.6	49.6			
TiO ₂	-	0.03	0.62	1.17	1.81			
AI_2O_3	-	32.4	4.6	16.8	15.2			
FeO _⊤	18.0	0.4	6.9	10.6	10.4			
MnO	0.25	0.01	0.20	0.187	0.188			
MgO	42.8	0.1	16.0	8.61	7.31			
CaO	-	15.7	20.1	11.8	11.8			
Na ₂ O	-	2.73	0.22	2.51	2.99			
An / Fo / Mg#	81	76	81					
	K _D Olivine	K _□ Plagioclase	K _D Clinopyroxene	ppm	ppm			
La	0.00040	0.1530	0.0515	2.92	5.72			
Pr	0.00080	0.1037	0.1500	1.37	2.44			
Sr	0.00019	1.7150	0.1570	155	216			
Nd	0.00100	0.0663	0.2770	8.00	13.01			
Zr	0.01000	0.0033	0.1950	70	109			
Sm	0.00130	0.0860	0.4620	2.98	4.19			
Υ	0.00500	0.0262	0.4670	27.0	28.1			
Equation Range (MgO wt. %)	Olivine fraction	Plagioclase fraction	Clinopyroxene fraction	Slope Al ₂ O ₃	Y- Intercept Al ₂ O ₃	Slope CaO	Y-Intercept CaO	Crystallization % (by lever rule)
8.7 - 7.5	0.33	0.67	-	0.99	8.08	-0.23	13.78	17%
7.5 - 6.1	0.11	0.53	0.36	1.06	7.54	1.11	3.75	30%
							Total:	47%

Notes: Major elements expressed in weight per cent, trace elements in ppm. Partition coefficients are from McKenzie and O'Nions (1991), Hauri *et al.* (1994), and Hart and Dunn (1993). The amount of crystallization was calculated by utilizing the lever rule.

Figure S6.1: (a, b) Best fit fractional crystallization model using CaO and Al₂O₃ liquid lines of descent to estimate mineral proportions. Composition of the minerals used for this model are given in Table S6.1. The extent of crystallization (lever rule) and the mineral proportions determined by this model were used to calculate trace element fractionation paths in figure 8f, g, and h.

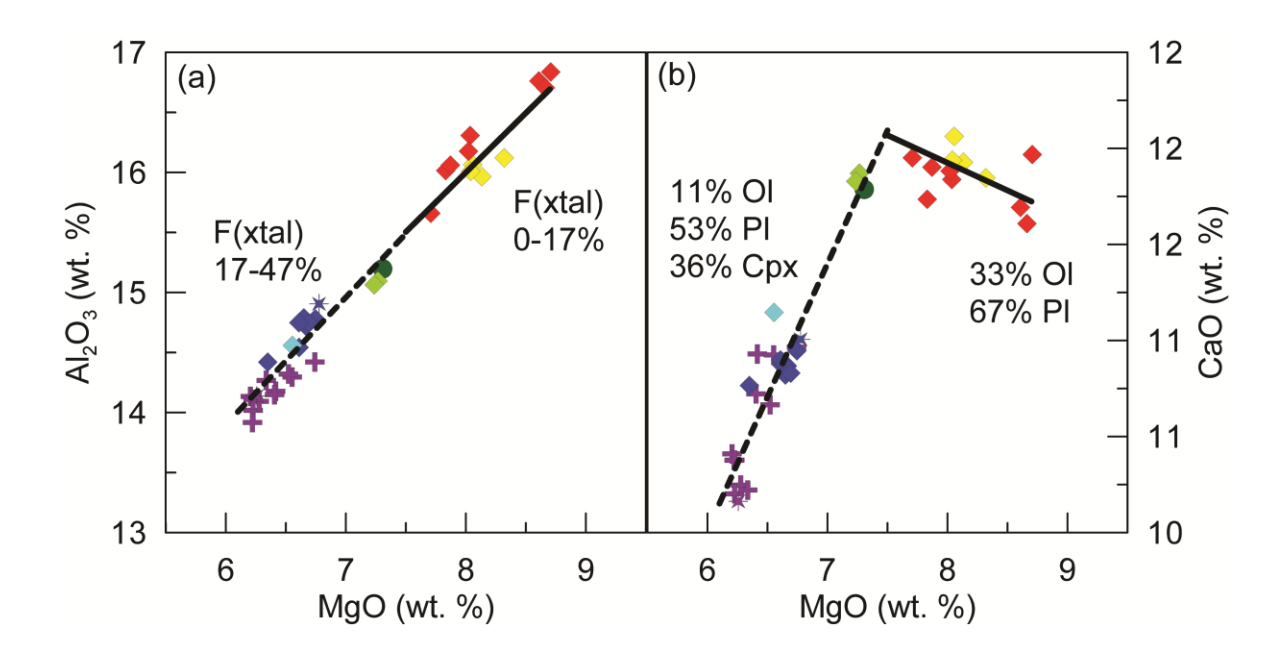
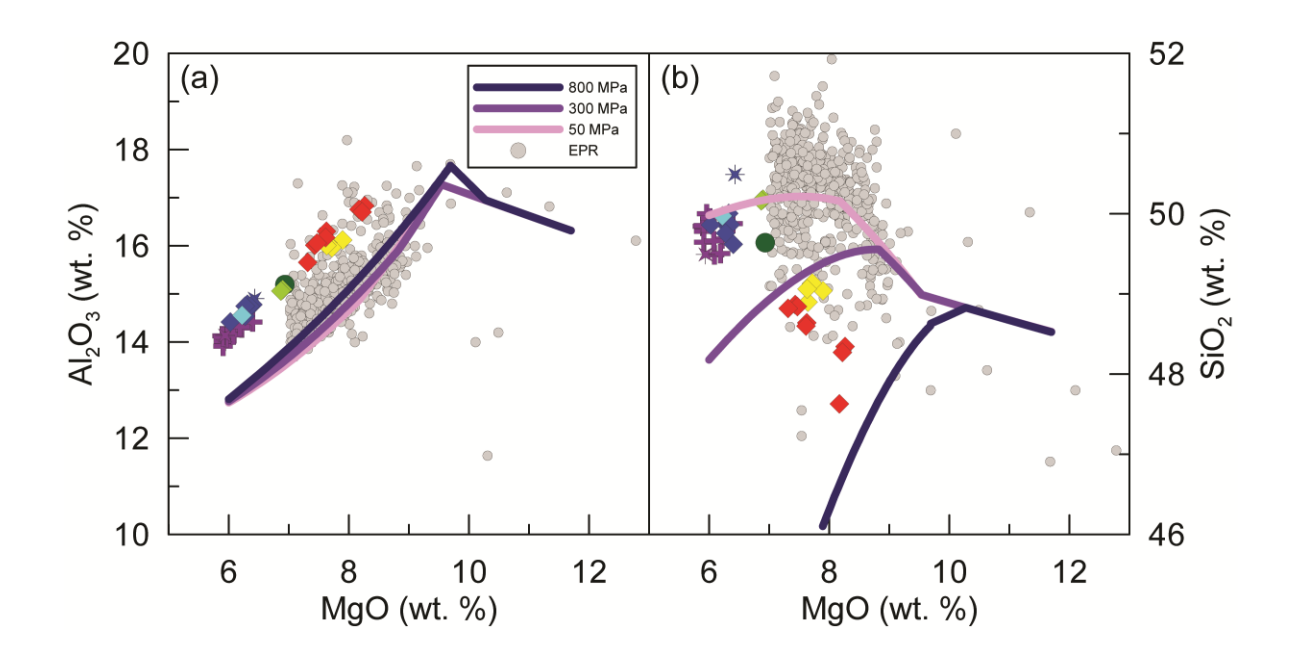


Figure S6.2: (a, b) Fractional crystallization models using the geochemical modelling program Petrolog3 (Danyushevsky & Plechov, 2011) at 50, 300, and 800 MPa. The initial composition was an average of "normal" olivine melt inclusions from the Siqueiros Transform (Danyushevsky *et al.*, 2004), interpreted to represent a potential parental MORB composition.



REFERENCES

Aigner-Torres, M., Blundy, J., Ulmer, P. & Pettke, T. (2007). Laser Ablation ICPMS study of trace element partitioning between plagioclase and basaltic melts: an experimental approach. *Contributions to Mineralogy and Petrology* **153**, 647-667.

Ames, W. F. (1977). *Numerical methods for partial differential equations*. 111 Fifth Avenue, New York, New York 10003: Academic Press Inc.

Arevalo, R. & McDonough, W. F. (2010). Chemical variations and regional diversity observed in MORB. *Chemical Geology* **271**, 70-85.

- Cherniak, D. J. (2002). Ba diffusion in feldspar. *Geochimica Et Cosmochimica Acta* **66**, 1641-1650.
- Danyushevsky, L. V. (2001). The effect of small amounts of H₂O on crystallisation of mid-ocean ridge and backarc basin magmas. *Journal of Volcanology and Geothermal Research* **110**, 265-280.
- Danyushevsky, L. V. & Plechov, P. (2011). Petrolog3: Integrated software for modeling crystallization processes. *Geochemistry Geophysics Geosystems* **12**, 10.1029/2011GC003516.
- Davis, F. A., Hirschmann, M. M. & Humayun, M. (2011). The composition of the incipient partial melt of garnet peridotite at 3 GPa and the origin of OIB. *Earth and Planetary Science Letters* **308**, 380-390.
- Ghiorso, M. S., Hirschmann, M. M., Reiners, P. W. & Kress, V. C. (2002). The pMELTS: A revision of MELTS for improved calculation of phase relations and major element partitioning related to partial melting of the mantle to 3 GPa. *Geochemistry Geophysics Geosystems* 3, 10.1029/2001gc000217.
- Hart, S. R. & Dunn, T. (1993). Experimental cpx/melt partitioning of 24 trace elements. *Contributions to Mineralogy and Petrology* **113**, 1-8.
- Hauri, E. H., Wagner, T. P. & Grove, T. L. (1994). Experimental and natural partitioning of Th, U, Pb and other trace-elements between garnet, clinopyroxene and basaltic melts. *Chemical Geology* **117**, 149-166.
- Jarosewich, E. (2002). Smithsonian microbeam standards. *Journal of Research of the National Institute of Standards and Technology* **107**, 681-685.
- McDonough, W. F. & Sun, S. S. (1995). The composition of the Earth. *Chemical Geology* **120**, 223-253.
- McKenzie, D. & O'Nions, R. K. (1991). Partial melt distributions from inversion of rare earth element concentrations. *Journal of Petrology* **32**, 1021-1091.
- Melson, W. G., O'Hearn, T. & Jarosewich, E. (2002). A data brief on the Smithsonian Abyssal Volcanic Glass Data File. *Geochemistry Geophysics Geosystems* **3**, 11.
- Navon, O. & Stolper, E. (1987). Geochemical consequences of melt percolation: The upper mantle as a chromatographic column. *Journal of Geology* **95**, 285-307.
- Nielsen, R. L. (2011). The effects of re-homogenization on plagioclase hosted melt inclusions. *Geochemistry Geophysics Geosystems* **12**.
- Pertermann, M. & Hirschmann, M. M. (2003). Anhydrous partial melting experiments on morb-like eclogite: Phase relations, phase compositions and mineral–melt partitioning of major elements at 2–3 GPa. *Journal of Petrology* **44**, 2173-2201.

- Pertermann, M., Hirschmann, M. M., Hametner, K., Günther, D. & Schmidt, M. W. (2004). Experimental determination of trace element partitioning between garnet and silica-rich liquid during anhydrous partial melting of MORB-like eclogite. *Geochemistry Geophysics Geosystems* 5, 10.1029/2003gc000638.
- Salters, V. J. M. & Stracke, A. (2004). Composition of the depleted mantle. *Geochemistry Geophysics Geosystems* **5**, 10.1029/2003gc000597.
- Takahashi, E. (1986). Melting of a dry peridotite KLB-1 up to 14 GPa: Implications on the origin of peridotitic upper mantle. *Journal of Geophysical Research-Solid Earth and Planets* **91**, 9367-9382.
- Tepley, F. J., III, Lundstrom, C. C., McDonough, W. F. & Thompson, A. (2010). Trace element partitioning between high-An plagioclase and basaltic to basaltic andesite melt at 1 atmosphere pressure. *Lithos* **118**, 82-94.
- Zellmer, G. F., Dulski, P., Iizuka, Y. & Perfit, M. R. (2012). Rates and processes of crystallization in on-axis and off-axis MOR basaltic melts. *Lithos* **154**, 1-15.

Link to Chapter 2

In Chapter 1 I proposed a petrogenetic model for the magmatic architecture of Taney Seamount-A based on geochemical analyses and modelling. I determined that melting of a two-component mantle, melt-rock interaction, and open-system evolution in a sub-caldera magma reservoir occurred prior to eruption of lavas on the seafloor. Evidence for melt-rock interaction presented in Chapter 1 includes erupted lavas with a geochemical signal defined by high Al₂O₃, low SiO₂ and a positive strontium anomaly. I proposed that this positive strontium anomaly was acquired during percolation of a melt through a MORB-type plagioclase cumulate matrix. Volatile saturation pressures of melt inclusions within large calcic plagioclase, which constitute the cumulate matrix, suggest that the melt-rock interaction occurred at or near the Moho.

In Chapter 2 I further investigate the magmatic processes occurring during melt-rock interaction at the Moho using the major, trace and volatile element geochemistry of the melt inclusions within the plagioclase crystal cargo. The unique major and trace element geochemistry of the most primitive melt inclusions cannot be explained by partial melting of the depleted MORB mantle. By contrast, the most differentiated melt inclusions have a geochemical signal with compositions similar to lavas erupted on the Taney Seamount-A edifice. Melt inclusions with intermediate major element compositions are transitional between these two endmember signals. These observations, in conjunction with thermodynamic modelling, lead me to develop a petrogenetic model for melt-rock interaction at the Moho in which episodic partial melting, magma mixing, and recrystallization of lower-crustal plagioclase-rich cumulates at the Moho are recorded in melt inclusions that carry a plagioclase cumulate signal. Later percolating melts underwent diffusive interaction with and entrained recrystallized plagioclase cumulates as shown in Chapter 1.

Chapter 2

Melt-rock interaction at the Moho: Evidence from crystal cargo in lavas from near-ridge seamounts

Jason P. Coumans, John Stix, David A. Clague and William G. Minarik and Graham D. Layne

Manuscript submitted to Geochimica et Cosmochimica Acta

ABSTRACT

The Taney Seamounts are a NW-SE trending linear, near mid-ocean ridge chain consisting of five volcanoes located on the Pacific plate 300 km west of San Francisco, California. Taney Seamount-A, the largest and oldest in the chain, is defined by four well-exposed calderas, which expose previously infilled lavas. The calderas can be differentiated in time by their cross-cutting relationships, creating a relative chronology. The caldera walls and intracaldera pillow mounds were sampled systematically by a remotely operated vehicle (ROV) to obtain stratigraphically-controlled samples, a unique aspect of this study.

The geochemistry of the seamount varies from more differentiated to more primitive with time (6.2 - 8.6 wt. % MgO), suggesting that the sub-caldera reservoir is open and undergoes periodic collapse, replenishment, crystallization, and eruption. The youngest and least differentiated lavas entrained a crystal cargo of high-anorthite plagioclase (An₈₀₋₉₀) with melt inclusion volatile saturation pressures indicating entrapment at the lower crust or upper mantle (8-10 km below the sea floor). Melt inclusions exhibit high Al₂O₃, low SiO₂, positive Sr and Eu anomalies, negative Zr and Nb anomalies, and (Ba/Nb)_N > 1 when normalized to primitive mantle. In comparison, the host lavas exhibit positive Sr anomalies, but no concurrent Eu, Zr, and Nb anomalies and (Ba_N/Nb_N) <1. We propose that a melt-rock interaction process defined by episodic partial melting, magma mixing, and recrystallization of lower-crustal plagioclase-rich cumulates at the Moho are recorded in melt inclusions that carry a plagioclase cumulate signal. Later percolating melts underwent diffusive interaction with, and entrained, recrystallized plagioclase cumulates resulting in the positive Sr signal but no Eu, Zr, Nb anomalies, and (Ba_N/Nb_N) < 1. These results demonstrate that melt-rock interaction at the lower crust or upper

mantle is an important process at Taney Seamount-A, and potentially other magmatic systems associated with seamount chains and ridge axes.

INTRODUCTION

The mid-ocean ridge system is the longest continuous chain of volcanoes, responsible for more than two-thirds of Earth's annual volcanic output (Crisp, 1984). Mid-ocean ridge basalt (MORB) is generated by decompression melting of the upwelling mantle beneath the ridge axis followed by transport through the crust. Petrologic studies indicate that MORB is too low in MgO to represent primary melts in equilibrium with its mantle source. This has been attributed primarily to fractional crystallization in shallow magma reservoirs. Hence measured compositions are back-calculated in order to reconstruct mantle melt compositions (Klein & Langmuir, 1987). These models assume that interaction with the oceanic crust is minimal during magma transport, and that shallow fractional crystallization exerts the dominant control on magma composition after segregation from the mantle. However, studies of oceanic plutonic rocks suggest that interaction between mantle-derived melt and cumulates in the lower oceanic crust could be as important as fractional crystallization in MORB petrogenesis (Bedard et al., 2000). A number of melt-rock interaction scenarios in the oceanic crust have been proposed based on studies of oceanic plutonic rocks, phenocryst melt inclusions, and xenoliths. These can be grouped into (1) assimilation, including cumulate partial melting and dissolution-reactionmixing mechanisms (Danyushevsky et al., 2004, Danyushevsky et al., 2003, Kamenetsky & Gurenko, 2007, Koepke et al., 2007, Kvassnes & Grove, 2008, Laubier et al., 2012, Ridley et al., 2006), and (2) porous flow interaction (Gurenko & Sobolev, 2006, Lissenberg & Dick, 2008, Lissenberg et al., 2013, Saal et al., 2007).

Episodic sill formation by melt ponding and crystallization at the Moho has been suggested as a method of lower oceanic crustal accretion (Kelemen *et al.*, 1997). Evidence for melt ponding at the Moho includes seismic studies of mid-ocean ridges which have detected a significant fraction of melt (2.5-17%) at the base of the oceanic crust (Canales *et al.*, 2009, Crawford & Webb, 2002, Singh *et al.*, 2006). In addition, melt inclusion volatile saturation studies at ridge settings indicate that a fraction of magmatic crystallization occurs in the lower oceanic crust (Shaw *et al.*, 2010, Wanless *et al.*, 2014, Wanless & Shaw, 2012). Since basaltic melt is buoyant with respect to the oceanic crust, it has been suggested that physical barriers such as impermeability zones (Korenaga & Kelemen, 1997) or regions of deformation (Natland & Dick, 2001) are required to impede vertical flow. Another scenario invokes a melt charged with olivine phenocrysts (~30%), resulting in a density similar to that of the lower oceanic crust and promoting lateral intrusion and further crystallization (Natland & Dick, 2009).

Previously formed cumulates in the lower oceanic crust with a residual melt fraction (e.g., <17%) inhibit the propagation of tensional cracks through the mushy lower oceanic crust (Bedard & Hebert, 1996). Mushy cumulates are less dense and have higher melt porosity than the underlying peridotite. They are thus easier to intrude, making them subject to infiltration by subsequent magma injections (Natland & Dick, 2009). This process is commonly described for layered intrusions such as the Rum complex (Leuthold *et al.*, 2014), and provides a mechanism to explain the relationship between lower oceanic crust accretion and melt-rock interactions.

Near-ridge seamounts are the predominant manifestation of off-axis magmatism. They are produced by basaltic melt that bypasses the axial reservoir through a separate magmatic plumbing system. For this reason, they have been studied as a "geochemical" window into the MORB mantle (Brandl *et al.*, 2012, Davis & Clague, 2000, Fornari *et al.*, 1988, Niu *et al.*, 2002).

A recent geochemical study of the magmatic architecture beneath the Taney near-ridge seamounts, 300 km west-southwest of San Francisco (Fig. 1), demonstrates that crustal modification at various levels is an important process in oceanic environments (Coumans *et al.*, 2015). Erupted lavas exhibit a geochemical signal defined by high Al₂O₃ and low SiO₂. The least evolved lavas on the seamount, which form pillow cones in the southeastern caldera, have positive strontium anomalies and entrain a crystal cargo of high-anorthite plagioclase that is not in equilibrium with the host glass. The plagioclase crystal cores exhibit complex textures suggesting melt-rock interaction. Using these observations, this manuscript examines the nature of melt-cumulate interactions in the deep crustal environment beneath Taney Seamount-A.

The aims of this manuscript are two-fold. (1) Analysis of melt inclusion volatile elements, specifically CO₂ and H₂O, enables us to infer melt ponding and crystallization of plagioclase in the lowermost crust or upper mantle. (2) Analysis of melt inclusion major and trace elements in plagioclase provides petrologic information associated with magmatic processes during melt-rock interaction at the lowermost crust or upper mantle.

STUDY AREA

Near-ridge seamounts form adjacent to fast- to intermediate-spreading ridges in a narrow zone between 5 and 30 km and are often distributed asymmetrically with respect to the axis of the spreading center (Scheirer & Macdonald, 1995). The region of near-ridge seamount formation is located in an area with extensive ridge parallel faulting. These faults probably facilitate melt transport to shallow magma reservoirs that bypass the axial magmatic system. The

orientation of seamount chains in the northeast Pacific Ocean is not aligned with relative or absolute plate motion. Instead, they appear to parallel calculated subaxial asthenospheric flow, suggesting that near-ridge seamount chains form from plate motion over a melting anomaly rooted in the upwelling mantle (Clague *et al.*, 2000).

Near-ridge seamounts resemble truncated cones with steep flanks (~25°) modified by complex caldera structures that are commonly offset towards the axis (e.g., Fig. 1b). The observation that offset calderas are breached towards the ridge axis indicates that the volcanoes migrate away from their magma source due to plate motion (Hammond, 1997). The flat-topped nature of these volcanoes has been attributed to the infilling of older calderas by younger lavas. Bedded volcaniclastites have been observed blanketing caldera flanks and floors. These deposits are related to explosive volcanism during caldera collapse events (Helo *et al.*, 2011, Portner *et al.*, 2014).

The Taney Seamounts, located at 36°N 45' and 125°W 25' (Fig. 1), are a short linear chain which formed adjacent to the western section of the now subducted Farallon Plate. The seamounts are labelled Taney-A through Taney-E from oldest to youngest based on the age of the underlying plate (northwest to southeast). The principle study area is Taney Seamount-A, which is the oldest and largest seamount in the chain (Fig. 1). A detailed description of the geology of Taney Seamount-A can be found in (Coumans *et al.*, 2015). The seamount is composed of at least four caldera collapse events that have been infilled by subsequent lava flows. The youngest and most primitive lavas on Taney-A are pillow cones which infill the largest caldera on the eastern flank. These primitive cone lavas exhibit a melt-cumulate interaction signal and entrain the largest proportion of plagioclase crystals. The pillow cones and their crystal cargo are the primary target of this study.

MATERIALS AND METHODS

Sampling and preparation

Sampling of Taney Seamount-A was accomplished during the 5-15 August 2010 Monterey Bay Aquarium Research Institute (MBARI) research cruise using the remotely operated vehicle (ROV) Doc Ricketts and research vessel (R/V) Western Flyer. Details about sampling locations and procedure during the research cruise are found in Coumans et al. (2015). Volcanic glass with plagioclase phenocrysts, preserved on pillow fragments, or pillow wedges, was crushed and sieved at 1 mm, 500 µm, 250 µm, and 125 µm. For certain samples polished thin sections of glassy pillow margins were made for electron microprobe analysis to maintain plagioclase crystals intact for in situ zoning analysis. A size fraction of 250 - 500 µm was used to make grain mounts of glass and plagioclase separates. Whole separated plagioclase grains were examined for melt inclusions prior to mounting using transmitted light microscopy. Grains with melt inclusions that were far from cracks and free of shrinkage bubbles were mounted in indium metal for secondary ion mass spectrometry (SIMS) analysis. Plagioclase grains with few melt inclusions were polished until the target inclusion was exposed, then mounted in epoxy for electron microprobe analysis. Each grain mount also contained small pieces of internal standard P1326-2, a Juan de Fuca Ridge (JdFR) basalt (Stix et al., 1995).

Electron microprobe analysis

Major element compositions for matrix glass, melt inclusions, and plagioclase crystals were measured with a JEOL 8900 instrument at McGill University, Montréal, Canada. The following routine was used for volcanic glass and melt inclusion analyses: an accelerating

voltage of 15 kV, a sample current of 20 nA for Si, Ti, Al, Fe, Mn, Mg, Ca, and Na (20 s); K and P (40 s); Cl (120 s); and S (60 s count time) using a defocused 5 μm diameter beam. Si, Al, Fe, Mg, Ca, Na were calibrated against Smithsonian mid-ocean ridge glass VG-2 standard (with MgO content adjusted to 7.07%) and K against Yellowstone rhyolite glass standard VG-568, with other elements calibrated using synthetic and natural minerals or oxides (the complete list of standards can be found in supplementary information Table S1.1). Analytical uncertainties were characterized by repeat measurements of VG-2 and our in-house standard P1326-2. The 2σ analytical errors are reported in supplementary information Table S1.2.

The following routine was used for plagioclase crystal analyses: an accelerating voltage of 15 kV and a sample current of 20 nA for Si, Ti, Al, Fe, Mg, Ca, Na, and K (20 s count time) using a defocused 5 µm diameter beam. Synthetic and natural minerals or oxides were used for calibration (supplementary information Table S1.1). Using the above analytical routine we observed no discernible sodium loss over the measurement time of approximately 3.5 minutes.

Secondary ion mass spectrometry

Volatile concentrations (H₂O, CO₂, F, Cl, and S) were measured on melt inclusions in plagioclase using a Cameca IMS 1280 ion microprobe at the Woods Hole Oceanographic Institution. Selected plagioclase crystals with exposed melt inclusions were mounted in indium metal to reduce the carbon background. The mounts first were dried in a vacuum oven at 110°C and 10⁻³ torr for ~12 hours. Storage prior to analysis was under 10⁻⁷ torr vacuum for ~24 hours. The samples were then held under higher vacuum in the machine airlock at 10⁻⁹ torr prior to analysis. The principle analytical procedure is described in Hauri *et al.* (2002). A primary ¹³³Cs⁺

ion beam with 1.2-1.5 nA current and 15 μm diameter was used to measure ¹²C⁻, ¹⁶O¹H⁻, ¹⁹F⁻, ³⁰Si⁻, ³²S⁻ and ³⁵Cl⁻. The magnet position for each secondary peak was calibrated before each spot, and a balanced electron flood was delivered to the sample surface in order to eliminate positive charging under the primary beam. The primary beam was rastered over a 30 x 30 μm area, and the surface was pre-sputtered for three minutes. A mechanical aperture was placed in the secondary ion image plane resulting in signal collection from a 15 x 15 μm analysis window on the sample surface. The data were collected over 10 blocks using cyclical peak switching, with counting times of 10 seconds for ¹²C⁻ and ¹⁶O¹H and 5 seconds for ¹⁹F⁻, ³⁰Si⁻, ³²S⁻ and ³⁵Cl⁻. Nine standard glasses were used to delineate empirical calibration curves for ¹²C/³⁰Si, ¹⁶O¹H/³⁰Si, ¹⁹F/³⁰Si, ³²S/³⁰Si and ³⁵Cl/³⁰Si versus the respective volatile element concentration (supplementary information Table S1.5 and Figure S1.1).

Our analytical session consisted of a total of 80 analyses, of which 10 were matrix glasses, 10 were in-run standards, 7 were mineral blanks, and 53 were melt inclusions. The 30 Si⁺ signal for all analyses ranged from 5 x 10^4 to 1.7 x 10^5 counts per second. The % relative standard deviation for 12 C/ 30 Si was lower than 5% for 74% of the melt inclusions and better than 10% for 92% of the melt inclusions. For 16 O¹H, 19 F, 32 S and 35 Cl/ 30 Si the % relative standard deviation was better than 5%. We deemed an element analysis acceptable under two filtering criteria: (1) the slope of the component counts per second during analysis was > 0 (supplementary information Figure S1.3), and (2) the % standard deviation of the isotope peak ratioed to 30 Si was < 15%. Repeated analysis (n=8) of our internal standard P1326-2 exhibited a systematic H₂O drift, decreasing with elapsed time during analysis from 0.31 to 0.26 wt.%. The systematic drift is attributed to a very small downward drift in background OH with time in vacuum. The water concentration of P1326-2 is 0.26 wt. % as determined by Fourier transform

infrared spectroscopy (FTIR) at McGill University (Gregor Lucic, McGill University, personal communication, 2015). Water concentrations of melt inclusions were corrected based on deviations of P1326-2 from the accepted value (supplementary information Figure S1.2). CO_2 , F, S, and Cl did not exhibit systematic drift and yielded 347 \pm 13 (1 σ) ppm, 209 \pm 4 ppm, 1294 \pm 23 ppm and 185 \pm 5 ppm, respectively, for P1326-2. These values are consistent with those obtained by Helo *et al.* (2011). We also analyzed the host mineral surface to obtain "blank" measurements for background concentration estimates near melt inclusion yielding 84 \pm 51 (1 σ) ppm CO_2 , 0.03 ± 0.02 H_2O , 29 ± 4 ppm F, 1 ± 1 ppm S, and 5 ± 2 ppm Cl.

Trace element concentrations were measured on melt inclusions in plagioclase using a Cameca IMS 4f ion microprobe at the MAF-IIC SIMS Facility of Memorial University of Newfoundland. The same grain mounts used for volatile characterization were cleaned, and then sputter coated with a 30–50 nm layer of gold to minimize charging of the sample during analysis. A primary beam of $^{16}\text{O}^-$ ions, accelerated through a nominal potential of 10 keV, was electrostatically focused into a 20 μ m diameter spot on the sample, providing a current of 15-20 nA. A combination of the 150 μ m image field setting of the transfer lens optics and a physical field aperture (FA) of 750 μ m limited the effective field of view of the sample to ~68 μ m diameter. A 250 μ m contrast aperture (CA) was used, with the entrance slit of the mass spectrometer narrowed to impinge on the CA image slightly, increasing the effective mass resolving power (M/ Δ M) to >350.

Each analysis comprised 8 cycles of magnetically switched counting on peaks for $^{30}\text{Si}^+$ (2s), $^{41}\text{K}^+$ (4s), $^{47}\text{Ti}^+$ (4s), $^{53}\text{Cr}^+$ (4s), $^{88}\text{Sr}^+$ (4s), $^{89}\text{Y}^+$ (6s), $^{90}\text{Zr}^+$ (6s), $^{93}\text{Nb}^+$ (10s), $^{138}\text{Ba}^+$ (8s),

¹³⁹La⁺ (8s), ¹⁴⁰Ce⁺ (8s), ¹⁴⁶Nd⁺ (8s), ¹⁴⁷Sm⁺ (8s), ¹⁵¹Eu⁺ (8s), ¹⁵³Eu⁺ (8s), ¹⁶³Dy⁺ (8s), ¹⁶⁷Er⁺ (8s), ¹⁷³Yb⁺ (8s), plus counting on a background position (29.67 Daltons; 1s) to monitor detection noise. Each spot area was pre-sputtered for a period of 150 s with a slightly rastered beam, to eliminate surface contamination before data acquisition. Total acquisition time for each spot analysis was thus ~20 min. Each individual cycle was monitored to detect any obvious inhomogeneities resulting from the primary beam sputtering through micro-inclusions with advancing depth in the sample, and such outlier cycles were rejected during initial reduction of the raw data.

Secondary ions were energy filtered by applying a voltage offset of -80 V to the nominal +4500 V sample accelerating voltage. This was combined with an energy window of ±30 eV to suppress isobaric interferences, by preferentially selecting higher-energy secondary ions, while still maintaining efficient ion transmission. Secondary ions were counted with an ETP 133H electron multiplier operated in pulse-counting mode with an overall counting system dead time of 12 ns. Maximum count rates on 30 Si⁺ were maintained at <10⁶ counts per second. The background signal ("dark noise") of the electron multiplier was typically lower than 1 count per minute.

The relative analytical error (2σ) was estimated for each spot using the internal precision (standard deviation of the mean) for each peak measured during each 8-cycle analysis. Measured secondary ion ratios relative to 30 Si⁺ were reduced to elemental concentrations by direct comparison to in-run measurements of standard glass 73. P1326-2 glass was run as a secondary standard. Measured ratios were normalized to SiO₂ concentrations as previously determine by EPMA. P1326-2 and 73 are natural basaltic composition glasses described in detail in Stix *et al.* (1995). Accepted concentrations used for these two materials are shown in supplementary

P1326-2, which was treated as a sample with elemental concentrations as determined by comparison to 73. Any small remaining interference of BaO on Eu was corrected by empirically correcting for ¹³⁵Ba¹⁶O⁺ and ¹³⁷Ba¹⁶O⁺ interferences by subtracting the signal ("peak stripping"), based on the direct measurement of ¹³⁸Ba⁺, from the measured peaks for ¹⁵¹Eu⁺ and ¹⁵³Eu⁺, respectively, to produce the correct natural abundance ratio for ¹⁵¹Eu/¹⁵³Eu.

Melt inclusion post-entrapment correction

Melt inclusions have been used by petrologists as a tool for looking through shallow level processes to investigate magma genesis (Sobolev & Shimizu, 1993). However, the assumption that melt inclusions represent unmodified mantle derived melts has come under question through the investigation of processes that may perturb compositions during and/or after trapping. Entrapment processes include boundary layer effects, which preserve anomalous compositions controlled by the relative diffusion of elements and the growth rate of the crystal (Baker, 2008). Post-entrapment processes include crystallization of the host (Danyushevsky *et al.*, 2002) diffusive re-equilibration (Cottrell *et al.*, 2002, Spandler *et al.*, 2007). If boundary layer diffusive processes were significant in our high-anorthite plagioclase inclusions, elements with slow diffusivity in the melt (e.g., Ti) would be enriched in the inclusion relative to the crystal, resulting in a low apparent partition coefficient (D_{Ti}). A comprehensive study of apparent D_{Ti} in high-anorthite plagioclase melt inclusions from mid-ocean ridges and seamounts has determined that this process is minor in these environments (Adams *et al.*, 2011).

Crystallization of the melt inclusion can occur after entrapment depending on quenching conditions. The host mineral is generally the first to crystallize on the wall of the melt inclusion

due to the pre-existing phase boundary which has low nucleation energy (Danyushevsky *et al.*, 2002, Roedder, 1979). These rims can be difficult to see optically because they may be similar in composition to the host mineral and can be extremely thin. For example, a spherical 30 μ m melt inclusion which has crystallized 20% by volume of the host mineral on the wall will only have a 2 μ m rim. Melt inclusion compositions were corrected by adding plagioclase numerically until they plotted on a linearly regressed olivine-plagioclase cotectic (supplementary information S3). The amount of calculated post entrapment crystallization varies from 0 - 26% with ~43% of the samples < 10% and ~92% of the samples < 15%.

RESULTS

Petrography

The plagioclase occurs as large single crystals, or in crystal clusters with or without olivine. Crystals and crystal clusters exhibit a wide variety of morphologies including tabular, acicular, euhedral, resorbed, and glomerocrystic with olivine. Plagioclase megacrysts up to 1.5 cm long occur as single crystals or crystal clusters with evidence for synneusis (Fig. 2). Chemical zonation in individual megacrysts is complex, with normal, reverse, and oscillatory patterns present. The megacrysts commonly have subrounded cores with typical anorthite contents of An_{80} to An_{90} , and thin rims (typically < 50 μ m) of An_{72} to An_{82} (Coumans *et al.*, 2015). Cores of the plagioclase megacrysts occasionally exhibit patchy or resorbed textures. Small microlites (10 - 150 μ m) in the pillow glass have anorthite contents that are ~3-5 An_{80} lower than the rims of the larger crystals, likely representing the last stages of crystallization.

These features suggest that the large plagioclase crystals erupted at the young constructional cones have experienced a protracted and complex crystallization process.

The plagioclase megacrysts commonly contain abundant melt inclusions, which can occur as thin bands or isolated throughout the crystal (Fig. 3). Primary melt inclusions have a fresh glassy appearance and regular shapes, while secondary melt inclusions have a brownish devitrified appearance and irregular shapes that crosscut crystal growth faces. Both primary and secondary melt inclusions are observed in individual crystals. We analyzed the primary melt inclusions, since they represent melt entrapment during crystal growth, whereas the secondary melt inclusions represent plagioclase resorption. Primary melt inclusions vary in size from < 10 µm to > 100 µm, with shapes from rounded to rectangular. Where the melt inclusions are rectangular, they are typically aligned and parallel to plagioclase growth faces. Bubbles are common but not ubiquitous in fresh melt inclusions. These bubbles represent the exsolution of a volatile phase due to changes in pressure, assisted by the greater thermal expansion of glass relative to the host crystal (Kent, 2008). Melt inclusions without shrinkage bubbles were selected for volatile analysis in order to minimize complications of vapour exsolution, which would affect CO₂ concentrations in particular.

Major element compositions

Melt inclusion major element compositions corrected for post-entrapment crystallization are presented in Figure 4. The host lavas have glass MgO contents from 7.8 to 8.6 wt. %, whereas the majority of melt inclusions vary from 8.5 to 10.5 wt. % MgO. A small number of inclusions with ~7.0 wt. % MgO are more fractionated than the host glasses (Fig. 4), indicating a

complex crystallization history. Chemical variation trends of the melt inclusions are similar to lavas erupted on the seamount; oxides such as FeO_T , TiO_2 , Na_2O , and K_2O increase with decreasing MgO (Fig. 4b, f, h) whereas Al_2O_3 decreases (Fig. 4c). Since Al_2O_3 and FeO_T olivine-plagioclase cotectic trends were used to correct post-entrapment crystallization, these elements have artificially low scatter. The anorthite content of the plagioclase host close to a melt inclusion (~10-100 μ m) is positively correlated with the MgO of the melt inclusion (Fig. 4b), consistent with plagioclase crystallization trends during decreasing temperature (Kohut & Nielsen, 2003).

Trace element compositions

Representative compatible and incompatible trace elements in melt inclusions are plotted against their MgO contents in Figure 5. As melt inclusions decrease in MgO, incompatible rare earth elements (REE) increase, consistent with conservation during progressive crystallization. Chromium exhibits variable behaviour depending on degree of fractionation. From 8.0 to 10.5 wt. % MgO, chromium is between 200-350 ppm, whereas from ~7.0 - 7.5 wt. % MgO chromium decreases from 250 to 150 ppm. The pronounced decrease in chromium could indicate the addition of a crystallizing phase into which Cr is compatible, such as clinopyroxene. The scatter in incompatible element trends (e.g., La, Nd, Y) at similar major element compositions indicates that concentrations of incompatible elements in the melt were variable or that the trace element analyses were imprecise. The variability is larger than can be explained by analytical precision for the trace elements (supplementary information Table S1.3). For example, Zr varies from ~1 - 130 ppm while the precision of Zr at 130 ppm is ~14 ppm (2σ). Hence the variability is real and

consistent with other studies of high-anorthite plagioclase melt inclusions that demonstrate the importance of multiple petrological processes (Adams *et al.*, 2011).

Incompatible trace element patterns normalized to primitive mantle for the plagioclase hosted melt inclusions are shown in Figure 6. Differentiated melt inclusions (MgO ~ 7.0 wt. %) exhibit profiles which resemble the main edifice lavas erupted at Taney Seamount-A. In contrast, more primitive melt inclusions have distinct profiles characterized by (1) enrichments of Sr and Eu relative to REE of similar incompatibility (Nd, Dy), (2) depletions of Nb and Zr relative to REE of similar incompatibility (La, Nd) and (3) (Ba/Nb)_N>1. The most primitive melt inclusions with MgO from 9.4 to 10.5 wt. % exhibit the largest anomalies, while more differentiated melt inclusions with MgO from 8.0 to 9.4 wt. % have smaller anomalies. The unique melt inclusion profiles exhibited by the primitive melt inclusions do not resemble typical MORB generated from decompression melting of depleted upper mantle (Arevalo & McDonough, 2010). The trace element profiles instead resemble plagioclase-rich cumulates sampled from the lower oceanic crust (Perk *et al.*, 2007).

Volatile element compositions

Chlorine and fluorine

Melt inclusion Cl and F concentrations vary from 40 - 280 ppm and 140 - 260 ppm, respectively. Most melt inclusions have F contents between 200 - 250 ppm. The larger variation of Cl compared to F suggests that different processes are controlling their concentrations in the melt (Fig. 7a). Furthermore, Cl/H₂O varies as a function of Cl, suggesting that the process which controls Cl does not directly affect F or H₂O (Fig. 7b). Nor are Zr depletions relative to REE of

similar incompatibility (Zr / Zr*) correlated with Cl, suggesting that Cl variability and the occurrence of negative Zr anomalies are not coupled (Fig. 7c).

CO_2 and H_2O

Melt inclusions in high-anorthite plagioclase from Taney Seamount-A exhibit a large range of CO₂ concentrations (617 - 3939 ppm), while H₂O is fairly restricted (0.25 - 0.38 wt. %). In contrast, the host glasses have low concentrations of CO₂ and exhibit less variation (89 - 142 ppm) at similar concentrations of H₂O (Fig. 7d). The H₂O concentrations in the host glasses and melt inclusions fall within the range observed in erupted MORB (Saal *et al.*, 2002). H₂O concentrations increase with decreasing MgO, suggesting that H₂O concentrations are primarily controlled by progressive crystallization (Fig. 7e). However, the CO₂ concentrations in the melt inclusions are both highly variable and comparatively high. The majority of melt inclusions (85%) have CO₂ concentrations from 1000 - 2000 ppm, with 45% of the population clustered in a narrow range from 1200-1600 ppm. Two inclusions have anomalously high CO₂ concentrations of 3500-4000 ppm. Compared to H₂O, CO₂ solubility in melts is highly dependent on pressure resulting in low concentrations at eruption depths caused by degassing.

Sulfur

Sulfur varies from 610 to 1310 ppm and is unique because it is the only volatile element buffered by an immiscible sulfide phase. As the concentration of FeO_T increases in the melt with differentiation, the S saturation limit increases, as shown by the increase in S in the melt inclusions with increasing FeO_T (Fig. 7f). Although we do not observe an immiscible sulfide phase, the S-FeO_T trend observed for the melt inclusions overlaps with the S-FeO_T trend for the

Taney-A matrix, edifice glasses, and the field for Pacific MORB using data from O'Neill & Jenner (2012). These relationships are best interpreted as sulfide saturation.

DISCUSSION

Near-ridge seamounts are important to understanding the chemistry of the underlying mantle, due to a magmatic plumbing system that bypasses the mid-ocean ridge axial reservoir. However, it is well known that processes in the uppermost mantle and lower oceanic crust can alter the composition of mantle-derived magmas. Melt inclusions are particularly useful to address this issue, as they trap an array of primary magma compositions. Hence they have the capability of revealing petrologic processes prior to eruption on the seafloor. High-anorthite (An₈₅₋₉₀) plagioclase crystals from Taney Seamount-A have abundant melt inclusions with a range in MgO (>9.0 wt. %) and elevated CO_2 (~45% between 1000-2000 ppm), which exhibit a unique geochemical signal characterized by high Al₂O₃, low SiO₂, positive Sr and Eu, negative Zr and Nb anomalies, and (Ba_N/Nb_N) > 1. We interpret this signal to represent melt-cumulate interaction below Taney Seamount-A, which we explain below.

High-Mg melts in calcium-rich plagioclase

Understanding the crystallization sequence of tholeitic basalts is crucial to elucidating magmatic processes at mid-ocean ridges (Grove & Bryan, 1983). Correcting for shallow crystallization processes is commonly necessary to evaluate MORB primitive melt characteristics (Gale *et al.*, 2014, Klein & Langmuir, 1987, Langmuir *et al.*, 1992, Niu & O'Hara,

2008). An important parameter is the point at which plagioclase first appears as a cotectic phase with olivine, which can have a significant effect on Al_2O_3 , CaO, and FeO contents. For example, Gale *et al.* (2014) have deduced from major and trace element characteristics of global MORB that plagioclase generally becomes a prominent cotectic phase between 8 and 9 wt. % MgO in the melt. However, a number of high-anorthite (An_{85-90}) plagioclase crystals at Taney Seamount-A and other locations, such as the Lamont Seamounts, contain melt inclusions with > 9.0 wt. % MgO (Nielsen, 2011). These observations indicate that some melts in oceanic environments which crystallize plagioclase have MgO > 9 wt. %.

A recent study of olivine-hosted melt inclusions from the FAMOUS region, Mid-Atlantic Ridge, have identified primitive high-Mg and high-Al melts (Laubier *et al.*, 2012). The high-Mg type (Fig. 8, purple circles) was interpreted to represent the most likely candidate for minimally modified melts from the mantle melting column. In contrast, the high-Al type (Fig. 8, pink circles) defined by high Al₂O₃, low SiO₂, and in some cases positive strontium anomalies, was interpreted to represent interaction with plagioclase-rich cumulates. Our crystallization modelling of a high-Mg olivine-hosted melt inclusion indicates a plagioclase stability MgO content of ~8.6 wt. %, consistent with the melt inclusions being potential candidates of MORB parental melts (Fig. 8, grey line). In contrast, the inflection of Al₂O₃ at MgO ~10.5 wt. % for the high-Al melt inclusions and lavas suggests that melts with a high Al₂O₃ and low SiO₂ geochemical signal crystallize plagioclase at MgO contents > 9 wt. % (Fig. 8). Therefore, the high Al₂O₃, low SiO₂ geochemical trends observed in our high-anorthite plagioclase melt inclusions may also be related to melt-plagioclase cumulate interaction, as suggested for high-Al olivine melt inclusions and lavas (Gale *et al.*, 2013, Laubier *et al.*, 2012).

Crystallization depths

The crystallization of tholeiitic magmas results in the accretion of oceanic crust, but, the locus of this crystallization is contentious (Kelemen et al., 1997, Quick & Denlinger, 1993). Recent understanding of crustal accretion indicates that magma reservoirs are present both in the lower oceanic crust and at shallow depths (Natland & Dick, 2009). new evidence for crystallization in the lower oceanic crust has been provided by volatile studies of olivine melt inclusions at a fast-spreading ridge (Wanless & Shaw, 2012), a volcano on a slow spreading ridge (Wanless et al., 2015), and a magmatically robust section of an ultraslow-spreading ridge (Shaw et al., 2010). Lower crustal crystallization at Taney Seamount-A is demonstrated by H₂O-CO₂ relationships in our melt inclusions from the high-anorthite plagioclase crystals. We calculated H₂O-CO₂ saturation pressures using VolatileCalc (Newman & Lowenstern, 2002) and converted these values to depths below the sea floor assuming a water column thickness of 2000 m and a crustal density of 2800 kg/m³. The H₂O-CO₂ saturation depths calculated for the Taney-A melt inclusions suggest that the majority (70%) of melt inclusions were trapped 6-12 km below the seafloor, with 45% of the samples concentrated at 8-10 km trapping depth (Fig. 9). These melt inclusion depths suggest that the large anorthite-rich plagioclase crystals formed near the Moho at the base of the lower oceanic crust or upper mantle.

Melt-rock interaction at the Moho

In addition to melt-rock interaction studies of lower oceanic rocks (Drouin *et al.*, 2009, Lissenberg & Dick, 2008, Lissenberg *et al.*, 2013), studies of lavas and melt inclusions from various locations (e.g., Iceland, Galapagos Islands, Mid-Atlantic Ridge, and Siqueiros

Transform) have shown the importance of primitive melts interacting with crustal cumulates to generate anomalous compositions (Danyushevsky et al., 2004, Danyushevsky et al., 2003, Esposito et al., 2011, Gurenko & Sobolev, 2006, Hann, 2012, Laubier et al., 2012, Saal et al., 2007). Based on a synthesis of this research, we identify at least two different melt-rock interaction geochemical signals: (1) positive Sr and Eu anomalies, negative Zr and Nb anomalies, and $(Ba_N/Nb_N) > 1$, and (2) positive Sr anomalies with no concurrent positive Eu anomaly, negative Zr and Nb anomalies, and (Ba_N/Nb_N) < 1. Compositions with only positive strontium anomalies have been attributed to melt percolation-diffusion through a plagioclase-rich mush zone (Saal et al., 2007). Since the diffusion rate of Sr²⁺ is 1-2 orders of magnitude faster than REE³⁺ and 3-4 orders of magnitude faster than high field strength elements, a strontium anomaly without concurrent Zr or Nb anomalies can be rapidly acquired during ascent (Cherniak, 2010). In contrast, negative Nb and Zr anomalies, positive Sr and Eu anomalies, and (Ba_N/Nb_N) > 1 reflect the trace element composition of plagioclase, which is depleted in Nb and Zr and enriched in Sr and Eu relative to REE³⁺ implying a more static, long-lived interaction of melt with coexisting plagioclase. The flux of Sr and Eu are enhanced both by their high diffusivity and high solubility in plagioclase.

It has been suggested that melt inclusions may undergo diffusive reequilibration with the host crystal and/or the external melt, with plagioclase particularly susceptible (Cottrell *et al.*, 2002, Qin *et al.*, 1992, Spandler *et al.*, 2007). If the melt inclusions do not undergo complete reequilibration through this process, then elements will be fractionated kinetically from each other based on their relative diffusivities through the host crystal. Slow diffusing elements such as Zr and Nb will not re-equilibrate rapidly and may remain representative of the initial entrained melt. In contrast, fast diffusing elements such as Sr may be representative of a distinct external

melt undergoing reequilibration with the crystal and melt inclusions therein. The low Zr and Nb concentrations in the Taney-A melt inclusions suggest that the initial melt was highly depleted in trace elements and not derived from the MORB source. One possibility is that the melt inclusions acquired their composition from a refractory upper mantle lithology. Melting of serpentinized harzburgite fluxed by Cl-rich fluids from deep hydrothermal circulation could produce ultradepleted melts (Benoit *et al.*, 1999, Nielsen *et al.*, 2000). This hypothesis is supported by Cl concentrations in the melt inclusions similar to lavas erupted on the seafloor (Fig. 7a, b) which are elevated relative to uncontaminated MORB (Michael & Cornell, 1998). However, the Cl concentrations in the melt inclusions are not correlated with the magnitude of the negative Zr anomaly (Fig. 7c). Furthermore, harzburgite melts would have high SiO₂, low Al₂O₃, and high CaO, opposite to what we observe. Although we cannot completely rule out that diffusive equilibration may have occurred (Adams *et al.*, 2011), we propose that melt-plagioclase cumulate interaction exerts the dominant control on the composition of the anomalous melt inclusions.

Modeling the melt-cumulate interaction

We investigated melt-plagioclase cumulate interaction by thermodynamic modelling of partial melting using alphaMELTS (Asimow & Ghiorso, 1998, Ghiorso & Sack, 1995, Smith & Asimow, 2005). There are a variety of lower oceanic crust lithologies and compositions available for such interactions (Coogan *et al.*, 2002). In order to provide a first order estimate of potential lower crust mineral compositions, we utilize average mineral compositions of lower crustal gabbros and troctolites from the Hess Deep Rift (Lissenberg *et al.* (2013), supplementary

information Table S4.2). The average mineral compositions of troctolite are more primitive (olivine \sim Fo₈₄, clinopyroxene \sim Mg# 87, and plagioclase \sim An₈₇) than the average layered olivine-gabbro (Fo₈₁, Mg# 85, and An₇₆,). The largest difference between the two mineral suites are the average plagioclase compositions, which vary by \sim 11 mol %. Model bulk cumulate compositions were calculated by varying the modal proportions of the average plagioclase, olivine and clinopyroxene compositions for both rock series. The plagioclase modes were varied from 60-90%, with the remaining modes of olivine and clinopyroxene calculated from a % clinopyroxene / (% olivine + % clinopyroxene) mass ratio from 0 to 1. The model cumulate bulk compositions were then equilibrated in alphaMELTS at their solidus (melt fraction < 0.5%) to compare the mineral modes and compositions between the bulk cumulate input and alphaMELTS output (supplementary information Figure S4.1). We then calculated an array of potential melt inclusion parental melts by performing equilibrium partial melting on the model cumulates at 300 MPa, to simulate lower crustal conditions.

The calculated melts are compared to the most primitive melt-inclusion compositions using SiO₂, Al₂O₃, MgO, CaO, and FeO as discriminants. The conditions (mineralogy, composition, and degree of melting) of best fit are determined by the root mean square error (*RMSE*) between the model and the most primitive melt inclusion (Fig. 10):

$$RMSE = \sqrt{\frac{\sum_{i=1}^{n} \left(X_{obs,i} - X_{\text{mod}el,i}\right)^{2}}{n}}$$
 (2)

The best fit (RMSE <1) alphaMELTS modelling indicates that the major element composition of the most primitive melt inclusions in high-anorthite plagioclase, which exhibit the high Al_2O_3 , low SiO_2 geochemical signal, can be reproduced by equilibrium partial melting

of a plagioclase-rich cumulate with evolved mineral compositions (olivine \sim Fo₈₁, clinopyroxene \sim Mg# 85, and plagioclase \sim An₇₆). In the best fit models, clinopyroxene is exhausted resulting in a troctolite restite. Therefore, partial melting of gabbroic assemblages is an alternative to crystallization from primitive melts for forming olivine-plagioclase cumulates. This former process has been implicated in forming troctolitic assemblages in layered intrusions (Leuthold *et al.*, 2014).

In order to investigate whether the plagioclase-cumulate partial melting model is consistent with the unique trace element signal defined by the positive Sr and Eu anomalies, negative Zr and Nb anomalies, and (Ba_N/Nb_N) <1, we must make an assumption in terms of the initial trace element compositions of the constituent minerals. This is not straightforward, as it has been shown that the trace element composition of lower oceanic material can be highly variable (Coogan et al., 2002, Gao et al., 2007). However, the most differentiated Taney-A melt inclusions have no Sr, Zr or Nb anomalies, only a minor positive Eu anomaly, and are trapped in An₇₇₋₈₀ plagioclase. Therefore, we interpret these differentiated melt inclusions with a mantle melting-derived trace element composition to represent the melt from which the cumulates were formed. We calculated the mineral trace element compositions using two sets of partition coefficients (supplementary information Table S4.1) and applied the best fit major element melting model. The results are shown in Figure 11. Although applying the two different sets of trace element mineral compositions does affect the resulting concentrations, especially the range in K coefficients, the overall pattern is consistent, demonstrating the influence of a plagioclaserich assemblage. The results indicate that the equilibrium melting model, which reproduces the major element composition of the primitive melt inclusions, also reproduces the positive Sr and Eu anomalies as well as the negative Zr and Nb anomalies. The process modelled here is

simplified and likely not a unique solution in nature due to a wide variety of cumulate compositions and thermal conditions at the Moho in oceanic environments. A more realistic process would involve continuous partial melting, mixing, and recrystallization of the cumulate pile. However, the modelling illustrates the requirement of a non-cotectic plagioclase-rich cumulate assemblage in forming the observed anomalies.

A PETROGENETIC MODEL

Using alphaMELTS geochemical modelling, we have demonstrated that partial melting of plagioclase-rich cumulates can explain the unique composition of melt inclusions in highanorthite plagioclase found at Taney Seamount-A pillow cones. We propose that this interaction between the plagioclase-rich cumulate pile and subsequent melt injection events is comparable to the melting-assimilation-storage-homogenization (MASH) system described for arc magmatism in Chile (Hildreth & Moorbath, 1988). The main difference between the systems is the host material, which below the Taney Seamounts are mafic cumulates in contrast to silicic crust. A similar comparison has been made for melt-mafic cumulate interaction processes at the Rum layered intrusion in Scotland (Leuthold, et al. 2014). Based on our findings we propose a multiple stage model (Fig. 12) defined by: (1) primitive mantle derived melts which pond laterally and crystallize near the Moho beneath the seamount, forming a differentiated cumulate pile, (2) subsequent injections of mantle derived melts near the Moho, which partially melt the differentiated cumulate pile, (3) mixing between the cumulate partial melt and injected basalt, in conjunction with crystallization, resulting in transitional melt inclusions, and (4) vertically infiltrative mantle-derived melt which percolates through the plagioclase-rich cumulate,

undergoing diffusive exchange and entraining the crystal cargo during transport to the shallow magmatic system.

Stage 1: Melt ponding and crystallization at the Moho

Primitive melts from the mantle pond at or near the Moho beneath the seamount, differentiating to form plagioclase-rich cumulates. The formation of such cumulates, as observed in the lower oceanic crust (Perk *et al.*, 2007), relies upon efficient physical separation of plagioclase and olivine in the differentiating melt body by processes such as gravitational or magmatic flow separation. Melt inclusions in differentiated plagioclase crystals (An₈₀₋₈₃) exhibit trace element profiles similar to the main edifice lavas at Taney Seamount-A (Fig. 6b), which lack negative Zr or Nb anomalies (Fig. 6a). Therefore, we propose that plagioclase-rich cumulates are formed from melts that are petrologically related to the Taney Seamount-A early edifice lavas. Differentiated plagioclase-rich cumulates, described above, provide the material for subsequent melt-rock interactions.

Despite the similarity between the trace element composition of the differentiated melt inclusions and the Taney-A edifice lavas, it is possible that the plagioclase cumulate was formed at the ridge axis. Studies of melt inclusions in high-anorthite plagioclase from the Juan de Fuca ridge have also identified melts which are highly depleted in high field strength elements (Adams *et al.*, 2011). In addition, they have observed the entire range in melt compositions from N- to E-MORB. Although it would be a coincidence, we cannot completely rule out that the cumulates were created at the ridge axis. However, this scenario is less likely because any cumulates formed at the ridge axis would have had approximately 1 to 2 million years to cool. If we assume

a simple half-space cooling model, which has been illustrated to approximate the oceanic geotherm, then the temperature at 8 km depth would be approximately 900°C at one million years, and 700°C at two million years. These temperatures are below the solidus for gabbroic compositions, so any available cumulate would be more difficult to intrude and require greater heat transfer to partially melt.

Stage 2: Melt replenishment and injection into the cumulate pile

Injections of hot, primitive basalt infiltrate the differentiated plagioclase cumulate described above. Heat exchange results in crystallization of the injected basalt and partial melting / assimilation of the differentiated plagioclase cumulate. The interaction of the crystallizing basalt with partially molten plagioclase cumulate results in the high Al₂O₃, low SiO₂ trend observed in plagioclase undersaturated olivine melt inclusions, as suggested for the FAMOUS region (Laubier *et al.*, 2012). The infiltrating basalt will preferentially assimilate plagioclase-rich material until reaching saturation. At this stage, plagioclase crystallization enables entrapment and preservation of the cumulate partial melts observed in our melt inclusions. Evidence for partial melting includes the resorbed nature of many plagioclase crystal cores and the complex crystal zoning patterns (Fig. 2). Our thermodynamic modelling demonstrates that the phase relationships of the cumulates, dominated by plagioclase in non-cotectic proportions, is required to explain both the major and trace element observations, as also suggested by similar studies (Gurenko & Sobolev, 2006, Saal *et al.*, 2007).

Stage 3: Melt mixing and crystallization

The gradual disappearance of the Zr, Nb, Sr and Eu anomalies (plagioclase-cumulate signature) as the plagioclase melt inclusions become more differentiated (lower MgO wt. %) is incompatible with crystallization exclusively. Although crystallization of plagioclase and olivine would reduce the magnitude of the positive Sr and Eu anomalies, due to compatible element partitioning behaviour, it would not sufficiently reduce the negative Zr and Nb anomalies observed in the transitional melt inclusions (Fig. 6, red field). Therefore, the reduction of the plagioclase-cumulate signal must be due to continual interaction of cumulate partial melts, which are highly depleted in Zr and Nb, with infiltrating basalt.

The injected basalt transfers heat to the plagioclase-cumulate, promoting partial melting / assimilation and the creation of a hybridization zone, similar to the contaminated boundary layer suggested by Danyushevsky *et al.* (2004). When the system becomes plagioclase saturated, the primitive (high MgO) cumulate partial melts are preserved. Crystallization, together with mixing of HFSE depleted plagioclase-cumulate partial melts and the infiltrative basalt, results in both a more differentiated major element composition and a reduction in the Zr, Nb, Sr, and Eu anomalies. The entrapment of melt during different stages of mixing and crystallization leads to a spectrum of compositions, as observed in the Taney Seamount-A melt inclusions.

Stage 4: Entrainment of plagioclase crystals during porous flow

The host lavas that entrain the plagioclase crystals construct the southeastern pillow cones, which are the youngest and least volumetric stage of magmatism at Taney Seamount-A. These late stage cones represent the final eruptive activity, when magma supply to Taney

Seamount-A was dwindling (Clague *et al.*, 2000). Melts which entrain plagioclase crystals must have travelled vertically through the cumulate pile, since they reach the surface. The lavas which erupt to form the older edifice lavas also may have entrained plagioclase crystals from the cumulate pile. However, the edifice lavas have undergone greater processing in a sub-caldera magma reservoir prior to eruption, due to greater melt supply, resulting in more differentiated compositions and potential removal of cumulate-derived plagioclase crystals in the shallow reservoir (Lange *et al.*, 2013).

The young cone lavas have key geochemical differences compared to the melt-inclusions trapped in the entrained plagioclase crystals. For example, they have more depleted compositions (lower LREE/MREE) compared to both melt inclusions with a mantle-derived signal and the edifice lavas. Furthermore, the cone lavas exhibit positive Sr anomalies with no concurrent Eu, Nb or Zr anomalies. In order to explain these chemical differences, the more depleted vertically ascending host lavas must have not been in trace element equilibrium with the more enriched cumulate pile, enabling diffusive exchange between the crystals and melt. Since the diffusivity of Sr is 1-2 orders of magnitude higher than REE and 3-4 orders of magnitude faster than HFSE, the host lavas acquired a kinetic fractionation of Sr without coeval Zr and Nb fractionations, as shown by Coumans *et al.* (2015).

Application to nature

The model proposed to explain the results is a unique solution through four stages, which is unlikely in nature. A realistic model would involve the continuous partial melting, assimilation, and crystallization of lower crustal gabbros. A continuous model is supported by the complex textures observed in the plagioclase crystals, and a higher frequency of high-

anorthite plagioclase (Coumans *et al.*, 2015), implying a greater amount of processing. The high-Mg nature of the plagioclase melt inclusions (10.5 wt. % MgO) implies that the temperature of entrainment is quite high. Therefore, melts that pond at the base of the Moho must be very primitive in order to supply sufficient energy for the degree of partial required to reproduce the most primitive plagioclase melt inclusions. The high Mg-type olivine melt inclusions from Laubier *et al.*, (2012) are sufficiently hot (12-16 wt. % MgO) to provide the energy for partial melting. High-Al type olivine melt inclusions from Laubier *et al.*, (2012) converge with the composition of the primitive Taney-A plagioclase melt inclusions (Fig. 8). These compositions could represent the interation and crystallization of a high-Mg type melt with a plagioclase cumulate until the melt becomes plagioclase saturated at ~10.5 wt. % MgO. The point of plagioclase saturation in the ponding melts represents the stage when the process transitions from partial melting of the cumulate to assimilation and crystallization, as recorded in the plagioclase melt inclusions. The presence of high anorthite plagioclase crystals at other near-ridge seamounts and mid-ocean ridges implies that this process may not be unique to Taney-A.

CONCLUSIONS

Erupted MORB is widely thought to represent mantle-derived melts that have been modified mainly by fractional crystallization, and can be back-calculated to equilibrium with the mantle (Klein & Langmuir, 1987). However, in certain magmatic systems, petrologic studies have illustrated that melt-plagioclase cumulate interactions are important. Examples include midocean ridges (Laubier *et al.*, 2012), hot spot-ridge interactions in the Galapagos (Saal *et al.*, 2007), large igneous provinces such as Iceland (Gurenko & Sobolev, 2006), and layered

intrusions such as the Rum complex (Leuthold *et al.*, 2014). An important question is the location of these melt-rock interactions in the magmatic architecture of oceanic systems. Recent understanding of crustal accretion indicates that magma reservoirs are present both in the lower oceanic crust and at shallow depths (Natland & Dick, 2009). Ponding of melt at the Moho provides a favourable environment for melt-rock interaction prior to eruption at the seafloor.

Melt inclusions in plagioclase crystals in lavas erupted at Taney Seamount-A have volatile saturation pressures that indicate crystallization at or near the Moho, indicating the presence of a deeper magma reservoir in near-ridge seamount environments. Furthermore, the melt inclusions exhibit unique chemical signatures that are consistent with melt-plagioclase cumulate interactions, indicating that such interactions play an important role at near-ridge seamounts. Based on our findings, we identify four stages of interaction.

- (1) During formation of the main volcanic edifice, primitive melts ponded laterally at the base of the oceanic crust due to a physical barrier, such as a permeability contrast or zone of deformation, and crystallize to form a differentiated plagioclase-rich cumulate.
- (2) Subsequent aliquots of primitive basalt were injected into the plagioclase cumulate-mush, likely above more dense olivine-rich cumulate. Thermodynamic modelling of plagioclase-rich cumulate partial melting reproduces the unique major and trace element signature of the most primitive Taney Seamount-A melt inclusions.
- (3) The reduction of the plagioclase-cumulate geochemical signal in more evolved melt inclusions is related to continued interaction between the cumulate partial melt and the differentiating basalt. Magma mixing coeval with crystallization produces melt inclusions that are transitional between the primitive and differentiated signals.

(4) Late-stage melts that are more depleted in incompatible elements underwent diffusive interaction with the cumulate pile during porous flow, entraining large plagioclase crystals. These melts erupted on the surface to form the young pillow cones within the most southeastern caldera of Taney Seamount-A.

ACKNOWLEDGEMENTS

We would like to thank the Monterey Bay Aquarium Research Institute (MBARI) for providing an opportunity for J.C. and J.S. to participate in the 2010 Taney Seamounts cruise. We thank the crew of the R.V. *Western Flyer* for ensuring a safe and successful cruise and the operators of the ROV *Doc Ricketts* for collecting precious samples. We also thank the Science Party (Jenny Paduan, Lonny Lundsten, Issy Yeo, Ryan Portner, Lucas Koth, Craig McClain, Justine Jackson-Ricketts, and Sarah Hardy) for their hard work executing the scientific program. Lang Shi provided essential support and advice for electron microprobe analyses at McGill. We thank the Woods Hole Oceanographic Institution and Brian Monteleone for their support during SIMS volatile analysis. We thank Glenn Piercey of the Memorial University of Newfoundland for assistance during SIMS trace element analysis. We are grateful to Gregor Lucic who analyzed H₂O by FTIR in a standard for us. Discussions with Don Baker, Marc-Antoine Longpré, and Roger Nielsen helped improve this manuscript measurably.

This work was funded by scholarships to J.C. from GEOTOP and McGill University, support to D.C. from MBARI through a grant from the David and Lucile Packard Foundation, and grants to J.S. from the Natural Sciences and Engineering Research Council of Canada.

REFERENCES

- Adams, D. T., Nielsen, R. L., Kent, A. J. R. & Tepley, F. J., III. (2011). Origin of minor and trace element compositional diversity in anorthitic feldspar phenocrysts and melt inclusions from the Juan de Fuca Ridge. *Geochemistry Geophysics Geosystems* 12.
- Arevalo, R. & McDonough, W. F. (2010). Chemical variations and regional diversity observed in MORB. *Chemical Geology* **271**, 70-85.
- Asimow, P. D. & Ghiorso, M. S. (1998). Algorithmic modifications extending MELTS to calculate subsolidus phase relations. *American Mineralogist* **83**, 1127-1132.
- Baker, D. R. (2008). The fidelity of melt inclusions as records of melt composition. *Contributions to Mineralogy and Petrology* **156**, 377-395.
- Bedard, J. H. & Hebert, R. (1996). The lower crust of the Bay of Islands ophiolite, Canada: Petrology, mineralogy, and the importance of syntexis in magmatic differentiation in ophiolites and at ocean ridges. *Journal of Geophysical Research-Solid Earth* **101**, 25105-25124.
- Bedard, J. H., Hebert, R., Berclaz, A. & Varfalvy, V. (2000). Syntexis and the genesis of lower oceanic crust. *Ophiolites and Oceanic Crust: New Insights from Field Studies and Ocean Drilling Program*, 105-119.
- Benoit, M., Ceuleneer, G. & Polve, M. (1999). The remelting of hydrothermally altered peridotite at mid-ocean ridges by intruding mantle diapirs. *Nature* **402**, 514-518.
- Brandl, P. A., Beier, C., Regelous, M., Abouchami, W., Haase, K. M., Garbe-Schoenberg, D. & Galer, S. J. G. (2012). Volcanism on the flanks of the East Pacific Rise: Quantitative constraints on mantle heterogeneity and melting processes. *Chemical Geology* **298**, 41-56.
- Canales, J. P., Nedimovic, M. R., Kent, G. M., Carbotte, S. M. & Detrick, R. S. (2009). Seismic reflection images of a near-axis melt sill within the lower crust at the Juan de Fuca ridge. *Nature* **460**, 89-93.
- Cherniak, D. J. (2010). Cation Diffusion in Feldspars. *Reviews in Mineralogy & Geochemistry* **72**, 691-733.
- Clague, D. A., Reynolds, J. R. & Davis, A. S. (2000). Near-ridge seamount chains in the northeastern Pacific Ocean. *Journal of Geophysical Research* **105**, 16541-16561.
- Coogan, L. A., Gillis, K. M., MacLeod, C. J., Thompson, G. M. & Hekinian, R. (2002). Petrology and geochemistry of the lower ocean crust formed at the East Pacific Rise and exposed at Hess Deep: A synthesis and new results. *Geochemistry Geophysics Geosystems* 3.

- Cottrell, E., Spiegelman, M. & Langmuir, C. H. (2002). Consequences of diffusive reequilibration for the interpretation of melt inclusions. *Geochemistry Geophysics Geosystems* 3, 26.
- Coumans, J. P., Stix, J., Clague, D. A. & Minarik, W. G. (2015). The Magmatic Architecture of Taney Seamount-A, NE Pacific Ocean. *Journal of Petrology* **56**, 1037-1067.
- Crawford, W. C. & Webb, S. C. (2002). Variations in the distribution of magma in the lower crust and at the Moho beneath the East Pacific Rise at 9°-10°N. *Earth and Planetary Science Letters* **203**, 117-130.
- Crisp, J. A. (1984). Rates of magma emplacement and volcanic output. *Journal of Volcanology* and Geothermal Research **20**, 177-211.
- Danyushevsky, L. V., Leslie, R. A. J., Crawford, A. J. & Durance, P. (2004). Melt inclusions in primitive olivine phenocrysts: The role of localized reaction processes in the origin of anomalous compositions. *Journal of Petrology* **45**, 2531-2553.
- Danyushevsky, L. V., McNeill, A. W. & Sobolev, A. V. (2002). Experimental and petrological studies of melt inclusions in phenocrysts from mantle-derived magmas: an overview of techniques, advantages and complications. *Chemical Geology* **183**, 5-24.
- Danyushevsky, L. V., Perfit, M. R., Eggins, S. M. & Falloon, T. J. (2003). Crustal origin for coupled 'ultra-depleted' and 'plagioclase' signatures in MORB olivine-hosted melt inclusions: evidence from the Siqueiros Transform Fault, East Pacific Rise. *Contributions to Mineralogy and Petrology* **144**, 619-637.
- Davis, A. S. & Clague, D. A. (2000). President Jackson Seamounts, northern Gorda Ridge: Tectonomagmatic relationship between on- and off-axis volcanism. *Journal of Geophysical Research* **105**, 27939-27956.
- Drouin, M., Godard, M., Ildefonse, B., Bruguier, O. & Garrido, C. J. (2009). Geochemical and petrographic evidence for magmatic impregnation in the oceanic lithosphere at Atlantis Massif, Mid-Atlantic Ridge (IODP Hole U1309D, 30° N). *Chemical Geology* **264**, 71-88.
- Esposito, R., Bodnar, R. J., Danyushevsky, L. V., De Vivo, B., Fedele, L., Hunter, J., Lima, A. & Shimizu, N. (2011). Volatile evolution of magma associated with the solchiaro eruption in the Phlegrean volcanic district (Italy). *Journal of Petrology* **52**, 2431-2460.
- Fornari, D. J., Perfit, M. R., Allan, J. F., Batiza, R., Haymon, R., Barone, A., Ryan, W. B. F., Smith, T., Simkin, T. & Luckman, M. A. (1988). Geochemical and structural studies of the Lamont seamounts: seamounts as indicators of mantle processes. *Earth and Planetary Science Letters* **89**, 63-83.
- Gale, A., Langmuir, C. H. & Dalton, C. A. (2014). The Global Systematics of Ocean Ridge Basalts and their Origin. *Journal of Petrology* **55**, 1051-1082.

- Gale, A., Laubier, M., Escrig, S. & Langmuir, C. H. (2013). Constraints on melting processes and plume-ridge interaction from comprehensive study of the FAMOUS and North Famous segments, Mid-Atlantic Ridge. *Earth and Planetary Science Letters* **365**, 209-220.
- Gao, Y., Hoefs, J., Hellebrand, E., von der Handt, A. & Snow, J. E. (2007). Trace element zoning in pyroxenes from ODP Hole 735B gabbros: diffusive exchange or synkinematic crystal fractionation? *Contributions to Mineralogy and Petrology* **153**, 429-442.
- Ghiorso, M. S. & Sack, R. O. (1995). Chemical mass-transfer in magmatic processes .4. A revised and internally consistent thermodynamic model for the interpolation and extrapolation of liquid-solid equilibria in magmatic systems at elevated-temperatures and pressures. *Contributions to Mineralogy and Petrology* **119**, 197-212.
- Grove, T. L. & Bryan, W. B. (1983). Fractionation of pyroxene-phyric morb at low-pressure an experimental-study. *Contributions to Mineralogy and Petrology* **84**, 293-309.
- Gurenko, A. A. & Sobolev, A. V. (2006). Crust–primitive magma interaction beneath neovolcanic rift zone of Iceland recorded in gabbro xenoliths from Midfell, SW Iceland. *Contributions to Mineralogy and Petrology* **151**, 495-520.
- Hammond, S. R. (1997). Offset caldera and crater collapse on Juan de Fuca Ridge-flank volcanoes. *Bulletin of Volcanology* **58**, 617-627.
- Hann, N. L. (2012). Geochemical diversity of near-ridge seamounts: Insights into oceanic magmatic processes and sources through trace element and isotopic chemistry. *Ph. D.* University of Florida
- Hauri, E., Wang, J. H., Dixon, J. E., King, P. L., Mandeville, C. & Newman, S. (2002). SIMS analysis of volatiles in silicate glasses 1. Calibration, matrix effects and comparisons with FTIR. *Chemical Geology* **183**, 99-114.
- Helo, C., Longpre, M.-A., Shimizu, N., Clague, D. A. & Stix, J. (2011). Explosive eruptions at mid-ocean ridges driven by CO₂-rich magmas. *Nature Geoscience* **4**, 260-263.
- Hildreth, W. & Moorbath, S. (1988). Crustal contributions to arc magmatism in the Andes of Central Chile. *Contributions to Mineralogy and Petrology* **98**, 455-489.
- Kamenetsky, V. S. & Gurenko, A. A. (2007). Cryptic crustal contamination of MORB primitive melts recorded in olivine-hosted glass and mineral inclusions. *Contributions to Mineralogy and Petrology* **153**, 465-481.
- Kelemen, P. B., Koga, K. & Shimizu, N. (1997). Geochemistry of gabbro sills in the crust-mantle transition zone of the Oman ophiolite: Implications for the origin of the oceanic lower crust. *Earth and Planetary Science Letters* **146**.
- Kent, A. J. R. (2008). Melt Inclusions in Basaltic and Related Volcanic Rocks. *Minerals, Inclusions and Volcanic Processes* **69**, 273-331.

- Klein, E. M. & Langmuir, C. H. (1987). Global correlations of ocean ridge basalt chemistry with axial depth and crustal thickness. *Journal of Geophysical Research-Solid Earth and Planets* **92**, 8089-8115.
- Koepke, J., Berndt, J., Feig, S. T. & Holtz, F. (2007). The formation of SiO₂-rich melts within the deep oceanic crust by hydrous partial melting of gabbros. *Contributions to Mineralogy and Petrology* **153**, 67-84.
- Kohut, E. J. & Nielsen, R. L. (2003). Low-pressure phase equilibria of anhydrous anorthite-bearing mafic magmas. *Geochemistry Geophysics Geosystems* **4**.
- Korenaga, J. & Kelemen, P. B. (1997). Origin of gabbro sills in the Moho transition zone of the Oman ophiolite: Implications for magma transport in the oceanic lower crust. *Journal of Geophysical Research-Solid Earth* **102**, 27729-27749.
- Kvassnes, A. J. S. & Grove, T. L. (2008). How partial melts of mafic lower crust affect ascending magmas at oceanic ridges. *Contributions to Mineralogy and Petrology* **156**, 49-71.
- Lange, A. E., Nielsen, R. L., Tepley, F. J. & Kent, A. J. R. (2013). The petrogenesis of plagioclase-phyric basalts at mid-ocean ridges. *Geochemistry Geophysics Geosystems* **14**, 3282-3296.
- Langmuir, C. H., Klein, E. M. & Plank, T. (1992). Petrological systematics of mid-ocean ridge basalts: Constraints on melt generation beneath ocean ridges. In: Phipps Morgan, J., Blackman, D. K. & Sinton, J. M. (eds.) *Mantle Flow and Melt Generation at Mid-Ocean Ridges. American Geophysical Union Monograph* **71**, 183-280.
- Laubier, M., Gale, A. & Langmuir, C. H. (2012). Melting and crustal processes at the FAMOUS segment (Mid-Atlantic Ridge): New insights from olivine-hosted melt inclusions from multiple samples. *Journal of Petrology* **53**, 665-698.
- Leuthold, J., Blundy, J. D., Holness, M. B. & Sides, R. (2014). Successive episodes of reactive liquid flow through a layered intrusion (Unit 9, Rum Eastern Layered Intrusion, Scotland). *Contributions to Mineralogy and Petrology* **168**.
- Lissenberg, C. J. & Dick, H. J. B. (2008). Melt–rock reaction in the lower oceanic crust and its implications for the genesis of mid-ocean ridge basalt. *Earth and Planetary Science Letters* **271**, 311-325.
- Lissenberg, C. J., MacLeod, C. J., Howard, K. A. & Godard, M. (2013). Pervasive reactive melt migration through fast-spreading lower oceanic crust (Hess Deep, equatorial Pacific Ocean). *Earth and Planetary Science Letters* **361**, 436-447.
- McDonough, W. F. & Sun, S. S. (1995). The composition of the Earth. *Chemical Geology* **120**, 223-253.

- Michael, P. J. & Cornell, W. C. (1998). Influence of spreading rate and magma supply on crystallization and assimilation beneath mid-ocean ridges: Evidence from chlorine and major element chemistry of mid-ocean ridge basalts. *Journal of Geophysical Research-Solid Earth* **103**.
- Natland, J. H. & Dick, H. J. B. (2001). Formation of the lower ocean crust and the crystallization of gabbroic cumulates at a very slowly spreading ridge. *Journal of Volcanology and Geothermal Research* **110**, 191-233.
- Natland, J. H. & Dick, H. J. B. (2009). Paired melt lenses at the East Pacific Rise and the pattern of melt flow through the gabbroic layer at a fast-spreading ridge. *Lithos* **112**.
- Newman, S. & Lowenstern, J. B. (2002). VOLATILECALC: a silicate melt-H₂O-CO₂ solution model written in Visual Basic for excel. *Computers & Geosciences* **28**.
- Nielsen, R. L. (2011). The effects of re-homogenization on plagioclase hosted melt inclusions. *Geochemistry Geophysics Geosystems* **12**.
- Nielsen, R. L., Sours-Page, R. E. & Harpp, K. S. (2000). Role of a Cl-bearing flux in the origin of depleted ocean floor magmas. *Geochemistry, Geophysics, Geosystems* 1, 1007.
- Niu, Y. & O'Hara, M. J. (2008). Global correlations of ocean ridge basalt chemistry with axial depth: A new perspective. *Journal of Petrology* **49**.
- Niu, Y., Regelous, M., Wendt, I. J., Batiza, R. & O'Hara, M. J. (2002). Geochemistry of near-EPR seamounts: importance of source vs. process and the origin of enriched mantle component. *Earth and Planetary Science Letters* **199**, 327-345.
- O'Neill, H. S. C. & Jenner, F. E. (2012). The global pattern of trace-element distributions in ocean floor basalts. *Nature* **491**.
- Perk, N. W., Coogan, L. A., Karson, J. A., Klein, E. M. & Hanna, H. D. (2007). Petrology and geochemistry of primitive lower oceanic crust from Pito Deep: implications for the accretion of the lower crust at the Southern East Pacific Rise. *Contributions to Mineralogy and Petrology* **154**, 575-590.
- Portner, R. A., Clague, D. A. & Paduan, J. B. (2014). Caldera formation and varied eruption styles on North Pacific seamounts: the clastic lithofacies record. *Bulletin of Volcanology* **76**.
- Qin, Z. W., Lu, F. Q. & Anderson, A. T. (1992). Diffusive reequilibration of melt and fluid inclusions. *American Mineralogist* **77**, 565-576.
- Quick, J. E. & Denlinger, R. P. (1993). Ductile deformation and the origin of layered gabbro in ophiolites. *Journal of Geophysical Research-Solid Earth* **98**, 14015-14027.

- Ridley, W. I., Perfit, M. R., Smith, M. C. & Fornari, D. J. (2006). Magmatic processes in developing oceanic crust revealed in a cumulate xenolith collected at the East Pacific Rise, 9 degrees 50 'N. *Geochemistry Geophysics Geosystems* 7.
- Roedder, E. (1979). Origin and significance of magmatic inclusions. *Bulletin De Mineralogie* **102**, 487-510.
- Saal, A. E., Hauri, E. H., Langmuir, C. H. & Perfit, M. R. (2002). Vapour undersaturation in primitive mid-ocean-ridge basalt and the volatile content of Earth's upper mantle. *Nature* **419**.
- Saal, A. E., Kurz, M. D., Hart, S. R., Blusztajn, J. S., Blichert-Toft, J., Liang, Y. & Geist, D. J. (2007). The role of lithospheric gabbros on the composition of Galapagos lavas. *Earth and Planetary Science Letters* 257, 391-406.
- Scheirer, D. S. & Macdonald, K. C. (1995). Near-axis seamounts on the flanks of the East Pacific Rise, 8°N to 17°N. *Journal of Geophysical Research* **100**, 2239–2259.
- Shaw, A. M., Behn, M. D., Humphris, S. E., Sohn, R. A. & Gregg, P. M. (2010). Deep pooling of low degree melts and volatile fluxes at the 85 degrees E segment of the Gakkel Ridge: Evidence from olivine-hosted melt inclusions and glasses. *Earth and Planetary Science Letters* **289**, 311-322.
- Singh, S. C., Harding, A. J., Kent, G. M., Sinha, M. C., Combier, V., Bazin, S., Tong, C. H., Pye, J. W., Barton, P. J., Hobbs, R. W., White, R. S. & Orcutt, J. A. (2006). Seismic reflection images of the Moho underlying melt sills at the East Pacific Rise. *Nature* **442**, 287-290.
- Smith, P. M. & Asimow, P. D. (2005). Adiabat_1ph: A new public front-end to the MELTS, pMELTS, and pHMELTS models. *Geochemistry Geophysics Geosystems* **6**.
- Sobolev, A. V. & Shimizu, N. (1993). Ultra-depleted primary melt included in an olivine from the Mid-Atlantic ridge. *Nature* **363**, 151-154.
- Spandler, C., O'Neill, H. S. C. & Kamenetsky, V. S. (2007). Survival times of anomalous melt inclusions from element diffusion in olivine and chromite. *Nature* **447**, 303-306.
- Stix, J., Gauthier, G. & Ludden, J. N. (1995). A critical-look at quantitative laser-ablation ICP-MS analysis of natural and synthetic glasses. *Canadian Mineralogist* **33**, 435-444.
- Wanless, V. D., Behn, M. D., Shaw, A. M. & Plank, T. (2014). Variations in melting dynamics and mantle compositions along the Eastern Volcanic Zone of the Gakkel Ridge: insights from olivine-hosted melt inclusions. *Contributions to Mineralogy and Petrology* **167**.
- Wanless, V. D. & Shaw, A. M. (2012). Lower crustal crystallization and melt evolution at midocean ridges. *Nature Geoscience* **5**.

Wanless, V. D., Shaw, A. M., Behn, M. D., Soule, S. A., Escartin, J. & Hamelin, C. (2015). Magmatic plumbing at Lucky Strike volcano based on olivine-hosted melt inclusion compositions. *Geochemistry Geophysics Geosystems* **16**, 126-147.

Table 1: Corrected major, trace, and volatile element data for melt inclusions and matrix glasses

from Taney Seamount-A.

Table 1. Corrected major, trace, and volatile element data for melt inclusions and matrix glasses from Taney Seamount-A	najor, trace, and \	olatile element	data tor melt inc	lusions and mat	rix glasses rroi	II Iariey Seario	urit-A			
Sample	D176_R3	D176_R3	D176_R3	D176_R3	D176_R3	D176_R3	D176_R3	D176_ R3	D176_R3	D176_R3
Plagioclase #	~	_	7	7	က	က	2	2	9	8
# I W	_	2	_	2	_	2	-	1 (R)	_	~
% PEC	6	6		15	10	41			о	∞
SiO ₂	49.2	48.9	49.0	48.7	49.2	48.9			49.2	48.9
TO ₂	0.41	0.43	1.40	1.56	0.33	0.33			0.33	0.95
Al ₂ O ₃	17.3	17.5	15.5	15.7	17.9	17.9			17.6	17.4
FeO _T	8.9	8.7	11.2	11.1	7.9	8.1			8.1	9.0
MnO	0.157	960.0	0.152	0.168	0.136	0.160			0.182	0.135
MgO	8.88	9.10	7.06	7.14	9.65	9.63			9.44	8.89
CaO	12.2	12.0	11.3	12.1	12.1	12.2			12.2	11.9
Na_2O	2.58	2.51	2.86	2.31	2.38	2.34			2.45	2.44
K ₂ 0	0.136	0.152	0.198	0.156	0.110	0.144			0.125	0.129
La	2.32	2.25	4.79	4.53	1.60	1.21	1.26	1.40	1.67	3.30
8	7.42	6.48	15.68	14.38	4.20	3.70	1.90	2.31	4.77	09.6
P	6.98	5.40	11.76	11.25	4.31	2.43	1.67	2.06	3.73	8.32
Sm	1.54	1.91	4.01	3.83	1.29	0.40	0.53	0.25	1.09	2.05
围	1.35	1.43	1.69	1.53	1.06	0.73	0.19	0.50	1.25	1.61
Š	2.10	2.03	6.81	4.50	1.46	0.94	0.99	0.77	1.41	2.45
Ъ	1.43	1.25	3.18	3.75	0.71	0.64	0.70	0.88	0.11	1.81
Yb	0.91	1.01	2.67	2.57	0.53	0.29	0.57	0.88	0.55	1.03
Ö	320	323	234	208	309	234	274	277	345	314
Ba	21.59	19.83	23.25	27.81	16.11	12.97	52.55	29.56	25.63	18.56
ζĊ	193	177	179	189	167	184	156	188	176	191
Q	0.71	0.68	4.63	3.89	0.51	0.27	2.28	2.59	0.57	2.25
>	12.9	12.5	33.1	29.0	6.7	4.9	4.4	4.3	5.9	14.9
Zr	14.3	15.9	102.1	93.8	11.8	7.7	47.9	48.2	9.7	58.5
8		1904	617		1278	3550			1204	
H ₂ O	0.34	0.32	0.38	0.42	0.29	0.28			0.33	0.37
L	234	222	212	189	224	204			247	245
S	888	898	1306	1095	260	269			829	821
۵	222	216	265	284	178	169			207	
Notes: Major elements and H ₂ O ex systematic instrumental drift based		pressed in w eight per cent, trace on deviation from the know n valu	per cent, trace the know n valu	elements and o le of P1326-2 (s	ther volatiles in supplementary i	ppm. MgO corr nformation S1).	ected to VG-2 = The data have	pressed in w eight per cent, trace elements and other volatiles in ppm. MgO corrected to VG-2 = 7.07 wt. %. Water has been corrected for lon deviation from the know n value of P1326-2 (supplementary information S1). The data have been corrected for post-entrapment	ater has been c for post-entrapr	orrected for nent

crystallization (% PEC). The totals for the uncorrected data are presented in supplementary information S2.

Plagioclase #	D176_R3	D176_R3	D176_R3	D176_R3	D176_R17	D176_R17	D176_R17	D176_R17	D176_R17
)		13	13	14	_	3	12	13	13
# I W		_	2	_	~	~	~	_	2
% PEC		17	∞	12	6	2	∞	9	7
SiO ₂		49.0	48.8	49.6	49.0	49.5	49.2	49.4	49.5
TiO ₂		0.48	0.56	0.43	0.71	0.79	0.78	0.57	0.61
Al ₂ O ₃		17.6	17.1	17.0	17.1	17.1	17.3	17.2	17.2
FeO _T		9.5	9.5	8.8	8.8	8.8	8.5	8.2	8.0
MnO		0.169	0.173	0.147	0.145	0.120	0.157	0.157	0.183
MgO		8.74	8.54	8.88	8.89	8.85	9.15	9.26	9.31
CaO		12.5	12.0	11.9	12.1	12.1	12.0	12.1	11.9
Na ₂ O		2.32	2.54	2.42	2.43	2.65	2.62	2.56	2.62
K ₂ O		0.151	0.168	0.145	0.158	0.136	0.136	0.120	0.131
La		1.76	1.91	1.53	2.63	2.93	2.95	2.46	2.67
లి		6.05	5.89	4.20	76.7	8.41	9.01	7.36	7.21
PN		4.93	5.56	3.53	80.9	7.31	7.04	5.55	5.03
Sm		0.88	1.33	0.73	1.56	1.64	1.81	2.15	1.99
B		1.17	1.03	0.99	1.42	1.39	1.60	1.17	1.29
à		1.83	1.69	0.61	1.81	2.40	2.53	1.93	1.89
ம்		0.67	0.92	0.48	1.17	1.71	1.24	1.18	1.25
Yb		0.77	1.03	0.45	06.0	1.08	1.11	0.93	1.40
Ö		245	244	247	333	351	341	337	319
Ba		14.35	13.41	14.88	17.52	22.24	18.73	16.30	15.31
Š		183	180	193	177	181	182	179	179
2		0.69	0.70	0.33	1.90	2.01	2.34	1.95	1.52
>-		9.4	10.8	5.1	9.6	12.2	13.4	11.0	10.2
Zr		11.8	14.6	8.2	34.6	38.3	45.9	40.3	24.6
005	1298				3939	1271	1144		
H ₂ O					0.25	0.30	0.28		
L					173	221	202		
S					999	803	841		
O					164	198	178		

500									
Sample	D176_R17	D176_R20							
Plagioclase #	13	_	2	က	က	9	9	9	7
# ■	3	_	2	~	2	_	2	ო	_
% PEC		1		2		41	41	15	7
SiO ₂		48.7	49.6	50.4		48.7	48.5	48.8	48.9
TIO ₂		0.75	1.87	99.0		0.29	0.25	0.23	0.88
Al ₂ O ₃		18.1	16.1	16.6		18.6	18.7	18.8	17.0
FeO _T		8.1	10.0	8.6		7.1	7.1	7.2	9.3
MnO		0.097	0.155	0.171		0.120	0.100	0.100	0.148
MgO		69.6	6.97	8.76		10.39	10.45	10.42	8.57
CaO		11.8	10.7	11.4		12.1	12.1	12.0	11.7
Na ₂ O		2.42	3.06	2.75		2.25	2.29	2.27	2.65
K ₂ 0		0.127	0.390	0.165		0.122	0.124	0.120	0.167
La		2.46		2.33		1.84	1.89	1.47	3.22
පී		7.53		7.07		5.63	5.50	5.34	9.33
P		6.97		5.89		3.51	4.06	4.02	8.25
Sm		1.98		1.30		1.00	1.47	1.22	2.41
긢		1.04		1.16		06.0	96.0	1.02	1.27
<u>~</u>		3.06		1.83		1.40	1.37	1.85	3.26
Ъ		1.35		1.16		0.87	0.74	0.57	1.47
Yb		1.74		0.78		0.74	0.67	0.57	1.25
Ö		316		296		207	224	220	301
Ba		23.68		18.65		13.07	13.47	12.23	15.99
Š		172		182		172	158	166	169
2		0.95		0.74		0.10	0.09	0.03	2.10
>-		16.2		9.8		8.6	9.1	8.6	16.8
Zr		24.3		17.8		2.2	1.9	1.3	40.3
80	1946	1417		1257					
H ₂ O	0.32	0.31	0.35	0.29	0.31			0:30	0.31
ш	232	237	203	223	232			202	225
S	825	857	1185	741	992			611	707
۵	184	96	103	168	179			75	26

505									
Sample	D176_R20								
Plagioclase #	6	6	6	6	6	11	11	11	11
#IW	_	2	3	4	2	_	2	က	4
% PEC	11	1	1		1	12	12	1	11
SiO ₂	48.9	49.1	49.1		49.0	49.0	49.2	49.2	48.7
TIO ₂	0.34	0.29	0.38		0.34	0.44	0.40	0.35	0.36
AI ₂ O ₃	18.1	18.0	18.2		18.0	18.3	18.0	18.0	17.9
FeO _⊤	7.5	7.3	7.6		7.6	7.9	7.5	7.5	7.4
MnO	0.187	0.167	0.112		0.104	0.174	0.153	0.189	0.105
MgO	66.6	10.03	9.95		9.91	9.85	96.6	9.94	96.6
CaO	11.9	12.0	11.9		11.8	11.9	11.9	11.9	11.8
Na ₂ O	2.37	2.34	2.33		2.28	2.32	2.39	2.38	2.37
K ₂ O	0.104	0.109	0.111		0.101	0.114	0.125	0.108	0.110
La	1.54	1.59	1.76	2.08	1.65	2.42	1.96	1.88	1.54
Se	4.32	4.22	4.97	6.05	5.13	7.07	5.66	4.77	4.64
PN	2.48	3.55	3.80	5.10	4.37	6.34	3.91	4.14	4.53
Sm	1.59	0.73	1.40	0.78	1.35	1.90	1.35	1.16	0.76
B	0.88	1.07	1.20	1.04	1.16	1.36	1.06	1.15	1.18
ò	0.90	1.06	1.10	1.24	1.50	2.42	1.36	1.76	1.29
Ъ	0.61	0.51	0.77	0.85	0.89	1.12	1.05	0.65	0.65
Yb	0.42	0.45	0.54	0.64	0.62	1.01	0.86	0.78	0.55
Ö	282	284	313	339	295	307	302	303	234
Ba	14.03	15.19	15.68	16.32	14.59	15.92	14.34	14.68	16.68
Š	154	152	164	160	170	172	171	170	218
Q	0.11	0.19	0.80	0.69	0:30	0.54	0.21	0.18	0.22
>-	6.4	4.9	6.7	7.3	7.2	12.3	9.1	8.2	9.9
Zr	1.9	4.3	15.9	18.1	8.3	14.9	6.1	4.4	5.1
co ₂							1193		1789
H ₂ O							0:30	0.31	0.33
L							223	230	229
S							716	790	785
O							46	85	80

Sample	D176_R20									
Plagioclase #	11	11	13	13	14	14	14	14	14	18
# W	2	9	~	7	_	7	က	4	2	_
% PEC	1		2	9	4	15	4	15	15	13
SiO ₂	49.2		49.9	50.4	48.3	48.6	48.8	48.5	48.5	48.3
TiO ₂	0.48		0.55	0.71	0.43	0.45	0.42	0.40	0.40	0.58
AI_2O_3	18.2		16.8	16.9	18.5	18.8	18.6	18.4	18.4	18.3
FeO _⊤	7.6		8.7	9.1	7.3	7.4	7.3	7.2	7.2	7.6
MnO	0.102		0.157	0.167	0.149	0.099	0.134	0.157	0.157	0.130
MgO	9.94		8.77	8.62	10.29	10.32	10.27	10.27	10.27	10.02
CaO	11.8		11.7	11.7	12.0	12.1	12.1	12.0	12.0	12.0
Na ₂ O	2.40		2.68	2.84	2.29	2.23	2.31	2.25	2.25	2.24
K ₂ 0	0.114		0.158	0.163	0.116	0.119	0.099	0.119	0.119	0.106
La	2.01	2.11	2.58	2.52	2.29	2.53	2.56	2.09		2.37
පී	5.40	5.87	7.24	7.53	7.19	7.13	7.15	6.14		7.16
P	4.08	4.46	5.79	6.40	5.71	5.36	5.15	4.57		6.53
Sm	1.36	1.82	2.18	1.63	2.00	2.34	1.07	1.29		2.58
III	1.03	1.13	1.16	1.37	1.23	1.37	1.12	1.33		1.09
à	1.09	1.48	2.75	2.26	2.25	2.14	2.06	2.32		2.16
Ъ	0.67	0.93	1.15	1.06	1.64	1.25	1.15	1.25		1.65
Yb	0.51	0.81	1.13	0.39	1.16	1.04	0.65	0.97		1.18
ŏ	295	328	338	313	302	273	300	307		221
Ba	15.56	17.21	20.82	19.32	20.87	20.32	14.48	14.70		14.75
ග්	153	149	179	187	175	166	171	172		191
Q	0.34	0.57	1.31	1.35	0.50	0.64	0.49	0.34		1.74
>	8.7	10.1	13.1	11.3	12.8	13.4	12.4	11.9		14.7
Zr	10.2	11.8	35.2	31.8	12.6	15.0	11.8	10.1		25.1
8	1262				1334	1160			1104	
H ₂ O	0.32				0.28	0.29			0.29	0:30
ш	225				221	223			225	
S	739				754	759			777	200
Q	99				42	40			42	

Sample	D176_R20	D176_R24	D176_R3	D176_R20						
Pagioclase #	19	20	20	22	23	23	25	11	9	18
# W	_	-	1 (R)	_	-	1 (R)	-	~	7	7
% PEC	12			1	9		9	8	26	21
SiO ₂	49.1	49.6	49.3	48.9	49.6		50.1	48.2	47.6	48.0
TIO ₂	0.29	1.62	1.68	0.54	1.00		0.93	0.89	0.34	0.44
Al ₂ O ₃	18.1	15.7	15.6	18.4	16.8		17.0	18.0	17.8	18.6
FeO _T	9.7	10.6	10.4	9.7	8.8		9.1	8.5	8.3	7.3
MnO	0.182	0.184	0.182	960.0	0.171		0.212	0.138	0.199	0.147
MgO	9.95	6.82	6.85	10.02	8.75		8.65	9.42	9.50	10.30
CaO	11.9	11.3	11.3	11.9	11.9		11.8	11.7	13.2	12.5
Na_2O	2.40	2.86	2.93	2.44	2.64		2.68	2.17	1.80	1.99
K ₂ O	0.119	0.293	0.340	0.128	0.160		0.176	0.149	0.095	0.114
La	1.50	10.13	9.53	1.37	2.78	2.82	3.45	3.60	1.44	2.20
පී	4.29	22.49	26.34	4.22	8.06	8.13	9.68	10.54	4.48	6.92
P	2.89	16.02	17.78	2.94	8.14	7.39	7.80	8.17	3.14	5.83
Sm	1.23	2.89	5.43	1.10	1.26	2.97	1.16	2.18	0.85	1.26
田	1.17	1.52	2.13	0.75	0.71	1.13	0.79	1.21	1.19	1.1
à	0.99	5.61	6.01	1.28	2.32	2.43	2.65	2.85	1.33	2.60
Ъ	0.62	3.09	3.66	0.73	1.19	1.69	1.96	2.01	0.58	1.71
Yb	0.32	2.38	3.49	0.75	1.44	1.13	1.75	0.98	0.48	1.1
Ö	284	155	184	166	252	267	286	337	291	216
Ba	14.69	49.46	53.08	21.13	18.94	15.69	20.14	18.40	18.06	16.04
Š	155	199	222	242	172	206	175	183	173	173
2	0.12	8.49	9.52	0.40	2.24	2.62	2.08	3.38	0.75	0.47
>-	4.4	29.4	32.6	6.4	13.7	14.9	16.4	15.0	6.3	13.4
Zr	3.0	115.0	129.1	12.3	46.0	46.9	50.1	59.8	15.5	11.6
80		1261	1623							
μo		0.34	0.36	0.33	0.34		0.35		0.29	0.30
L		207	210	229	225		228		201	
S		1289	1306	803	841		890		899	699
Ö		181	187	134	174		202		177	

Sample	D176_R20	D176_R24	D176_R24	D176_R3	D176_R17	D176_R20	D176_R24
Pagioclase #	18	2	2				
#₩	က	_	7	Matrix	Matrix	Matrix	Matrix
% PEC	11	7	7				
SiO ₂	47.4	49.5	49.2	48.9	48.6	48.8	47.6
<u>10</u> 2	0.44	0.56	0.52	1.49	1.43	1.54	1.17
4I ₂ O ₃	17.5	18.0	18.3	16.0	16.3	16.1	16.8
-eO₁	7.9	8.4	8.4	10.2	6.6	10.3	10.6
M PO	0.149	0.144	0.146	0.192	0.178	0.165	0.187
VgO	9.52	9.44	9.56	7.83	8.04	7.87	8.61
CaO	12.0	11.0	11.0	11.8	11.9	11.9	11.8
Va ₂ O	2.27	2.55	2.45	2.84	2.75	2.79	2.51
%0	0.124	0.173	0.205	0.210	0.193	0.197	0.117
р	2.31	2.13	2.46	5.31	4.96	5.30	2.92
ළ	7.76	5.55	6.54	14.56	13.65	13.81	7.70
9	6.72	4.10	4.34	11.91	11.38	12.04	8.00
Sm	1.56	1.21	1.47	3.79	3.60	3.72	2.98
æ	1.18	0.89	1.17	1.32	1.30	1.38	1.11
Š	2.73	1.06	1.65	5.17	5.00	5.29	4.89
'n	1.37	99.0	0.70	3.01	3.04	3.23	2.99
q)	1.41	0.44	0.50	2.88	2.80	2.81	2.82
Ċ	260	256	283	229	261	290	241
3a	17.80	17.60	22.19	44.41	37.25	33.01	14.64
ά	171	199	168	196	194	198	155
9	1.17	0.33	0.41	5.55	5.07	5.38	2.58
~	15.6	6.4	6.9	29.5	28.7	28.7	27.0
Zr	17.7	9.4	9.4	101.6	2.96	100.3	70.0
202				124	92	88	142
양		0.21		0.40	0.33	0.34	0.23
		143		239	219	225	147
"		615		1000	992	1015	952
7				007			•

Table 2: Plagioclase major element data from Taney Seamount-A

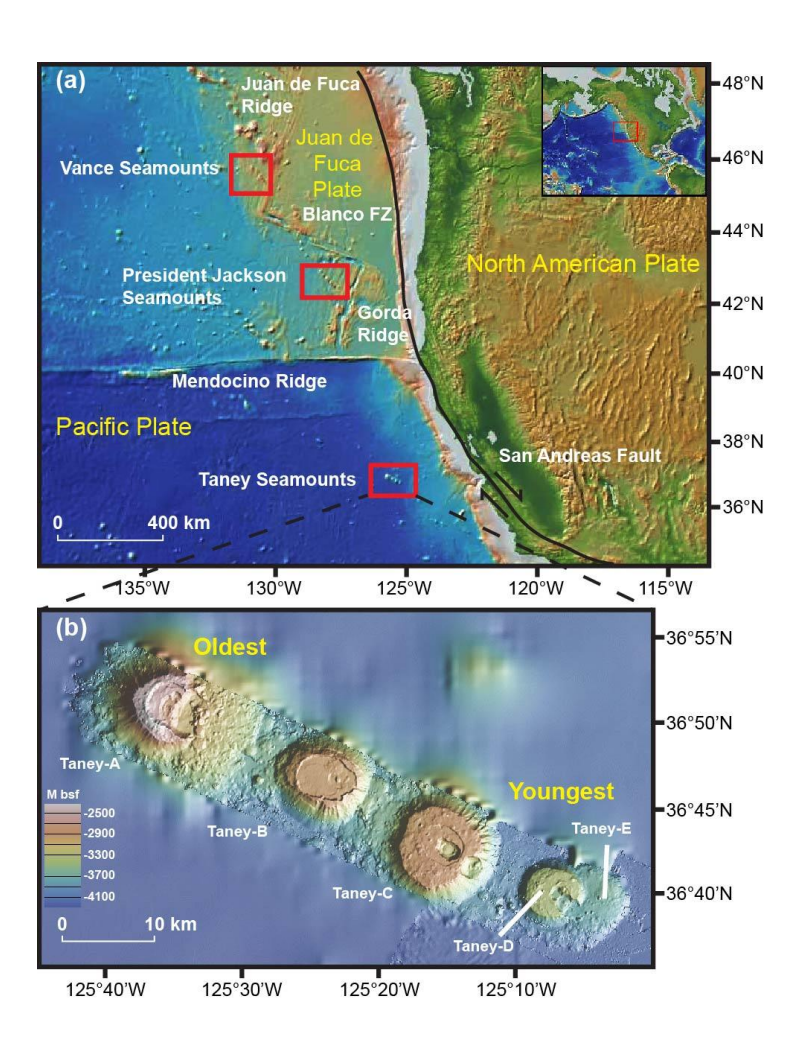
Sample	D176_R3	D176_R3	D176_R3	D176_R3	D176_R3	D176_R3	D176_R3	D176_R3	D176_R3	D176_R3
Plagioclase #	-	-	2	2	3	3	9	8	8	6
#IW	~	2	_	2	-	2	_	_	2	~
SiO ₂	46.2	46.3	47.3	49.0	46.1	46.1	46.3	46.6	47.0	46.4
TIO ₂	0.02	0.02	0.02	0.00	0.02	0.04	0.00	0.03	0.00	0.01
Al ₂ O ₃	33.6	33.4	32.7	32.1	33.7	33.6	33.4	33.5	33.3	33.7
FeO _T	0.4	0.5	0.5	0.5	0.4	0.4	0.4	0.4	0.4	0.4
MgO	0.15	0.16	0.15	0.18	0.17	0.17	0.17	0.16	0.20	0.15
CaO	17.6	17.6	16.7	15.7	17.6	17.7	17.6	17.2	17.0	17.7
Na ₂ O	1.36	1.36	1.89	2.48	1.43	1.40	1.40	1.61	1.75	1.38
K ₂ 0	0.022	0.055	0.027	0.025	0.018	0.005	0.030	0.025	0.017	0.021
Total	98.36	99.39	99.29	66.66	99.47	99.52	99.37	99.55	99.57	99.73
mol fraction An	0.88	0.88	0.83	0.78	0.87	0.87	0.87	0.86	0.84	0.88
Table 2. Continued										
Sample	D176_R3	D176_R3	D176_R3	D176_R17	D176_R17	D176_R17	D176_R17	D176_R17	D176_R17	D176_R20
Plagioclase #	13	13	14	1	3	12	13	13	13	1
#IW	~	2	_	2	~	_	_	2	က	~
SiO ₂	45.9	46.0	47.3	46.7	46.5	46.4	46.5	46.5	46.5	46.3
TIO ₂	0.03	0.00	0.02	0.04	0.02	0.01	00.00	0.03	0.03	0.01
Al ₂ O ₃	33.7	33.6	33.2	33.4	33.4	33.2	33.6	33.3	33.3	33.7
FeO _⊤	0.4	0.4	0.4	0.4	0.4	0.4	0.4	0.4	0.4	0.3
MgO	0.13	0.16	0.19	0.18	0.16	0.18	0.18	0.16	0.16	0.16
CaO	17.7	17.7	16.9	17.2	17.4	17.3	17.3	17.2	17.2	17.5
Na ₂ O	1.38	1.34	1.75	1.66	1.53	1.53	1.52	1.55	1.55	1.42
K ₂ O	0.028	0.039	0.011	0.043	0.029	0.019	0.027	0.018	0.018	0.020
Total	99.32	99.30	99.64	69.66	99.44	20.66	99.60	99.22	99.22	99.49
mol fraction An	0.88	0.88	0.84	0.85	0.86	98.0	0.86	0.86	0.86	0.87

Sample	D176_R20									
Hagioclase #	2	2	3	9	9	9	7	6	6	6
# W	_	2,3	1,2	_	7	က	_	~	2	ဇ
SiO ₂	47.6	47.9	47.9	45.7	45.8	46.2	46.9	46.8	46.7	46.8
TIO ₂	0.01	0.05	0.00	0.02	0.00	0.00	0.02	0.02	0.02	0.02
Al ₂ O ₃	33.0	32.5	32.5	33.6	33.8	34.3	33.4	33.3	33.5	33.3
FeO₁	0.4	0.5	0.4	0.3	0.4	0.3	0.4	0.3	0.3	0.3
MgO	0.12	0.14	0.19	0.18	0.17	0.19	0.17	0.20	0.17	0.18
CaO	16.7	16.2	16.4	17.7	17.7	17.9	17.1	17.2	17.4	17.2
Na ₂ O	1.93	2.18	2.11	1.26	1.30	1.31	1.67	1.61	1.54	1.62
K 20	0.040	0.042	0.027	0.033	0.024	0.015	0.021	0.025	0.028	0.018
Total	99.75	99.42	99.48	98.72	99.13	100.17	29.66	99.45	99.72	99.50
mol fraction An	0.83	0.80	0.81	0.89	0.88	0.88	0.85	0.86	0.86	0.85
Table 2. Continued										
Sample	D176_R20									
Plagioclase #	6	11	11	11	11	13	13	14	14	14
# I W	4,5	_	7	ო	4,5,6	_	2	~	2	ဇ
SiO ₂	46.6	46.8	46.6	46.4	46.7	47.4	47.9	46.1	46.0	46.3
TIO2	0.02	0.00	0.00	0.00	0.03	0.02	0.03	0.03	0.01	0.00
AI_2O_3	33.3	33.6	33.5	33.8	33.6	33.1	32.4	34.3	34.0	33.8
FeO₁	0.3	0.4	0.3	0.4	0.3	0.4	0.4	0.3	0.3	0.3
MgO	0.16	0.18	0.19	0.18	0.19	0.18	0.19	0.19	0.17	0.17
CaO	17.5	17.4	17.4	17.5	17.4	16.9	16.4	17.9	17.8	17.8
Na ₂ O	1.50	1.62	1.52	1.48	1.46	1.76	2.10	1.32	1.26	1.34
K ₂ 0	0.023	0.031	0.002	0.031	0.013	0.027	0.033	0.024	0.020	0.009
Total	99.51	99.93	99.48	99.74	99.80	99.76	99.49	100.12	99.53	99.74
mol fraction An	0.87	0.86	0.86	0.87	0.87	0.84	0.81	0.88	0.89	0.88

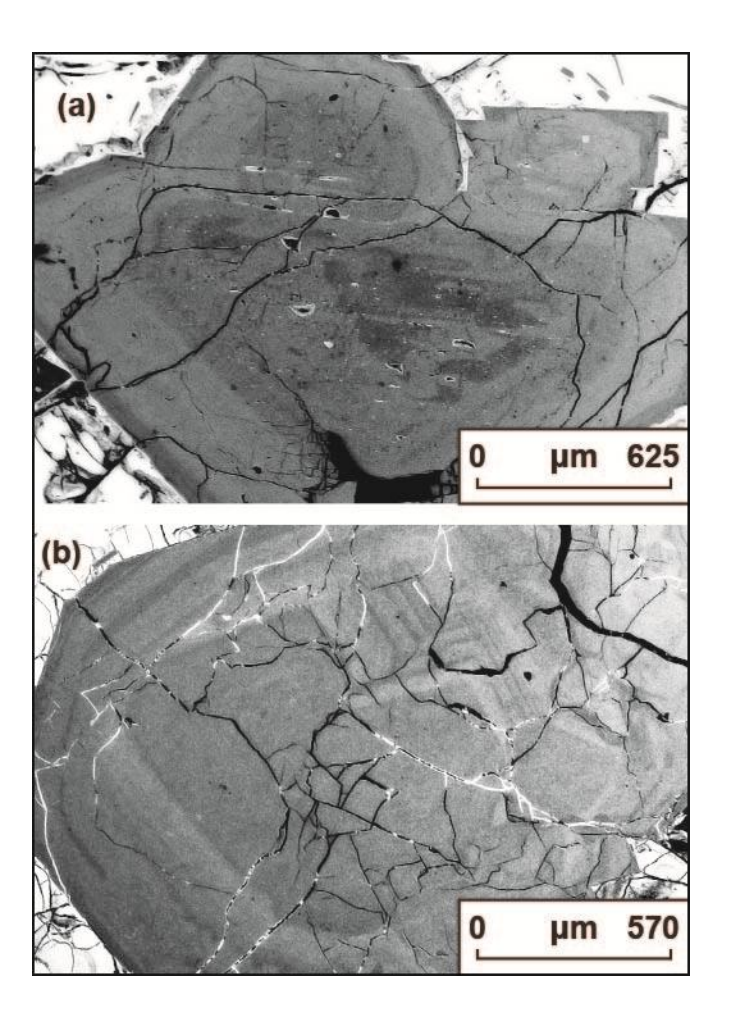
Sample	D176_R20	D176_R24	D176_R3	D176_R20						
Plagioclase #	14	18	19	20	22	23	25	11	9	18
# I W	4,5	_	~	~	~	-	_	_	7	2
SiO ₂	45.8	46.2	46.7	48.2	46.7	47.5	47.3	46.6	46.4	45.9
TiO ₂	0.02	0.03	0.02	0.05	0.01	0.03	0.02	0.02	0.01	0.00
AI ₂ O ₃	33.9	33.9	33.4	32.1	33.7	33.2	33.0	33.3	33.6	34.0
FeO _⊤	0.3	0.4	0.3	0.5	0.3	0.4	9.0	0.4	0.4	0.3
MgO	0.18	0.24	0.18	0.15	0.17	0.19	0.17	0.18	0.18	0.18
CaO	17.9	17.6	17.2	16.1	17.5	16.8	16.9	17.4	17.5	17.9
Na ₂ O	1.30	1.35	1.60	2.26	1.48	1.86	1.86	1.50	1.42	1.30
K ₂ O	0.024	0.024	0.029	0.046	0.022	0.030	0.029	0.026	0.018	0:030
Total	99.41	99.79	99.46	99.44	96.66	99.92	99.73	99.35	99.50	69.66
mol fraction An	0.88	0.88	0.86	0.80	0.87	0.83	0.83	0.87	0.87	0.88

Sample	D176_R20	D176_R24	D176_R24
Plagioclase #	18	2	2
# W	က	_	2
SiO ₂	45.9	46.8	46.6
TIO ₂	0.03	0.02	0.02
Al ₂ O ₃	33.9	33.7	33.7
FeO _T	0.3	0.3	0.3
MgO	0.16	0.18	0.18
CaO	17.8	17.3	17.3
Na ₂ O	1.28	1.58	1.51
K ₂ 0	0.032	0.031	0.026
Total	66.36	99.92	99.64
mol fraction An	0.88	0.86	0.86

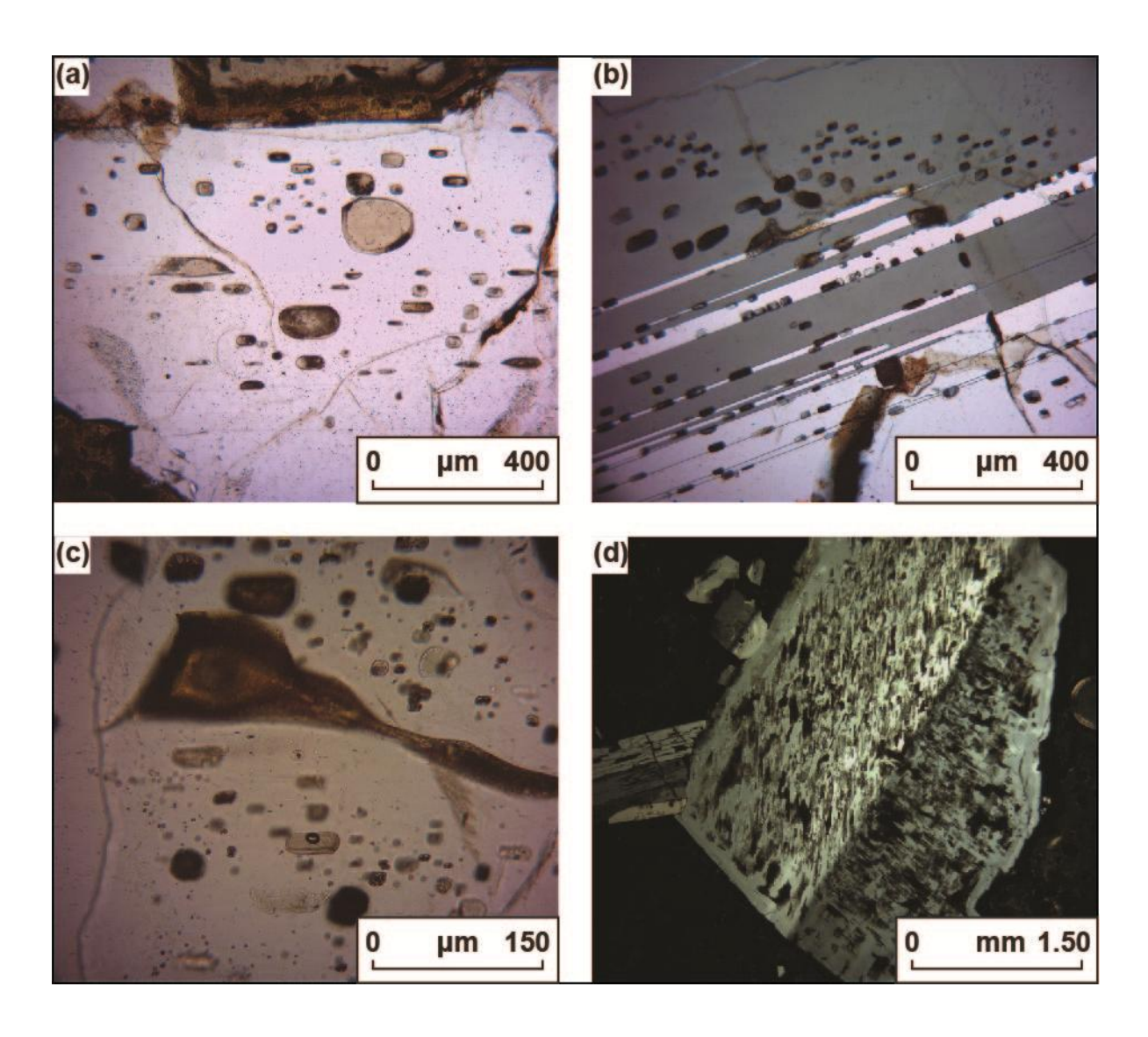
(a) Location of the Taney, Vance and President Jackson seamount chains in relation to other important geologic features in the North Pacific Ocean. The Taney Seamount chain is located near 36°N 45' and 125°W 25' on the Pacific plate, 300 km west of San Francisco, and formed adjacent to the now subducted Farallon Spreading Center. (b) DEM image of the Taney Seamounts. The volcanoes are labeled from oldest to youngest (Taney A-E) after Clague *et al.* (2000). Like other near-ridge seamounts, the volcanic edifices are defined by steep sides and truncated tops. Taney Seamount-A is the largest of the five seamounts and exhibits the most complex morphological features including multiple caldera collapses.



Electron backscattered images of large plagioclase crystals in glassy pillow margins. Lower anorthite contents are darker while higher anorthite contents are lighter. These crystals exhibit reverse zonation where the patchy, resorbed cores have a lower anorthite content compared to the region between the core and the rim. Furthermore, the growth textures in the cores of these crystals exhibit evidence for synneusis. The rims have anorthite contents which are in equilibrium with small microlites in the matrix glass. The textures of the plagioclase crystals suggest that they have undergone a protracted and complex crystallization history.



Transmitted light photomicrographs of melt inclusions in plagioclase crystals. (a) Glassy primary melt inclusions with rounded to square shapes and sizes from < $10~\mu m$ to > $100~\mu m$. (b) Small glassy primary melt inclusions commonly form in bands that parallel growth faces. (c) An example of a secondary melt inclusion with an irregular devitrified appearance. Primary melt inclusions are also present, in some cases with vapour bubbles. (d) Some plagioclase crystals have cores with a large proportion of secondary melt inclusions, giving a corroded appearance and illustrating the complex petrologic history.



Major element variations of Taney Seamount-A plagioclase melt inclusions compared to young pillow cone lavas, host lavas (pillow cones), and older main edifice lavas (Coumans *et al.*, 2015). (a, c-f) The majority of melt inclusions are more primitive than the host lavas. A small cluster of differentiated melt inclusions are similar to the edifice lavas which represent the main volume of the seamount. (b) The anorthite content of the plagioclase host <100 μm from the melt inclusion is positively correlated with the MgO content of the inclusion, consistent with plagioclase crystallization trends with decreasing temperature (Kohut & Nielsen, 2003).

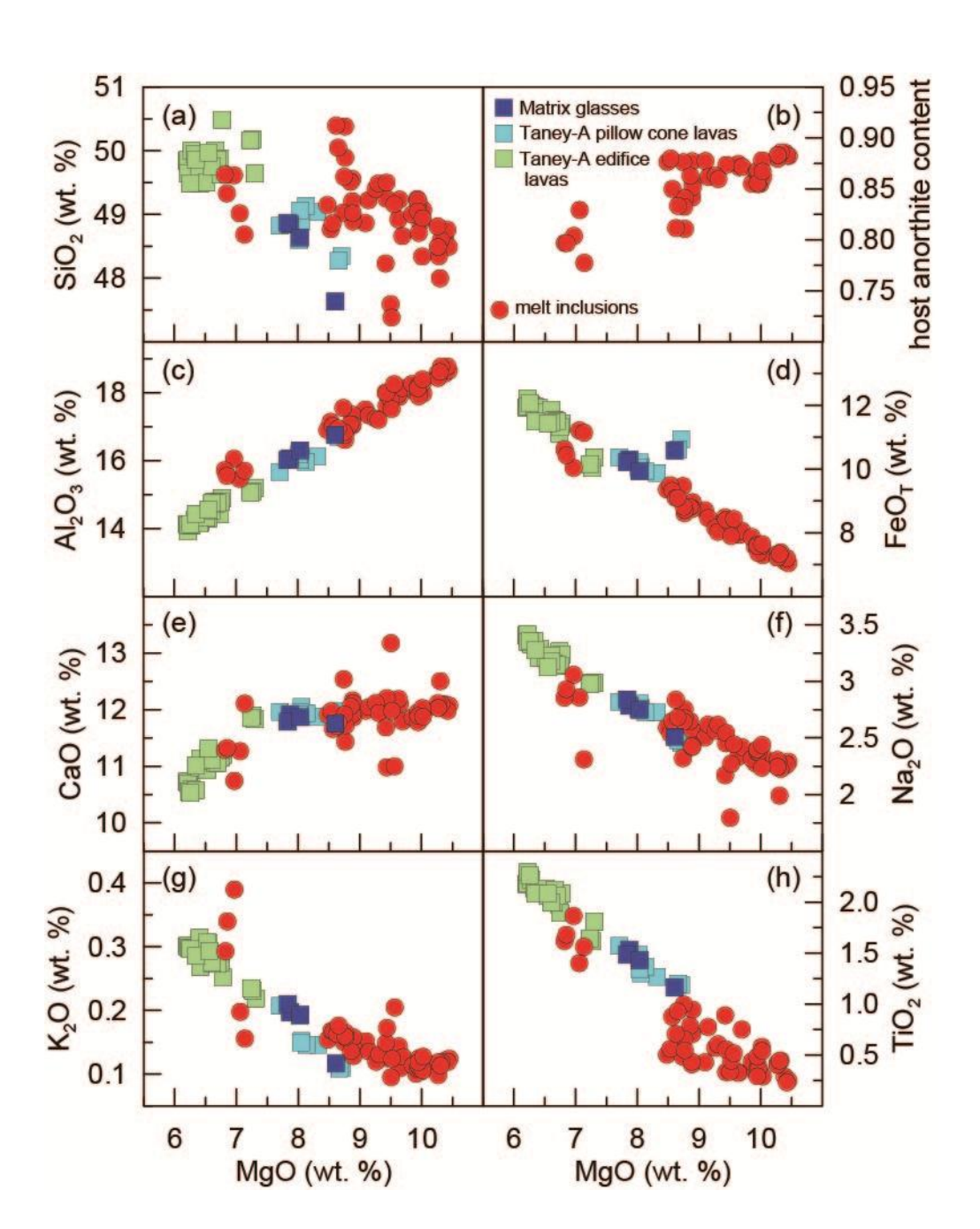
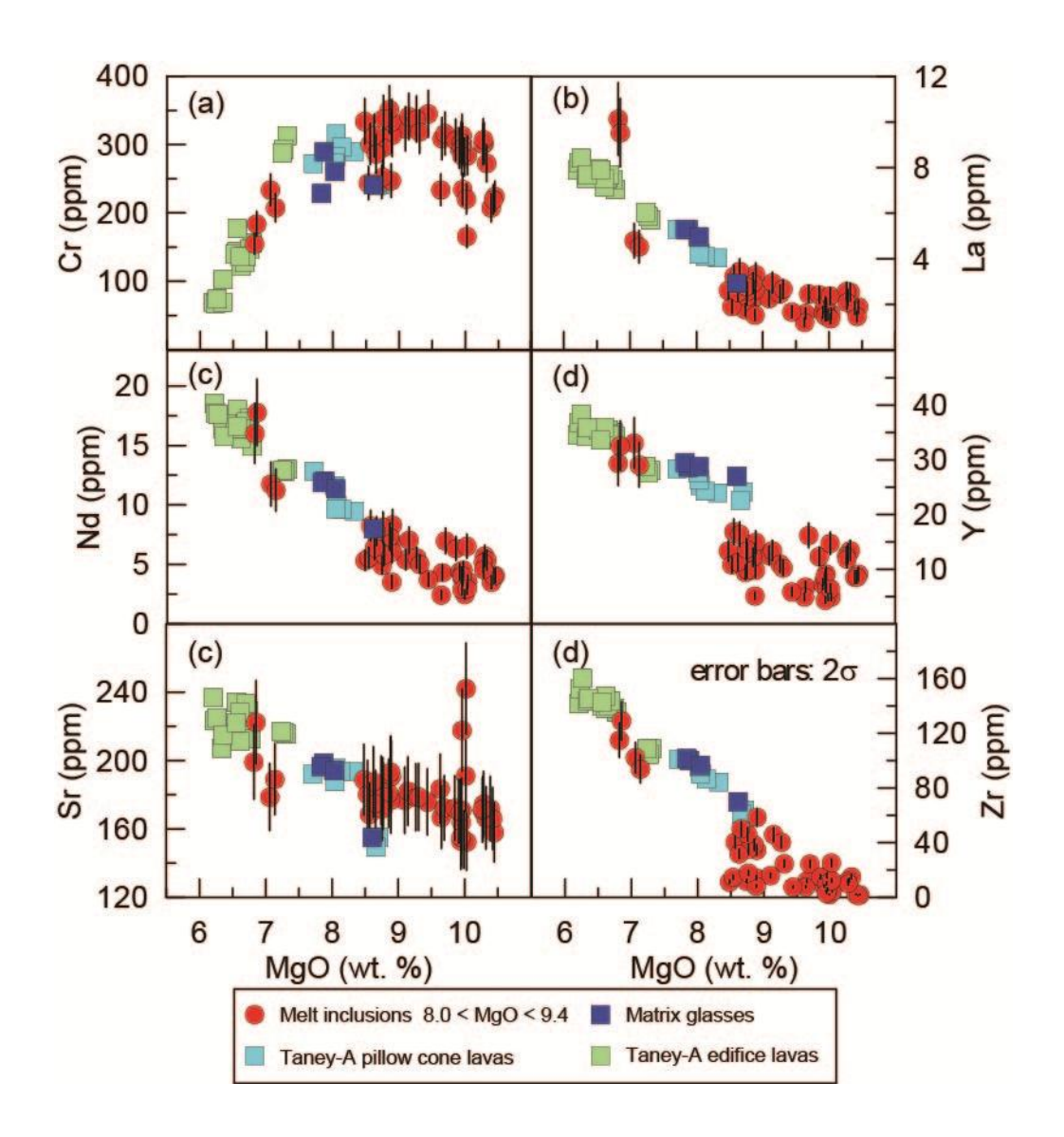
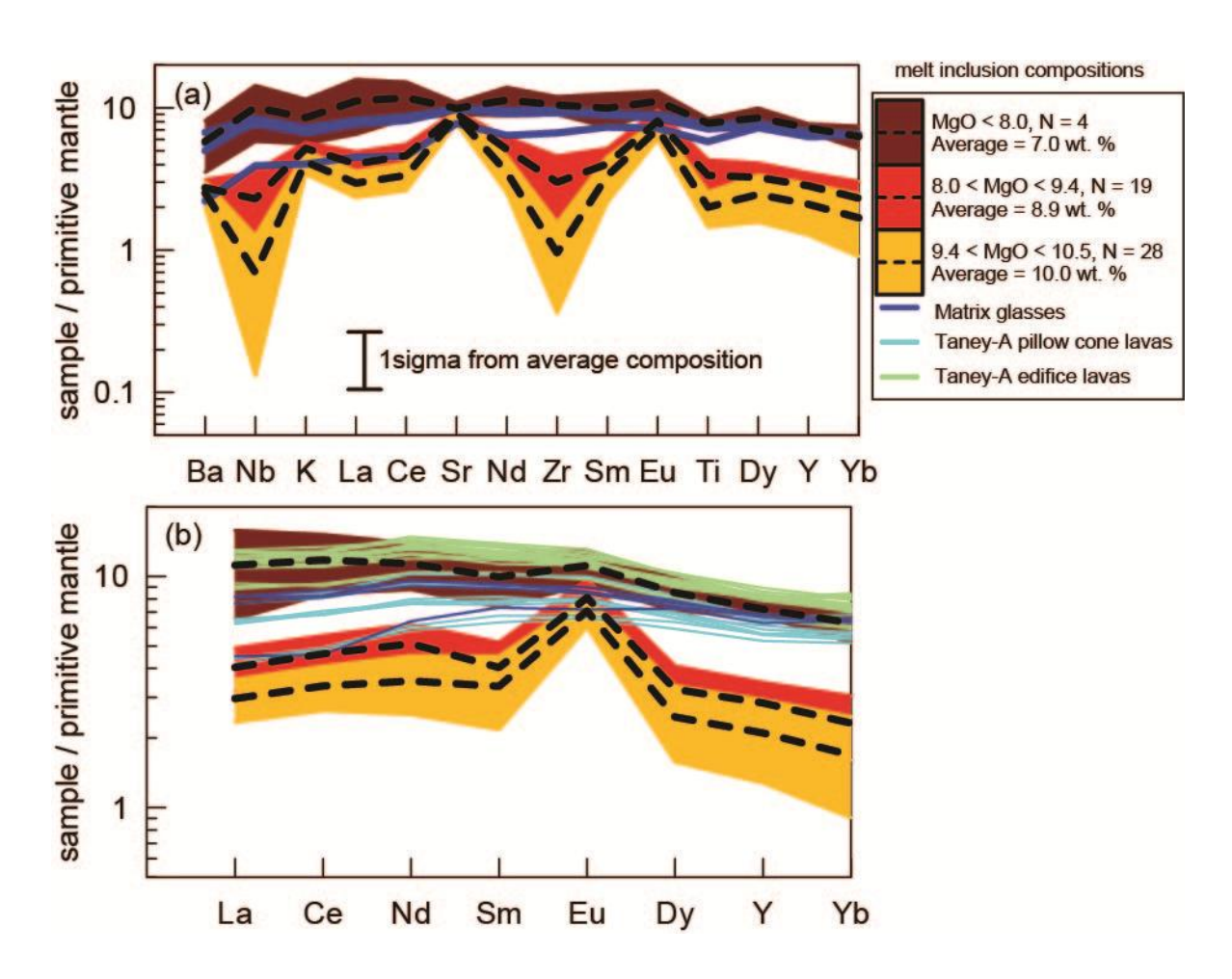


Figure 5

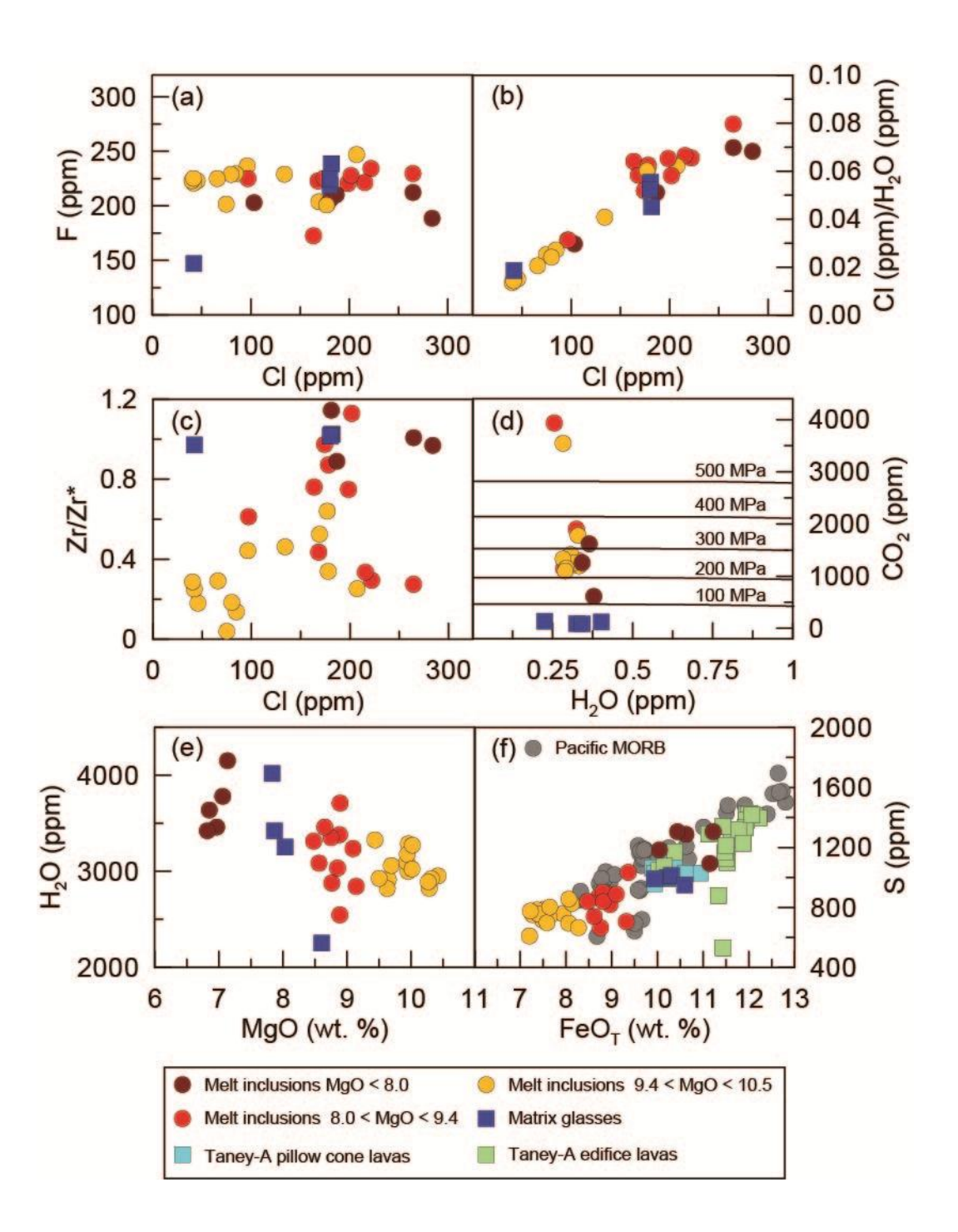
SIMS trace element plots of the Taney Seamount-A melt inclusions and lavas. Concentrations of incompatible trace elements (La, Nd, Y, Sr, Zr) increase with crystallization. Chromium is incompatible during olivine and plagioclase crystallization but becomes compatible when clinopyroxene is a major liquidus phase, as illustrated by strongly decreasing concentrations at low MgO. The differentiated melt inclusions have trace element compositions similar to the edifice lavas. The error bars represent 2σ variability.



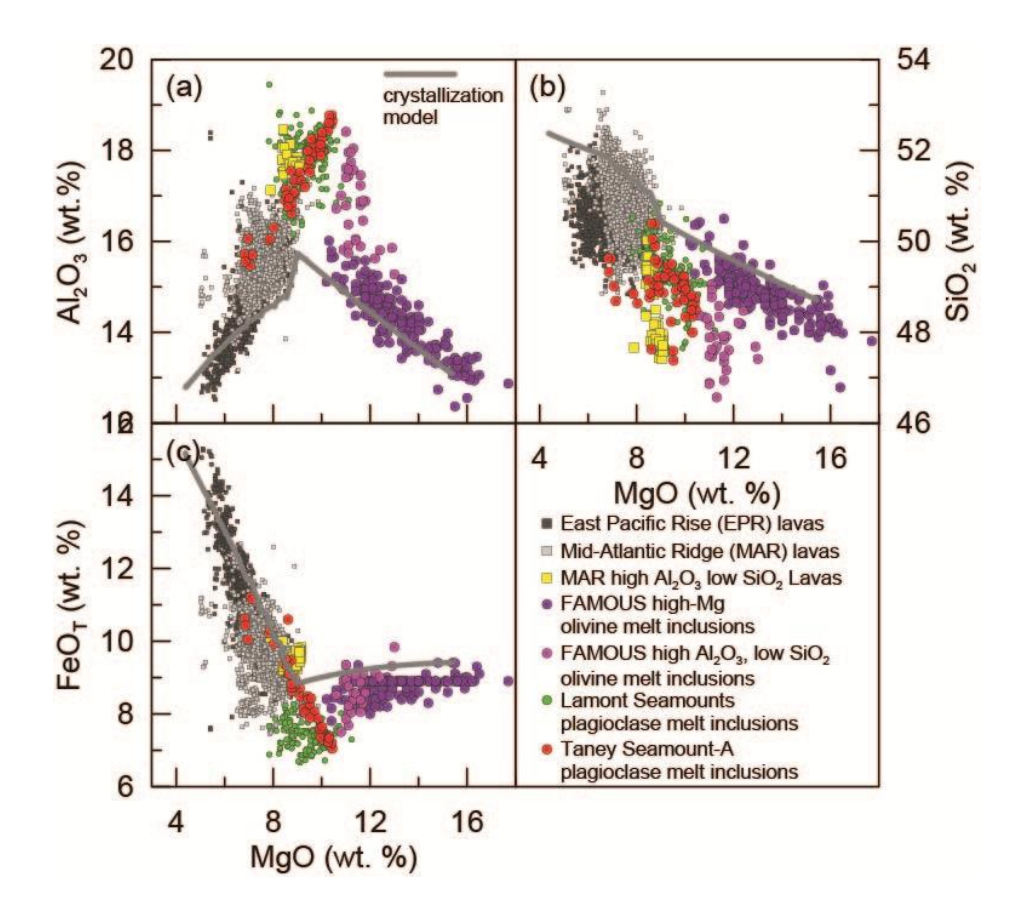
(a) Trace element spidergrams normalized to PUM (McDonough & Sun, 1995) of Taney Seamount-A melt inclusions separated into three groups based on MgO. The most differentiated melt inclusions (MgO wt. % < 8.0) have trace element profiles which resemble mantle-derived melts. The most primitive melt inclusions (9.4 < MgO wt. % < 10.5) have large positive Sr and Eu anomalies, negative Zr and Nb anomalies, and $(Ba/Nb)_N > 1$. The intermediate melt inclusions (8.0 < MgO wt. % < 9.4) have trace element profiles that are transitional. (b) REE normalized to PUM (McDonough & Sun, 1995) demonstrate that the differentiated melt inclusions resemble the Taney-A edifice lavas, suggesting that they are petrologically related.



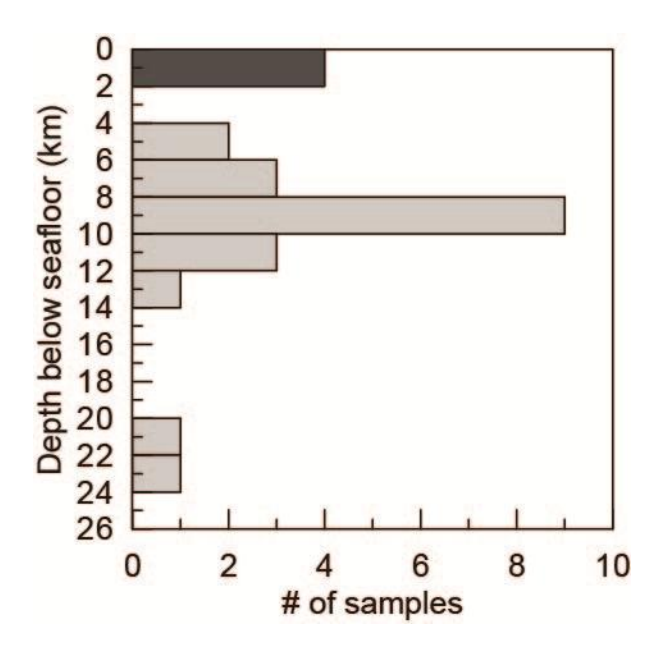
(a) Cl exhibits larger variation than F, suggesting that different processes are controlling their concentrations in the melt. (b) The increase in Cl/H₂O with Cl indicates that Cl is added to the melt but not H₂O. The addition of Cl in melt inclusions at lower crust depths could represent some amount of seawater alteration. (c) The Zr anomaly (Zr/Zr*) is not correlated to the concentration of Cl in the melt inclusions, suggesting that they are unrelated. (d) H₂O-CO₂ concentrations in melt inclusions and matrix glasses. The melt inclusions show a wide range of CO₂ concentrations compared to H₂O, while the matrix glasses are degassed. A cluster of melt inclusions with H₂O-CO₂ volatile saturation pressures at 200-300 MP suggests that plagioclase crystallized at or near the Moho. (e) H₂O concentrations increase with decreasing MgO, consistent with incompatible behaviour during crystallization. (f) The concentration of sulfur is positively correlated with the FeO_T content in the melt. The FeO_T trend of the melt inclusion data similar to Taney Seamount-A and Pacific MORB trends.



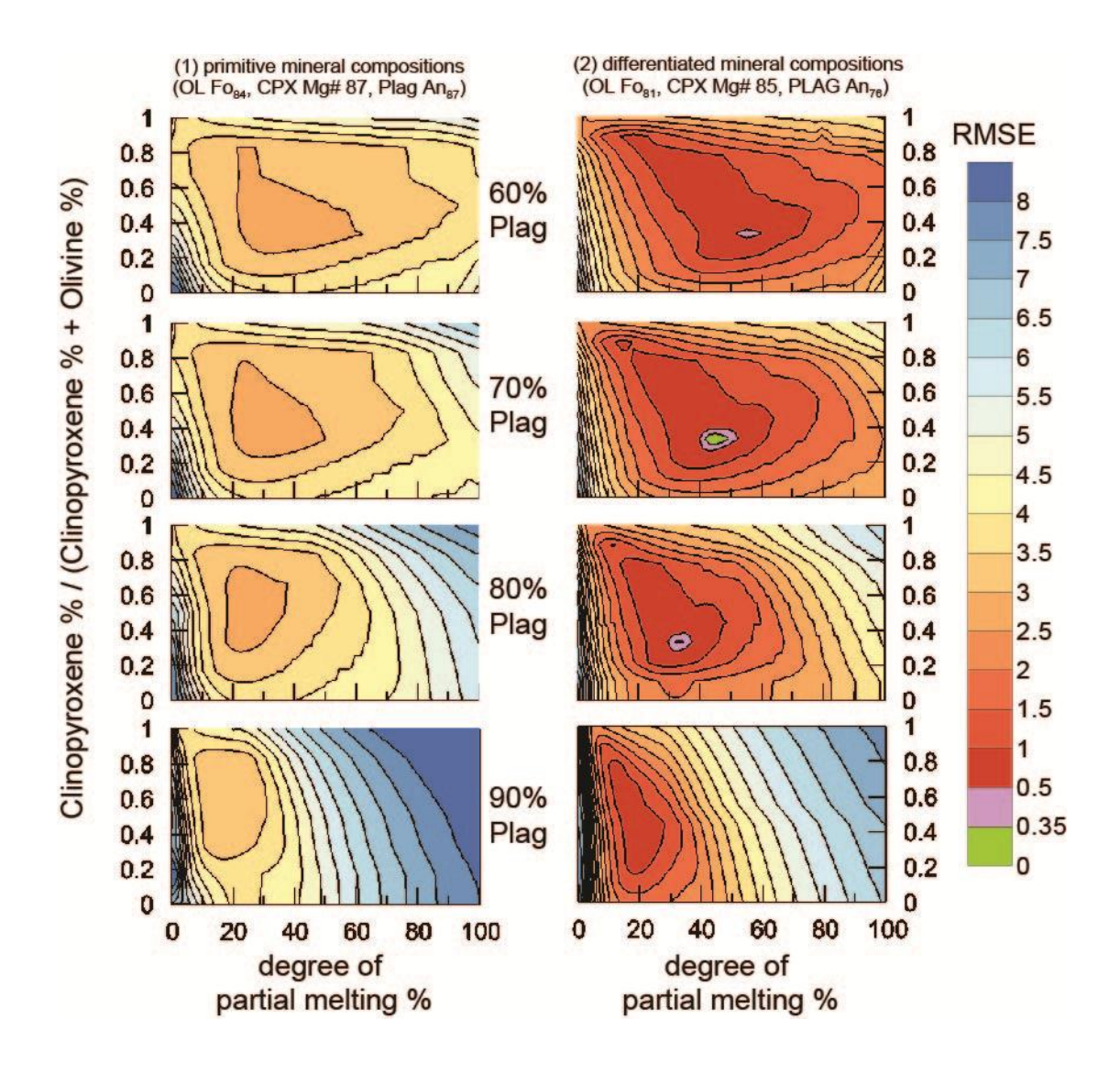
Major element variations for lavas and melt inclusions from various systems. Lavas are from the East Pacific Rise, Mid-Atlantic ridge (including high Al₂O₃, low SiO₂ examples), and Taney Seamount-A. Melt inclusions are from the FAMOUS region (high-Mg and high Al₂O₃, low SiO₂ series), Lamont Seamounts, and Taney Seamount-A. The high-Mg series of FAMOUS melt inclusions (purple circles) have been interpreted to represent the most likely candidate for minimally modified melts from the mantle melting column. In contrast, the high Al₂O₃, low SiO₂ series of FAMOUS melt inclusions (pink circles) have been interpreted to represent interaction with a plagioclase rich cumulate. Plagioclase crystallization occurs between 8-9 wt. % MgO for liquids derived from the FAMOUS High-Mg series, in agreement with the global analysis by Gale *et al.* (2014).



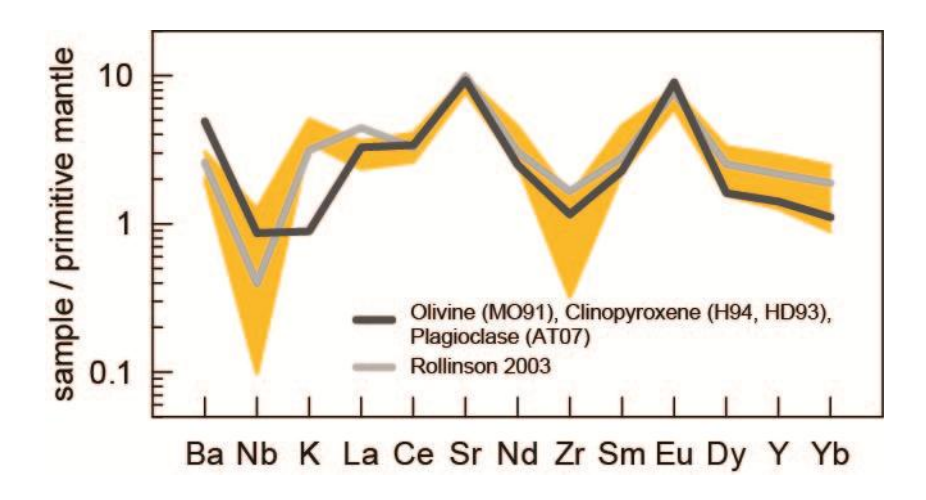
The majority of melt inclusions have volatile saturation depths of 6-10 kilometers below the seafloor, assuming a water depth of 2000 meters and a basalt density of 2800 kg/m³. These depths suggest that the large plagioclase crystals entrained in glassy pillow rims crystallized in the uppermost mantle and/or lower oceanic crust.



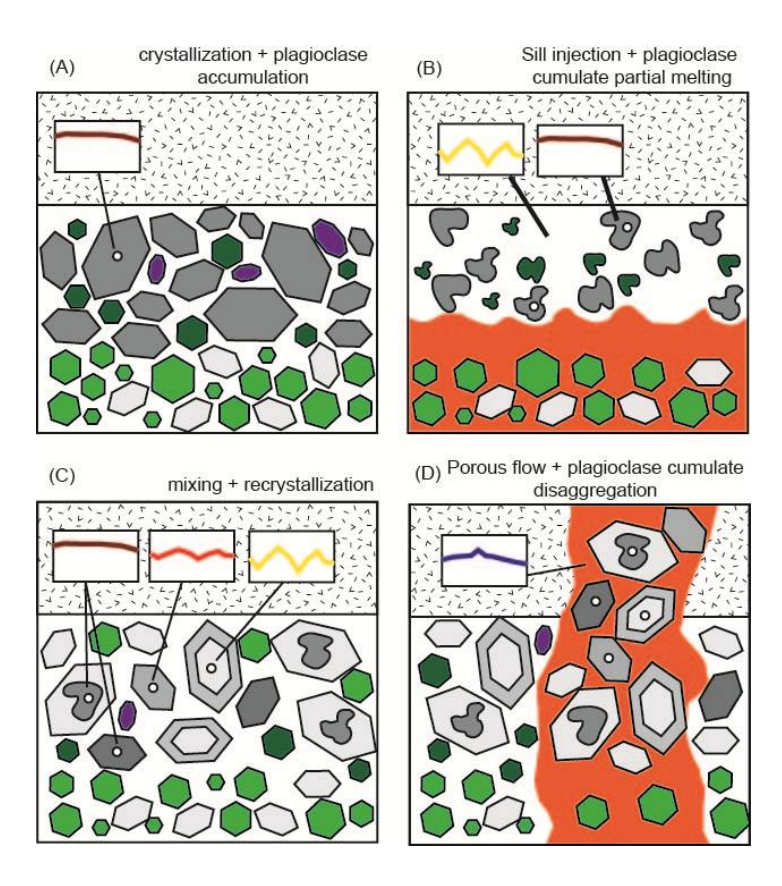
Modelling results of a cumulate equilibrium partial melting array. Two series of mineral compositions were used in the modelling: (1) primitive mineral compositions retrieved from average lower crust troctolite and (2) differentiated mineral compositions retrieved from average lower crustal layered olivine-gabbros. In each of these series, the mineral modes of plagioclase, clinopyroxene, and olivine are varied. The conditions (mineralogy, composition, and degree of melting) of best fit are determined by the root mean square error (*RMSE*) between the model and the primitive (9.42 < MgO wt. % < 10.5) melt inclusions.



Trace element results of the best fit melting model using two sets of partition coefficients (supplementary information S3). Although the model is dependent on the partition coefficients, the overall pattern is consistent and reproduces the positive Sr and Eu and negative Zr and Nb anomalies observed in the primitive melt inclusions.



Schematic diagram of magmatic processes at Moho depths. (a) Primitive melts pond near the Moho, differentiating to form plagioclase-rich cumulates. (b) Injections of hot, primitive basalt laterally infiltrate the warm, differentiated plagioclase cumulate. Heat transfer results in crystallization of the primitive basalt and partial melting of the differentiated cumulate. (c) The gradual disappearance of the Zr, Nb, Sr and Eu anomalies as the melt inclusions become more differentiated is related to interaction between the cumulate partial melt and the differentiating sill. Mixing coeval with crystallization generates the transitional melt inclusions. (d) Late stage melts that are more depleted in incompatible elements undergo diffusion with the cumulate pile during porous flow, entraining large plagioclase crystals and acquiring a positive Sr anomaly without concurrent negative Zr and Nb anomalies.



Supplementary Information S1: Standards, error analysis, and volatile calibration.

Table S1.1: List of standards used in analyses

Standard	Material	Element(s)	Producer / Reference	Method	Analyses
VG-2		. ,		EPMA	Glass
VG-2	Basaltic glass	Si, Al, Fe, Mg, Ca, Na	Smithsonian	(McGill)	Glass
VG-568	Rhyolite Glass	K	Smithsonian	EPMA (McGill)	Glass
SPESS	Spessartine	Mn	C.M.Taylor	ÈPMA	Glass
FLAP	Apatite	P	C.M Taylor	(McGill) EPMA	Glass
	•			(McGill) EPMA	
PYRI	Pyrite	S	C.M Taylor	(McGill)	Glass
VANA	Vanadinite	CI	Cameca	EPMA (McGill)	Glass
TiO ₂	Rutile	Ti	C.M Taylor	EPMA (McGill)	Glass, Plagioclase
Amelia Albite	Albite	Na	C.M Taylor	EPMA (McGill)	Plagioclase
Astimex Sanidine	Sanidine	Si, Al, K	Astimex 53	EPMA (McGill)	Plagioclase
DIOP	Diopside	Ca, Mg	C.M Taylor	EPMA (McGill)	Plagioclase
Fe ₂ O ₃	Hematite	Fe	C.M Taylor	EPMA (McGill)	Plagioclase
73	Glass	La, Ce, Nd, Sm, Eu, Dy, Er, Yb, Ba, Sr, Nb, Zr, Y, Cr	†	SIMS (MUN)	Glass
GL07-51-3	Glass	CO ₂ , H ₂ O, F, S, Cl	‡	SIMS (WHOI)	Glass
ALV-519-4-1	Glass	H ₂ O, F, S, Cl	‡	SIMS (WHOI)	Glass
GL07-D52-5	Glass	CO ₂ , H ₂ O, F, S, Cl	‡	SIMS (WHOI)	Glass
EN113-46D	Glass	CO ₂ , H ₂ O, F, S	‡	SIMS (WHOI)	Glass
FRND-6001	Glass	S, Cl	‡	SIMS (WHOI)	Glass
ALV-1654-3	Glass	H ₂ O, F, S, Cl	‡	SIMS (WHOI)	Glass
JD-17H	Glass	H ₂ O	‡	SIMS (WHOI)	Glass
ALL107-D20-3	Glass	H ₂ O	‡	SIMS (WHOI)	Glass
ALV-1649-3	Glass	CO ₂ , H ₂ O, F, S, Cl	‡	SIMS (WHOI)	Glass
NS-1	Glass	CO ₂	‡	SIMS (WHOI)	Glass

Notes: † Internal standard used at Memorial University Newfoundland. ‡ Compositions and location found in Helo et al., (2011) and references therein.

Table S1.2: Reproducibility and accuracy of the electron microprobe for VG-2

Oxide	Analysis no	umber						
(Wt. %)	1	2	3	4	5	6	7	8
SiO ₂	50.9	51.0	51.0	51.2	51.0	51.1	50.8	51.0
TiO ₂	1.78	1.67	1.92	1.79	1.91	1.90	1.90	1.75
Al_2O_3	14.1	14.0	14.2	14.2	14.0	14.1	14.1	14.1
FeO_T	11.7	11.6	12.0	11.9	11.7	12.1	11.8	11.9
MnO	0.246	0.227	0.185	0.238	0.199	0.246	0.199	0.229
MgO	6.67	6.65	6.63	6.70	6.65	6.70	6.74	6.62
CaO	11.1	11.1	11.1	11.1	11.1	11.2	11.1	11.0
Na₂O	2.61	2.66	2.64	2.59	2.60	2.57	2.56	2.65
K ₂ O	0.209	0.208	0.215	0.229	0.229	0.215	0.221	0.225
SO₃	0.348	0.315	0.373	0.362	0.326	0.349	0.381	0.341
P_2O_5	0.172	0.23	0.469	0.357	0.254	0.107	0.339	0.215
Cl	0.063	0.008	0.083	0.004	0.012	0	0	0
Total	99.87	99.61	100.89	100.68	99.95	100.60	100.18	100.05

Notes: All oxides and elements in weight per cent. The reference for VG-2 (NMNH 111240-52) is from the Smithsonian microbeam standards (Jarosewich, 2002). † The calibration value used during analyses is 6.71; we have corrected our data to 7.07 which represents the updated value. The reproducibility error of P_2O_5 and SO3 is large, thus we exclude these analyses from our MI data.

Table S1.2 Cont'd

Oxide	Analysis n	umber			Std. Dev.	Std. Dev.	ref. value
(Wt. %)	9	10	11	Average	<u>(+ 2σ abs)</u>	<u>(+ 2σ %)</u>	(VG-2)
SiO ₂	50.8	50.9	50.9	51.0	0.2	0.4	50.8
TiO ₂	1.66	1.84	1.85	1.81	0.19	10.2	1.85
Al_2O_3	14.1	14.1	14.2	14.1	0.1	1.0	14.1
FeO⊤	11.4	11.7	11.9	11.8	0.4	3.5	11.8
MnO	0.177	0.17	0.172	0.208	0.060	28.8	0.220
MgO	6.62	6.65	6.66	6.66	0.07	1.1	† (7.07)
CaO	11.0	11.2	11.0	11.1	0.1	1.3	11.1
Na₂O	2.58	2.50	2.59	2.60	0.09	3.5	2.62
K ₂ O	0.214	0.201	0.213	0.216	0.018	8.3	0.200
SO₃	0.348	0.372	0.339	0.350	0.041	11.6	0.350
P_2O_5	0.044	0.639	0.209	0.276	0.337	122.1	0.220
CI	0	0	0.063	0.021	0.064	300.3	0.030
Total	99.06	100.13	100.05	100.10	1.02	1.0	99.86

Table S1.3a: Reproducibility and accuracy of trace elements by SIMS for P1326-2

Element	Analysis nu	ımber						
(ppm)	1	2	3	4	5	6	7	8
La	4.3	4.3	5.3	4.9	5.2		4.6	4.7
Ce	13.3	14.6	14.7	15.2	14.9	16.9	14.5	13.7
Nd	11.9	10.5	13.4	13.6	13.0	13.0	12.0	12.0
Sm	1.4	3.7	3.8	2.9	3.3	3.7	2.9	3.8
Eu	0.8	1.6	1.8	1.7	1.3	1.7	1.7	1.5
Dy	5.0	6.7	6.5	5.4	5.4	6.2	5.6	4.2
Er	2.8	2.9	3.3	3.2	2.7	4.1	3.4	3.3
Yb	1.9	2.7	3.0	2.7	2.4	2.8	2.6	2.9
Ва	22.9	24.0	25.7	25.8	25.3	25.4	24.1	24.0
Sr	151	155	169	157	164	174	158	154
Nb	4.2	3.8	4.1	3.9	4.0	4.4	4.1	3.9
Zr	85.9	85.0	97.9	92.7	92.2	99.0	92.4	88.5
Υ	30.3	29.9	32.6	33.0	32.5	35.4	31.8	30.5
Cr			351	344	338	379	351	326

Notes: The reference for P1326-2, a Juan de Fuca Ridge (JdFR) basalt is from Stix *et al.*, (1995). Analyses were performed at Memorial University Newfoundland on a Cameca IMS 4F ion microprobe.

Table S1.3a Cont'd

Element	Ana	lysis nur	mber			Std. Dev.	Std. Dev.	ref. value
(ppm)	9	10	11	12	Average	<u>(+ 1σ abs)</u>	<u>(+ 1σ %)</u>	(P1326-2)
La	4.6	4.9	4.8	5.4	4.8	0.4	7.9	4.7
Ce	13.9	15.4	14.0	15.8	14.7	1.0	6.7	12.7
Nd	12.3	11.6	11.6	13.7	12.4	1.0	7.9	10.8
Sm	3.7	4.3	4.0	4.3	3.5	0.8	22.9	3.4
Eu	1.6	1.7	1.8	2.0	1.6	0.3	18.7	1.3
Dy	5.9	6.3	5.6	6.5	5.8	0.7	12.7	5.3
Er	3.2	3.0	3.4	4.3	3.3	0.5	14.8	3.3
Yb	2.7	3.0	3.3	3.0	2.7	0.3	12.4	3.1
Ва	23.1	25.3	23.4		24.4	1.1	4.4	25.0
Sr	159	163	153	172	161	8	5	153
Nb	4.0	4.0	3.9	4.4	4.1	0.2	5.1	4.4
Zr	90.2	94.1	88.1	98.3	92.0	4.7	5.1	94.0
Υ	30.5	32.6	31.1	34.0	32.0	1.7	5.2	33.0
Cr	332	354	314	362	345	19	5	

Table S1.3b: Reproducibility and accuracy of trace elements by SIMS for standard 73

Element	Analysis	s number						
(ppm)	1	2	3	4	5	6	7	8
La	45.4	44.9	45.6	46.0	47.4	44.3	43.7	45.6
Ce	94.9	95.9	99.5	97.5	99.3	92.9	92.0	95.6
Nd	41.3	41.5	40.3	39.8	44.4	40.7	39.4	38.3
Sm	7.4	7.4	7.5	6.8	8.3	8.6	7.3	8.2
Eu	2.2	2.1	2.7	1.0	2.4	2.1	3.0	2.5
Dy	4.7	5.3	5.3	5.9	7.0	5.5	4.8	5.2
Er	2.8	2.7	3.8	2.7	3.7	3.4	3.3	3.0
Yb	2.7	3.2	2.8	2.7	2.4	2.5	2.6	2.3
Ва	318.1	317.7	343.0	338.5	363.1	329.5	316.7	335.4
Sr	549	550	580	560	607	550	539	569
Nb	61.6	60.7	63.3	61.4	64.4	60.0	59.0	61.3
Zr	320.5	319.6	327.5	315.3	329.8	304.5	309.8	307.4
Υ	28.6	28.5	30.0	29.7	31.2	29.0	28.9	29.3
Cr			80	75	87	88		85

Notes: The reference for 73, an alkaline basalt, is from Stix *et al.*, (1995). Analyses were performed at Memorial University Newfoundland on a Cameca IMS 4F ion microprobe.

Table S1.3b Cont'd

Element	Ana	alysis num	nber		Std. Dev.	Std. Dev.	ref. value
(ppm)	9	10	11	Average	<u>(+ 1σ abs)</u>	<u>(+ 1σ %)</u>	73
La	47.3	50.4	48.6	46.3	2.0	4.3	46.3
Ce	101.4	106.8	103.2	98.1	4.5	4.6	98.1
Nd	39.8	43.8	44.1	41.2	2.0	5.0	41.3
Sm	9.1	7.6	7.6	7.8	0.7	8.5	7.9
Eu	2.5	2.6	2.2	2.3	0.5	22.9	2.3
Dy	6.5	5.7	6.1	5.6	0.7	12.4	5.7
Er	3.1	3.3	3.8	3.2	0.4	12.5	3.3
Yb	2.5	2.5	3.5	2.7	0.3	13.0	2.9
Ва	352.1	367.7	358.1	340.0	18.5	5.5	340.0
Sr	626	613	594	576	30	5	576
Nb	67.3	67.6	66.1	63.0	3.0	4.8	63.0
Zr	344.5	336.2	337.7	323.0	13.2	4.1	323.0
Υ	32.3	31.6	30.8	30.0	1.3	4.3	30.0
Cr	93	87	91	86	6	7	85

Table S1.4: Reproducibility and accuracy of volatile elements by SIMS for P1326-2

Element	Ar	nalysis nu	ımber			
(ppm)	1	2	3	4	5	6
CO ₂		337		367	350	351
H ₂ O (wt. %)	0.31	0.30	0.33	0.31	0.30	0.28
F	214	211	209	212	210	207
S	1272	1299	1286	1271	1283	1281
Cl	182	186	186	179	182	182

Notes: Analyses were performed at Woods Hole Oceanographic Institute on a Cameca IMS 1280 ion microprobe.

Table S1.4 Cont'd

Element				Std. Dev.	Std. Dev.	ref. value
(ppm)	7	8	Average	<u>(+ 1σ abs)</u>	<u>(+ 1σ %)</u>	(P1326-2)
CO ₂	348	331	351	13	3.6	327
H_2O	0.26	0.26	0.31	0.03	8.6	0.265
F	204	205	210	3	1.7	191
S	1320	1330	1282	22	1.7	1277
CI	191	192	183	5	2.5	160

Table S1.5: Composition of standards used for volatile element calibration

Element	Standard					
(wt. %)	GL07-51-3	ALV-519-4-1	GL07-D52-5	EN113-46D	FRND-6001	ALV-1654-3
SiO ₂	49.46	49.1	48.59	49.5	54.78	56.6
TiO ₂	2.45	0.78	2.67	1.07	0.48	2.33
Al_2O_3	14.9	16.6	15.94	15.78	15.61	11.3
FeO⊤	10.92	8.04	10.76	9.16	8.38	14.9
MnO	0.15	0.14	0.15	0.15	0.16	0.25
MgO	6.79	9.51	6.3	8.29	6.42	2.49
CaO	10.59	12.47	10.14	13.18	10.93	7.16
Na₂O	2.82	2.08	3.34	2.52	1.5	3.2
K₂O	0.26	0.08	0.39	0.05	0.55	0.36
P_2O_5	0.24		0.31	0.21	0.11	0.63
Total	98.58	98.86	98.59	99.91	98.92	99.22
CO ₂ (ppm)	125		88	237		
H ₂ O (wt. %)	0.443	0.17	1	0.112		1
F (ppm)	299	90	431	124		997
S (ppm)	1126	950	1183	877	38	1562
CI (ppm)	182	45	322		927	2914

Notes: The standard references are found in the supplementary information from Helo et al., (2011).

Table S1.5: Composition of standards used for volatile element calibration

Element	Standard				
(wt. %)	JD-17H	ALL107-D20-3	ALV-1649-3	NS-1	P1326-2
SiO ₂	48.59	49.82	51.25	49.4	50
TiO ₂	1.85	0.63	2.69	1.54	1.53
Al_2O_3	13.42	17.38	11.9	14.78	14.48
FeO _⊤	12.73	7.53	15.3	9.25	10.82
MnO			0.24	0.19	0.16
MgO	7.05	9.94	4.71	8.95	7.3
CaO	10.81	13.06	9.23	10.69	12.18
Na₂O	2.68	1.65	2.65	2.95	2.76
K ₂ O	0.17	0.02	0.2	0.21	0.17
P_2O_5	0.16	0.11	0.44	0.1	0.12
Total	97.46	100.14	98.61	98.06	99.52
CO ₂ (ppm)			161	3150	327
H_2O (wt. %)	2.49	0.05	0.61		0.265
F (ppm)			445		191
S (ppm)			1640		1277
CI (ppm)			1433		160

Figure S1.1: Known standard compositions (Table S1.5) versus measured isotope ratios (counts per second/counts per second). The data are linearly regressed through the origin with the exception of H₂O. (a-e) The curves used for the analyses. (f) CO₂ standard data with a high-CO₂ standard glass (NS-1) illustrating the linearity of the calibration over a large range of CO₂.

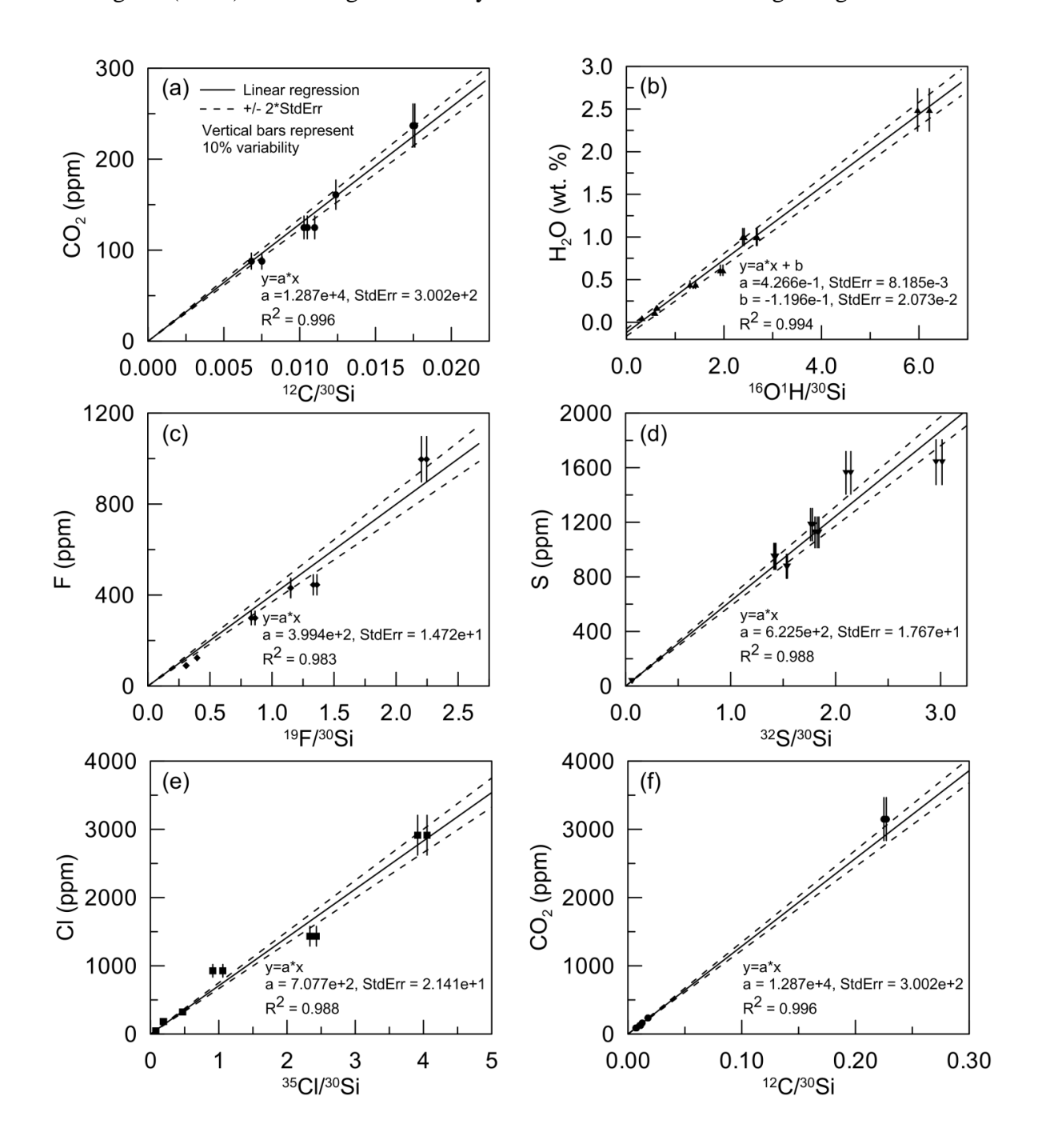


Figure S1.2: The water concentrations of P1326-2 exhibit a systematic drift, decreasing with elapsed time during analysis. The water concentration of P1326-2 is 0.26 wt. % determined by Fourier transform infrared spectroscopy (FTIR) at McGill University, consistent with SIMS analyses by Helo, et al. (2011). Water concentrations of melt inclusions were corrected based on deviations of P1326-2 from the accepted value.

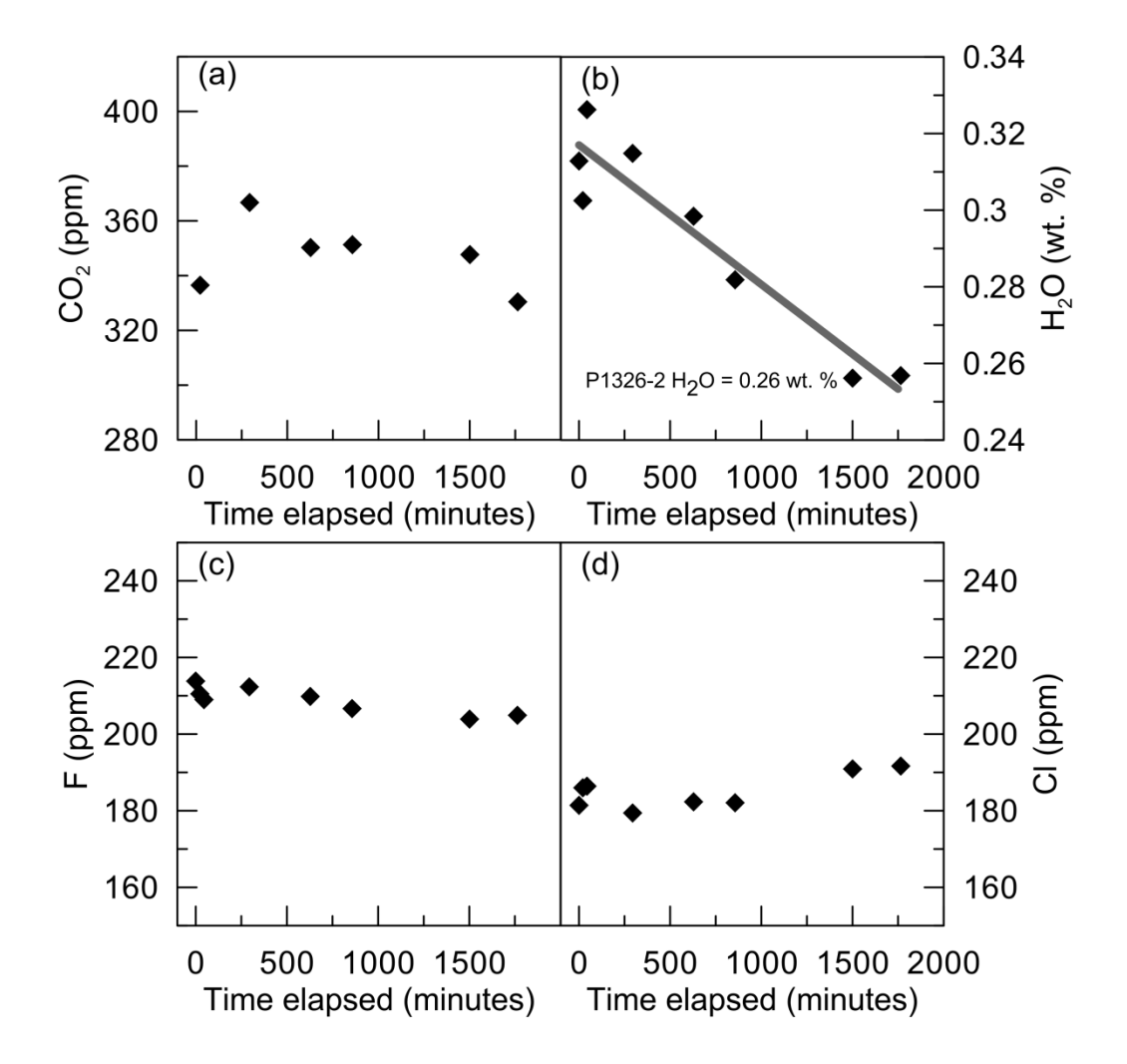
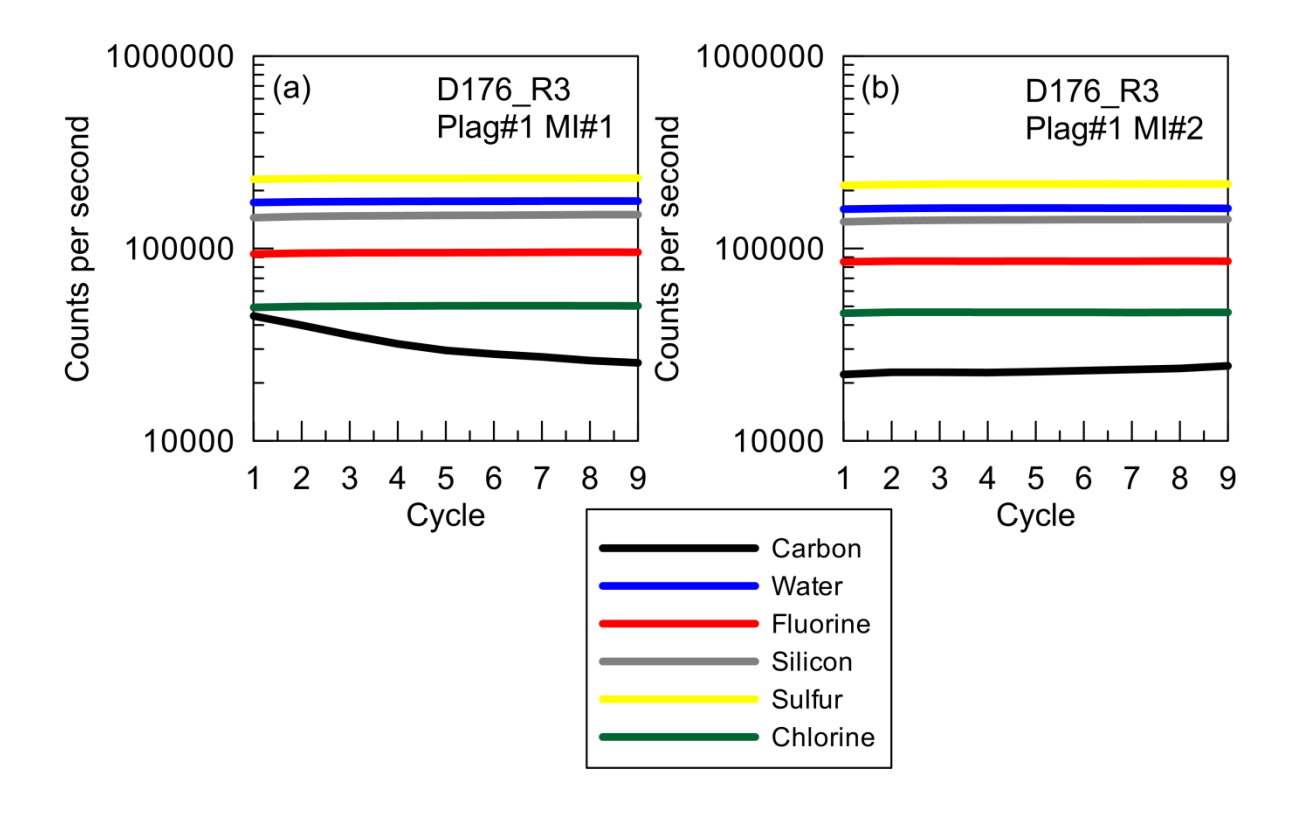


Figure S1.3: Counts per second for each element during analysis of two melt inclusions in a single crystal. (a) The decreasing counts of carbon over the measurement duration suggests that the element is analytically unstable. (b) In this measurement the carbon signal is stable. For consistency, we only report analyses that have a stable single defined by slight positive slope similar to 30 Si, and a % standard deviation of the component/ 30 Si > 15%.



Supplementary Information S2: Melt inclusion and matrix glass data not corrected for post entrapment crystallization.

 Supplementary Table S2.1 : Major, trace, and volatile element data for melt inclusions and matrix glasses from Taney Seamount-A

 Sample
 D176_R3
 <t

Plagioclase #	1	1	2	2	3	3	5	5	6	8
MI#	1	2	1	2	1	2	1	1 (R)	1	1
SiO ₂	49.5	49.1	49.0	48.6	49.6	49.4			49.6	49.1
TiO ₂	0.45	0.47	1.40	1.84	0.36	0.37			0.37	1.03
Al_2O_3	15.7	15.9	15.5	12.8	16.1	15.4			16.0	15.9
FeO _T	9.8	9.6	11.2	13.0	8.8	9.3			8.9	9.7
MnO	0.172	0.106	0.152	0.197	0.151	0.186			0.201	0.147
MgO	9.72	10.02	7.06	8.35	10.72	11.15			10.41	9.67
CaO	11.6	11.4	11.3	11.5	11.5	11.3			11.6	11.4
Na₂O	2.70	2.63	2.86	2.28	2.49	2.49			2.56	2.51
K₂O	0.147	0.162	0.198	0.179	0.120	0.166			0.135	0.138
Total	100.065	99.586	99.512	99.410	100.020	100.362			99.972	99.966
La	2.5	2.5	4.8	5.3	1.8	1.4	1.3	1.4	1.84	3.59
Ce	8.1	7.1	15.7	16.8	4.6	4.3	1.9	2.3	5.24	10.41
Nd	7.6	5.9	11.8	13.2	4.8	2.8	1.7	2.1	4.11	9.04
Sm	1.7	2.1	4.0	4.5	1.4	0.5	0.5	0.2	1.21	2.23
Eu	1.4	1.5	1.7	1.7	1.1	8.0	0.2	0.5	1.33	1.69
Dy	2.3	2.2	6.8	5.3	1.6	1.1	1.0	0.8	1.56	2.66
Er	1.6	1.4	3.2	4.4	0.8	0.7	0.7	0.9	0.12	1.97
Yb	1.0	1.1	2.7	3.0	0.6	0.3	0.6	0.9	0.60	1.12
Cr	349	355	234	243	342	270	274	277	380	341
Ba	23.3	21.6	23.3	31.9	17.6	14.7	52.6	29.6	27.89	19.95
Sr	191	175	179	186	165	181	156	188	174	189
Nb	8.0	8.0	4.6	4.6	0.6	0.3	2.3	2.6	0.63	2.45
Υ	14.2	13.8	33.1	34.1	7.5	5.7	4.4	4.3	6.5	16.2
Zr	15.7	17.5	102.1	110.1	13.1	8.9	47.9	48.2	8.3	63.7
CO ₂	0	2101	617	0	1422	4120			1329	
H₂O	0.37	0.36	0.38	0.48	0.32	0.33			0.37	0.40
F	256	244	212	221	249	236			272	266
S	971	955	1306	1281	843	806			913	893
a	240	234	265	325	195	192			225	

Notes: Major elements and H_2O expressed in w eight per cent, trace elements and other volatiles in ppm. MgO corrected to VG-2 = 7.07 wt. %. Water has been corrected for systematic instrumental drift based on deviation from the known value of P1326-2 (supplementary information S1). This data have not been corrected for post-entrapment crystallization.

Supplementary	Table	S2.1	Cont'd
---------------	-------	------	--------

Sample	D176_R3	D176_R3	D176_R3	D176_R3	D176_R17	D176_R17	D176_R17	D176_R17	D176_R17
Plagioclase #	9	13	13	14	1	3	12	13	13
MI#	1	1	2	1	1	1	1	1	2
SiO ₂	49.3	49.7	49.0	49.9	49.3	49.7	49.5	49.6	49.7
TiO ₂	0.54	0.58	0.61	0.49	0.78	0.83	0.84	0.61	0.65
Al_2O_3	15.8	14.2	15.6	14.8	15.4	16.2	16.0	16.1	16.1
FeO _⊤	9.9	11.3	10.3	9.9	9.6	9.3	9.2	8.7	8.6
MnO	0.206	0.204	0.189	0.167	0.160	0.127	0.170	0.167	0.196
MgO	9.02	10.52	9.31	10.06	9.80	9.32	9.90	9.87	9.96
CaO	11.5	11.5	11.4	11.3	11.6	11.8	11.6	11.8	11.6
Na ₂ O	2.67	2.52	2.65	2.51	2.51	2.71	2.71	2.63	2.69
K ₂ O	0.163	0.176	0.180	0.163	0.170	0.142	0.146	0.126	0.139
Total	100.017	101.031	99.728	99.509	99.822	100.586	100.303	99.871	99.775
La	2.8	2.1	2.1	1.7	2.9	3.1	3.2	2.6	2.9
Се	8.7	7.2	6.4	4.7	8.8	8.8	9.7	7.8	7.7
Nd	5.7	5.9	6.1	4.0	6.7	7.7	7.6	5.9	5.4
Sm	1.5	1.1	1.4	8.0	1.7	1.7	2.0	2.3	2.1
Eu	1.6	1.3	1.1	1.1	1.5	1.4	1.7	1.2	1.3
Dy	2.6	2.2	1.8	0.7	2.0	2.5	2.7	2.1	2.0
Er	1.6	0.8	1.0	0.5	1.3	1.8	1.3	1.3	1.3
Yb	1.2	0.9	1.1	0.5	1.0	1.1	1.2	1.0	1.5
Cr	355	294	266	279	366	370	369	359	341
Ва	20.7	16.8	14.5	16.6	19.1	23.3	20.1	17.2	16.2
Sr	188	179	179	190	175	180	180	177	177
Nb	0.4	0.8	0.8	0.4	2.1	2.1	2.5	2.1	1.6
Υ	14.2	11.4	11.8	5.8	10.8	12.8	14.5	11.7	11.0
Zr	12.0	14.3	15.9	9.3	38.2	40.4	49.8	42.9	26.3
CO_2	1381				4351	1339	1240		
H₂O	0.35				0.28	0.32	0.31		
F	244				190	232	219		
S	1099				734	950	911		
CI	279				178	207	191		

Supplementary	Table S2.1	Cont'd
---------------	------------	--------

Sample	D176_R17	D176_R20							
Plagioclase #	13	1	2	3	3	6	6	6	7
MI#	3	1	2	1	2	1	2	3	1
SiO ₂		49.0	49.6	50.5		49.1	48.9	49.2	49.0
TiO ₂		0.85	1.87	0.69		0.33	0.29	0.28	0.95
Al_2O_3		16.1	16.1	15.8		16.0	16.1	16.0	15.7
FeO _T		9.1	10.0	9.0		8.3	8.2	8.4	10.0
MnO		0.110	0.155	0.179		0.140	0.117	0.118	0.160
MgO		10.93	6.97	9.18		12.11	12.15	12.22	9.24
CaO		11.1	10.7	11.2		11.2	11.1	11.0	11.2
Na ₂ O		2.55	3.06	2.79		2.42	2.46	2.44	2.73
K ₂ O		0.141	0.390	0.172		0.137	0.141	0.138	0.179
Total		100.309	99.443	99.854		99.956	99.738	100.071	99.630
La		2.8		2.4		2.1	2.2	1.7	3.5
Ce		8.5		7.4		6.5	6.4	6.2	10.0
Nd		7.9		6.2		4.1	4.7	4.7	8.9
Sm		2.2		1.4		1.2	1.7	1.4	2.6
Eu		1.1		1.2		1.0	1.1	1.1	1.3
Dy		3.4		1.9		1.6	1.6	2.2	3.5
Er		1.5		1.2		1.0	0.9	0.7	1.6
Yb		2.0		8.0		0.9	8.0	0.7	1.3
Cr		356		310		241	260	257	324
Ba		26.3		19.4		14.9	15.3	14.0	17.1
Sr		170		181		169	155	163	167
Nb		1.1		8.0		0.1	0.1	0.0	2.3
Υ		18.3		10.3		10.0	10.6	10.1	18.2
Zr		27.5		18.7		2.6	2.3	1.6	43.5
CO ₂	1946	1601		1319					
H₂O	0.32	0.34	0.35	0.30	0.31			0.34	0.33
F	232	267	203	234	232			236	243
S	825	965	1185	776	766			716	762
CI	184	107	103	175	179			86	103

Supplementary	Table	S2.1	Cont'd
---------------	-------	------	--------

Sample	D176_R20								
Plagioclase #	9	9	9	9	9	11	11	11	11
MI#	1	2	3	4	5	1	2	3	4
SiO ₂	49.1	49.4	49.5		49.3	49.3	49.6	49.6	49.0
TiO ₂	0.38	0.33	0.42		0.38	0.50	0.45	0.39	0.40
Al_2O_3	16.2	16.0	16.2		16.0	16.2	15.9	16.0	16.0
FeO _T	8.4	8.2	8.5		8.5	8.9	8.5	8.4	8.2
MnO	0.210	0.189	0.127		0.118	0.198	0.174	0.213	0.118
MgO	11.22	11.31	11.21		11.17	11.16	11.30	11.16	11.16
CaO	11.3	11.3	11.2		11.1	11.1	11.2	11.3	11.1
Na ₂ O	2.46	2.44	2.42		2.38	2.41	2.51	2.49	2.48
K ₂ O	0.114	0.120	0.123		0.111	0.125	0.142	0.118	0.122
Total	99.606	99.412	100.177		99.358	100.177	99.909	99.935	99.132
La	1.7	1.8	2.0	2.1	1.9	2.7	2.2	2.1	1.7
Ce	4.8	4.7	5.6	6.1	5.8	8.0	6.4	5.3	5.2
Nd	2.8	4.0	4.3	5.1	4.9	7.2	4.4	4.6	5.1
Sm	1.8	0.8	1.6	0.8	1.5	2.2	1.5	1.3	0.9
Eu	1.0	1.2	1.3	1.0	1.3	1.5	1.1	1.2	1.3
Dy	1.0	1.2	1.2	1.2	1.7	2.7	1.5	2.0	1.4
Er	0.7	0.6	0.9	0.9	1.0	1.3	1.2	0.7	0.7
Yb	0.5	0.5	0.6	0.6	0.7	1.1	1.0	0.9	0.6
Cr	316	319	352	339	331	347	341	340	262
Ba	15.5	16.9	17.4	16.3	16.2	17.7	16.0	16.2	18.4
Sr	152	150	162	160	168	170	169	168	215
Nb	0.1	0.2	0.9	0.7	0.3	0.6	0.2	0.2	0.3
Υ	5.5	5.6	7.6	7.3	8.2	14.0	10.4	9.2	7.4
Zr	2.1	4.9	17.9	18.1	9.3	16.9	7.0	5.0	5.7
CO ₂							1357		2008
H₂O							0.34	0.35	0.37
F							253	258	257
S							812	887	879
Cl							51	93	88

Sample	D176_R20									
Plagioclase #	11	11	13	13	14	14	14	14	14	18
MI#	5	6	1	2	1	2	3	4	5	1
SiO ₂	49.6		50.0	50.5	48.7	49.1	49.2	49.0	49.0	48.6
TiO ₂	0.54		0.58	0.75	0.50	0.53	0.49	0.47	0.47	0.66
Al_2O_3	16.2		15.9	15.9	15.9	16.0	16.0	15.8	15.8	16.0
FeO _T	8.6		9.2	9.6	8.4	8.7	8.5	8.4	8.4	8.6
MnO	0.115		0.166	0.177	0.174	0.117	0.157	0.184	0.184	0.149
MgO	11.19		9.24	9.13	11.95	12.14	11.97	12.02	12.02	11.44
CaO	11.1		11.4	11.4	11.1	11.1	11.2	11.0	11.0	11.2
Na₂O	2.52		2.73	2.88	2.45	2.40	2.47	2.41	2.41	2.37
K₂Ō	0.127		0.165	0.171	0.131	0.137	0.114	0.135	0.135	0.118
Total	100.447		99.708	100.908	99.789	100.606	100.347	99.688	99.688	99.817
La	2.3	2.1	2.7	2.7	2.7	3.0	3.0	2.4		2.7
Ce	6.1	5.9	7.6	8.0	8.3	8.3	8.3	7.1		8.1
Nd	4.6	4.5	6.1	6.8	6.6	6.3	6.0	5.3		7.4
Sm	1.5	1.8	2.3	1.7	2.3	2.8	1.3	1.5		3.0
Eu	1.1	1.1	1.2	1.4	1.3	1.5	1.2	1.5		1.2
Dy	1.2	1.5	2.9	2.4	2.6	2.5	2.4	2.7		2.5
Er	0.8	0.9	1.2	1.1	1.9	1.5	1.3	1.5		1.9
Yb	0.6	0.8	1.2	0.4	1.3	1.2	0.8	1.1		1.3
Cr	331	328	356	331	350	320	349	359		251
Ba	17.2	17.2	21.8	20.3	23.8	23.4	16.5	16.8		16.6
Sr	151	149	178	186	172	163	168	169		188
Nb	0.4	0.6	1.4	1.4	0.6	0.8	0.6	0.4		2.0
Υ	9.8	10.1	13.8	12.0	14.9	15.8	14.5	13.9		16.8
Zr	11.5	11.8	37.1	33.7	14.6	17.7	13.8	11.8		28.7
CO ₂	1423				1554	1368			1294	
H₂O	0.36				0.33	0.34			0.34	0.34
F	253				257	262			263	
S	830				875	891			908	799
a	73				48	46			48	

Sample	D176_R20	D176_R24	D176_R3	D176_R20						
Plagioclase #	19	20	20	22	23	23	25	11	6	18
MI#	1	1	1 (R)	1	1	1 (R)	1	1	2	2
SiO ₂	49.4	49.6	49.3	49.2	49.7		50.2	48.4	48.0	48.6
TiO ₂	0.33	1.62	1.68	0.61	1.06		0.99	0.96	0.45	0.56
Al_2O_3	16.1	15.7	15.6	16.4	15.8		15.9	16.7	12.4	14.5
FeO _T	8.6	10.6	10.4	8.6	9.3		9.7	9.2	11.0	9.2
MnO	0.206	0.184	0.182	0.108	0.182		0.226	0.150	0.268	0.186
MgO	11.25	6.82	6.85	11.28	9.28		9.21	10.19	12.71	13.00
CaO	11.2	11.3	11.3	11.2	11.6		11.4	11.2	11.7	11.1
Na ₂ O	2.51	2.86	2.93	2.56	2.69		2.74	2.23	1.93	2.18
K ₂ O	0.131	0.293	0.340	0.141	0.168		0.186	0.159	0.122	0.136
Total	99.826	99.696	99.555	100.458	100.136		100.937	99.387	98.897	99.615
La	1.7	10.1	9.5	1.5	2.9	2.8	3.7	3.9	1.9	2.8
Ce	4.8	22.5	26.3	4.7	8.5	8.1	10.3	11.4	5.9	8.7
Nd	3.3	16.0	17.8	3.3	8.6	7.4	8.3	8.8	4.2	7.3
Sm	1.4	2.9	5.4	1.2	1.3	3.0	1.2	2.4	1.1	1.6
Eu	1.3	1.5	2.1	0.8	0.7	1.1	0.8	1.3	1.4	1.3
Dy	1.1	5.6	6.0	1.4	2.5	2.4	2.8	3.1	1.8	3.3
Er	0.7	3.1	3.7	0.8	1.3	1.7	2.1	2.2	8.0	2.1
Yb	0.4	2.4	3.5	0.8	1.5	1.1	1.9	1.1	0.6	1.4
Cr	321	155	184	186	267	267	305	364	387	271
Ba	16.3	49.5	53.1	23.4	19.9	15.7	21.3	19.7	23.2	19.6
Sr	153	199	222	239	171	206	174	182	167	169
Nb	0.1	8.5	9.5	0.5	2.4	2.6	2.2	3.7	1.0	0.6
Υ	4.9	29.4	32.6	7.2	14.5	14.9	17.4	16.2	8.4	16.9
Zr	3.4	115.0	129.1	13.9	48.8	46.9	53.3	64.8	20.8	14.7
CO ₂		1261	1623							
H₂O		0.34	0.36	0.37	0.35		0.37		0.39	0.37
F		207	210	258	239		243		268	
S		1289	1306	903	892		947		891	842
а		181	187	148	183		213		227	

Sample	D176_R20	D176_R24	D176_R24	D176_R3	D176_R17	D176_R20	D176_R24
Plagioclase #	18	2	2				
MI#	3	1	2	Matrix	Matrix	Matrix	Matrix
SiO ₂	47.6	49.7	49.5	48.9	48.6	48.8	47.6
TiO ₂	0.50	0.60	0.58	1.49	1.43	1.54	1.17
Al_2O_3	15.5	16.8	16.3	16.0	16.3	16.1	16.8
FeO _T	8.8	9.0	9.5	10.2	9.9	10.3	10.6
MnO	0.167	0.154	0.165	0.192	0.178	0.165	0.187
MgO	10.69	10.12	10.78	7.83	8.04	7.87	8.61
CaO	11.3	10.5	10.2	11.8	11.9	11.9	11.8
Na ₂ O	2.40	2.62	2.57	2.84	2.75	2.79	2.51
K₂O	0.136	0.183	0.228	0.210	0.193	0.197	0.117
Total	97.567	100.139	99.926				
La	2.6	2.3	2.8	5.3	5.0	5.3	2.9
Ce	8.7	5.9	7.3	14.6	13.6	13.8	7.7
Nd	7.5	4.4	4.9	11.9	11.4	12.0	8.0
Sm	1.7	1.3	1.7	3.8	3.6	3.7	3.0
Eu	1.3	0.9	1.3	1.3	1.3	1.4	1.1
Dy	3.1	1.1	1.9	5.2	5.0	5.3	4.9
Er	1.5	0.7	0.8	3.0	3.0	3.2	3.0
Yb	1.6	0.5	0.6	2.9	2.8	2.8	2.8
Cr	291	274	318	229	261	290	241
Ba	19.7	18.7	24.6	44.4	37.2	33.0	14.6
Sr	169	197	166	196	194	198	155
Nb	1.3	0.4	0.5	5.6	5.1	5.4	2.6
Υ	17.5	6.8	7.7	29.5	28.7	28.7	27.0
Zr	19.9	10.1	10.6	101.6	96.7	100.3	70.0
CO ₂				124	92	89	142
H₂O		0.22		0.40	0.33	0.34	0.23
F		153		239	219	225	147
S		658		1000	992	1015	952
CI				182	181	180	42

Supplementary Information S3: Post entrapment crystallization correction.

As a method of correcting for post-entrapment crystallization of host plagioclase, melt inclusions are re-homogenized by heating until they are saturated in both olivine and plagioclase (Nielsen, 2011, Nielsen et al., 1995, Sinton et al., 1993, Sours-Page et al., 2002). However, reheating can lead to volatile loss through fracture pathways if the inclusions are breached (Kent, 2008). To avoid volatile loss, we did not reheat our melt inclusions. Instead, melt inclusion compositions were corrected by adding plagioclase numerically to a linearly regressed olivineplagioclase cotectic. We define the olivine-plagioclase cotectic with East Pacific Rise and Mid-Atlantic Ridge data from the Smithsonian Volcanic Glass File (Melson et al., 2002), and melt inclusions in high anorthite (An₈₂₋₉₀) crystals from the Lamont seamount chain that have been rehomogenized by heating (Nielsen, 2011). When the olivine-plagioclase cotectic is regressed for MgO-Al₂O₃ and MgO-FeO, the uncorrected melt inclusions plot off of the cotectic caused by variable degrees of plagioclase crystallization (Fig S3.1). The melt inclusions were then corrected to the average of the regressed MgO-Al₂O₃ and MgO-FeO_T olivine-plagioclase cotectics by addition of the plagioclase composition <100 µm from each inclusion (Table 2). The amount of post-entrapment crystallization was determined by the lever rule (Fig. S3.1 c, d).

Trace elements were corrected by using the standard Rayleigh fractionation equation:

$$C_{liq}^{i} = C_{liq}^{0} F^{(k_d - 1)}$$
 (1)

where for a given element C_{liq}^{i} is the concentration in the liquid at a fraction F of liquid remaining after post-entrapment crystallization, C_{liq}^{0} is the concentration in the liquid at entrapment, and K_d is the plagiclase-melt partition coefficient (table S3.1). Volatile elements (H₂O, CO₂, F, Cl, and S) were corrected by assuming a partition behaviour of a refractory

element with similar incompatibility (Ce, Nb, Nd, K, and Dy, respectively). The initial compositions can be found in supplementary information S2 and the recalculated compositions with percentage post-entrapment crystallization are found in Table 1. The amount of calculated post entrapment crystallization varies from 0 - 26% with $\sim 43\%$ of the samples < 10% and $\sim 92\%$ of the samples < 15% (Fig S3.2).

Table S3.1: Partition coefficients used for post entrapment crystallization correction.

Element	Plagioclase (An ₈₇)	
La	0.035	
Ce	0.048 †	
Nd	0.023	
Sm	0.009	
Eu	0.379	
Dy	0.025 †	
Er	и и	
Yb	0.027 †	
Ва	0.149	
Sr	1.110	
Nb	0.0011	
Zr	0.006	
Υ	0.0075 †	
Cr	0.035 †	
K	-	

Notes: Partition coefficients for post entrapment crystallization correction were from experiments with ~ 87 mol. % plagioclase anorthite contents (Tepley, et al. 2010). † Partition coefficients for elements not available in Tepley, et al. (2010) were from Aigner-Torres, et al. (2007).

Figure S3.1: Regression of the Al₂O₃ and FeO_T olivine-plagioclase cotectic using lavas erupted at the East Pacific Rise, Mid-Atlantic ridge, and rehomogenized melt inclusions in high-anorthite plagioclase from the Lamont Seamounts. (a, b) Melt inclusions from Taney Seamount-A plot off of the cotectic by crystallization of the host plagioclase. (c, d) Individual analyses were corrected by numerically adding the plagioclase compositions <100 μm from each melt inclusion to the minimum variance from the Al₂O₃ and FeO_T cotectic. East Pacific Rise and Mid-Atlantic ridge data are from the Smithsonian volcanic glass file (Melson *et al.*, 2002) and rehomogenized high anorthite melt inclusions are from (Nielsen, 2011).

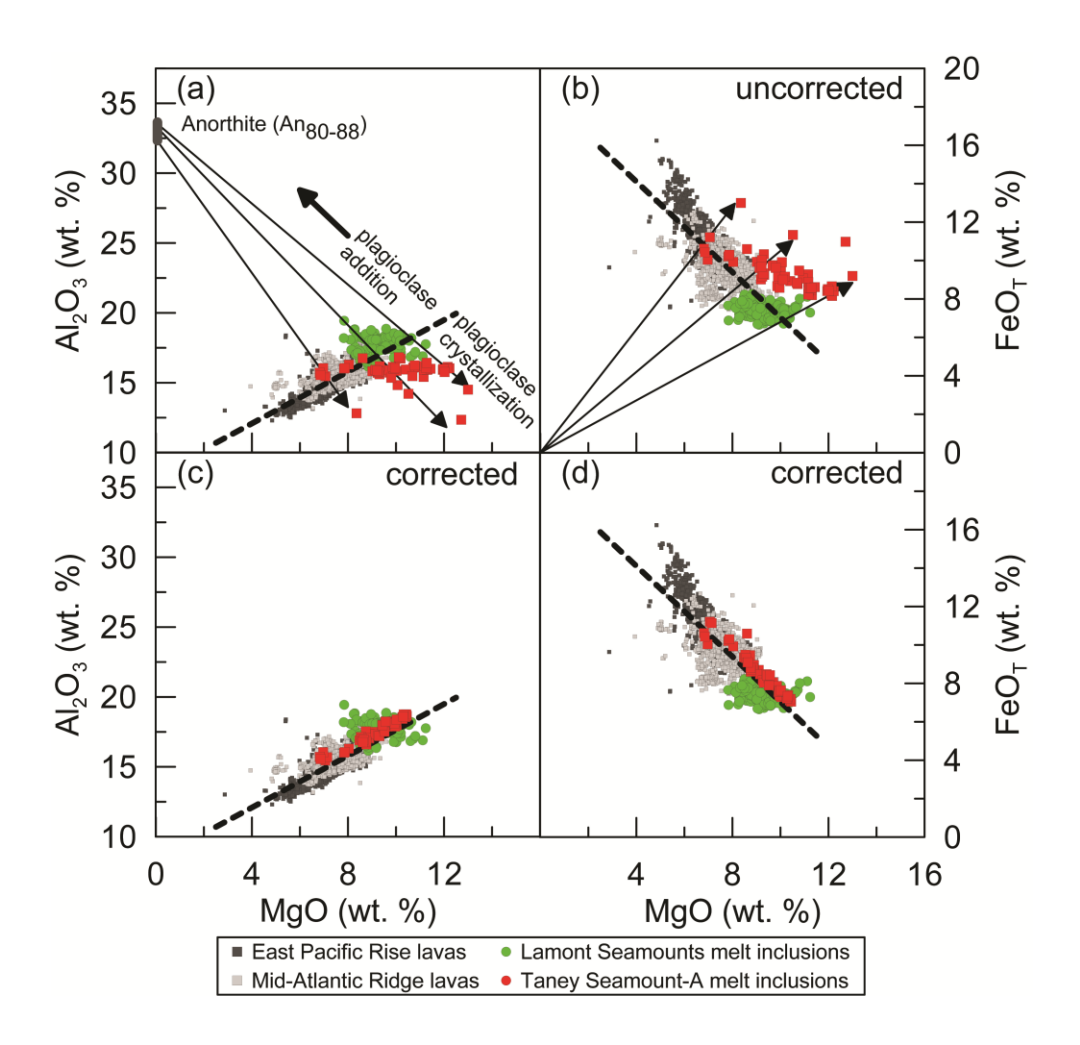
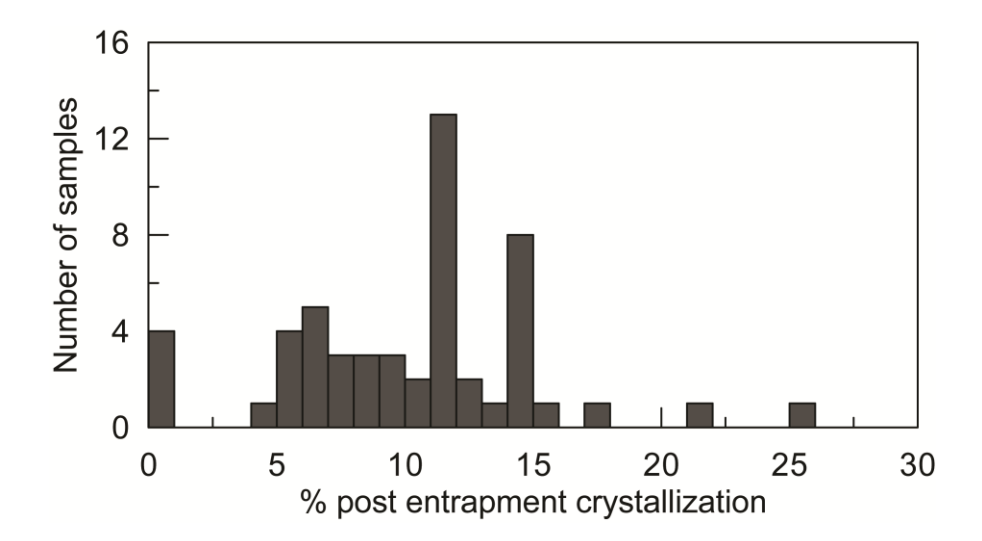


Figure S3.2: Histogram of calculate post entrapment crystallization percentages. Approximately 43% of the samples have calculate post entrapment crystallization < 10%, and ~93% have less than 15%.



Supplementary Information S4: Parameters for alphaMELTS modelling.

Model cumulate bulk compositions used for partial melting modelling were created by mixing variable proportions of lower crustal mineral compositions (Table S4.2). Two series of cumulate compositions were created using average mineral compositions from lower crustal troctolites and olivine gabbros (Lissenberg et al., 2013). The bulk compositions were equilibrated in alphaMELTS to a melt fraction < 0.5%, approximating the solidus (Table S4.3). The differences between the alphaMELTS equilibrated phase proportions and compositions and the mixing proportions and lower crustal mineral compositions (Δ = alphaMELTS - mixing) are illustrated in Figure S4.1. The alphaMELTS determined mineral modes are within + 2% for olivine, + 2-6% for clinopyroxene and - 2-6% for plagioclase when compared to the model mineral mixing proportions. The alphaMELTS determined mineral compositions for both the troctolite and olivine gabbro series are within ± 2 Fo for olivine, ± 3 Mg# for clinopyroxene, and ± 3 An for plagioclase. For a given model bulk composition, alphaMELTS calculates a greater proportion of clinopyroxene and lesser plagioclase. As a result, the alphaMELTS equilibrated clinopyroxene is more aluminum rich compared to the lower oceanic crust clinopyroxenes in order to maintain Al₂O₃ mass balance.

Table S4.1: Partition coefficients used for alphaMELTS equilibrium melting models

Mineral	Clinopyroxene ¹	Olivine ¹	Plagioclase ¹	Clinopyroxene ²	Olivine ²	Plagioclase ²
Reference	Rolli	inson, (199	3)	Hauri <i>et al.,</i> (1994)	McKenzie & O'Nions (1991)	Aigner-Torres et al.,(2007)
La	0.056	0.007	0.190	0.0515	0.0004	0.062
Ce	0.092	0.0060	0.110	0.108	0.0005	0.048
Nd	0.230	0.0059	0.090	0.277	0.001	0.037
Sm	0.445	0.0070	0.072	0.462	0.0013	0.049
Eu	0.474	0.0074	0.443	0.458	0.0016	0.379
Dy	0.582	0.013	0.063	0.711	0.0017	0.025
Er	0.583	0.026	0.057	0.66	0.0015	" "
Yb	0.542	0.049	0.056	0.633	0.0015	0.027
Ва	0.026	0.010	0.230	0.0058	0.0003	0.259
Sr	0.060	0.014	1.830	0.157	0.00019	1.633
Nb	0.005	0.010	0.010	0.0081	0.01	0.029
Zr	0.100	0.012	0.048	0.195	0.01	0.0022
Υ	0.900	0.010	0.030	0.467 ‡	0.005	0.0075
Cr	34.000	0.700	0.000	1.66	0.3	0.035
K	0.038	0.007	0.170	0.0072 ‡	0.00018	0.204

Notes: ‡ Partition coeffecients for elements not available in Hauri *et al.*,(1994) were from Hart & Dunn, (1993). Two sets of partition coefficients^{1,2} were used in the alphaMELTS modelling to investigate partitioning dependence.

Table S4.2: Average mineral compositions from lower crustal rocks at Hess Deep (Lissenberg et al., 2013)

	1	Γroctolite		Olivine Gabbro					
Mineral	Clinopyroxene	Olivine	Plagioclase	Clinopyroxene	Olivine	Plagioclase			
SiO ₂	50.30	39.45	45.56	52.82	39.39	48.80			
TiO ₂	1.22	-	0.06	0.30	-	0.03			
Al_2O_3	3.36	-	34.49	2.42	-	32.37			
FeO _T	4.25	15.06	0.39	5.86	17.99	0.43			
MnO	0.14	0.24	0.02	0.15	0.25	0.01			
MgO	16.45	45.36	0.06	17.78	42.82	0.08			
CaO	23.26	-	18.01	20.29	-	15.73			
Na₂O	0.25	-	1.45	0.26	-	2.73			
Mg#, Fo, An	87.3	84.3	87.0	84.3	81.0	76.0			

Notes: All oxides are in wt. %. The compositions represent mineral averages of troctolites and olivine gabbros from the Hess Deep (Lissenberg *et al.*, 2013). Mg#, Fo, An represent the magnesium number, forsterite content, or anorthite content of the mineral.

Table S4.3:Comparison between bulk and alphaMELTS solidus equilibrated mineral modes and compositions.

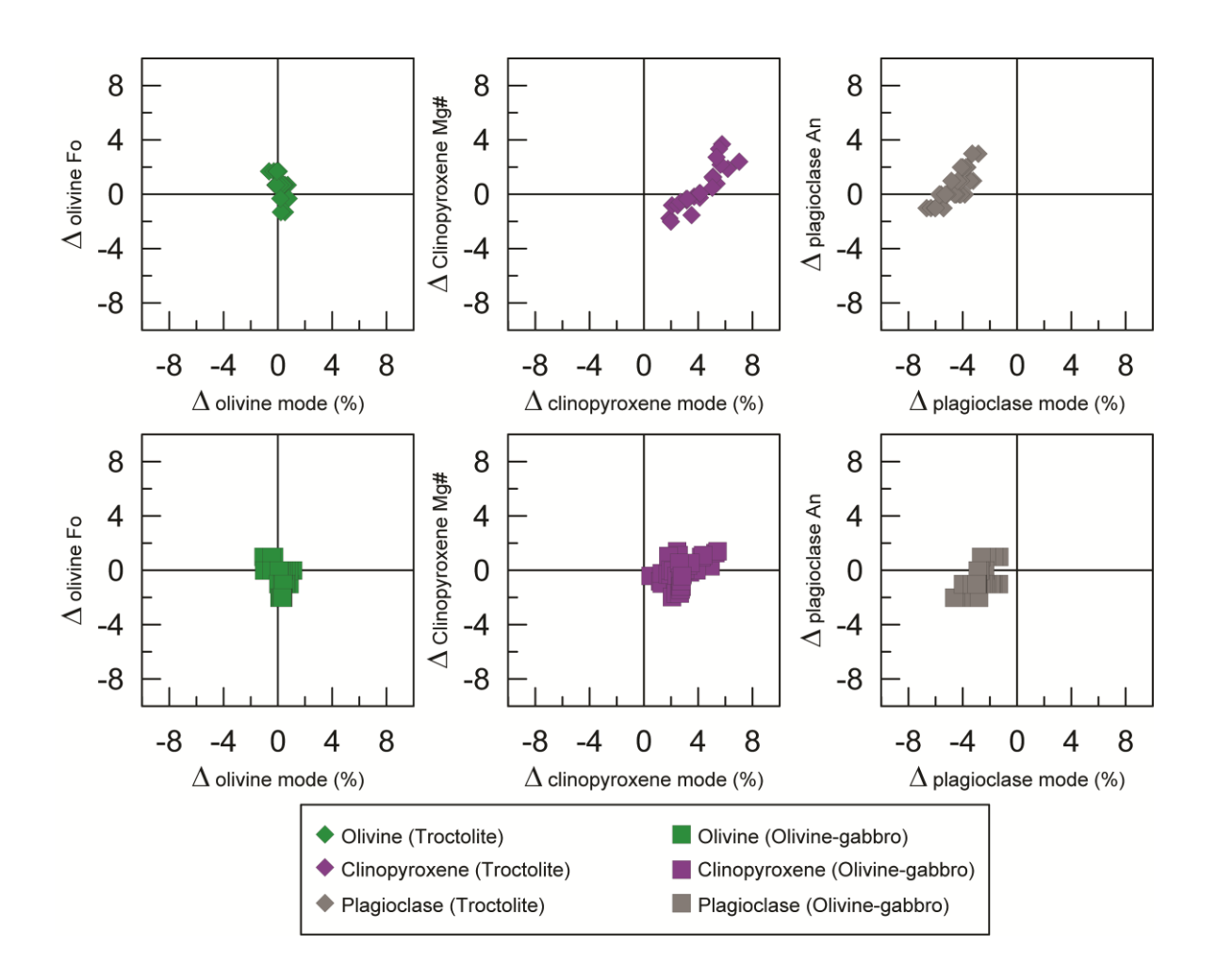
Rock Series	Bulk Olivine		Bulk Clinopyroxene		Bulk Plagioclase		alphaMELTS Olivine		alphaMELTS Clinopyroxene		alphaMELTS Plagioclase	
Mode % Composition	Mode	Fo	Mode	Mg#	Mode	An	Mode	Fo	Mode	Mg#	Mode	An
Troctolite	40	84	-	-	60	87	41	84	>1	-	57	90
Troctolite	36	84	4	87	60	87	37	84	6	85	57	88
Troctolite	32	84	8	87	60	87	33	85	11	87	56	87
Troctolite	28	84	12	87	60	87	29	85	16	87	56	87
Troctolite	20	84	20	87	60	87	20	86	25	88	55	86
Troctolite	12	84	28	87	60	87	11	86	35	89	53	86
Troctolite	-	-	40	87	60	87	-	-	46	91	54	86
Troctolite	30	84	-	-	70	87	31	84	>1	-	67	90
Troctolite	27	84	3	87	70	87	27	85	5	85	67	88
Troctolite	24	84	6	87	70	87	24	85	10	85	66	87
Troctolite	21	84	9	87	70	87	21	85	13	87	66	87
Troctolite	15	84	15	87	70	87	15	86	20	88	65	87
Troctolite	9	84	21	87	70	87	9	86	27	89	64	86
Troctolite	-	-	30	87	70	87	-	-	36	90	64	86
Troctolite	20	84	-	-	80	87	21	83	>1	-	77	90
Troctolite	18	84	2	87	80	87	18	85	4	86	76	89
Troctolite	16	84	4	87	80	87	16	85	7	87	76	88
Troctolite	14	84	6	87	80	87	14	85	10	87	75	87
Troctolite	10	84	10	87	80	87	10	86	15	88	75	87
Troctolite	6	84	14	87	80	87	6	86	20	89	74	87
Troctolite	-	-	20	87	80	87	-	-	25	90	74	87
Troctolite	10	84	-	-	90	87	10	83	2	-	86	89
Troctolite	9	84	1	87	90	87	9	84	3	86	86	89
Troctolite	8	84	2	87	90	87	8	85	5	86	86	89
Troctolite	7	84	3	87	90	87	7	85	6	<i>8</i> 7	86	88
Troctolite	5	84	5	87	90	87	5	85	9	<i>8</i> 7	85	88
Troctolite	3	84	7	87	90	87	3	86	12	88	85	87
Troctolite	-	-	10	87	90	87	-	-	15	89	84	87

Notes: Model cumulate compositions were created by bulk addition of the mineral compositions for each rock type (Table S3.2) in variable modal proportions. The model cumulate composition was equilibrated in alphaMELTS to a melt fraction less than 0.5%, and the output modes and mineral compositions are presented.

Table S4.3 Cont'd

Rock Series	Bulk Olivine		Bulk Clinopyroxene		Bulk Plagioclase		alphaMELTS Olivine		alphaMELTS Clinopyroxene		alphaMELTS Plagioclase	
Mode % Composition	Mode	Fo	Mode	Mg#	Mode	An	Mode	Fo	Mode	Mg#	Mode	An
Olivine Gabbro	40	81	-	-	60	76	41	81	-	-	59	77
Olivine Gabbro	36	81	4	84	60	76	37	81	4	84	59	<i>7</i> 5
Olivine Gabbro	32	81	8	84	60	76	33	81	9	84	58	<i>7</i> 5
Olivine Gabbro	28	81	12	84	60	76	28	81	14	84	58	<i>7</i> 5
Olivine Gabbro	24	81	16	84	60	76	24	81	19	84	57	<i>7</i> 5
Olivine Gabbro	20	81	20	84	60	76	20	81	24	84	57	<i>7</i> 5
Olivine Gabbro	16	81	24	84	60	76	15	82	28	85	56	<i>7</i> 5
Olivine Gabbro	12	81	28	84	60	76	11	82	33	85	56	74
Olivine Gabbro	8	81	32	84	60	76	7	82	37	86	55	74
Olivine Gabbro	4	81	36	84	60	76	3	81	41	86	55	74
Olivine Gabbro	-	-	40	84	60	76	-	-	42	86	57	74
Olivine Gabbro	30	81	-	-	70	76	31	80	>1	-	68	77
Olivine Gabbro	27	81	3	84	70	76	28	80	4	83	68	<i>7</i> 5
Olivine Gabbro	24	81	6	84	70	76	25	81	7	84	68	<i>7</i> 5
Olivine Gabbro	21	81	9	84	70	76	22	81	11	84	68	<i>7</i> 5
Olivine Gabbro	18	81	12	84	70	76	18	81	14	84	67	<i>7</i> 5
Olivine Gabbro	15	81	15	84	70	76	15	81	18	84	67	<i>7</i> 5
Olivine Gabbro	12	81	18	84	70	76	12	81	21	84	67	<i>7</i> 5
Olivine Gabbro	9	81	21	84	70	76	9	82	25	84	66	<i>7</i> 5
Olivine Gabbro	6	81	24	84	70	76	6	82	28	85	66	<i>7</i> 5
Olivine Gabbro	3	81	27	84	70	76	3	81	31	85	66	<i>7</i> 5
Olivine Gabbro	-	-	30	84	70	76	-	-	33	85	67	<i>7</i> 5
Olivine Gabbro	20	81	-	-	80	76	20	80	1	-	78	77
Olivine Gabbro	18	81	2	84	80	76	19	80	4	85	78	76
Olivine Gabbro	16	81	4	84	80	76	17	80	6	84	78	<i>7</i> 5
Olivine Gabbro	14	81	6	84	80	76	15	80	8	84	78	<i>7</i> 5
Olivine Gabbro	12	81	8	84	80	76	13	80	10	84	78	<i>7</i> 5
Olivine Gabbro	10	81	10	84	80	76	10	81	12	84	77	<i>7</i> 5
Olivine Gabbro	8	81	12	84	80	76	8	81	15	84	77	<i>7</i> 5
Olivine Gabbro	6	81	14	84	80	76	6	81	17	84	77	<i>7</i> 5
Olivine Gabbro	4	81	16	84	80	76	4	81	19	85	77	<i>7</i> 5
Olivine Gabbro	2	81	18	84	80	76	2	80	21	85	77	<i>7</i> 5
Olivine Gabbro	-	-	20	84	80	76	-	-	23	85	77	<i>7</i> 5
Olivine Gabbro	10	81	-	-	90	76	10	79	2	-	87	77
Olivine Gabbro	9	81	1	84	90	76	9	79	3	82	87	76
Olivine Gabbro	8	81	2	84	90	76	8	79	4	83	87	76
Olivine Gabbro	7	81	3	84	90	76	7	79	6	83	87	76
Olivine Gabbro	6	81	4	84	90	76	6	80	7	83	87	75
Olivine Gabbro	5	81	5	84	90	76	5	80	8	83	87	<i>7</i> 5
Olivine Gabbro	4	81	6	84	90	76	4	79	9	84	87	<i>7</i> 5
Olivine Gabbro	3	81	7	84	90	76	3	79	10	83	87	<i>7</i> 5
Olivine Gabbro	2	81	8	84	90	76 	2	79	11	84	87	75
Olivine Gabbro	1	81	9	84	90	76	1	79	12	84	87	<i>7</i> 5
Olivine Gabbro	0	81	10	84	90	76	-	-	13	83	87	75

Figure S4.1: The differences between the alphaMELTS equilibration calculation and the mineral mixing model (Δ = alphaMELTS - mixing) are presented in the above figures. The Fo, Mg# and An contents of the olivine, clinopyroxene, and plagioclase for both rock series are similar to the lower oceanic crustal compositions. AlphaMELTS calculates a greater proportion of clinopyroxene at the expense of plagioclase for a given model bulk compositions.



References:

- Aigner-Torres, M., Blundy, J., Ulmer, P. & Pettke, T. (2007). Laser Ablation ICPMS study of trace element partitioning between plagioclase and basaltic melts: an experimental approach. *Contributions to Mineralogy and Petrology* **153**, 647-667.
- Hart, S. R. & Dunn, T. (1993). Experimental cpx/melt partitioning of 24 trace elements. *Contributions to Mineralogy and Petrology* **113**, 1-8.
- Hauri, E. H., Wagner, T. P. & Grove, T. L. (1994). Experimental and natural partitioning of Th, U, Pb and other trace-elements between garnet, clinopyroxene and basaltic melts. *Chemical Geology* **117**, 149-166.
- Helo, C., Longpre, M.-A., Shimizu, N., Clague, D. A. & Stix, J. (2011). Explosive eruptions at mid-ocean ridges driven by CO₂-rich magmas. *Nature Geoscience* **4**, 260-263.
- Jarosewich, E. (2002). Smithsonian microbeam standards. *Journal of Research of the National Institute of Standards and Technology* **107**, 681-685.
- Kent, A. J. R. (2008). Melt Inclusions in Basaltic and Related Volcanic Rocks. *Minerals, Inclusions and Volcanic Processes* **69**, 273-331.
- Lissenberg, C. J., MacLeod, C. J., Howard, K. A. & Godard, M. (2013). Pervasive reactive melt migration through fast-spreading lower oceanic crust (Hess Deep, equatorial Pacific Ocean). *Earth and Planetary Science Letters* **361**, 436-447.
- McKenzie, D. & O'Nions, R. K. (1991). Partial melt distributions from inversion of rare earth element concentrations. *Journal of Petrology* **32**, 1021-1091.
- Melson, W. G., O'Hearn, T. & Jarosewich, E. (2002). A data brief on the Smithsonian Abyssal Volcanic Glass Data File. *Geochemistry Geophysics Geosystems* **3**, 11.
- Nielsen, R. L. (2011). The effects of re-homogenization on plagioclase hosted melt inclusions. *Geochemistry Geophysics Geosystems* **12**.
- Nielsen, R. L., Crum, J., Bourgeois, R., Hascall, K., Forsythe, L. M., Fisk, M. R. & Christie, D. M. (1995). Melt inclusions in high-An plagioclase from the Gorda Ridge: an example of the local diversity of MORB parent magmas. *Contributions to Mineralogy and Petrology* **122**.
- Rollinson, H. R. (1993). *Using Geochemical Data: Evaluation, Presentation, Interpretation*: Longman Scientific & Technical.
- Sinton, C. W., Christie, D. M., Coombs, V. L., Nielsen, R. L. & Fisk, M. R. (1993). Near-primary melt inclusions in anorthite phenocrysts from the Galapagos Platform. *Earth and Planetary Science Letters* **119**.

- Sours-Page, R., Nielsen, R. L. & Batiza, R. (2002). Melt inclusions as indicators of parental magma diversity on the northern East Pacific Rise. *Chemical Geology* **183**, 237-261.
- Stix, J., Gauthier, G. & Ludden, J. N. (1995). A critical-look at quantitative laser-ablation ICP-MS analysis of natural and synthetic glasses. *Canadian Mineralogist* **33**, 435-444.
- Tepley, F. J., III, Lundstrom, C. C., McDonough, W. F. & Thompson, A. (2010). Trace element partitioning between high-An plagioclase and basaltic to basaltic andesite melt at 1 atmosphere pressure. *Lithos* **118**, 82-94.

Link to Chapter 3

The previous two chapters investigate magmatic processes that occurred at Taney Seamount-A during melt generation in the mantle, melt-rock interaction during transport, and evolution in a shallow sub-caldera magma reservoir. These chapters utilized a combination of geochemical analyses from erupted lavas and entrained plagioclase crystals and geochemical modelling. Chapter 3 is a departure from petrologic investigation of magmatic processes and is instead focused on the physical volcanic processes that occur during caldera collapse at near-ridge seamounts.

Near-ridge seamounts have well developed calderas on both the apex and the flanks of the edifice. For example, Taney Seamount-A has at least four calderas, with the youngest and largest caldera truncating the southeastern flank of the edifice. The aim of this chapter is to investigate how the position of a volcanic edifice affects caldera collapse. I use scaled analogue experiments in conjunction with a three dimensional (3D) laser scanner and digital particle image velocimetry techniques. Based on the experimental results, I propose that the presence and position of a volcanic edifice affects the resulting caldera structure and evolution. An offset edifice promotes a trapdoor style of caldera collapse defined by an asymmetric fault structure. Evidence of asymmetric collapse in nature includes the tilting of near-ridge seamount offset calderas towards the ridge axis, and similar asymmetric fault structures at Sierra Negra caldera in the Galápagos, which is a subaerial analogue to near-ridge seamounts in terms of its physical dimensions and morphology.

Chapter 3

Caldera collapse at near-ridge seamounts: An experimental investigation

Jason P. Coumans and John Stix

Manuscript in final preparation for submission to a scientific journal

ABSTRACT

Collapse calderas are sub-circular volcanic depressions caused by subsidence of the magma reservoir roof during an eruption. Scaled physical models of caldera collapse using flat topography have been instrumental in investigating the spatial and temporal development of calderas, in particular, two distinctive sets of concentric ring faults, one reverse and one normal. More recent analogue studies have investigated the effect of non-flat topography which alters the principle stress trajectories and resulting collapse structure. This work provides a premise for investigating how naturally scaled topographic loads may affect caldera collapse in relation to shallow magma reservoirs.

The objective of this study is to understand how a naturally scaled near-ridge seamount affects caldera collapse from both a central and offset position as the seamount migrates above the magma reservoir as a result of plate motion. We utilize scaled analogue models of caldera collapse in conjunction with three dimensional (3D) laser scanning and digital particle image velocimietry (DPIV) to investigate caldera collapse dynamics at near-ridge seamounts. Experiments using a seamount cone positioned centrally above the magma reservoir result in (1) increased subsidence along the inner, outward dipping faults and (2) a preference to more symmetric collapse patterns as indicated by the subsidence profile and structure of the caldera relative to experiments from the offset cone where collapse was asymmetric and trapdoor in nature, with the center of greatest subsidence displaced away from the region of largest topographic load. For these latter experiments, subsidence was focused where the roof was thinnest along an initial reverse fault followed by a transition to an antithetic graben structure. The asymmetric collapse in the experiments results in a caldera with a tilted profile. Offset calderas at near-ridge seamounts are tilted towards the ridge axis, suggesting that they may have

collapsed asymmetrically consistent with our experiments. Furthermore, the graben structure observed in asymmetric collapse experiments is consistent with structures observed in some natural trapdoor volcanoes.

INTRODUCTION

Collapse calderas are complex volcanic depressions that have been recognized on Earth and in the solar system. On Earth, caldera diameters vary from less than a kilometer to tens of kilometers, with eruptive volumes ranging from a few km³ to more than 5000 km³ (Cole *et al.*, 2005). The largest known caldera in the solar system is Olympus Mons on Mars, a nested complex consisting of six collapse centers that together measure 80 x 65 km in diameter (Mouginis-Mark & Rowland, 2001). Collapse calderas are observed in all volcanic systems ranging from basaltic to silicic in composition; they form in divergent, convergent and intraplate settings. Large eruptions associated with caldera collapse have been hypothesized to cause massive extinctions of flora and fauna. For example, the large ~74 ka caldera forming eruption at Toba caldera in Indonesia has been hypothesized to have caused a human population bottleneck in the Late Pleistocene (Ambrose, 1998). The ubiquitous occurrence of calderas and their potential societal impacts highlight their significance and has encouraged research into mechanisms of how they form.

Our recent understanding of caldera formation has advanced due to a combination of field (Kennedy & Stix, 2003), numerical (Folch & Martí, 2004), and experimental studies (Kennedy *et al.*, 2004, Martí *et al.*, 1994, Roche *et al.*, 2000). Analogue studies of caldera collapse have been particularly useful because they permit researchers to investigate their structural evolution with time, and also confirm field based observations at laboratory scales.

Two of the most important discoveries are the different end-member collapse styles and the subsurface structural progression during caldera formation. These end-members include plate or piston, trapdoor, piecemeal, and downsag styles of subsidence. However, many calderas have multiple styles and can progress from one style to another (Cole *et al.*, 2005). Various analogue studies of caldera collapse have investigated a range of parameters which may affect caldera collapse style, including (1) the ratio of the magma reservoir depth to the magma reservoir diameter (Acocella *et al.*, 2001, Burchardt & Walter, 2010, Geyer *et al.*, 2006, Kennedy *et al.*, 2004, Martí *et al.*, 1994, Roche *et al.*, 2000), (2) regional stresses (Holohan *et al.*, 2005), (3) magma reservoir geometry (Roche *et al.*, 2000), (4) cyclical inflation and deflation (Walter & Troll, 2001), and (5) topography (Lavallée *et al.*, 2004). Despite differences in experimental setup and parameters, a key and consistent observation is that caldera collapse comprises four main stages defined by (1) downsag, (2) outward dipping reverse faults, (3) peripheral downsag, and (4) peripheral inward dipping normal faults (Acocella, 2007).

In many cases, calderas are associated with volcanic systems having significant topographic relief in the form of a volcanic edifice, small cones, or other constructional features. Short chains of basaltic seamounts, such as the Taney Seamounts, are common on the flanks of fast- to intermediate-spreading ridges in the Pacific Ocean. These seamounts are modified by well developed calderas on both the apex and flanks of the edifice (Fig. 1). However, due to subsequent caldera infilling by effusive eruptions, little is known whether the style of caldera collapse changes when the edifice is translated away from the magma reservoir by plate movements. Topographic relief affects the load on the magma reservoir and shifts the stress trajectories between the roof of the reservoir and the surface (Jaeger & Cook, 1969, Lavallée *et al.*, 2004, Pinel & Jaupart, 2005). Furthermore, the slope of a volcanic edifice provides an

inclined surface, in contrast to a mainly horizontal surface for large caldera systems. Therefore, the presence, position, and slope of a volcanic edifice may affect both the caldera collapse style and its dynamics.

A clear example of calderas associated with such an edifice are found at Taney Seamount-A (Fig. 1). This is the largest seamount in the Taney chain with a 15 km in diameter at its base, a minimum pre-collapse height of 1400 m, and a minimum volume of ~190 km³. The edifice has been modified by at least four caldera collapse structures, of which three are central on the edifice and one is offset. The largest caldera consumed the majority of the southeastern flank of the edifice and also truncated the three central calderas with a minimum subsidence of 400 m. The focus of this paper is to investigate how the position of a volcanic edifice relative to the underlying magma reservoir affects caldera collapse structure and style. In order to investigate this phenomenon, we use scaled analogue experiments to simulate a caldera. Caldera evolution is observed with time using a three-dimensional (3D) laser scanner to create digital elevation maps (DEM) and digital particle image velocimetry (DPIV) to observe surface faulting. Therefore, we can investigate both structural and dynamic behaviour during caldera collapse with the aim of studying and understanding the role of topographic position on caldera collapse at near-ridge seamount environments.

METHODOLOGY

Scaling

In order to effectively model natural systems at laboratory conditions, a systematic scaling analysis must be performed. An applicable analogue model requires geometric similarity between the natural system and the model. In order to investigate the structural and dynamic

response to seamount edifice position over the reservoir, the following key parameters must be scaled: length (L^*) , gravity (g^*) , time (T^*) , cohesion (c^*) and viscosity (η^*) . These parameters define the physical dimensions of the system, behaviour of the crustal material, eruption time and behaviour of the magma. The scaling relationships used in these experiments are outlined in Hubbert (1937) and follow those applied by Lavallée *et al.* (2004) and Kennedy *et al.* (2004). The average natural dimensions observed for near-ridge seamounts, using the analysis from Hammond (1997), are a basal diameter of 7 ± 2 km, a height of 1 ± 0.4 km, and a slope of $\sim 25 \pm 9^\circ$. Therefore, we scaled our experiments to these dimensions:

$$L^* = \frac{d}{D} = \frac{0.45 \text{ m}}{7000 \text{ m}} = 6.4 \times 10^{-5}$$

where d is the basal diameter of the experimental cone, D is the diameter of the natural nearridge seamount volcanic edifice, and L^* is the length ratio. The length scale is applied to all dimensions, such as topography, the depth of the magma reservoir, and the diameter of the magma reservoir. Therefore, our 0.3 m diameter experimental magma reservoir represents a \sim 5 km diameter magma reservoir in nature.

Since the gravitational conditions for the experiment and the natural case are the same, scaling must be relative to a gravity ratio (g^*) of 1. The time ratio is a function of the gravity ratio and length ratio as follows:

$$g^* = \frac{L^*}{T^{*2}}$$

$$T^* = \sqrt{L^*} = \sqrt{6.4 \times 10^{-5}} = 0.008$$

The time ratio (T^*) is the experimental time (t) divided by the natural time (T). The time required for a large caldera to form on a near-ridge seamount is unknown; however, caldera collapses documented for several basaltic volcanoes suggest that the subsidence time could range anywhere from hours to months, and could be continuous or incremental (Stix & Kobayashi, 2008). Our experimental time is 600 s which scales to 21 hours for a natural system:

$$T = \frac{t}{T*} = \frac{600 \text{ s}}{0.008} = 75000 \text{ s} = ~21 \text{ h}$$

In order to scale the cohesion of materials, the density ratio is required. The density ratio (ρ^*) of compacted sand (1650 kg m⁻³) to basaltic rock (2800 kg m⁻³) is equal to 0.59. Sand cohesion (c^*) was scaled to the rock strength of basalt using the stress ratio (σ^*) , which is a product of the density ratio (ρ^*) , gravity ratio (g^*) , and length ratio (L^*) :

$$c^* = \sigma^* = g * \times \rho * \times L^* = 3.8 \times 10^{-5}$$

The tensile strength of volcanic rock is on the order of 10^7 Pa, but can be as low as 10^6 Pa with jointing and fracturing (Kennedy *et al.*, 2004). If we assume a natural tensile strength on the order of 10^6 Pa, the analogue model requires a cohesion of ~40 Pa using the scaling calculated above. Laboratory shear tests on dry granular materials indicate that values for cohesion increase from ~ 0 Pa at zero normal stress to 137-247 Pa at normal stresses greater than ~250-900 Pa (Schellart, 2000). Therefore, we conclude that sand is a reasonable analogue for the brittle behaviour of rocks.

The viscosity of magma is also an important parameter that needs to be considered in the scaling process. The viscosity ratio η^* is :

$$\eta^* = T * \times \sigma^* = 3.1 \times 10^{-7}$$

Since the viscosity of water is 10^{-3} Pa s, the scaling relationship indicates that a natural magma would have a viscosity on the order of 10^3 Pa s. The viscosity of dry basalt varies from 10^2 to 10^4 Pa s from 1200° C to 1000° C (Giordano & Dingwell, 2003); therefore, we conclude that water is a suitable analogue material for basaltic magma.

Experimental setup

The main layout of the apparatus is shown in Figure. 2. The experimental setup consists of a cylinder of 1 m diameter and 1.4 m height, filled with dry sand with a bulk density of 1600 - 1650 kg m⁻³. The analogue magma reservoir is a polyvinyl chloride (PVC) balance disk. For all experiments the bladder was inflated with water to 5 L in order to avoid irregularities on the edges. When inflated, the bladder has the geometric shape of an oblate ellipsoid with a horizontal diameter of approximately 0.30 m and a vertical thickness at the center of approximately 0.15 m. At this capacity, the bladder initially contracts elastically due to a decrease in the overpressure, followed by mainly vertical deflation as water continues to be evacuated.

The inflated bladder was aligned horizontally within the cylinder. Individual sand layers were placed on top of the bladder in 0.025 m increments. Each sand layer increment was compacted using a wooden board to minimize pore space and coated with a thin layer of white industrial quartz sand (sandblasting sand) as a colour marker. The analogue edifice was made in the shape of a truncated cone scaled to approximate near ridge seamounts in the Pacific Ocean. The cone was constructed from three 2.5 cm thick layers of compacted sand with 45 cm, 30 cm,

and 20 cm diameters. The slope of the cone was smoothed and compacted to $\sim 25 + 5^{\circ}$. The top of the bladder was located beneath the cone from 0.6 to 1 cm which scales to a depth of ~1 to 1.5 km, representing the estimated depth of shallow crustal magma reservoirs at near-ridge seamounts, such as the Taney Seamounts (Clague et al., 2000). Withdrawal of magma was simulated by evacuating the water through a tube leading from the bottom of the bladder. This scenario mimics a natural system where magma is injected into horizontal dykes away from the reservoir, resulting in caldera collapse. This style of magma evacuation has been observed at Miyakejima volcano (Burchardt & Walter, 2010). The flow rate was monitored and controlled by a flowmeter connected to a peristaltic pump. The evacuation rate was 0.2 l min⁻¹ for 10 minutes, resulting in a total evacuation volume of 2 liters, or $\sim 40\%$ of the bladder volume. The resulting deformation was controlled only by the weight of the overlying sand, as no far field stress was applied to the system. The evolution of the caldera was recorded using a still camera placed over the experiment with photographs taken every 5 s. At the conclusion of each experiment, the caldera was filled with sand to create a flat surface and wetted so that fault structures were preserved. The caldera was then cut into 1/8th sections and imaged.

Laser scanning

Three-dimensional (3D) laser scans of each experimental caldera were performed at 2.5 minute intervals using a NextEngine 3D scanner to create digital elevation maps (DEM), in order to document the detailed evolution of the caldera structure during the course of the experiment. The scanner uses twin arrays of four 10 mW solid-state lasers at a wavelength of 650 nm. The optical sensor comprises twin 3.0 megapixel complementary metal-oxide-semiconductors (CMOS). The scanner was used in extended mode with a maximum field area of 0.40 x 0.55 m and a point capture density on the target surface of 20points cm⁻². In this extended mode, the

dimensional accuracy at the distance range used ($\sim 400\text{-}500 \text{ mm}$) is $\sim \pm 0.5$ - 1 mm. Each DEM image is composed of 9 scans that have been stitched together. The DEM maps were then rotated, aligned, and cropped so that they could be subtracted from each other to create elevation difference maps. The difference maps were used to observe changes in deformation and subsidence with time.

Digital particle image velocimetry

Digital particle image velocimetry (DPIV) is a tool used for investigating flow patterns in nature. In DPIV analyses, two images at a known time step are used to calculate the distance a particle has traveled in the image plane. The velocities of the particles in the image plane can then be calculated from the distance and the known timestep. We utilized DPIV to investigate the [relative] horizontal movement of sand grains on the surface in response to vertical subsidence during evacuation of the reservoir. Images were recorded using a camera oriented 2 m vertically above each experiment with an image interval of 5 s. The DPIV software used to analyze the frame series was PIVlab (Thielicke & Stamhuis, 2014). Built-in contrast limited adaptive histograph equalization (CLAHE) and high-pass pre-analysis filters with window sizes of 20 and 64 pixels, respectively, were applied to increase resolution, in order to detect individual sand grains (see Thielicke & Stamhuis (2014) for details). The DPIV settings used in our analysis were a Fast Fourier Transform (FFT) window deformation with three passes. The first pass used a window size of 128 pixels with a step of 64 pixels, the second pass a window size of 64 pixels with a step of 32 pixels, and the third pass a window size of 32 pixels with a step of 16 pixels. The frame series time step chosen was a 30 s interval. The result was a vector field illustrating the relative motion of the horizontal surface during vertical deformation. In order to highlight regions of vertical subsidence, we used a built-in algorithm within PIVlab to calculate divergence, which measures expansion or compression of the vector field in two dimensions (x, y) as defined below:

$$Divergence = \Theta = \frac{\partial u}{\partial x} + \frac{\partial v}{\partial y}$$

where u and v represent the velocity components in the x and y directions, respectively.

RESULTS

Here we present results from the caldera collapse experiments representing different positions of a volcanic edifice relative to the magma reservoir beneath. Our goal is to illustrate how caldera collapse styles vary as a seamount moves laterally away from the magma reservoir during plate motion. We have identified three scenarios with different styles of caldera collapse: (1) a volcanic edifice that is completely offset from the reservoir, (2) a volcanic edifice centered over the reservoir, and (3) a volcanic edifice partially offset from the reservoir. We utilize 3D scans of caldera experiments at 2.5 minute increments and post-experiment cross sections to describe the full fault evolution of the calderas. We performed duplicates of certain experiments to confirm reproducibility of the data (supplementary information S1). The 3D time series of the representative experiments is shown in Figure 3. The general evolution of experimental calderas has been thoroughly described by Acocella (2007); here we are principally interested in how a volcanic edifice and its position relative to the magma reservoir beneath affect caldera evolution. Therefore, we do not examine general caldera formation.

Caldera development

Completely offset volcanic edifice

Upon evacuation of the reservoir, initial subsidence was defined by sagging towards the center of the bladder, as demonstrated by the inward tilting of the sand. The first fault to reach the surface was a shallow (\sim 40° at the base of the roof) outward-dipping fault at the location of maximum sagging east of the central reservoir. The fault limbs propagated towards the region of least subsidence in an arcuate fashion, steepening to 60° at depth and joining to form a complete elliptical ring fault system. The initial fault-controlled subsidence was asymmetric, with the subsidence focussed where the first fault breached the surface (Fig. 4 a; Fig. 5 a, 0-2.5 min).

Between 2.5 and 5 minutes a second, steeper (~80° at the base of the roof) outward-dipping fault breached the surface east of the first fault. The steeper fault propagated to the north and south in a curvilinear fashion, encircling the first outward-dipping fault system. As subsidence continued, steep inward-dipping faults (~80-85° at the base of the roof) developed at the western edge of the edifice margin, as well as in the north and south of the caldera, splaying off the second outward dipping fault system (Fig. 4 a; Fig. 5 a, 2.5-5 min). Between 5 and 7.5 minutes, the peripheral inward-dipping faults in the north and south propagated to the west forming an outer ring fault system, shifting the locus of subsidence to a more central location. In addition, the eastern inward-dipping fault initiated a small sector collapse on the edge of the volcanic edifice as the fault propagated towards the north and the south to complete the outer inward dipping ring fault structure (Fig. 4 a; Fig. 5 a, 5-7.5 min). From 7.5 to 10 minutes, subsidence occurred along both the peripheral inward-dipping ring fault structures and the

enclosed outward-dipping fault structures. The result was more symmetric subsidence during the late stages of the experiment.

Centered volcanic edifice

Upon initial evacuation of the reservoir, the center of the volcanic cone underwent sagging, manifested by the tilting of sand inward towards the center of the reservoir as seen in cross section. The first fault to breach the surface was a shallow, outward-dipping (~40° at depth) fault initiating asymmetric collapse to the northwest (Fig. 4 b; Fig. 5b, 0-2.5 min). The fault initially propagated in an arcuate fashion, transitioning to linear segments towards the region of lowest subsidence and steepening to ~85° at depth.

Between 2.5 and 5 minutes a second, steeper outward-dipping fault with a $\sim 60^{\circ}$ dip at depth formed further to the northwest. This fault propagated in a curvilinear fashion, enclosing the previously formed outward-dipping fault towards the region of least subsidence and forming a complete ring fault system with a somewhat polygonal appearance. Between 5 and 7.5 minutes subsidence was controlled by the aforementioned outward-dipping ring fault system which promoted symmetric collapse as a coherent block (Fig. 4 b; Fig. 5b, 5-7.5 min). From 7.5 to 10 minutes steep (80° - 85° at depth) inward-dipping faults developed in the northwest and southeast of the caldera structure outside the subsidence controlling outward-dipping ring fault (Fig. 4 b; Fig. 5b, 7.5-10 min). These peripheral late-stage inward-dipping faults did not form a complete ring structure.

Partially offset volcanic edifice (10 cm and 20 cm offsets)

Upon initial evacuation of the reservoir, the flank of the volcanic cone sagged inwards as expressed by the inward tilting of horizontal strata. The first fault to breach the surface was a

shallow outward-dipping reverse fault. The fault breached the surface where the depth of the reservoir beneath the overlying topography was a minimum. For the 10 cm offset edifice, the initial fault was \sim 45° at depth while the 20 cm offset edifice had an initial fault dip of \sim 20-30° at depth. The initial faults propagated in a curvilinear manner resembling a horseshoe shape. The faults steepened to \sim 85° at depth for the 10 cm offset experiment and \sim 70° at depth for the 20 cm offset experiment.

Between 2.5 and 5 minutes, graben structures developed directly opposite the region of greatest subsidence. The graben structures were controlled by interior outward-dipping and peripheral inward-dipping normal faults forming a hinge zone (Fig. 4 c-d; Fig. 5 c-d, 2.5-5 min). The result was two main regions of subsidence, one controlled by the initial shallow reverse faults on the cone flank, and the other by the graben feature directly opposite the region of initial subsidence.

From 5 to 7.5 minutes, subsidence shifted to the hinge zone as the graben fault system developed. In the case of the 20 cm offset experiment, subsidence in the hinge zone was greater than subsidence controlled by the initial shallow outward-dipping faults (Fig. 4 c-d; Fig. 5 c-d, 5-7.5 min). The final phase of subsidence (7.5-10 minutes) was more centrally located within the caldera, and more balanced between the initial subsidence controlling faults and hinge zone graben (Fig. 4 c-d; Fig. 5 c-d, 7.5-10 min). Overall, subsidence was asymmetric relative to the reservoir, reflecting the asymmetry of the fault system (Fig. 4 c-d; Fig. 5 c-d, 0-10 min).

Vertical cross sections and fault maps

Vertical cross sections for select experiments are shown in Figure 7 and were used in conjunction with the 3D laser scans to create the fault maps illustrated in Figure 6. The initial

subsidence caused by sagging is clearly shown by the inward tilting of strata in each of the cross sections, regardless of the experimental conditions. The initial interior faults are outward-dipping, become steeper with depth and distance away from the center of subsidence, and propagate upward from the reservoir to the surface. By contrast, the peripheral faults, when developed, are all inward dipping, linear, and generally propagate from the surface downwards. Motion on inward dipping faults is always normal, while motion on outward dipping faults can be normal or reverse (Fig. 5 a, c and d). Graben structures are developed in experiments with the edifice partially offset relative to the reservoir, resulting in a strong component of asymmetric subsidence.

Digital particle image velocimetry

The digital particle image velocimetry (DPIV) results for the centered volcanic edifice and 20 cm offset volcanic edifice are presented in Figures 8 a and b, respectively. The vector field calculated from the image series represents horizontal movement of the surface in response to vertical subsidence when the reservoir is evacuated. The calculated divergence, which is the derivative of the vector field, highlights regions of vertical surface deformation. A negative divergence value indicates regions where the vector field is converging, analogous to a compression regime. By contrast, a positive divergence value indicates regions where the image plane is expanding, analogous to an extension regime. The regions of negative divergence highlight movement on the inner outward-dipping reverse faults. By contrast, the regions of positive divergence illustrate regions of peripheral sagging and extension resulting in the formation of inward-dipping normal faults.

The DPIV divergence results for the centered edifice experiment show the propagation of faults in response to subsidence. By 2 minutes, the region of greatest negative divergence, was represented by the initial outward-dipping reverse fault to the northwest (Fig 8a, 2 min). As subsidence continued, the region of negative divergence transitioned to the southwest due to the propagation of the outward-dipping reverse fault. This was consistent with the subsidence shifting towards the southwest (Fig 8 a, 7 min). The positive divergence was represented by a circumferential ring, highlighting the outer inward-dipping normal fault that formed in response to peripheral sagging. The DPIV divergence results from the 20 cm offset edifice experiment highlighted the asymmetric nature of the subsidence and associated faulting. At 2.5 minutes, the region of greatest negative divergence was represented by the initial outward-dipping reverse fault (Fig 8 b, 2.5 min). At 5.5 minutes, the DPIV results illustrate the formation of the antithetic graben structure represented by the region positive divergence, consistent with the subsidence shift to the east (Fig 8 b, 5.5 min). The results had fine enough detail to highlight the multiple small displacement normal faults between the two main graben faults (Fig 8 b, 5.5-7 min). To summarize, the DPIV results for both experiments highlighted which faults were active and whether they were normal or reverse, for any given time. The DPIV results were consistent with both the subsidence evolution at the surface and the cross-sections.

DISCUSSION

The results of the above experiments indicate that the position of a volcanic edifice relative to the underlying magma reservoir is influential in determining the resulting style of caldera collapse. In the following discussion we use the structural and 3D scanner results from our experiments to examine the effect of a volcanic edifice on caldera collapse for (1) a centered and completely offset volcanic edifice, and (2) a partly offset volcanic edifice. We then discuss

the fault mechanics associated with the different styles of caldera collapse observed for the different positions of the volcanic edifice. Finally, we apply our experimental results to natural examples of caldera collapse at near-ridge seamounts in the Pacific Ocean.

Centrally-located and fully offset calderas on volcanic edifices

Near-ridge seamounts in the Pacific Ocean morphologically resemble truncated cones with flat tops (Smith, 1988). The origin of these flat tops has been attributed to the infilling of a previously formed caldera with lava (Clague *et al.*, 2000). The depths of magma reservoirs on near-ridge seamounts are not definitively known. However, the observation that some calderas engulf almost the entire edifice, in addition to its ring fault boundaries, suggests that the magma reservoirs are shallow, possibly as shallow as 1 km (Clague *et al.*, 2000). Such collapse styles are akin to caldera subsidence experiments with low aspect ratios where the roof is thin relative to its diameter (Acocella, 2007, Martí *et al.*, 1994, Roche *et al.*, 2000). At such shallow depths, a volcanic edifice will play a more significant role than for a deep magma reservoir because the load differential across the magma reservoir and the topographic variability are greater.

Experiments with a centered volcanic edifice and a completely offset volcanic edifice exhibit symmetric sagging above the bladder followed by the formation of outward-dipping reverse faults with angles of 40°-50° at the base of the roof. The caldera evolution of the completely offset volcanic cone was akin to experiments that had no edifice (Supplementary Information S1). In both types of experiments, subsidence was initially asymmetric and throw greatest where the fault first breached the surface (Fig. 5 a-b, 0-2.5 min). Both experiments developed a second set of more steeply outward-dipping (65°-80° at the base of the roof) reverse faults outside the initial faults, but they propagated differently. When the edifice was centered

over the reservoir, the second set of reverse faults formed a complete outward-dipping ring structure. By contrast, when the edifice was completely offset, reverse faults propagated from their point of origin only halfway around the caldera, creating a semi-circular fault trace. With further subsidence, the reverse faults changed into inward-dipping normal faults, forming a ring structure with variable fault orientation.

The completion of the ring structure for the centered experiments, regardless of fault orientation, caused subsidence to be manifested as a symmetric style of collapse. This was observed by a change in subsidence to a central location within the caldera (Fig. 4 a-b, 5-7.5 minutes). The centered edifice developed peripheral inward-dipping normal fault segments only during the last stage of the experiment. This was in contrast to the completely offset volcanic edifice experiment, which exhibited a significant fraction of its subsidence on a peripheral normal fault ring system by 7.5 minutes into the experiment. For the completely offset volcanic edifice experiment, subsidence on a number of small displacement reverse faults at the inner part of the caldera, in addition to the outer peripheral faults, facilitated a more chaotic style of caldera collapse forming discrete blocks.

Hence, the main effects of a centered volcanic edifice above the magma reservoir are the following: (1) the growth of peripheral fault systems is suppressed; (2) subsidence is concentrated on an inner set of outward-dipping reverse faults; (3) the caldera collapse style is more piston-like and less chaotic or piecemeal. The outward propagation of the caldera is reduced due to the suppression of peripheral extensional faults, which results in greater subsidence on the inner set of outward-dipping reverse faults and a smaller caldera in terms of planar area.

Partial offset calderas

Partly offsetting the position of a volcanic edifice relative to the reservoir resulted in a unique style of caldera collapse. Upon evacuation of the magma reservoir, subsidence began initially on the flank of the edifice, due to its offset position. Because the magma reservoir is located above a sloped surface of ~25°, the depth of sand above the reservoir is variable. Therefore, the first fault to breach the surface occurred where the reservoir roof thickness was lowest on the flank. Subsidence was asymmetric at the location of initial faulting, with the amount of asymmetry dependent upon the degree of offset. The experiment with a 20 cm offset edifice had a more asymmetric initial subsidence pattern than the experiment with 10 cm offset, likely due to the greater variation in roof thickness over the subsiding parts of the reservoir when the edifice was offset by 20 cm. The thickness of the roof for the 20 cm offset experiment varies from 4.5 cm at the thinnest location to 16 cm at the thickest, while the thickness of the roof for the 10 cm offset experiment varies from 6 cm to 14.5 cm. In addition, the dips of the initial subsidence controlling reverse faults for the 20 cm offset experiment were shallower (20°- 30° at the base of the roof), compared to the 10 cm offset experiment (45° at the base of the roof).

Asymmetric subsidence facilitated by the initial outward-dipping reverse fault caused continuous tilting of the edifice into the faulted region (Fig. 5 c-d). This contrasts with the centered topography experiments where sagging and subsidence were centered over the reservoir, resulting in circumferentially inward tilting of the strata from the edge of the reservoir towards the center (Fig. 5 a-b). For experiments with a partly offset volcanic edifice, the region directly opposite the zone of greatest subsidence was a hinge zone, represented by the boundary between static material outside the caldera and the inwardly tilting roof material. In both the 10 cm and 20 cm offset experiments, graben structures developed in the hinge zone antithetic to the

region of initial subsidence. The 20 cm offset experiment, which had a more asymmetric subsidence pattern, also had greater vertical displacement on the graben structure (2 cm) compared to the 10 cm offset experiment (1.5 cm) (Fig 9. a-b).

Once these graben structures developed on the edifice, the bulk of subsidence became focussed at the hinge region in order to accommodate the buildup of flexural tension from asymmetric tilting (Fig. 4 c-d, 5-7.5 min). As a result, the calderas had a complete ring system comprising asymmetric fault structures, with reverse faults at topographically lower levels of the edifice and hinged graben structures at topographically higher levels. Continued subsidence on both types of fault structures during the final stage of the experiment resulted in less asymmetric collapse (Fig. 4 c-d, 5-7.5 min). However, the final subsidence pattern in these experiments is highly asymmetric, with a style of collapse which is clearly representative of trapdoor calderas (Cole *et al.*, 2005).

To summarize, the main effects of partly offsetting the volcanic edifice from the reservoir are the following: (1) asymmetric collapse initiates in the region of least overburden above the reservoir; (2) overlying roof material tilts towards the region of initial collapse; (3) a graben structure and hinge zone develop which are antithetic to the region of subsidence, resulting in a trapdoor caldera. Hence, a partly offset edifice generates an asymmetric caldera controlled by an initial reverse fault which breaches the surface where the roof is thinnest, and a later antithetic graben structure in response to flexural tension.

Fault mechanics

Analogue studies of caldera collapse from different laboratories that use various apparatus, materials, and experimental conditions have revealed a consistent pattern of deformation. The

general stages of caldera collapse, as summarized by Acocella (2007), are as follows: (1) downsag, (2) outward-dipping reverse ring faults, (3) peripheral downsag, and (4) peripheral inward-dipping ring faults. Our experiments show important differences with this model beginning at stage 2.

The addition of a centered volcanic edifice above the magma reservoir promoted the formation of a complete outward-dipping reverse fault ring which was more circular than reverse fault systems in experiments with a completely offset edifice or no edifice. Our centered edifice experiments accommodated most of the fault-related caldera subsidence by suppressing the formation of peripheral normal faults. We propose that the primary control on this behaviour was due to the faults breaching a sloped rather than horizontal surface. The formation of peripheral normal faults is the result of gravity-driven subsidence in the wedge above an outward-dipping reverse fault. The peripheral gravitational downsag causes tilting of the material towards the outward-dipping reverse fault. Because the slope of the edifice in the peripheral region dips in the same direction as the reverse faults, additional subsidence of the footwall is required to create sufficient overburden in the hanging wall wedge to initiate gravitational downsag and eventual failure as a normal fault (Fig. 10 a-b). Therefore, when a sloped edifice is present over the reservoir, a greater amount of subsidence occurs on outward-dipping reverse faults prior to outward growth of the caldera.

Partly offsetting the position of the volcanic edifice relative to the reservoir produces a unique caldera fault pattern that also differs from the general progression described earlier (Acocella, 2007, Geyer *et al.*, 2006, Martí *et al.*, 1994, Roche *et al.*, 2000). The resulting fault structure was asymmetric and defined by (1) an initial subsidence controlling reverse fault developed at the minimum thickness of the roof and (2) an antithetic graben structure.

Subsidence was initially greatest on the reverse fault, then was translated to the graben structure resulting in a "see-saw" type of subsidence in a temporal sense. The graben structure accommodated the inward tilting of the strata at the hinge zone of the caldera. This can be seen by the progressive rotation of strata within the graben by a series of increasingly steep outward-dipping normal faults, which are bounded by a peripheral inward-dipping normal fault, the overall pattern resembling a fish backbone (Fig 8. c). Similar structures were observed in analogue experiments investigating caldera collapse on the axial region of fast-spreading ridges (Lagabrielle *et al.*, 2001). Here the authors observed the formation of peripheral graben with a similar cross sectional pattern that accommodated tilting and rotation of a block towards the location of subsidence in the axial region.

Application to near-ridge seamounts

The observations we have presented show that the addition of a volcanic edifice and its position relative to an underlying magma reservoir have important effects upon caldera collapse. Near-ridge seamounts in the Pacific Ocean retain clear evidence of caldera collapse, both centered over a reservoir and in an offset position. Collapse structures vary in size from summit craters less than 1 km to calderas greater than 1 km with some as large as ~10 km (Batiza *et al.*, 1984, Clague *et al.*, 2000, Hammond, 1997). The calderas typically have very steep walls that truncate subhorizontal lava flows and commonly form nested structures. The closest subaerial analogue with similar dimensions to near-ridge seamounts are the flat-topped basaltic volcanoes that comprise the Galápagos Islands (Munro & Rowland, 1996, Simkin, 1972). We now discuss the potential implications of our results on caldera collapse evolution at these seamount structures.

Structural studies of the Lamont Seamounts, a near-ridge seamount chain adjacent to the East Pacific Rise (EPR), identified prominent and arcuate constructional fissure ridges which are positioned adjacent to the caldera wall (Fornari *et al.*, 1988). Constructional cones and ridges also have been observed at Taney Seamount-A on both caldera floors and rims (Fig. 1 b) (Clague *et al.*, 2000), and distinctive arcuate fissures forming a circumferential pattern have been observed on western Galápagos volcanoes (Munro & Rowland, 1996, Simkin, 1972). It has been suggested that outward-dipping reverse faults at calderas could facilitate magma transport to the surface (Acocella, 2007). The results of our experiments suggest that the presence of a centered seamount edifice would promote deformation on the inner outward-dipping reverse faults at the expense of peripheral normal faulting. Therefore, the construction of arcuate ridges found at near-ridge seamounts, such as MOK from the Lamont chain, Taney Seamount-A, and other near-ridge seamounts, may be facilitated by an increased preference of subsidence on outward-dipping reverse faults.

Offset caldera collapse at near-ridge seamounts in the Pacific Ocean has been extensively documented, generally occurring on the ridge side of the edifice (Hammond, 1997). Our experiments indicate that caldera collapse on the flank of the edifice results in trapdoor caldera structures defined by an initial reverse fault and an antithetic graben structure. Certain structural features suggest asymmetric collapse is occurring at near-ridge seamount systems. For example, the summits and floors of some calderas are tilted towards the ridge axis (Fig. 11). One hypothesis for the preferential tilting of the originally horizontal surfaces is by subsidence of the underlying crust beneath the edifice during movement away from the ridge axis (Clague *et al.*, 2000). We propose a different explanation where asymmetric caldera collapse occurred on the

edifice flank resulting in a tilted surface, similar to our observations for a partly offset edifice caldera collapse.

Although the graben structures, which are an important element in our offset caldera collapse experiments, are not directly observed at near-ridge seamounts possibly due to destruction by post-caldera processes, they are observed on other basaltic volcanoes. Trapdoor collapse at Sierra Negra volcano in the Galápagos has a graben structure located in the western section of the caldera (Fig. 12) (Jónsson *et al.*, 2005, Reynolds *et al.*, 1995). It was hypothesized that the western region with the graben was formed when the caldera floor pivoted as a unit in a trapdoor fashion (Reynolds *et al.*, 1995). These workers proposed that the associated sinuous ridge may represent part of the caldera floor which deformed rigidly during lateral stretching as a result of vertical and lateral growth of the volcano. Although the origin of the structure may not be exactly the same as observed in our experiments, the tectonic behaviour defined by tilting of a coherent block is similar. Therefore, we propose that the unique caldera collapse mechanism we observed in our partly offset caldera collapse experiments also occurs in nature and should be considered at near-ridge seamounts and other volcanoes as well.

Taney Seamount-A is a remarkable seamount that has formed at least four caldera collapse structures. The largest and most recent caldera truncates the entire southeastern edge of the edifice flank. Geochemical studies of the young pillow cones on the wall of the southeastern caldera and on the floor indicate that they are geochemically similar, but differ from edifice lava compositions (Coumans *et al.*, 2015). The pillow cone lavas are more primitive, which means they spent less time crystallizing in a shallow magma reservoir compared to the edifice lavas. The formation of fault structures during caldera collapse creates weaknesses in the crust that provide pathways for magma to travel. The faults formed during the collapse of the large caldera

on the southeastern flank of Taney-A may have provided pathways for magmas that formed the pillow cone on the caldera wall. The caldera faults potentially opened the system making it easier for magma to travel to the surface, reducing the potential crystallization time reflected in the more primitive compositions. Therefore, structures formed due to caldera collapse may affect magma evolution by opening the subsurface.

CONCLUSIONS

Analogue experiments of caldera collapse demonstrate that the presence and position of a volcanic edifice above a magmatic reservoir have an important effect on the resulting caldera collapse structure. Our principal findings are the following:

- (1) The presence of a volcanic edifice directly above a reservoir promotes a more symmetric collapse on an inner outward-dipping reverse fault structure due to the suppression of deformation on peripheral normal faults.
- (2) The formation of peripheral faults on a volcanic edifice centered over a magmatic reservoir is suppressed due to deformation on a slope that dips in the same direction as the subsidence controlling reverse faults. A greater amount of subsidence is required on the hanging wall in order to provide sufficient gravitational instability to promote collapse on the overriding wedge.
- (3) Partly offsetting the volcanic edifice promotes an asymmetric style of caldera collapse along an initial outward-dipping reverse fault located where the roof is thinnest. The resulting flexural tension due to the asymmetric tilting of the roof into the faulting region facilitates the formation of an antithetic graben structure and a trapdoor style of collapse.
- (4) Structures observed in our offset caldera collapse experiments apply to the tilting of near-

ridge seamount offset calderas towards the ridge axis. Furthermore, the graben structure observed in our trapdoor experimental calderas is similar to graben structures observed at natural trapdoor calderas.

There remain several important parameters of caldera collapse at near-ridge seamounts that have not been considered. Previous caldera collapse experiments have shown that tectonic interaction can play an important role on caldera collapse processes (Holohan *et al.*, 2005). Midocean ridge parallel faults have similar spacing to compared to individual seamounts in a chain (Clague *et al.*, 2000). These ridge-parallel faults may affect caldera collapse processes at near-ridge seamounts by providing a region of weakness where faulting may focus preferentially. In addition, preconditioning of the volcanic edifice by either magmatic inflation or previous caldera collapse has not been investigated in this study, and could be important. For example, experiments by Walter & Troll (2001) demonstrated that during multi-stage caldera activity, previously formed faults are reactivated. Therefore, the focus of future work should investigate the relative effects of previously formed structures and edifice position on caldera collapse in order to obtain a full understanding of caldera collapse processes at near-ridge seamounts.

ACK NOWLEDGEMENTS

We would like to thank Peter Coumans, Rowan Wollenberg, Sarah Bodeving and Gregor Lucic for assistance with various experiment preparations and lending their equipment. We also acknowledge Anne-Sophie Berg and Philip Lypaczewski for their hard work as laboratory assistants. This work was funded by scholarships to J.C from GEOTOP and McGill University, and by grants to J.S. from the Natural Sciences and Engineering Research Council of Canada.

REFERENCES

- Acocella, V. (2007). Understanding caldera structure and development: An overview of analogue models compared to natural calderas. *Earth-Science Reviews* **85**, 125-160.
- Acocella, V., Cifelli, F. & Funiciello, R. (2001). Formation of nonintersecting nested calderas: insights from analogue models. *Terra Nova* **13**, 58-63.
- Ambrose, S. H. (1998). Late Pleistocene human population bottlenecks, volcanic winter, and differentiation of modern humans. *Journal of Human Evolution* **34**, 623-651.
- Batiza, R., Fornari, D. J., Vanko, D. A. & Lonsdale, P. (1984). Craters, calderas, and hyaloclastites on young pacific seamounts. *Journal of Geophysical Research* **89**, 8371-8390.
- Burchardt, S. & Walter, T. (2010). Propagation, linkage, and interaction of caldera ring-faults: comparison between analogue experiments and caldera collapse at Miyakejima, Japan, in 2000. *Bulletin of Volcanology* **72**, 297-308.
- Clague, D. A., Reynolds, J. R. & Davis, A. S. (2000). Near-ridge seamount chains in the northeastern Pacific Ocean. *Journal of Geophysical Research* **105**, 16541-16561.
- Cole, J. W., Milner, D. M. & Spinks, K. D. (2005). Calderas and caldera structures: a review. *Earth-Science Reviews* **69**, 1-26.
- Coumans, J. P., Stix, J., Clague, D. A. & Minarik, W. G. (2015). The magmatic architecture of Taney Seamount-A, northeast Pacific Ocean. *Journal of Petrology*.
- Folch, A. & Martí, J. (2004). Geometrical and mechanical constraints on the formation of ring-fault calderas. *Earth and Planetary Science Letters* **221**, 215-225.
- Fornari, D. J., Perfit, M. R., Allan, J. F., Batiza, R., Haymon, R., Barone, A., Ryan, W. B. F., Smith, T., Simkin, T. & Luckman, M. A. (1988). Geochemical and structural studies of the Lamont seamounts: seamounts as indicators of mantle processes. *Earth and Planetary Science Letters* **89**, 63-83.
- Geyer, A., Folch, A. & Martí, J. (2006). Relationship between caldera collapse and magma chamber withdrawal: An experimental approach. *Journal of Volcanology and Geothermal Research* **157**, 375-386.
- Giordano, D. & Dingwell, D. (2003). Viscosity of hydrous Etna basalt: implications for Plinian-style basaltic eruptions. *Bulletin of Volcanology* **65**, 8-14.

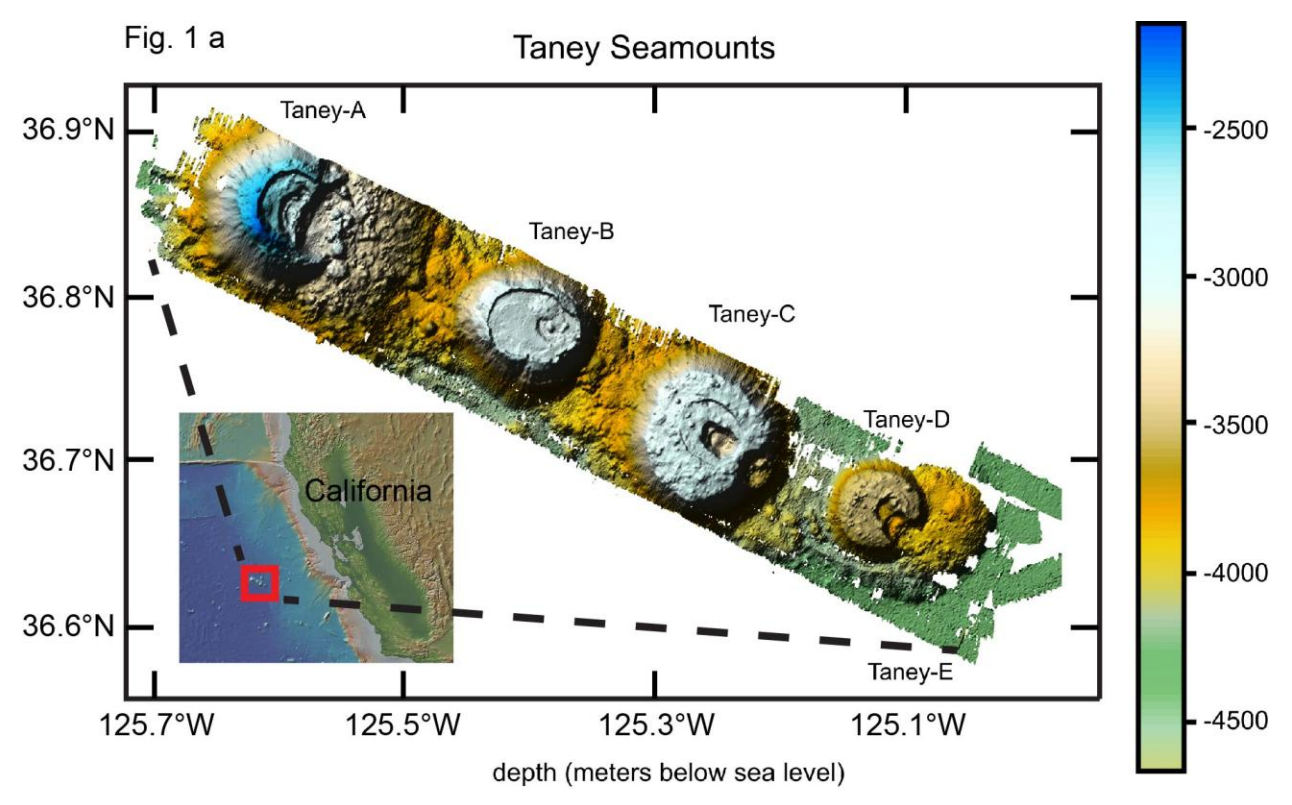
- Hammond, S. R. (1997). Offset caldera and crater collapse on Juan de Fuca Ridge-flank volcanoes. *Bulletin of Volcanology* **58**, 617-627.
- Holohan, E. P., Troll, V. R., Walter, T. R., Münn, S., McDonnell, S. & Shipton, Z. K. (2005). Elliptical calderas in active tectonic settings: an experimental approach. *Journal of Volcanology and Geothermal Research* **144**, 119-136.
- Hubbert, M. K. (1937). Theory of scale models as applied to the study of geologic structures. *Geological Society of America Bulletin* **48**, 1459-1520.
- Jaeger, J. C. & Cook, N. G. W. (1969). Fundamentals of rock mechanics. London: Methuen.
- Jónsson, S., Zebker, H. & Amelung, F. (2005). On trapdoor faulting at Sierra Negra volcano, Galápagos. *Journal of Volcanology and Geothermal Research* **144**, 59-71.
- Kennedy, B. & Stix, J. (2003). Igneous Rock Associations of Canada 2. Stages in the Temporal Evolution of Calderas. 2003.
- Kennedy, B., Stix, J., Vallance, J. W., Lavallee, Y. & Longpre, M. A. (2004). Controls on caldera structure: Results from analogue sandbox modeling. *Geological Society of America Bulletin* **116**, 515-524.
- Lagabrielle, Y., Garel, E., Dauteuil, O. & Cormier, M.-H. (2001). Extensional faulting and caldera collapse in the axial region of fast spreading ridges: Analog modeling. *Journal of Geophysical Research: Solid Earth* **106**, 2005-2015.
- Lavallée, Y., Stix, J., Kennedy, B., Richer, M. & Longpre, M. A. (2004). Caldera subsidence in areas of variable topographic relief: results from analogue modeling. *Journal of Volcanology and Geothermal Research* **129**, 219-236.
- Martí, J., Ablay, G. J., Redshaw, L. T. & Sparks, R. S. J. (1994). Experimental studies of collapse calderas. *Journal of the Geological Society* **151**, 919-929.
- Mouginis-Mark, P. J. & Rowland, S. K. (2001). The geomorphology of planetary calderas. *Geomorphology* **37**, 201-223.
- Munro, D. C. & Rowland, S. K. (1996). Caldera morphology in the western Galápagos and implications for volcano eruptive behavior and mechanisms of caldera formation. *Journal of Volcanology and Geothermal Research* **72**, 85-100.
- Pinel, V. & Jaupart, C. (2005). Caldera formation by magma withdrawal from a reservoir beneath a volcanic edifice. *Earth and Planetary Science Letters* **230**, 273-287.
- Reynolds, R. W., Geist, D. & Kurz, M. D. (1995). Physical volcanology and structural development of Sierra Negra volcano, Isabela Island, Galápagos archipelago. *Geological Society of America Bulletin* **107**, 1398-1410.

- Roche, O., Druitt, T. H. & Merle, O. (2000). Experimental study of caldera formation. *Journal of Geophysical Research* **105**, 395–416.
- Schellart, W. P. (2000). Shear test results for cohesion and friction coefficients for different granular materials: scaling implications for their usage in analogue modelling. *Tectonophysics* **324**, 1-16.
- Simkin, T. (1972). Origin of some flat-topped volcanoes and guyots. *Geological Society of America Memoirs* **132**, 183-194.
- Smith, D. K. (1988). Shape analysis of Pacific seamounts. *Earth and Planetary Science Letters* **90**, 457-466.
- Stix, J. & Kobayashi, T. (2008). Magma dynamics and collapse mechanisms during four historic caldera-forming events. *Journal of Geophysical Research-Solid Earth* **113**, 1-14.
- Thielicke, W. & Stamhuis, E. J. (2014). PIVlab—Towards user-friendly, affordable and accurate digital particle image velocimetry in MATLAB. *Journal of Open Research Software* **2**, e30.
- Walter, T. & Troll, V. (2001). Formation of caldera periphery faults: an experimental study. *Bulletin of Volcanology* **63**, 191-203.

FIGURE CAPTIONS

Figure 1

a) DEM image of the Taney Seamounts. The volcanoes are labeled from oldest to youngest (Taney-A-E) after Clague *et al.*, (2000). The volcanic edifices are characterized by steep sides, truncated tops and complex caldera structures. Taney Seamount-A exhibits caldera structures both with central and partial offset on the edifice. b) DEM image of the largest and oldest Taney Seamount (A) using 1-meter resolution data collected using an autonomous underwater vehicle superimposed over EM300 data. Remotely operated vehicle (ROV) dive tracks from the 2010 cruise are shown.



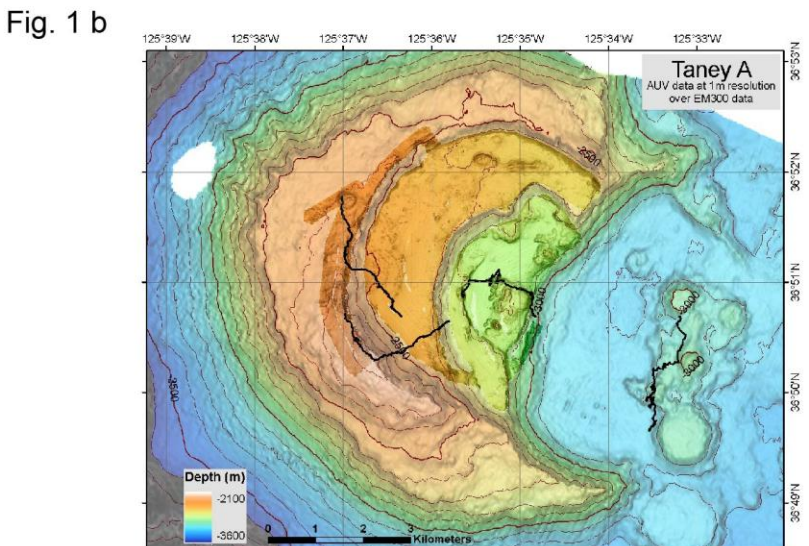


Figure 2

Experimental setup showing a cylinder containing dry sand, camera, rubber bladder, flowmeter and pump.

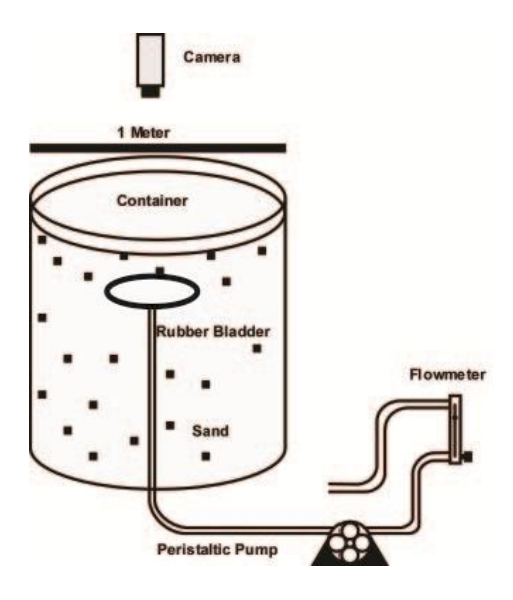
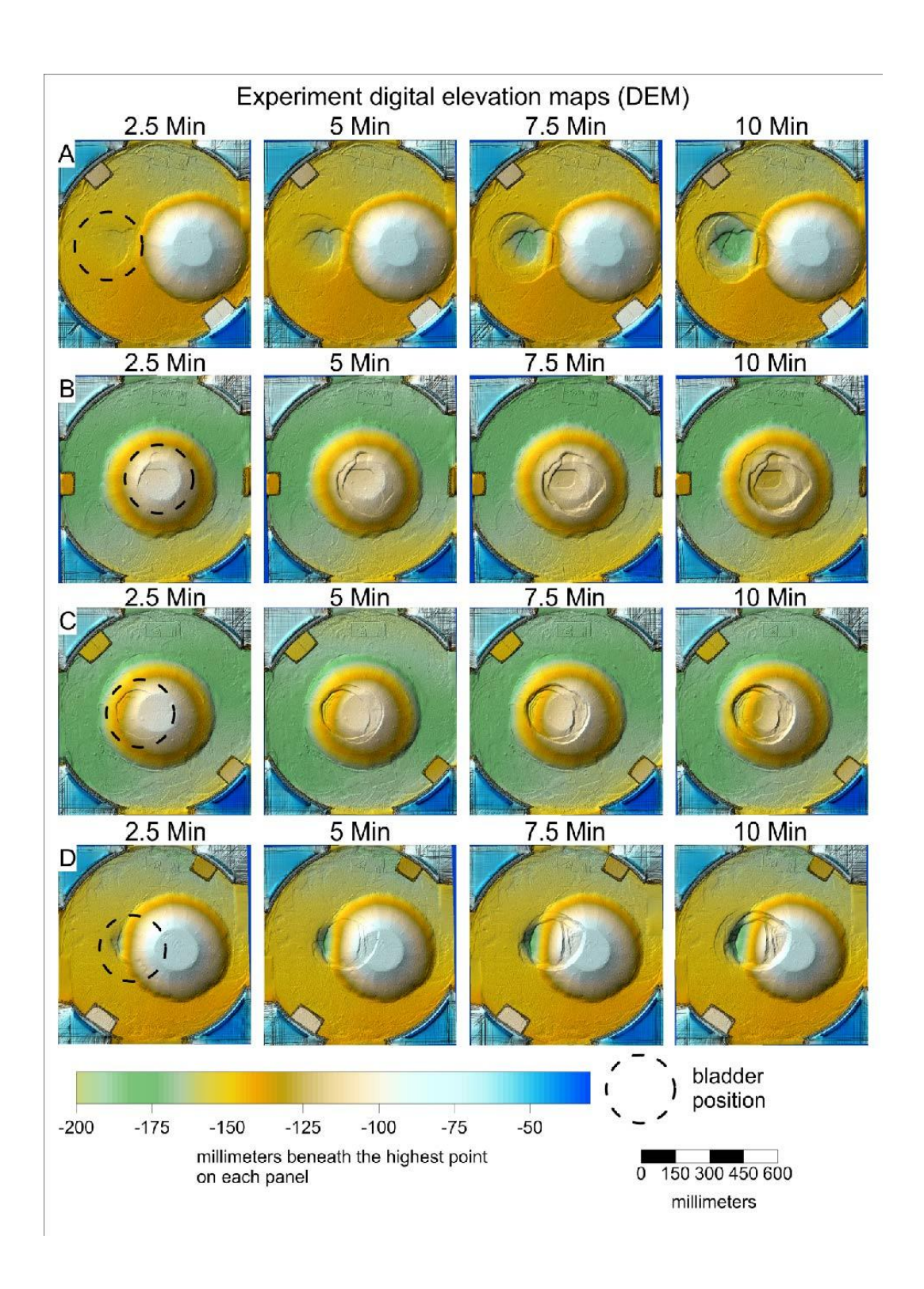


Figure 3

Digital elevation maps (DEM) of select experiments at 2.5 minute increments with different edifice positions above the reservoir. (a) The position of the edifice was completely offset from the reservoir. (b) The position of the edifice was centered over the reservoir. (c) The position of the edifice was partly offset from the reservoir by 10 cm. (d) The position of the edifice was partly offset from the reservoir by 20 cm.



Subsidence evolution of select experiments during each 2.5 minute increment. The final panel in each experiment represents the total subsidence over the length of the experiment. The subsidence difference maps were calculated by subtracting the DEMs of successive time increments. (a) The position of the edifice was completely offset from the reservoir. (b) The position of the edifice was centered over the reservoir. (c) The position of the edifice was partly offset from the reservoir by 10 cm. (d) The position of the edifice was partly offset from the reservoir by 20 cm.

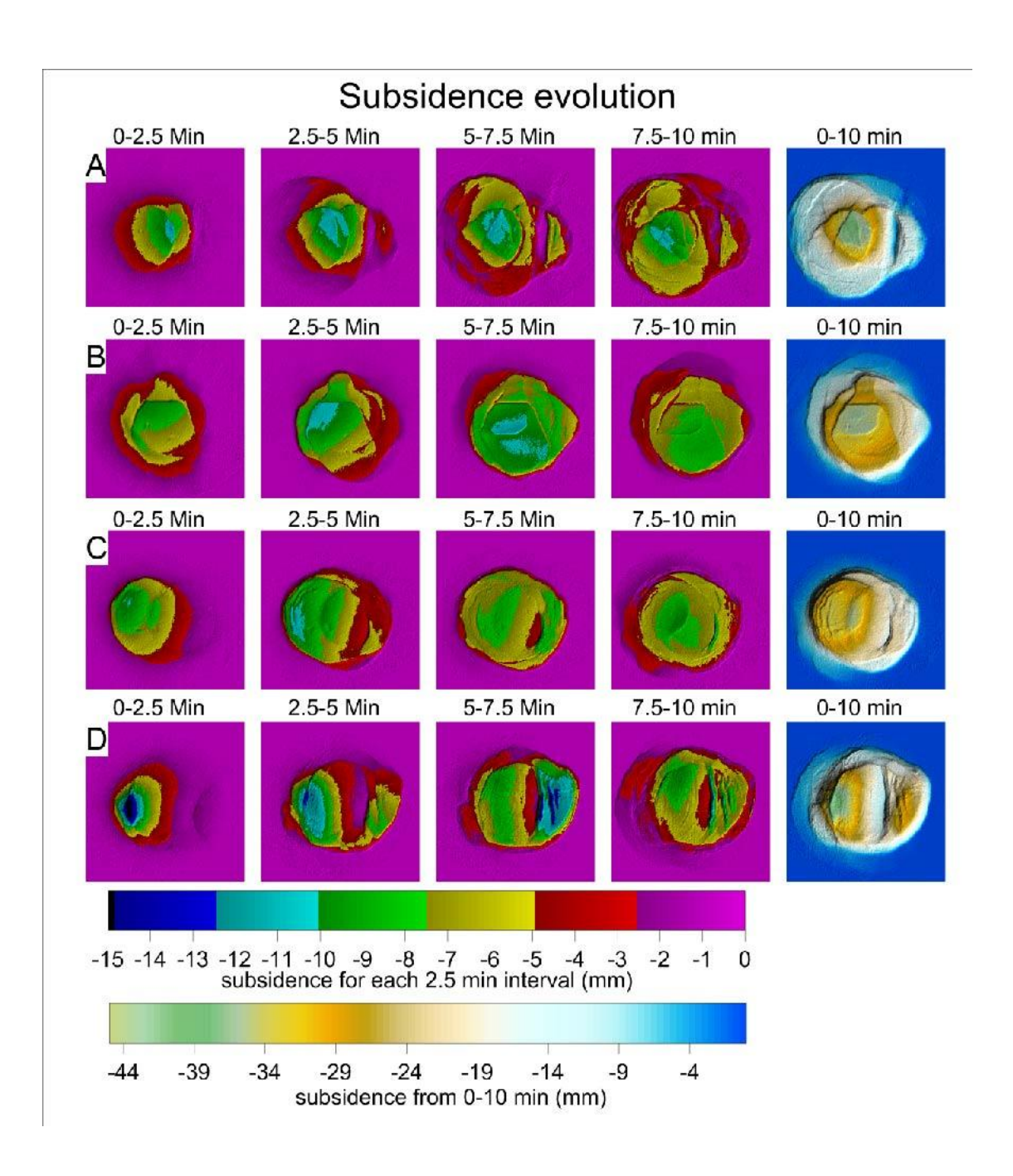
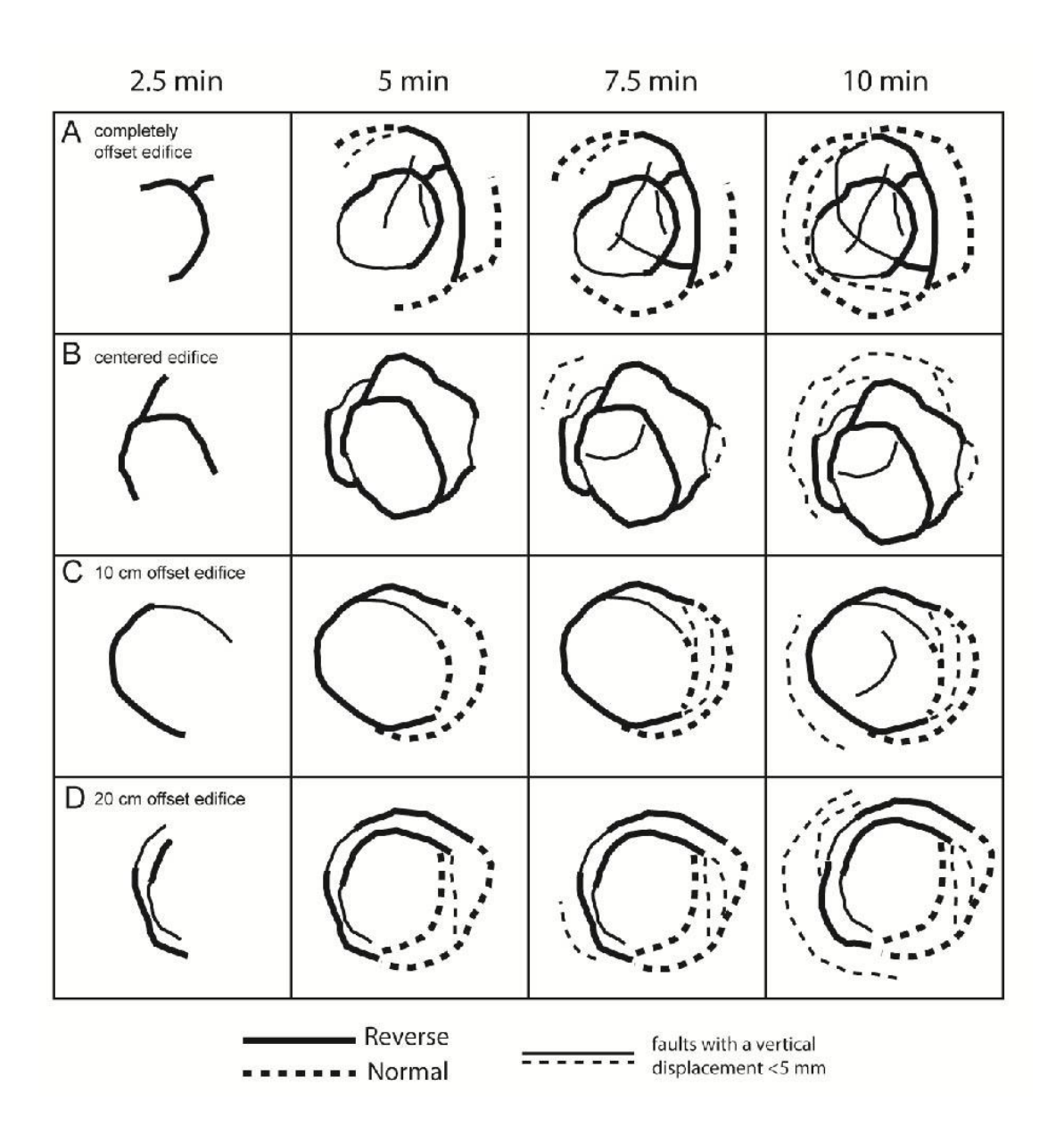


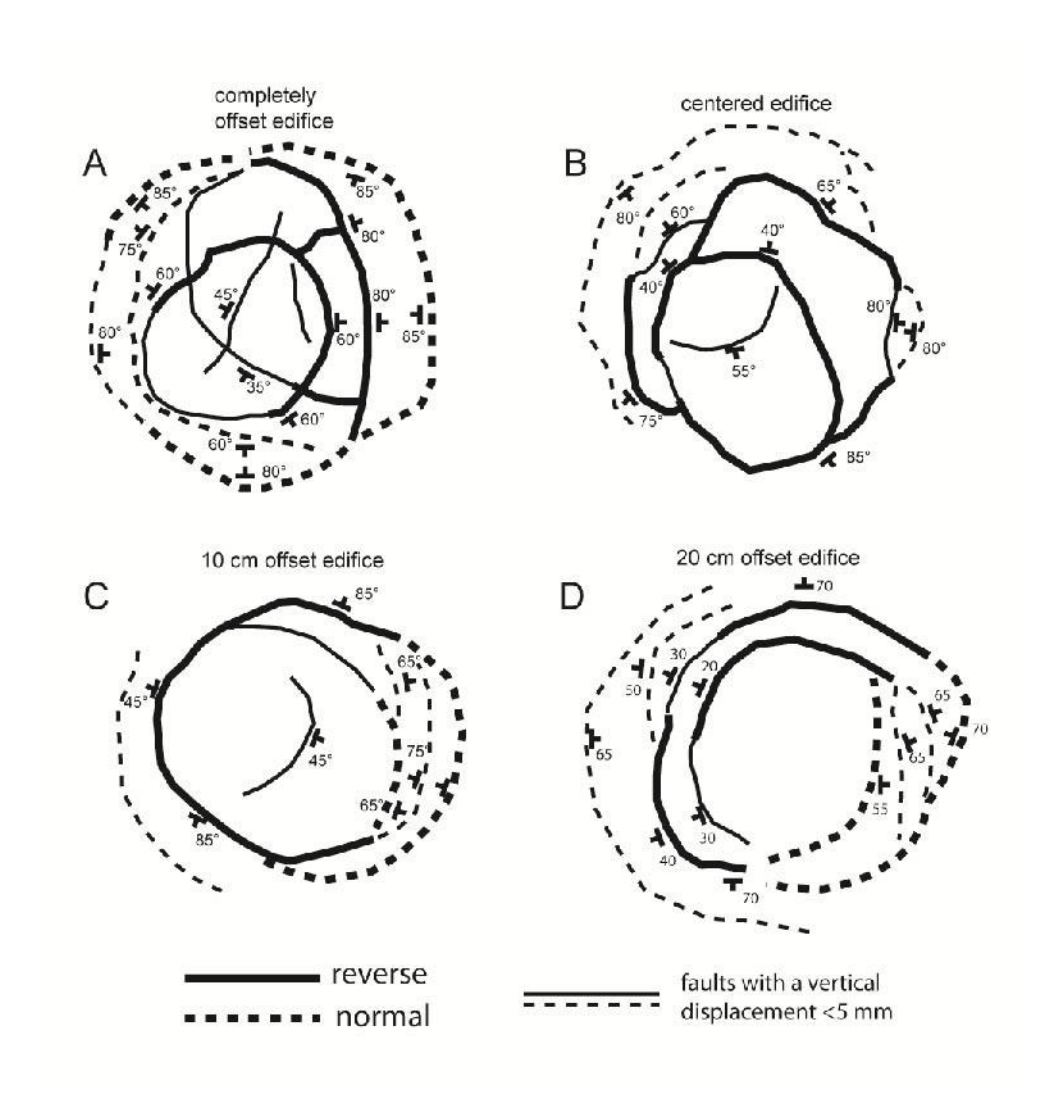
Figure 5

Fault progression for select experiments for each 2.5 minute increment. Thick dashed lines represent a normal fault, thick full lines represent reverse faults. Thin lines represent faults with a final displacement of <5 mm. Experiment labels are the same as shown in Figures 3 and 4.

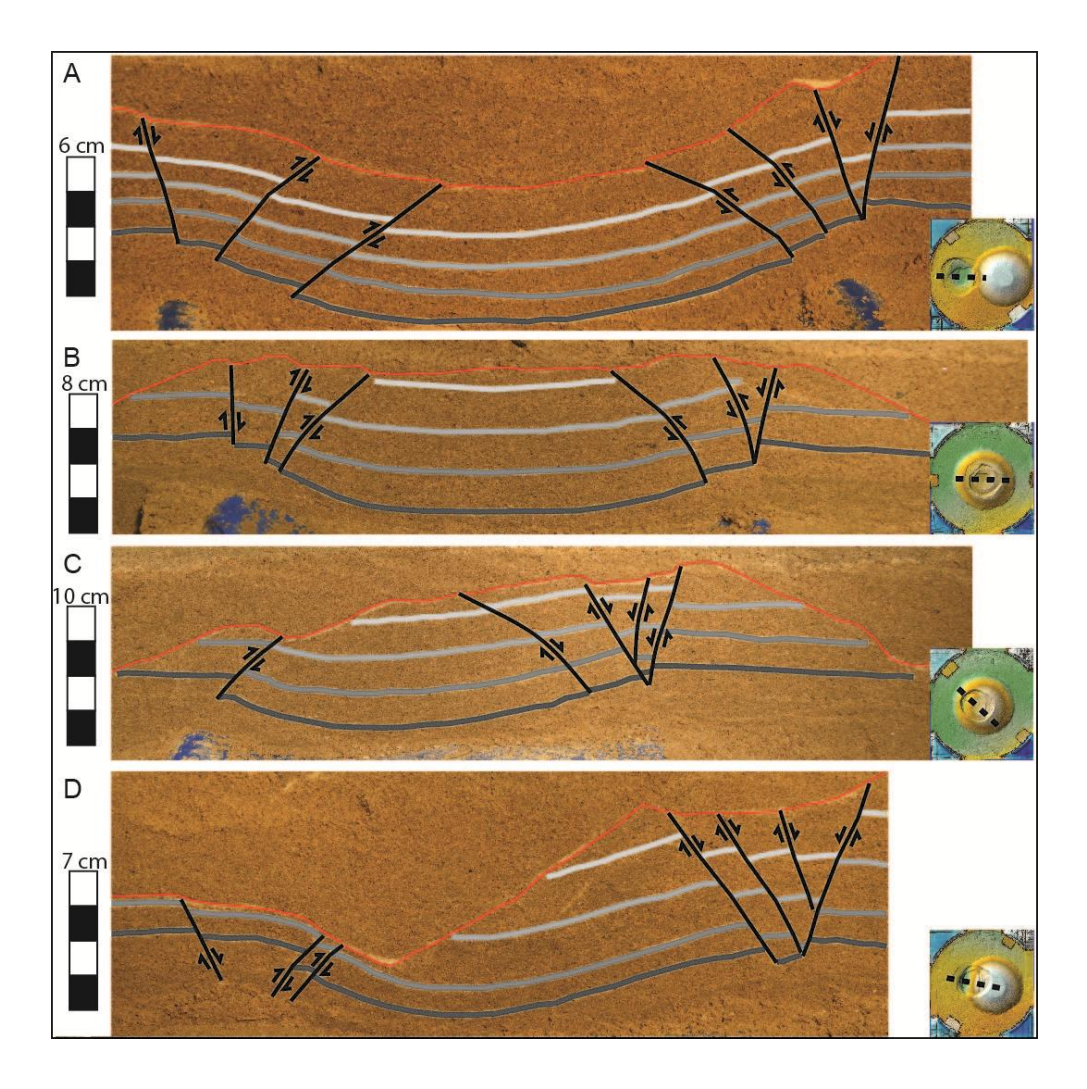


Final fault maps of select experiments with fault dip angles from the base of the caldera roof.

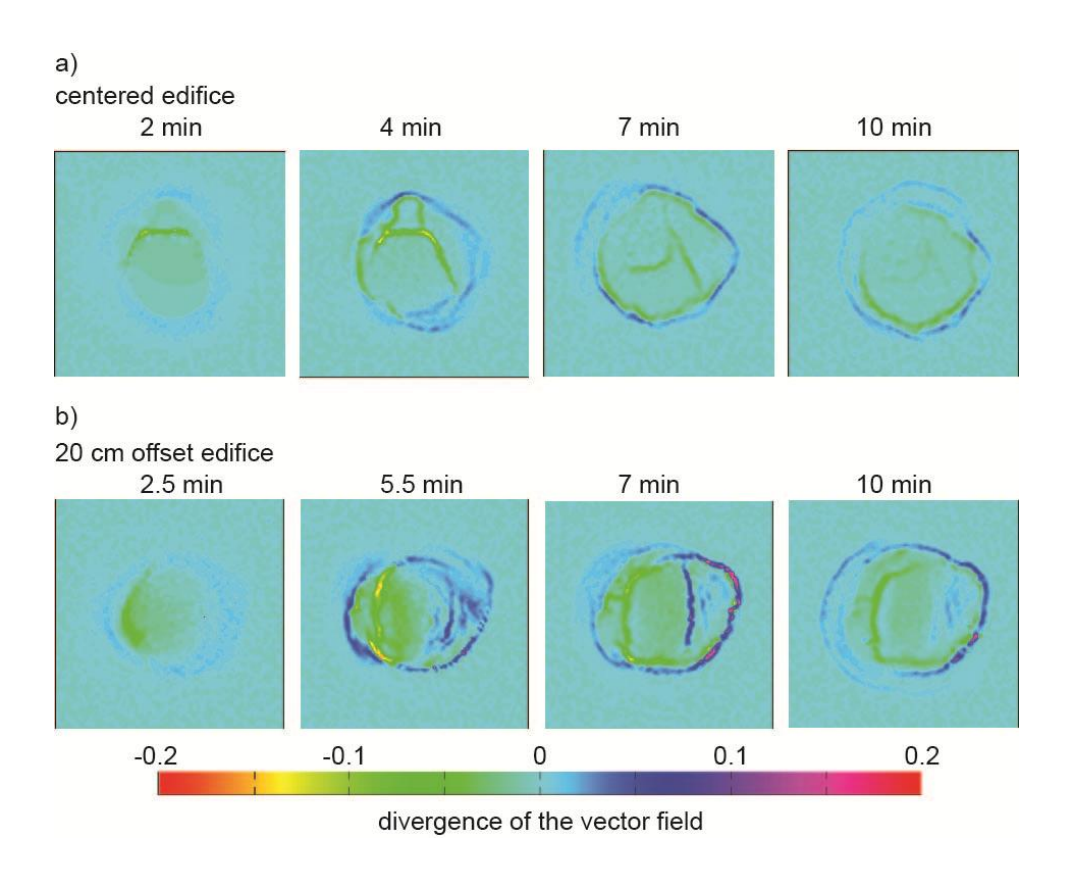
Dashed lines represent a normal faults, full lines represent reverse faults. Thin lines represent faults with a final displacement of <5 mm.



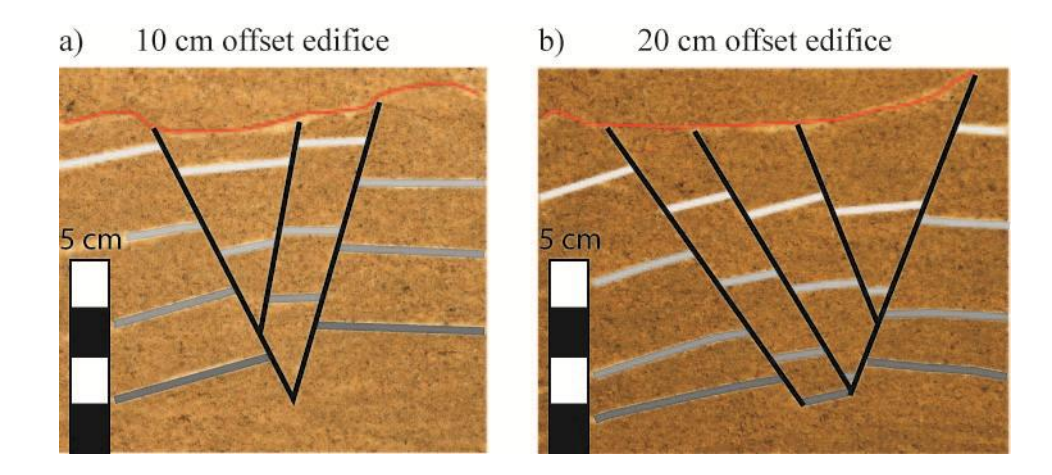
Cross sections and plan view images of select experiments. Thick black lines represent faults, thin red line represents the surface of the caldera. (a, b) For experiments where the caldera is either completely offset from the volcanic edifice, or the caldera is centered over the volcanic edifice, subsidence is controlled by inner sets of outward-dipping reverse faults. (b) Compared to a completely offset edifice shown in (a), subsidence is more piston-like when the edifice is centered. (c, d) For experiments where the caldera is partly offset relative to the edifice, subsidence was focused along an initial reverse fault followed by subsidence along antithetic graben structure on the opposite side of the caldera.



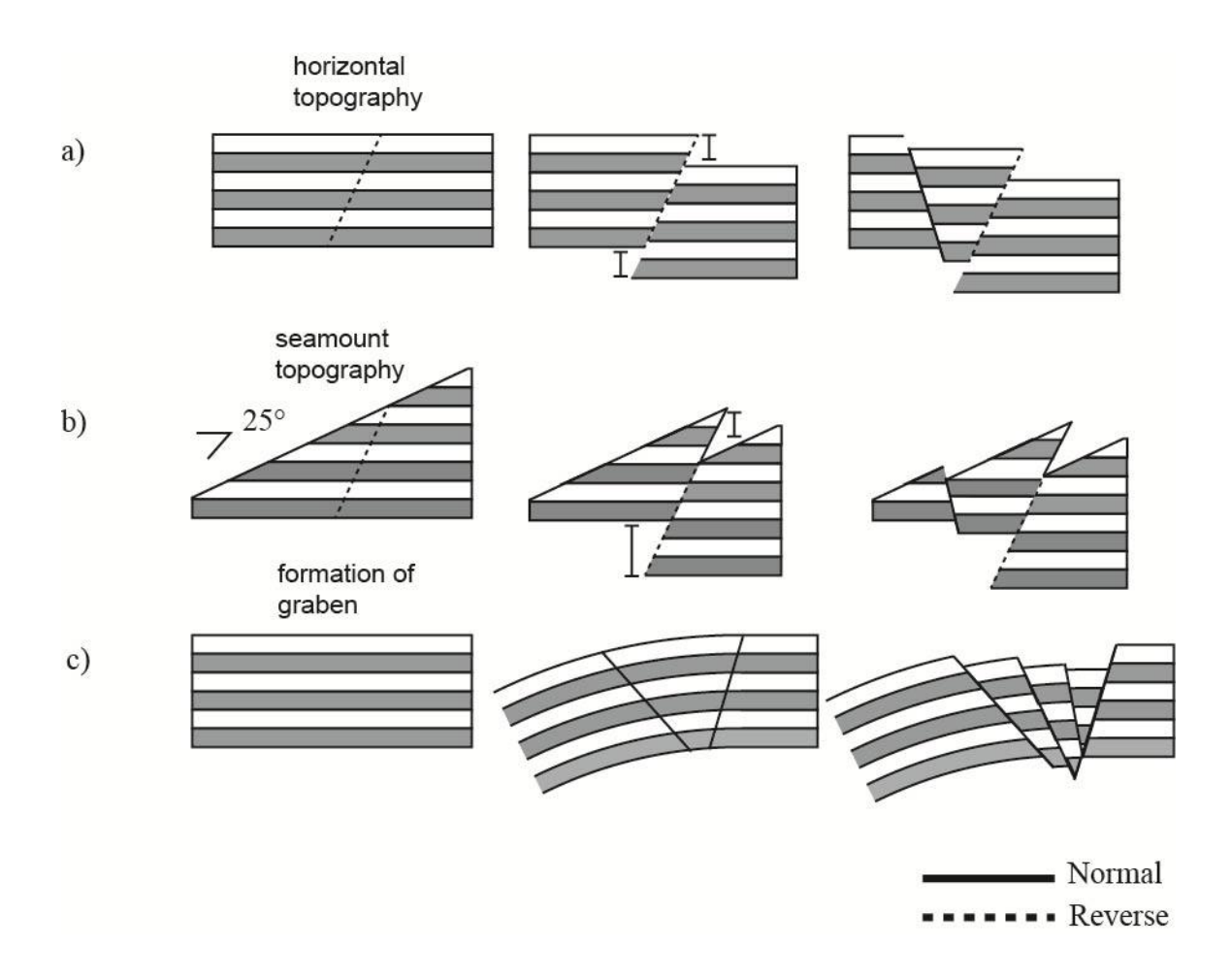
DPIV results for (a) a centered volcanic edifice and (b) a 20 cm offset volcanic edifice. A negative divergence value indicates regions where the vector field is converging. A positive divergence value indicates regions where the vector field is expanding. Regions of negative divergence highlight faults with a reverse motion, while regions of positive divergence highlight faults with a normal motion and downsag.



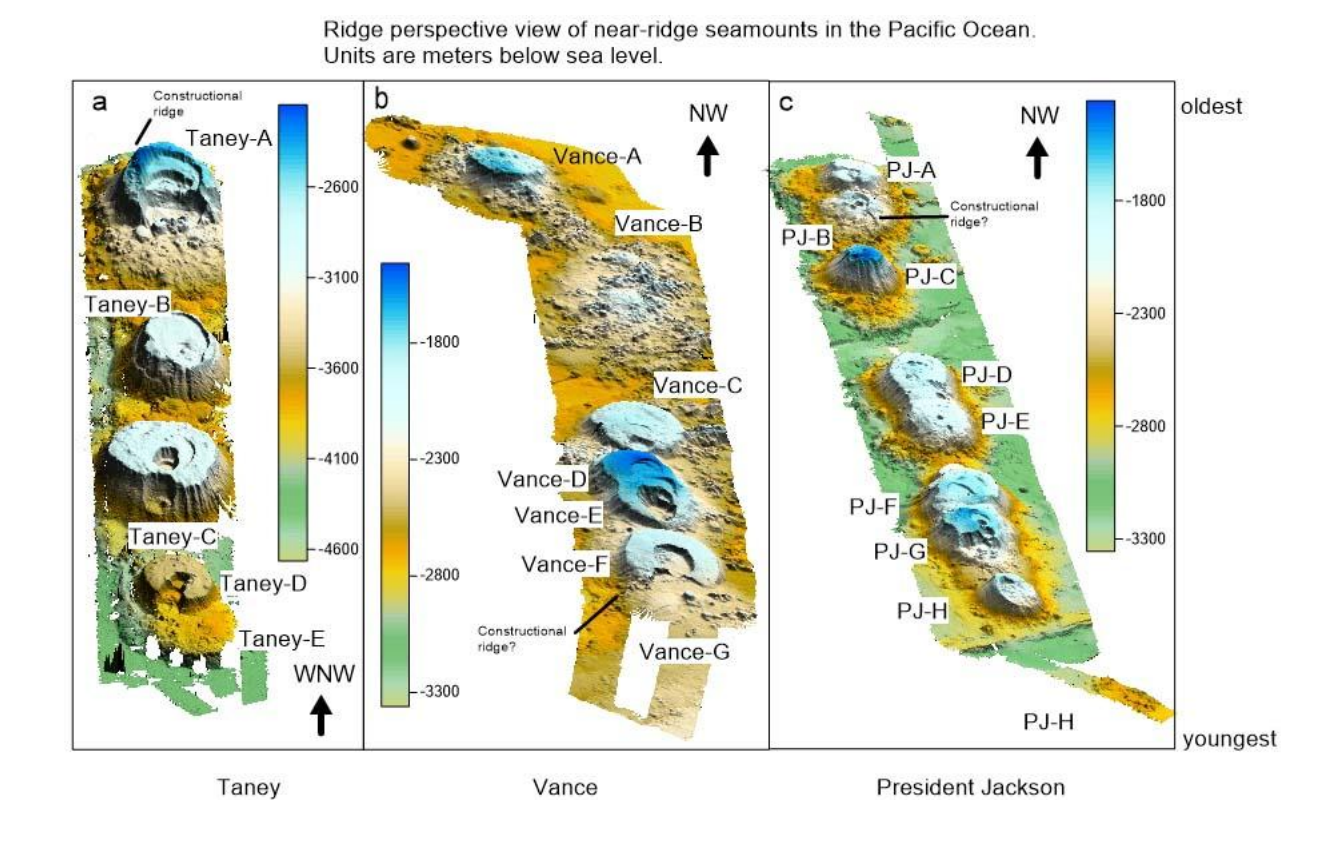
Close-up images of the graben structures that form in hinge zones of the offset edifice experiments for (a) 10 cm offset, and (b) 20 cm offset. The graben structures are bounded by outward-dipping and inward-dipping reverse faults resembling a keystone.



Schematic diagrams for fault mechanics observed in selected experiments associated with (a) peripheral extension resulting in formation of an inward-dipping normal fault (b) With a slope, greater subsidence is required on the hanging wall in order to provide sufficient gravitational instability to promote collapse on the overriding wedge. (c) The formation of a keystone graben is due to flexural tension from the inward tilting of the roof.

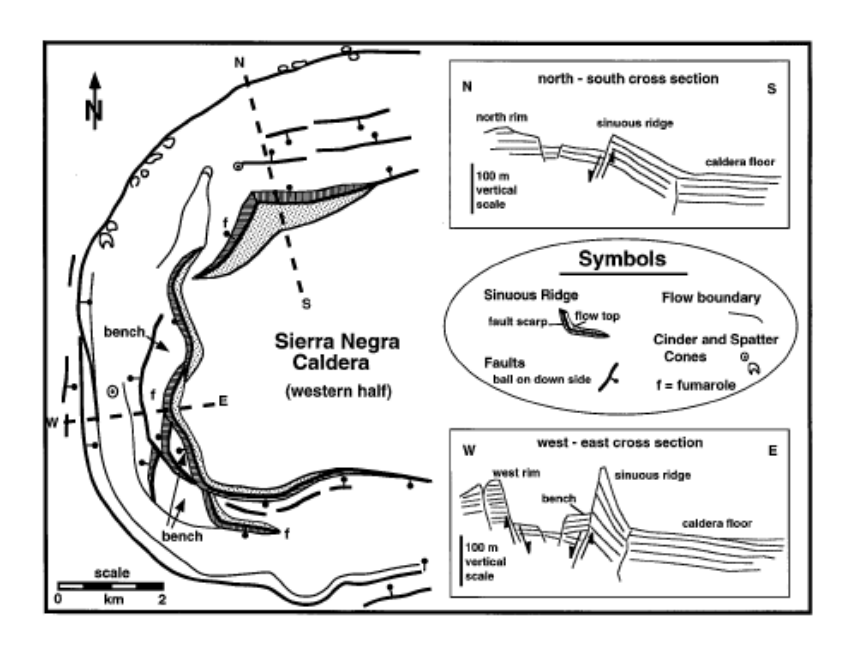


Digital elevation maps of near-ridge seamount chains in the northeast Pacific Ocean. Experiments performed in this study suggest that trapdoor caldera collapse on edifice flanks results in tilted calderas. Some offset calderas at near-ridge seamounts exhibit calderas that tilt towards the ridge axis, similar to our observations for a partly offset edifice caldera collapse. The presence of volcanic constructional ridges near caldera margins suggests that collapse-related structures may provide pathways for magma to the surface.



251

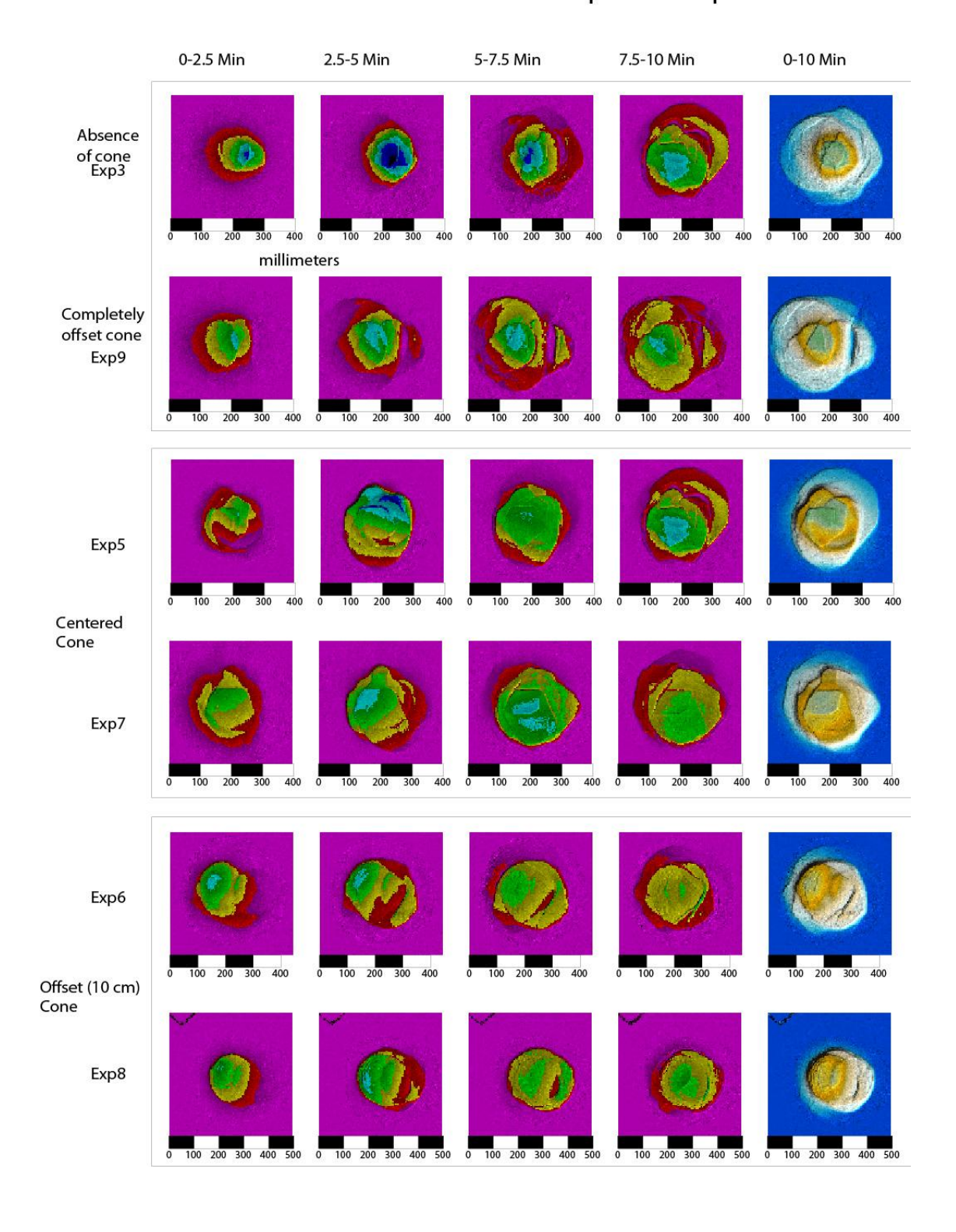
Geological map from Reynolds *et al.* (1995) showing the western part of the summit of Sierra Negra Galapagos Islands. Cross sections across the deformed region show a graben structure similar to our trapdoor caldera experiments formed by a partly offset volcanic edifice.



Supplementary Information S1: Reproducibility of experiments

Figure S1.1: Subsidence evolution of duplicate experiments during each 2.5 minute increment. The evolution of experiments without a cone, or a cone that is completely offset, is similar. The similar fault patterns and resulting subsidence evolution of duplicate experiments with a centered volcanic cone demonstrate that the observations presented in this paper are reproducible. The reproducibility of the asymmetric fault pattern for experiments with a 10 cm offset edifice shows that the formation of an antithetic graben is a robust feature of these experiments.

Subsidence evolution of duplicate experiments



CONCLUSIONS

The main findings of this thesis are the following:

- 1. Taney Seamount-A lavas vary from typical peridotite-derived mid-ocean ridge basalt compositions (N-MORB) to those with an apparent residual garnet signature. Geochemical and thermodynamic modelling demonstrates that decompression melting of a MORB mantle peridotite re-fertilized by garnet pyroxenite partial melts can reproduce the observed garnet signature.
- 2. Replenishing magmas contain large, anorthite-rich plagioclase with textural evidence of melt-rock interaction. The enrichment of elements in the lavas that are incorporated in plagioclase provides chemical evidence for melt-rock interaction.
- 3. Volatile saturation pressures of melt inclusions within the large anorthite-rich plagioclase crystals suggest that they are crystallizing at the Moho. Therefore, melt-rock interaction beneath Taney Seamount-A occurs in the lower oceanic crust or upper mantle prior to magmas entering the shallow sub-caldera plumbing system.
- 4. Melt inclusions within the anorthite-rich plagioclase exhibit compositions that are similar to lavas erupted on the edifice; these compositions cannot be generated by partial melting of the MORB mantle. A melt-rock interaction process defined by episodic partial melting, magma mixing, and recrystallization of plagioclase cumulates at the Moho reproduces the anomalous melt inclusion compositions. Diffusive interaction between later percolating melts and the plagioclase cumulate reproduces the melt-rock chemical signal observed in the erupted lavas.

- 5. Variations in lava geochemistry with time are consistent with an open-system sub-caldera reservoir that undergoes periodic collapse, replenishment, shallow crystallization, and eruption.
- 6. Analogue experiments of caldera collapse scaled to near-ridge seamounts indicate that the presence and position of a volcanic edifice has an important effect on the resulting caldera structure. A centered volcanic edifice promotes greater subsidence on an inner set of outward-dipping reverse faults and a more symmetric collapse style. By contrast, an offset volcanic edifice promotes trapdoor style caldera collapse on an asymmetric fault structure. Asymmetric collapse induced by the position of the edifice may cause the tilting of the caldera toward the ridge axis at near-ridge seamounts.

Contributions to knowledge

Geochemical analyses of lavas, crystals, and melt inclusions, complemented by geochemical modelling, constrain the magmatic processes that occur beneath Taney Seamount-A. The discovery of a magmatic architecture characterized by the melting of a mixed lithology mantle, melt-rock interaction at the Moho, and open-system evolution in a sub-caldera magma reservoir indicates that magmatic processes at near-ridge seamounts are more complicated than previously thought. This has important implications not only for the study of near-ridge seamounts, but other volcanoes in oceanic environments as well. Principally, this study illustrates the importance of understanding the full range of all magmatic processes that occur prior to eruption on the seafloor, before making assumptions about the nature of the magmatic source. This work also provides a large, detailed geochemical dataset for a single near-ridge seamount with a well-constrained relative chronology, a unique aspect of this study. Analogue studies of caldera collapse provide new insights into the effect of a volcanic edifice above a

magma reservoir. In particular, the evolution of trapdoor collapse and the resulting caldera structures are significant. These results have implications for near-ridge seamounts and other oceanic basaltic volcanoes, such as those found in the Galápagos Islands.

Topics for future research

Isotopic studies of the erupted lavas may provide complementary evidence for the importance of a garnet-bearing assemblage in the formation of Taney Seamount-A lavas. Specifically, the Lu-Hf isotopic system has been shown to be sensitive to partial melting in the presence of a garnet-bearing assemblage. Therefore, isotopic studies may provide further information on partial melting of a two-component mantle beneath near-ridge seamounts.

High resolution trace element analysis of the large anorthite-rich plagioclase crystals may help to further constrain the melt-rock interaction processes occurring at the Moho. In particular, analyses of elements with different diffusivities in plagioclase (e.g., Sr and Zr) could help to further refine the crystal-melt diffusion model presented in this study. Analyses of these elements may also provide further information on the variability of melts in contact with crystals. Recent trace element studies of high-anorthite plagioclase at mid-ocean ridge environments have shown that the variability is greater than that observed in melt inclusions.

Additional analogue experiments could be performed which investigate the role of ridgeparallel faults or previously-formed caldera faults on caldera collapse. Fault structures in the crust provide a zone of weakness which could preferentially facilitate subsidence during caldera collapse. Therefore, previously formed structures may have an effect, in addition to the presence and position of the volcanic edifice on the resulting caldera collapse behaviour at near-ridge seamounts.